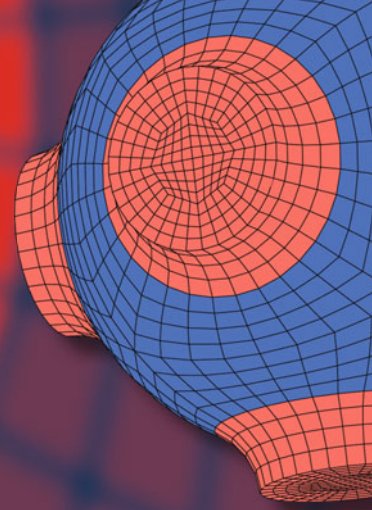Holm Altenbach
Danila Prikazchikov
Andrea Nobili  *Editors*

# Mechanics of High-Contrast Elastic Solids

## Contributions from Euromech Colloquium 626

Springer

# Advanced Structured Materials

Volume 187

**Series Editors**

Andreas Öchsner, Faculty of Mechanical Engineering, Esslingen University of Applied Sciences, Esslingen, Germany

Lucas F. M. da Silva, Department of Mechanical Engineering, Faculty of Engineering, University of Porto, Porto, Portugal

Holm Altenbach (D), Faculty of Mechanical Engineering, Otto von Guericke University Magdeburg, Magdeburg, Sachsen-Anhalt, Germany

Common engineering materials are reaching their limits in many applications, and new developments are required to meet the increasing demands on engineering materials. The performance of materials can be improved by combining different materials to achieve better properties than with a single constituent, or by shaping the material or constituents into a specific structure. The interaction between material and structure can occur at different length scales, such as the micro, meso, or macro scale, and offers potential applications in very different fields.

This book series addresses the fundamental relationships between materials and their structure on overall properties (e.g., mechanical, thermal, chemical, electrical, or magnetic properties, etc.). Experimental data and procedures are presented, as well as methods for modeling structures and materials using numerical and analytical approaches. In addition, the series shows how these materials engineering and design processes are implemented and how new technologies can be used to optimize materials and processes.

Advanced Structured Materials is indexed in Google Scholar and Scopus.

Holm Altenbach · Danila Prikazchikov ·
Andrea Nobili

Editors

# Mechanics of High-Contrast Elastic Solids

Contributions from Euromech
Colloquium 626

Springer

*Editors*
Holm Altenbach Ⓘ
Fakultät für Maschinenbau
Otto-von-Guericke-Universität
Magdeburg, Sachsen-Anhalt, Germany

Danila Prikazchikov Ⓘ
School of Computing and Mathematics
Keele University
Keele, Staffordshire, UK

Andrea Nobili Ⓘ
Department of Engineering Enzo Ferrari
University of Modena and Reggio Emilia
Modena, Italy

# Preface

This book is an outgrowth of the Euromech Colloquium No. 626 entitled "Mechanics of High Contrast Elastic Composites", held in a virtual format in the period 06–08 September 2021, under the auspices of the European Society of Mechanics. During this event, which attracted 56 participants from 19 countries, it could be noted that a variety of interesting phenomena arises when widely different mechanical properties are cunningly joined together to produce new composite materials. This fruitful meeting paved the way for developing a new insight into the diverse and multifaceted realm of engineered materials and the applications thereof. Falling upon these lines, this volume collects 14 papers elaborating the outcome of high contrast from different complementary perspectives, ranging from experimental to numerical results, from analytical investigation to mathematical modelling. The spectrum of the addressed topics is wide in nature, as it moves from the strength of bio-inspired composites to stochastic homogenisation of high-contrast media while sweeping through delicate aspects in the formulation of boundary conditions arising from a generalisation of Saint-Venant's principle in strongly inhomogeneous laminates, yet encompassing asymptotically consistent theories of micro-structured plates and metamaterials for extreme deformations, etc. As cases in point of the diverse outcomes associated with high contrast, we point to studies on the dynamics of bi-laminated plates with a soft viscoelastic core as well as to novel results concerning engineered aggregates for the enhanced dynamic performance of concrete (meta-concrete).

Besides its natural academic interest, the subject matter of this volume is additionally motivated by conspicuous practical applications, among which we mention the development of lightweight structures, novel biomedical composites, and the design of soft robotics, to name only a few. Great emphasis is placed on the development of mathematical models as well as on their extrapolation. In this context, the study of layered structures takes paramount importance for it offers great insight into more complex problems while expressing the most common structure of composite materials. Along this line, the mechanics of layered elastic structures is considered to address the statics, dynamics, and buckling of multi-layered high-contrast plates (C. Boutin). Equally, studies on the delamination between the layers of a three-layered shell (L. Aghalovyan et al.) are reported, as well as the use of dispersive analysis to

detect the presence of a sandy layer in a stratified half-space (Sergey V. Kuznetsov). Another important topic covered in this volume is related to the consideration of reinforced materials and structures, featuring a review of the multiform approaches pursued in the literature (H. Altenbach), as well as consideration of a technical multiple particle inverse problem for fibre-reinforced composites (V. Mityushev et al.). One more relevant area of investigation concerns periodic media and, specifically, the study of frequency bands in silver-mean quasi-crystalline-generated waveguides (Z. Chen et al.), the proposition of tunable porous periodic structures (J. Li et al.), a generalisation of the Fourier Law of heat transfer in 1D nonlocal lattices with short and long interactions (E. Nuñez del Prado et al.), the calculation of effective properties of multi-phase periodic laminated Cosserat composite by means of a two-scale homogenisation technique (Y. Espinosa-Almeyda et al.), and the investigation of the dynamic response of a beam with an attached periodic array of resonators (M. Nieves and A. Movchan). Also, we mention the contributions dealing with finite multi-component structures, including a numerical approach to nonlinear vibrations of stepped beams and frames with high-contrast elastic properties (R. Pušenjak and A. Nikonov), a study of localised vibrations in two-component cylindrical panels (G. Ghulghazaryan and L. Ghulghazaryan), and investigation of the snap-through instability of the von Mises two-bar truss (M. Pelliciari et al.). Finally, the dynamic modelling of silica aerogels is investigated, accounting for micro-structural effects in such highly inhomogeneous lightweight composites (R. Abdusalamov et al.). We hope that the enthusiasm and dedication of these valuable contributions may form an interesting read for the mechanics community.

Magdeburg, Germany                                                        Holm Altenbach
Modena, Italy                                                                  Andrea Nobili
Keele, UK                                                            Danila Prikazchikov
September 2022

# Contents

# Chapter 1
# Adjustment of Micro-structure Parameters of Aggregated Structures for Dynamic Modeling of Silica Aerogels

**Rasul Abdusalamov, Mikhail Itskov, Julius Kaplunov, and Danila Prikazchikov**

**Abstract** This paper is concerned with elucidating the effect of aggregated structures of silica aerogels on their dynamic behavior. The micro-structure is modeled using the diffusion-limited cluster–cluster aggregation method. The eigenfrequencies are evaluated numerically by the finite element method for the aggregated structures. The obtained results are compared with the analytical and numerical solutions for a representative cuboid volume of a homogeneous linearly elastic material subject to periodic boundary conditions for displacements. In this case, the interpretation of finite element computations is not straightforward since the eigenforms corresponding to periodic boundary conditions depend on arbitrary phase shifts in sinusoidal functions. Although the developed approach appears to be robust for matching the smallest eigenfrequencies, its implementation to higher ones may apparently need establishment of a more elaborated continuum framework.

## 1.1 Introduction

The first aerogel was created in 1931 by Samuel Stephens Kistler and his colleagues by replacing the liquid in jelly with gas without causing shrinkage [1]. They created a nanostructured open porous solid with incredibly fascinating properties. Up until today, aerogels are renowned in particular for their extremely low density and high porosity. Through the years the synthesis process (sol–gel process) of aerogels has changed, nevertheless, their fascinating properties remain. The variety of aerogel

R. Abdusalamov (✉) · M. Itskov
Department of Continuum Mechanics, RWTH Aachen University, Aachen, Germany
e-mail: abdusalamov@km.rwth-aachen.de

M. Itskov
e-mail: itskov@km.rwth-aachen.de

J. Kaplunov · D. Prikazchikov
School of Computing and Mathematics, Keele University, Keele, United Kingdom
e-mail: j.kaplunov@keele.ac.uk

D. Prikazchikov
e-mail: d.prikazchikov@keele.ac.uk

types ranges from polymer to carbon, cellulose, and starch aerogels. However, silica aerogels are the most widely used ones and are also examined in this work. Silica aerogels have large sound absorption properties and very low sound velocities. Additionally, their extremely low thermal conductivity makes them an ideal thermal isolator. They are quite brittle and their mechanical properties highly depend on the fractality of the micro-structure. Yet, their application ranges from thermal insulation of houses and pipelines to aerospace applications.

The mechanical properties of aerogels have been analyzed in various studies and modeling approaches for the prediction of their material behavior have likewise been investigated [2–4]. The modeling approaches range from classical continuum mechanical solutions to using atomistic and mesoscale methods [5–7]. The focus of most investigations lies in determining the effects of structural characteristics on the overall mechanical properties. Therefore, properties such as the fractal dimension and the pore size distribution are correlated to experimental data. A common coarse-grained simulation approach is the micro-structure generation using the diffusion-limited cluster–cluster aggregation (DLCA) method. The sol–gel process is mimicked by the random bonding of particles and the generation of clusters. As discovered by Hasmy et al. [8] the structures generated using the DLCA method had structural and mechanical properties that agreed well with experimental results.

Although the acoustic properties of aerogels are equally fascinating, so far they have not been extensively studied from the experimental point of view as well as in the domain of modeling. One of the first experimental investigations by Gross et. al. determined the longitudinal sound velocity for varying densities [3]. An important observation was that the air pressure inside the pores had no influence on the sound velocity leading to the conclusion that the interaction between the skeleton and the air inside the pores has no influence. Additionally, the sound velocity scales according to a simple power law with $c_1 \propto \rho^\alpha$ with respect to the density $\rho$. The exponent $\alpha$ was determined with 1.3 [9]. Among the modeling approaches, the Johnson–Champoux–Allard (JCA) [10] has been used so far for the determination of the sound absoption coefficients of silica aerogel granules which can be used in aircraft cabins [11, 12].

To the best of our knowledge, the effect of the micro-structure on the acoustic properties has not been investigated from a modeling point of view. The approach of this work is the investigation of the acoustic properties of micro-structures generated using the DLCA method by performing a modal analysis. The eigenfrequencies determined by this means are compared with the eigenfrequencies obtained from an analytical approach describing the dispersion relation. In addition, a numerical continuum mechanical modal analysis is performed and compared with the analytical and the numerical DLCA model results. The generation of the cluster structures is explained in Sect. 1.2. Furthermore, the derivation of the dispersion relation is presented. A testing framework for comparing the analytical and numerical results is presented in Sect. 1.3. Last but not least, the presented work is summarized in Sect. 1.4.

## 1.2 Methodology

In this section, the diffusion-limited cluster–cluster aggregation (DLCA) method will be explained in detail. An explanation is given of how the method works and how it has been implemented for modal analysis. Furthermore, an analytical solution for the derivation of the dispersion relation is presented, which is used for the comparison with the numerical approach.

### 1.2.1 Diffusion-Limited Cluster–Cluster Aggregation (DLCA) Method

The DLCA method is one of the many aggregation approaches that lead to the generation of cluster structures through the Brownian motion of particles. The initial method was proposed by Meakin [13] as well as Botet and Jullien [14]. An adapted procedure of the algorithm is shown in Sect. 1.1. Although the algorithm is executed in 3D, for the sake of simplification, the explanation will be provided in 2D. First, a cuboid with periodic boundary conditions is created. Subsequently, two types of particles, referred to as walker and seed particles are initialized at random or specified positions within the periodic domain (see Fig. 1.1a). Both seeds and walkers undergo a random walk process and once a walker undercuts a critical distance $\varepsilon_{\mathrm{krit}}$ to a seed it diffuses to the seed and becomes a seed itself. Both particles are permanently connected for future time steps. Gradually, walker particles diffuse, and clusters are formed (see Fig. 1.1b and c). Two different clusters can also be connected if the distance between any two particles falls below $\varepsilon_{\mathrm{krit}}$ (see Fig. 1.1d). The process stops once a single cluster structure forms (see Fig. 1.1e). This algorithm has different inputs that can influence the structural properties of the final cluster. These inputs are for example the particle radius $r$, the seed and walker step sizes, $s_{\mathrm{S}}$ and $s_{\mathrm{W}}$, specifying that the distance particles can walk in a time step as well as the particle concentration $\bar{\rho}$. The DLCA method was implemented in MATLAB and *exports an Abaqus input deck*. A representative volume element (RVE) is created for FEM simulations. Each



(a) Time step 1    (b) Time step 2    (c) Time step 3    (d) Time step 4    (e) Time step 5
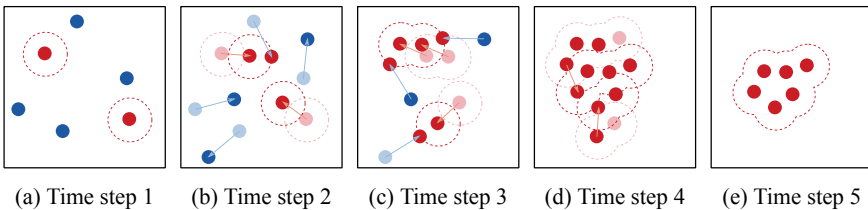
**Fig. 1.1** Visualization of DLCA algorithm with seeds (red) and walkers (blue) in a 2D domain for different time steps. With each time step, walker particles are connecting to the seeds resulting in the formation of clusters

particle connection is modeled as beam element, thus all three deformation modes of a particle bond, namely bending, torsion, and stretching can be described. Periodic boundary conditions replace particle connections that cross the domain boundaries. Note that Young's modulus for each beam elements was adjusted for each aggregated structure such that the overall stiffness response corresponds to the provided Young modulus of the considered silica aerogel. Poisson's ratio is specified as obtained from the density-dependent experimental values.

### *1.2.2  Derivation of the Dispersion Relation*

The displacement vector $u$ can be decomposed by means of the Helmholtz theorem as $u = \mathrm{grad}\varphi + \mathrm{curl}\Psi$, where $\varphi$ and $\Psi$ are known as the longitudinal potential and the shear potential, respectively. Thus, under the assumption of time-harmonic dependence of the displacements and potentials, the two Helmholtz equations of motion are given by

$$\Delta\varphi + \frac{\omega^2}{c_1^2}\varphi = 0 \qquad \text{and} \qquad \Delta\Psi + \frac{\omega^2}{c_2^2}\Psi = 0 \,, \qquad (1.1)$$

where $\omega$ is frequency, $c_1$ and $c_2$ denote the longitudinal and shear wave speeds, respectively, and the time dependent factor $\exp(-i\omega t)$ is omitted for brevity. Consider, for example, the longitudinal wave potential $\varphi$, with the procedure for the shear potential being very similar. For a domain within the Cartesian coordinates $x, y, z$ occupying a cuboid with associated dimensions $l_1$, $l_2$, and $l_3$ (see Fig. 1.2), the periodicity conditions are provided for the scalar potential $\varphi$ in the form

$$\varphi(x, y, z, t) = \varphi(x + l_1, y, z, t) = \varphi(x, y + l_2, z, t) = \varphi(x, y, z + l_3, t) \,. \quad (1.2)$$

Note that for this type of conditions, a periodic solution of $(1.1)_1$, $(1.2)$ is found as

$$\varphi = A \cos\left[\frac{2\pi n_1 x}{l_1} + \gamma_1\right] \cos\left[\frac{2\pi n_2 y}{l_2} + \gamma_2\right] \cos\left[\frac{2\pi n_3 z}{l_3} + \gamma_3\right] \,, \qquad (1.3)$$

specified up to the arbitrary value of phase shifts $\gamma_i$, $i = 1, 2, 3$. Here the integers $n_1$, $n_2$, and $n_3$ correspond to the mode number in the corresponding direction. For the analytical solution, an elastic layer with periodic boundary conditions corresponding to the micro-structure of a silica aerogel is considered (see Fig. 1.2).

On substituting the solution (1.3) into the governing Helmholtz equation $(1.1)_1$, the following dispersion relation can be derived

$$\frac{\omega_i l_3}{2\pi c_i} = \sqrt{\frac{l_3^2 n_1^2}{l_1^2} + \frac{l_3^2 n_2^2}{l_2^2} + n_3^2} \quad \text{with} \quad i = 1, 2 \quad \text{and} \quad n_1, n_2, n_3 = 1, 2 \ldots n \,,$$
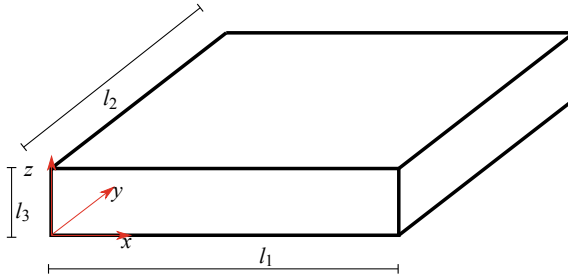
**Fig. 1.2** Sketch of periodic aerogel RVE micro-structure with the cuboid side lengths $l_1$, $l_2$, and $l_3$. The given lengths will be used to generate aggregated structures using the DLCA method as well as to generate a continuous structure for comparison

where $\omega_i$ is the angular frequency. In the low frequency range, it can be assumed that $n_3 = 0$ and $n_1 \sim n_2 \sim 1$, thus the dispersion relation is simplified to

$$\omega_i = 2\pi c_i \sqrt{\frac{n_1^2}{l_1^2} + \frac{n_2^2}{l_2^2}} \; . \tag{1.4}$$

This continuum mechanics approach will be compared with the modal analysis of the RVE model for the micro-structure as well as with the modal analysis of a continuous model within the same length scale.

For high frequencies, when $n_1 \sim n_2 \sim n_3 \sim 1$, the dispersion relation can be approximated with $\frac{l_3}{l_1} = \varepsilon \ll 1$ by

$$\frac{\omega_i l_3}{2\pi c_i} \approx n_3 \left[ 1 + \varepsilon^2 \left( \frac{n_1^2 + n_2^2}{2 n_3^2} \right) \right] \; .$$

## 1.3  Comparison of Analytical and Numerical Results

In [3], the longitudinal and shear wave velocities as well as Young's modulus and Poisson's ratio for aerogels of different densities have been measured (see Table 1.1). However, the fractality, as well as the particle size of the specified samples are not provided in this study. Thus, it is not entirely possible to correlate the aerogel structures with the DLCA clusters. Nevertheless, numerical simulations can help to understand the effect of the fractality as well as the particle size on the overall dynamic properties. With the known skeleton densities of the silica aerogel samples, one can evaluate the concentration. The porosity $\phi$ of the aerogels is calculated using the bulk density $\rho_a = 2200 \frac{\text{kg}}{\text{m}^3}$ and the skeleton density $\rho_s$ by (see [15])

**Table 1.1** Density dependent aerogel properties from [3] specifying the skeleton density $\rho_s$, static Young's modulus $E_s$, Young's modulus from sound velocity $E_c$, Poisson's ratio $\nu$ as well as longitudinal and transverse sound velocities $c_1$ and $c_2$

| $\rho_s\left[\frac{\text{kg}}{\text{m}^3}\right]$ | $E_s\left[\frac{\text{MN}}{\text{m}^2}\right]$ | $E_c\left[\frac{\text{MN}}{\text{m}^2}\right]$ | $\nu$ | $c_1\left[\frac{\text{m}}{\text{s}}\right]$ | $c_2\left[\frac{\text{m}}{\text{s}}\right]$ |
|---|---|---|---|---|---|
| 78 | $1.2 \pm 0.1$ | $1.04 \pm 0.01$ | 0,205 | $122.3 \pm 0.1$ | $74.5 + \pm 0.5$ |
| 158 | $3,25 \pm 0.08$ | $3,39 \pm 0.05$ | 0,228 | $157.4 \pm 0.5$ | $93.4 \pm 1$ |
| 262 | $11,8 \pm 0.2$ | $24,8 \pm 0.2$ | 0,22 | $330 \pm 1$ | $197 \pm 5$ |

$$\phi = 1 - \frac{\rho_a}{\rho_s} = 1 - \bar{\rho} \ .$$

Thus, the values of the concentration $\bar{\rho}$ may be calculated for the three scenarios considered in Table 1.1, resulting in $\bar{\rho}_1 = 0.0355$, $\bar{\rho}_2 = 0.0718$, and $\bar{\rho}_3 = 0.1191$. For the simulations below, the unit system is set to [nm,ng,ms]. In this case, the resulting eigenfrequencies will be determined in kHz. The numerical experiments are initially limited to aerogels with the density $\rho = 158\,\text{kgHz}^3$. For the Abaqus calculations, the Lanczos eigensolver is adapted. In total, 100 eigenmodes are determined.

### 1.3.1 Testing of the Abaqus Code for a 3D Continuous Elastic Layer

For the purpose of the eigenmode visualization, the dimensions of the cuboid are specified as $h = \sqrt{5} \cdot 150\,\text{nm}$, $l_1 = \sqrt{3} \cdot 150\,\text{nm}$ and $l_2 = 150\,\text{nm}$. The eigenmodes may be determined for the low frequency case with $n_3 = 0$ and $n_1 \sim n_2 \sim 1$, see (1.4), using the material properties specified in Table 1.1. The results corresponding to the longitudinal and shear wave speeds $c_1$ and $c_2$ are displayed in Tables 1.2 and 1.3.

The eigenfrequencies versus the mode numbers are also shown in Fig. 1.3 and compared with the numerical data for a continuous structure. The mode type is classified for the obtained numerics. The latter coincide well with analytics. Only the

**Table 1.2** Eigenfrequencies $\omega_1$ for $n_1$ and $n_2$ for $c_1$ in MHz

| $n_2 \setminus n_1$ | 0 | 1 | 2 | 3 | 4 |
|---|---|---|---|---|---|
| 0 | 0.00 | 2948.55 | 5897.10 | 8845.65 | 11794.20 |
| 1 | 3806.56 | 4814.96 | 7018.95 | 9629.92 | 12393.26 |
| 2 | 7613.12 | 8164.16 | 9629.92 | 11670.69 | 14037.90 |
| 3 | 11419.68 | 11794.20 | 12852.43 | 14444.88 | 16416.83 |
| 4 | 15226.24 | 15509.11 | 16328.32 | 17609.20 | 19259.84 |

**Table 1.3** Eigenfrequencies $\omega_2$ for $n_1$ and $n_2$ for $c_2$ in MHz

| $n_2 \setminus n_1$ | 0 | 1 | 2 | 3 | 4 |
|---|---|---|---|---|---|
| 0 | 0.00 | 1749.65 | 3499.29 | 5248.94 | 6998.59 |
| 1 | 2258.78 | 2857.16 | 4164.99 | 5714.32 | 7354.07 |
| 2 | 4517.57 | 4844.55 | 5714.32 | 6925.30 | 8329.99 |
| 3 | 6776.35 | 6998.59 | 7626.54 | 8571.49 | 9741.62 |
| 4 | 9035.14 | 9202.99 | 9689.11 | 10449.17 | 11428.65 |

**Fig. 1.3** Visualization of eigenfrequencies over mode number for longitudinal and transverse sound velocities $c_1$ and $c_2$ as well as the results from the modal analysis of the continuous structure
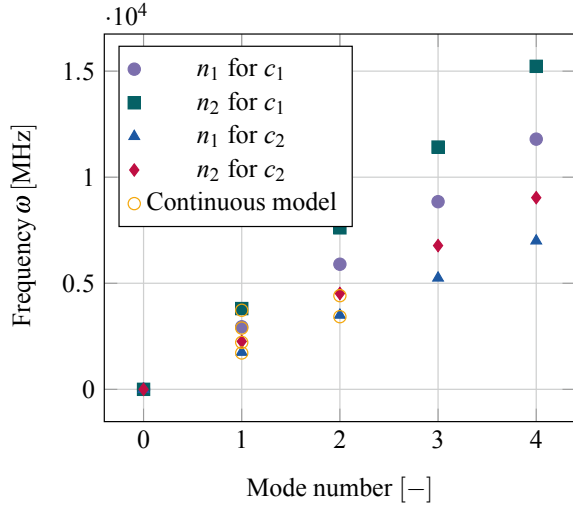


first 7 eigenmodes have been determined numerically; for a greater frequency, a finer mesh is required. It should also be noted that Abaqus indicates several eigenmodes for certain eigenfrequencies, due to arbitrary phase shifts $\gamma_i$ in formula (1.3). One eigenmode is illustrated in Fig. 1.4.

### 1.3.2 Numerical Analysis of Cuboid DLCA Structure

For the numerical investigation of the cuboid DLCA structures, a total of 25 samples have been investigated. All clusters have been generated with a concentration of $\bar{\rho}_2 = 0.0718$. The particle radii have been varied and are specified with $r \in [5.5 \text{ nm}, 5.0 \text{ nm}, 4.5 \text{ nm}, 4.0 \text{ nm}, and \text{ } 3.5 \text{ nm}]$. The seed and walker step sizes where given with $s_S = 0.3$ nm and $s_W = 0.3$ nm. A total of 5 clusters are generated for each parameter combination.

The influence of the particle radius on the eigenfrequencies can also be determined (see Fig. 1.5). With decreasing radius, the eigenfrequencies tend to decrease too.
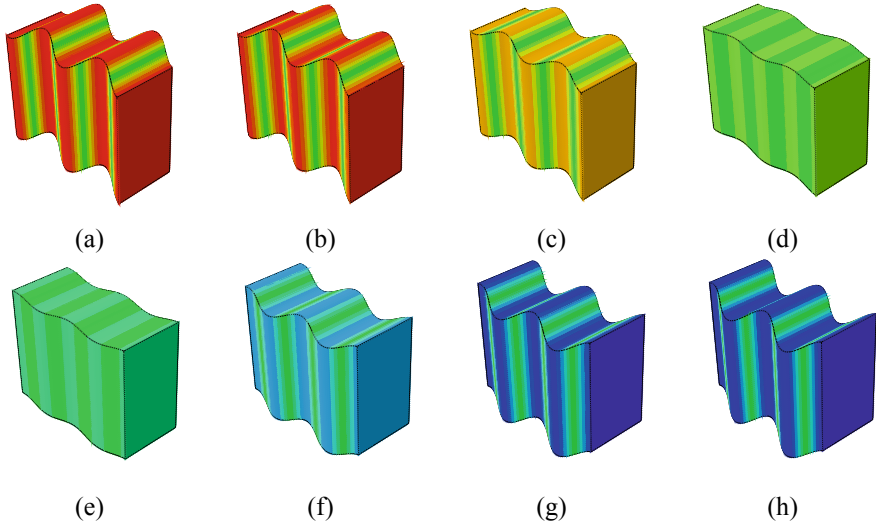
**Fig. 1.4** Eigenmodes for a continuous plate

**Fig. 1.5** Influence of the particle radius on the eigenfrequencies
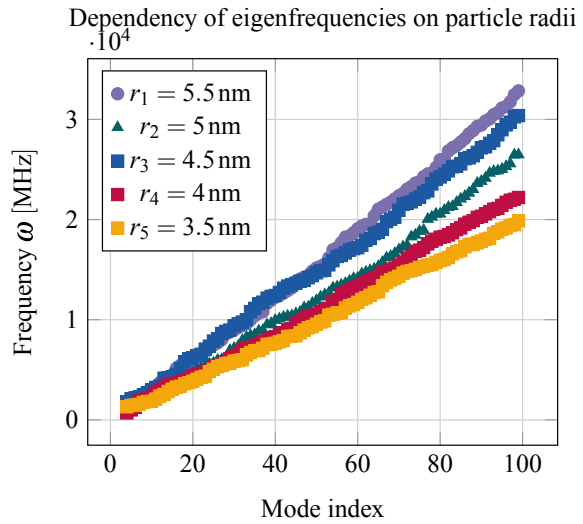


Note that here the mode index is depicted since the classification of eigenmodes is challenging. It is not possible to classify the eigenmodes properly due to the fact that the structure is randomly generated. Since tangling bonds are not removed, they appear to create eigenfrequencies which have localized effects. Additionally, several modes can be determined for one specific frequency, since the phase shift is not determined uniquely. Nevertheless, due to the fact that the properties of the micro-

**Fig. 1.6** Visualization of the dependency of the first eigenfrequency on the particle radius

Dependency of first eigenfrequency on particle radius
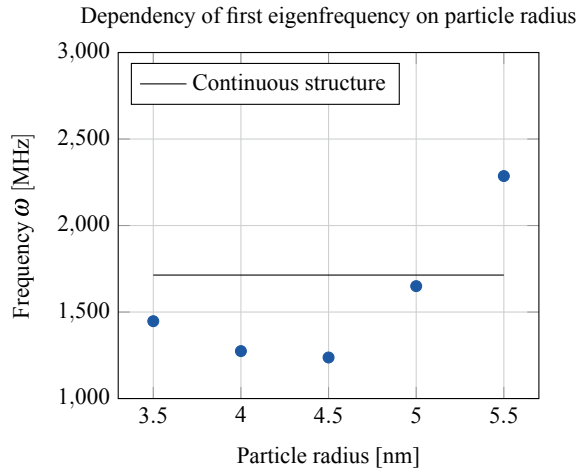


structure are not known, a clear correlation is not possible. However, a qualitative effect of changing the particle size seems to have an effect on the eigenfrequency.

Furthermore, one can note that the influence of the particle radius on the first eigenfrequency seems to differ from the general tendency. As visualized in Fig. 1.6, it appears that depending on the particle size of the aggregated structure the first eigenfrequency is the smallest for a particle size of 4.5 nm. For comparison, the first determined natural frequency from the continuous structure was depicted. Thus, the effect of the radius seems to be nonlinear. Of particular interest would be a comparison with experimental results where micro-structural parameters are known.



(a)                 (b)                 (c)                 (d)

(e)                 (f)                 (g)                 (h)
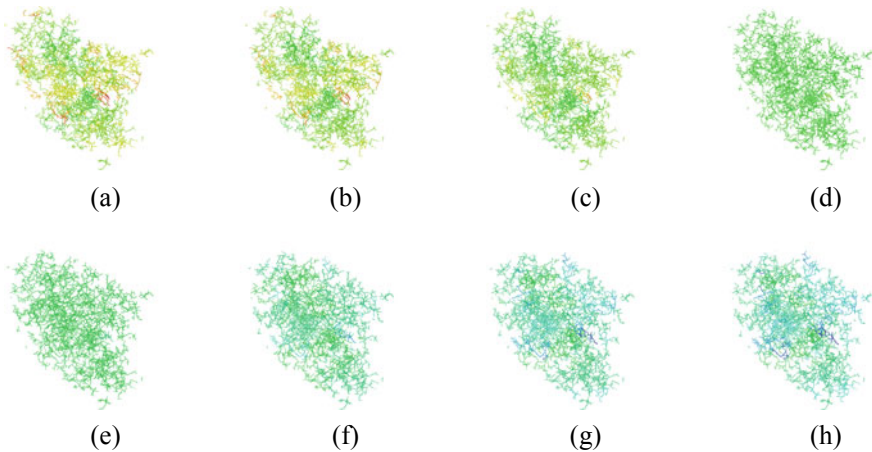
**Fig. 1.7** Visualization of an eigenmode for DLCA structure with the particle radius of 3.5 nm

In addition, for a structure with the particle radius of 3.5 nm, one eigenmode is visualized in Fig. 1.7. Compared to the continuous structure, it is clearly visible that it is harder to characterize the eigenmode.

## 1.4   Conclusions

The classification of eigenmodes appears to be non-trivial even for the classical linear isotropic framework. The point is that for chosen periodic boundary conditions imposed on the displacements the eigenfunctions of interest depend not only on arbitrary amplitudes, but also on an additional shifts in phases, see (1.3). To the best of our knowledge, the implementation of such periodic conditions for modal analysis within Abaqus has not been yet fully understood. As a result, interpretation of the numerical data causes substantial challenges.

The classification of the eigenmodes of the aggregated structures is an even greater problem due to a number of sophisticated phenomena, including the randomness of the structure and extra localized vibration modes caused by the so-called dangling bonds, e.g. see [16]. It is also observed that the particle size significantly effects the values of eingenfrequencies for aggregated structures with the same concentration.

The developed approach is robust to adjust micro-structure parameters enabling to match the smallest eigenfrequency (see Fig. 1.6). At the same time, matching of higher eigenfrequencies is not that straightforward because of the above mentioned challenges. In addition, even for the smallest eigenvalue, a further validation of the obtained results based on experimental measurements, including micro-structural characterization, is required. In this case, a more sophisticated continuum model than given by Eqs. (1.1) might be adapted.

## References

1. Kistler SS (1931) Coherent expanded aerogels and jellies. Nature 127(3211):741
2. Parmenter KE, Milstein F (1998) Mechanical properties of silica aerogels. J Non-Cryst Solids 223(3):179–189
3. Gross J, Reichenauer G, Fricke J (1988) Mechanical properties of sio2 aerogels. J Phys D Appl Phys 21(9):1447
4. Woignier Thierry, Primera Juan, Alaoui Adil, Etienne Pascal, Despestis Florence, Calas-Etienne Sylvie (2015) Mechanical properties and brittle behavior of silica aerogels. Gels 1(2):256–275
5. Patil Sandeep P, Rege Ameya, Itskov Mikhail, Markert Bernd (2018) Fracture of silica aerogels: an all-atom simulation study. J Non-Cryst Solids 498:125–129
6. Maximiano Pedro, Durães Luísa, Simões Pedro (2019) Overview of multiscale molecular modeling and simulation of silica aerogels. Ind Eng Chem Res 58(41):18905–18929

7. Abdusalamov Rasul, Scherdel Christian, Itskov Mikhail, Milow Barbara, Reichenauer Gudrun, Rege Ameya (2021) Modeling and simulation of the aggregation and the structural and mechanical properties of silica aerogels. J Phys Chem B 125(7):1944–1950 PMID: 33566614

8. Hasmy A, Foret M, Pelous J, Jullien R (1993) Small-angle neutron-scattering investigation of short-range correlations in fractal aerogels: Simulations and experiments. Phys Rev B Condens Matter 48(13):9345–9353

9. Gross J, Fricke J, Hrubesh LW (1992) Sound propagation in sio2 aerogels. J Acoust Soc Am 91(4):2004–2006

10. Johnson DL, Koplik J, Dashen R (1987) Theory of dynamic permeability and tortuosity in fluid-saturated porous media. J Fluid Mech 176:379–402

11. Abawi Y, Langfeldt F, Gleine W, Milow B (2020) Application of the Johnson-Champoux-Allard model for the calculation of the sound absorption coefficient of aerogel granules based on inverse characterization for the determination of the granules parameters. DAGA 2020-46. Jahrestagung für Akustik

12. Hesse C, Allebrodt P, Rege A (2020) Multi-Physikalische Untersuchungen zum Transmissionsverhalten neuartiger Kabinenseitenwände. Deutsche Gesellschaft für Luft-und Raumfahrt-Lilienthal-Oberth eV

13. Meakin Paul (1983) Formation of fractal clusters and networks by irreversible diffusion-limited aggregation. Phys Rev Lett 51:1119–1122

14. Botet R, Jullien R (1988) A theory of aggregating systems of particles: the clustering of clusters process. In: Annales de Physique, vol 13. EDP Sciences, pp 153–221

15. He Song, Huang Yajun, Chen Guangnan, Feng Mengmeng, Dai Huaming, Yuan Bihe, Chen Xianfeng (2019) Effect of heat treatment on hydrophobic silica aerogel. J Hazard Mater 362:294–302

16. Ma H-S, Roberts AP, Prévost J-H, Jullien R, Scherer GW (2000) Mechanical structure–property relationship of aerogels. J Non-Cryst Solids 277(2-3):127–141

# Chapter 2
# 3D Dynamic Problems for Three-Layered Shells with Delamination Between the Layers

**Lenser Aghalovyan, Lusine Ghulghazaryan, and Parandzem Hambardzumyan**

**Abstract** 3D dynamic problems for three-layered orthotropic elastic shells are considered, with a free upper face and prescribed displacements between the first and second layers with the conditions of ideal contact and with a separation between the second and third layers. A long-wave asymptotic solution has been constructed, and the thickness resonances have been determined. The obtained results may find further applications in the evaluation of the parameters of earthquakes.

**Keywords** Asymptotic method · Layered shell · Inclinometer · Earthquake prediction

## 2.1 Introduction

Lithospheric plates of the Earth are natural layered structures. The vast majority of earthquakes are the result of tectonic movements of the Earth's Lithospheric plates and their interactions, which are subject to relative movements along their contacting surfaces ("seismic zones") [1].

Two types of tectonic movements of the Lithospheric plates are marked out depending on the origin of the earthquakes: slow-moving (age-old) and fast-moving (jump-like). Slow-moving processes are quasi-static and can last for tens of years; as a result, deformations accumulate in the Lithospheric plates and individual blocks of the Earth's crust, which, having reached a critical value of the order of $10^{-4}$, and according to the well-known Japanese seismologist Rikitake [2], about $4.7 * 10^{-5}$, lead to global destruction (earthquake), and the main part of the huge potential deformation energy accumulated over the years is released in the form of bulk elastic

L. Aghalovyan · L. Ghulghazaryan (✉)
Institute of Mechanics of NAS RA, Yerevan, Armenia
e-mail: lusina@mail.ru

L. Aghalovyan
e-mail: lagal@sci.am

L. Ghulghazaryan · P. Hambardzumyan
Armenian State Pedagogical University, Yerevan, Armenia

longitudinal P- and shear S-waves, as well as Rayleigh and Love surface waves. Since the speed of propagation of longitudinal waves is always greater than the speed of propagation of transverse waves, by fixing the time of arrival of these waves at a given point, by their difference, it is possible to establish the distance of the earthquake source from a given station, and according to the data of three stations, its location. Fast-moving processes (foreshock, earthquake, aftershock) are dynamic and for their description, it is necessary to solve the corresponding nonclassical dynamic problem of the theory of elasticity for a layered packet. The problem is called nonclassical in the sense that the boundary conditions are set only on the front surface of the packet. In order to reduce the influence of measurements of external anomalous (mainly atmospheric) factors on the data of truly occurring processes inside the package (Lithospheric Plate), in seismology, measuring instruments (inclinometers, strainmeters, etc.) began to be placed inside the package at some distance from the front surface and according to the data of these devices to form a more objective idea of the stress–strain state of the package.

The asymptotic method for solving singularly perturbed differential equations [3] allows solving these types of problems [4]. The asymptotic method is widely used in studies to investigate the statics and dynamics of thin-walled elastic structures [13, 14], and publications [5, 6], where accounting for the effects of pre-stress, nonlocality, high contrast, as well as in contact problems for solids.

The dynamic nonclassical 3D problem of the theory of elasticity for a layered package of orthotropic plates, when the measurement data are taken from the contact surface between certain layers inside the package, was solved in [7]. The dynamic problem of a two-layered plate in the presence of viscous resistance in both layers is considered in the 3D formulation, where the values of the displacement vector components are collected from inclinometers and other measuring instruments at the contact surface between the layers, and was solved in [8]. The dynamic nonclassical 3D problem for layered orthotropic shells with complete contacts between the layers, when the measurement data are taken from the contact surface between certain layers inside the package, was solved in [9].

Forced vibrations of a single-layer shell and a two-layer shell with complete and incomplete contacts between the layers, when the boundary conditions are specified on the upper and lower surfaces of the shell, are considered in [10–12].

Over time, the strength of the bond between some layers can be compromised, and delamination will occur between the individual layers of the package. In this work, the corresponding dynamic problem of the theory of elasticity is solved, when the measuring instruments are placed inside the package, and separation takes place between the second and third layers.

## 2.2  Forced Vibrations of a Three-Layered Shell When There is a Separation Between the Second and Third Layers

Consider a three-layered elastic orthotropic shell, occupying the domain $D = \{\alpha, \beta, \gamma; \alpha, \beta \in D_0, 0 \leq \gamma \leq h_1 + h_2 + h_3\}$, where $D_0$—a face surface of the first layer, $\alpha, \beta$—lines of curvature of surface $D_0$, and $\gamma$—rectangular axis directed downwards perpendicular to surface $D_0$. The non-trivial solutions are sought for the problem of dynamics in the given triorthogonal coordinate system, subject to nonclassical boundary conditions. In order to reduce the length of algebraic computations, the analysis below is presented in terms of the components of non-symmetric stress tensor $\tau_{ij}$; see [3, 16].

The formulation of the problem includes equations of motion

$$
\frac{1}{AB} \frac{\partial}{\partial \alpha} \left( B \tau_{\alpha\alpha}^{(j)} \right) - k_\beta \tau_{\beta\beta}^{(j)} + \frac{1}{AB} \frac{\partial}{\partial \beta} \left( A \tau_{\beta\alpha}^{(j)} \right) + k_\alpha \tau_{\alpha\beta}^{(j)} + \left( 1 + \frac{\gamma}{R_1} \right) \frac{\partial \tau_{\alpha\gamma}^{(j)}}{\partial \gamma} + \frac{2 \tau_{\alpha\gamma}^{(j)}}{R_1}
$$

$$
= \rho^{(j)} \left( 1 + \frac{\gamma}{R_1} \right) \left( 1 + \frac{\gamma}{R_2} \right) \frac{\partial^2 U^{(j)}}{\partial t^2}
$$

$$
(A \leftrightarrow B; \alpha \leftrightarrow \beta; R_1, R_2; U, V), \quad j = I, II, III \tag{2.1}
$$

$$
\frac{\partial \tau_{\gamma\gamma}^{(j)}}{\partial \gamma} - \left( \frac{\tau_{\alpha\alpha}^{(j)}}{R_1} + \frac{\tau_{\beta\beta}^{(j)}}{R_2} \right) + \frac{1}{A} \frac{\partial \tau_{\alpha\gamma}^{(j)}}{\partial \alpha} + \frac{1}{B} \frac{\partial \tau_{\beta\gamma}^{(j)}}{\partial \beta} + k_\beta \tau_{\alpha\gamma}^{(j)} + k_\alpha \tau_{\beta\gamma}^{(j)}
$$

$$
= \rho^{(j)} \left( 1 + \frac{\gamma}{R_1} \right) \left( 1 + \frac{\gamma}{R_2} \right) \frac{\partial^2 W^{(j)}}{\partial t^2}
$$

$$
\left( 1 + \frac{\gamma}{R_1} \right) \tau_{\alpha\beta}^{(j)} = \left( 1 + \frac{\gamma}{R_2} \right) \tau_{\beta\alpha}^{(j)} \quad \text{(symmetry relation)}
$$

constitutive relations for an orthotropic solid

$$
\left( 1 + \frac{\gamma}{R_2} \right) \left( \frac{1}{A} \frac{\partial U^{(j)}}{\partial \alpha} + k_\alpha V^{(j)} + \frac{W^{(j)}}{R_1} \right) = \left( 1 + \frac{\gamma}{R_1} \right) a_{11}^{(j)} \tau_{\alpha\alpha}^{(j)}
$$

$$
+ \left( 1 + \frac{\gamma}{R_2} \right) a_{12}^{(j)} \tau_{\beta\beta}^{(j)} + a_{13}^{(j)} \tau_{\gamma\gamma}^{(j)}
$$

$$
(A, B; \alpha \leftrightarrow \beta; R_1 \leftrightarrow R_2; U \leftrightarrow V; a_{11}, a_{22}; a_{13}, a_{23})
$$

$$\left[1+\left(\frac{1}{R_1}+\frac{1}{R_2}\right)+\frac{\gamma}{R_1 R_2}\right]\frac{\partial W^{(j)}}{\partial \gamma}$$

$$=\left(1+\frac{\gamma}{R_1}\right)a_{13}^{(j)}\tau_{\alpha\alpha}^{(j)}+\left(1+\frac{\gamma}{R_2}\right)a_{23}^{(j)}\tau_{\beta\beta}^{(j)}+a_{33}^{(j)}\tau_{\gamma\gamma}^{(j)}$$

$$\left(1+\frac{\gamma}{R_1}\right)\left(\frac{1}{B}\frac{\partial U^{(j)}}{\partial \beta}-k_\beta V^{(j)}\right)+\left(1+\frac{\gamma}{R_2}\right)\left(\frac{1}{A}\frac{\partial V^{(j)}}{\partial \alpha}-k_\alpha U^{(j)}\right)$$

$$=\left(1+\frac{\gamma}{R_1}\right)a_{66}^{(j)}\tau_{\alpha\beta}^{(j)} \tag{2.2}$$

$$\left[1+\gamma\left(\frac{1}{R_1}+\frac{1}{R_2}\right)+\frac{\gamma^2}{R_1 R_2}\right]\frac{\partial U^{(j)}}{\partial \gamma}-\left(1+\frac{\gamma}{R_2}\right)\frac{U^{(j)}}{R_1}$$

$$+\frac{1}{A}\left(1+\frac{\gamma}{R_2}\right)\frac{\partial W^{(j)}}{\partial \alpha}=\left(1+\frac{\gamma}{R_1}\right)a_{55}^{(j)}\tau_{\alpha\gamma}^{(j)}$$

$$(A,\,B;\,\alpha,\,\beta;\,R_1\leftrightarrow R_2;\,U,\,V;\,a_{55},\,a_{44})$$

where $k_\alpha$, $k_\beta$—geodesic curvatures, $A$, $B$—coefficients of the first quadratic form, $R_1$, $R_2$—main curvature radii of surface $D_0$, $\rho^{(j)}$—mass volume densities of the layers, $a_{ik}^{(j)}$—elastic constants ($a_{ik}^{(j)}=a_{ki}^{(j)}$), and $j$—number of the layer.

Let the upper face $\gamma=0$ be traction-free:

$$\tau_{\alpha\gamma}^I(\alpha,\beta,0,t)=0,\ \tau_{\beta\gamma}^I(\alpha,\beta,0,t)=0,\ \tau_{\gamma\gamma}^I(\alpha,\beta,0,t)=0 \tag{2.3}$$

On the contact surface between the first and second layers, the values of the displacements of the points of the contact surface are known, as data from inclinometers or other measuring means:

$$U^I(\alpha,\beta,h_1,t)=U^{II}(\alpha,\beta,h_1,t)=U^+(\alpha,\beta)\exp(i\Omega t),(U,V,W) \tag{2.4}$$

where $\Omega$ is a given excitation frequency of forced vibrations. Complete contact between the first and second layers is assumed:

$$\tau_{\alpha\gamma}^I(\alpha,\beta,h_1,t)=\tau_{\alpha\gamma}^{II}(\alpha,\beta,h_1,t),\left(\tau_{\alpha\gamma},\tau_{\beta\gamma},\tau_{\gamma\gamma}\right) \tag{2.5}$$

$$U^I(\alpha,\beta,h_1,t)=U^{II}(\alpha,\beta,h_1,t),(U,V,W) \tag{2.6}$$

and there is a delamination between the second and third layers:

$$\tau_{\alpha\gamma}^{II}(\alpha,\beta,h_1+h_2,t)=\tau_{\alpha\gamma}^{III}(\alpha,\beta,h_1+h_2,t),\left(\tau_{\alpha\gamma},\tau_{\beta\gamma},\tau_{\gamma\gamma}\right)$$

$$U^{III}(\alpha,\beta,h_1+h_2,t)-U^{II}(\alpha,\beta,h_1+h_2,t)=k_1\tau_{\gamma\gamma}^{II}(\alpha,\beta,h_1+h_2,t)$$

$$(U, V; k_1, k_2)$$

$$W^{II}(\alpha, \beta, h_1 + h_2, t) = W^{III}(\alpha, \beta, h_1 + h_2, t) \tag{2.7}$$

Let us introduce the scaling $\alpha = R\xi, \beta = R\eta, \gamma = \varepsilon R\zeta = h\zeta, U = Ru, V = Rv, W = Rw, \tau_{mk}^{(j)} = \mu\tilde{\tau}_{mk}^{(j)}, \rho^{(j)} = \rho\tilde{\rho}^{(j)}$, where total thickness $h = h_1 + h_2 + h_3$ and $R$ is a typical linear size of the shell (e.g. least of the radii of curvature and associated linear sizes of surface $D_0, h \ll R$), $\mu$ and $\rho$ are typical values of elastic moduli and density, respectively, $\varepsilon = h/R$ as a small geometrical parameter, and $k_1, k_2$ are proportionality coefficients.

The solutions' transformed equations are sought in the form:

$$Q_{\alpha\beta}^{(j)} = Q_{mk}^{(j)}(\xi, \eta, \zeta) \exp(i\Omega t), (\alpha, \beta, \gamma); m, k = 1, 2, 3; j = I, II, III \tag{2.8}$$

where $Q_{\alpha\beta}^{(j)}$ denotes any of the stress or displacement components. As a result, we arrive at a singularly perturbed system in respect of $Q_{mk}^{(j)}$ with a small parameter $\varepsilon$. The stresses and displacements are now represented in asymptotic form as

$$\tilde{\tau}_{mk}^{(j)}(\xi, \eta, \zeta) = \varepsilon^{-1+s}\tilde{\tau}_{mk}^{(j,s)}(\xi, \eta, \zeta), m, k = 1, 2, 3; s = \overline{0, N}; j = I, II, III$$

$$\begin{aligned}
&\left(u^{(j)}(\xi, \eta, \zeta), v^{(j)}(\xi, \eta, \zeta), w^{(j)}(\xi, \eta, \zeta)\right) \\
&= \varepsilon^s\left(u^{(j,s)}(\xi, \eta, \zeta), v^{(j,s)}(\xi, \eta, \zeta), w^{(j,s)}(\xi, \eta, \zeta)\right)
\end{aligned} \tag{2.9}$$

The notation $s = \overline{0, N}$ here and below, denoting summation along the dummy index $s$ within the region of $0, N$.

As follows from (2.9), there is a significant distinction from the conventional classical problem, related to relative orders, in particular, all stress components are asymptotically of the same order, and so are all displacements, therefore the traditional assumptions of plate and shell theory are invalid.

On substituting (2.9) into the dimensionless forms of the governing equations—(2.1), (2.2)—we arrive at a system for determining the unknown coefficients of expansion $Q_{mk}^{(j,s)}$ taking the form:

$$\tilde{\tau}_{12}^{(j,s)} = P_{1\tau}^{(j,s-1)}, \tilde{\tau}_{21}^{(j,s)} = P_{1\tau}^{(j,s-1)} - r_2\zeta\tilde{\tau}_{21}^{(j,s-1)} + r_1\zeta\tilde{\tau}_{12}^{(j,s-1)}$$

$$e_1^{(j,s)} = P_{2\tau}^{(j,s-1)}, e_2^{(j,s)} = P_{3\tau}^{(j,s-1)}$$

$$\frac{\partial\tilde{\tau}_{12}^{(j,s)}}{\partial\zeta} + \tilde{\Omega}_*^2\tilde{\rho}^{(j)}u^{(j,s)} = P_{6\tau}^{(j,s-1)}$$

$$\tilde{\Omega}_*^2 = \frac{\rho}{\mu}h^2\Omega^2, \quad \tilde{a}_{mk}^{(j)} = \mu a_{mk}^{(j)} \tag{2.10}$$

$$(13, 23, 33; u, v, w; 6\tau, 5\tau, 4\tau)$$

$$\frac{\partial u^{(j,s)}}{\partial \zeta} - \tilde{a}_{55}^{(j)}\tilde{\tau}_{13}^{(j,s)} = P_u^{(j,s-1)}, \quad \frac{\partial v^{(j,s)}}{\partial \zeta} - \tilde{a}_{44}^{(j)}\tilde{\tau}_{23}^{(j,s)} = P_v^{(j,s-1)}$$

$$\frac{\partial w^{(j,s)}}{\partial \zeta} - e_3^{(j,s)} = P_w^{(j,s-1)}$$

where

$$
\begin{aligned}
P_{1\tau}^{(j,s-1)} =& \frac{1}{\tilde{a}_{66}^{(j)}}\frac{1}{B}\frac{\partial u^{(j,s-1)}}{\partial \eta} - k_\beta R v^{(j,s-1)} + \frac{1}{A}\frac{\partial v^{(j,s-1)}}{\partial \xi} - k_\alpha R u^{(j,s-1)} \\
&+ r_1\zeta\left(\frac{1}{B}\frac{\partial u^{(j,s-2)}}{\partial \eta} - k_\beta R v^{(j,s-2)}\right) \\
&+ r_2\zeta\left(\frac{1}{A}\frac{\partial v^{(j,s-2)}}{\partial \xi} - k_\alpha R u^{(j,s-2)}\right) - r_1\zeta\tilde{a}_{66}^{(j)}\tilde{\tau}_{12}^{(j,s-1)}
\end{aligned}
$$

$$
\begin{aligned}
P_{2\tau}^{(j,s-1)} =& \frac{1}{A}\frac{\partial u^{(j,s-1)}}{\partial \xi} + k_\alpha R v^{(j,s-1)} + r_1 w^{(j,s-1)} - r_1\zeta\tilde{a}_{11}^{(j)}\tilde{\tau}_{11}^{(j,s-1)} \\
&- r_2\zeta\tilde{a}_{12}^{(j)}\tilde{\tau}_{22}^{(j,s-1)} + r_2\zeta\left(\frac{1}{A}\frac{\partial u^{(j,s-2)}}{\partial \xi} + k_\alpha R v^{(j,s-2)} + r_1 w^{(j,s-2)}\right)
\end{aligned}
$$

$$(2\tau, 3\tau; A, B\alpha, \beta; r_1 \leftrightarrow r_2; \xi, \eta; u \leftrightarrow v; \tau_{11} \leftrightarrow \tau_{22}; a_{11}, a_{22}) \tag{2.11}$$

$$
\begin{aligned}
P_{4\tau}^{(j,s-1)} =& r_1\tilde{\tau}_{11}^{(j,s-1)} + r_2\tilde{\tau}_{22}^{(j,s-1)} - \frac{1}{A}\frac{\partial \tilde{\tau}_{13}^{(j,s-1)}}{\partial \xi} - \frac{1}{B}\frac{\partial \tilde{\tau}_{23}^{(j,s-1)}}{\partial \eta} - k_\beta R \tilde{\tau}_{13}^{(j,s-1)} \\
&- k_\alpha R \tilde{\tau}_{23}^{(j,s-1)} - \tilde{\rho}^{(j)}(r_1 + r_2)\zeta\tilde{\Omega}_*^2 w^{(j,s-1)} - \tilde{\rho}^{(j)}r_1 r_2\zeta^2\tilde{\Omega}_*^2 w^{(j,s-2)}
\end{aligned}
$$

$$
\begin{aligned}
P_{5\tau}^{(j,s-1)} =& \frac{1}{AB}\frac{\partial}{\partial \eta}\left(A\tilde{\tau}_{22}^{(j,s-1)}\right) + k_\alpha R \tilde{\tau}_{11}^{(j,s-1)} - \frac{1}{AB}\frac{\partial}{\partial \xi}\left(A\tilde{\tau}_{12}^{(j,s-1)}\right) - k_\beta R \tilde{\tau}_{21}^{(j,s-1)} \\
&- r_2\zeta\frac{\partial \tilde{\tau}_{23}^{(j,s-1)}}{\partial \zeta} - 2r_2\tilde{\tau}_{23}^{(j,s-1)} \\
&- (r_1 + r_2)\zeta\tilde{\rho}^{(j)}\tilde{\Omega}_*^2 v^{(j,s-1)} - \tilde{\rho}^{(j)}r_1 r_2\zeta^2\tilde{\Omega}_*^2 v^{(j,s-2)}
\end{aligned}
$$

$$(5\tau, 6\tau; A \leftrightarrow B; \alpha \leftrightarrow \beta; r_2, r_1; \xi \leftrightarrow \eta; v, u; \tau_{11} \leftrightarrow \tau_{22}; \tau_{12} \leftrightarrow \tau_{21}; \tau_{23}, \tau_{13})$$

$$P_u^{(j,s-1)} = -\zeta(r_1 + r_2)\frac{\partial u^{(j,s-1)}}{\partial \zeta} - \zeta^2 r_1 r_2\frac{\partial u^{(j,s-2)}}{\partial \zeta} + r_1 u^{(j,s-1)}$$

$$+ \zeta r_1 r_2 u^{(j,s-2)} - \frac{1}{A} \frac{\partial w^{(j,s-1)}}{\partial \xi} - \frac{\zeta r_2}{A} \frac{\partial w^{(j,s-2)}}{\partial \xi} + r_1 \zeta \tilde{a}_{55}^{(j)} \tilde{\tau}_{13}^{(j,s-1)}$$

$$(u, v; A, B; r_1 \leftrightarrow r_2; \xi, \eta; \tau_{13}, \tau_{23}; a_{55}, a_{44})$$

$$P_w^{(j,s-1)} = -\zeta(r_1 + r_2) \frac{\partial w^{(j,s-1)}}{\partial \zeta} - \zeta^2 r_1 r_2 \frac{\partial w^{(j,s-2)}}{\partial \zeta}$$

$$+ r_1 \zeta \tilde{a}_{13}^{(j)} \tilde{\tau}_{11}^{(j,s-1)} + r_2 \zeta \tilde{a}_{23}^{(j)} \tilde{\tau}_{22}^{(j,s-1)}$$

$$r_1 = \frac{R}{R_1}, r_2 = \frac{R}{R_2}, e_i^{(j,s)} = \tilde{a}_{i1}^{(j)} \tilde{\tau}_{11}^{(j,s)} + \tilde{a}_{i2}^{(j)} \tilde{\tau}_{22}^{(j,s)} + \tilde{a}_{i3}^{(j)} \tilde{\tau}_{33}^{(j,s)}$$

$$i = 1, 2, 3; j = I, II, III$$

Using relations (2.10), the components of the stress tensor are expressed in terms of $u^{(j,s)}, v^{(j,s)}, w^{(j,s)}$:

$$\tilde{\tau}_{13}^{(j,s)} = \frac{1}{\tilde{a}_{55}^{(j)}} \left[ \frac{\partial u^{(j,s)}}{\partial \zeta} - P_u^{(j,s-1)} \right], \quad \tilde{\tau}_{23}^{(j,s)} = \frac{1}{\tilde{a}_{44}^{(j)}} \left[ \frac{\partial v^{(j,s)}}{\partial \zeta} - P_v^{(j,s-1)} \right]$$

$$\tilde{\tau}_{12}^{(j,s)} = P_{1\tau}^{(j,s-1)}, \tilde{\tau}_{21}^{(j,s)} = P_{1\tau}^{(j,s-1)} - r_2 \zeta \tilde{\tau}_{21}^{(j,s-1)} + r_1 \zeta \tilde{\tau}_{12}^{(j,s-1)} \qquad (2.12)$$

$$\tilde{\tau}_{11}^{(j,s)} = \frac{1}{\Delta^{(j)}} \left[ \Delta_2^{(j)} \frac{\partial w^{(j,s)}}{\partial \zeta} + \Delta_{23}^{(j)} P_{2\tau}^{(j,s-1)} + \Delta_1^{(j)} P_{3\tau}^{(j,s-1)} - \Delta_2^{(j)} P_w^{(j,s-1)} \right]$$

$$(11, 22, 33; \Delta_2, \Delta_3, \Delta_{12}; \Delta_{23}, \Delta_1, \Delta_2; \Delta_1, \Delta_{13}, \Delta_3)$$

where

$$\Delta_1^{(j)} = \tilde{a}_{13}^{(j)} \tilde{a}_{23}^{(j)} - \tilde{a}_{33}^{(j)} \tilde{a}_{12}^{(j)}, \Delta_2^{(j)} = \tilde{a}_{12}^{(j)} \tilde{a}_{23}^{(j)} - \tilde{a}_{22}^{(j)} \tilde{a}_{13}^{(j)}$$

$$\Delta_3^{(j)} = \tilde{a}_{13}^{(j)} \tilde{a}_{12}^{(j)} - \tilde{a}_{11}^{(j)} \tilde{a}_{23}^{(j)}, \Delta^{(j)} = \tilde{a}_{11}^{(j)} \Delta_{23}^{(j)} + \tilde{a}_{13}^{(j)} \Delta_2^{(j)} + \tilde{a}_{12}^{(j)} \Delta_1^{(j)}$$

$$\Delta_{ik}^{(j)} = \tilde{a}_{ii}^{(j)} \tilde{a}_{kk}^{(j)} - (\tilde{a}_{ik}^{(j)})^2, \quad i, k = 1, 2, 3, \quad j = I, II, III \qquad (2.13)$$

To determine the components of the displacement vector, according to formula (2.10), the following equations are obtained:

$$\frac{\partial^2 u^{(j,s)}}{\partial \zeta^2} + \tilde{a}_{55}^{(j)} \tilde{\Omega}_*^2 \tilde{\rho}^{(j)} u^{(j,s)} = \tilde{a}_{55}^{(j)} P_{6\tau}^{(j,s-1)} + \frac{\partial P_u^{(j,s-1)}}{\partial \zeta}$$

$$(u, v; a_{55}, a_{44}; 6\tau, 5\tau)$$

$$\frac{\partial^2 w^{(j,s)}}{\partial \zeta^2} + \frac{\Delta^{(j)}}{\Delta_{12}^{(j)}} \tilde{\Omega}_*^2 \tilde{\rho}^{(j)} w^{(j,s)} = F_w^{(j,s-1)} \qquad (2.14)$$

$$F_w^{(j,s-1)} = \frac{1}{\Delta_{12}^{(j)}} \left[ \Delta^{(j)} P_{4\tau}^{(j,s-1)} - \Delta_2^{(j)} \frac{\partial P_{2\tau}^{(j,s-1)}}{\partial \zeta} - \Delta_3^{(j)} \frac{\partial P_{3\tau}^{(j,s-1)}}{\partial \zeta} + \Delta_{12}^{(j)} \frac{\partial P_w^{(j,s-1)}}{\partial \zeta} \right]$$

$$j = I, II, III$$

The solutions of Eq. (2.14) have the form

$$u^{(j,s)}(\xi, \eta, \zeta) = C_1^{(j,s)}(\xi, \eta) sin \chi^{(j,u)} \zeta + C_2^{(j,s)}(\xi, \eta) cos \chi^{(j,u)} \zeta + \overline{u}^{(j,s)}(\xi, \eta, \zeta)$$
$$(u, v, w; 1, 3, 5; 2, 4, 6), j = I, II, III$$

$$(2.15)$$

where

$$\chi^{(j,u)} = \sqrt{\tilde{a}_{55}^{(j)} \tilde{\rho}^{(j)}} \tilde{\Omega}_*, \chi^{(j,v)} = \sqrt{\tilde{a}_{44}^{(j)} \tilde{\rho}^{(j)}} \tilde{\Omega}_*, \chi^{(j,w)} = \sqrt{\frac{\Delta^{(j)} \tilde{\rho}^{(j)}}{\Delta_{12}^{(j)}}} \tilde{\Omega}_*$$

and $\overline{u}^{(j,s)}, \overline{v}^{(j,s)}, \overline{w}^{(j,s)}$ are particular solutions of Eq. (2.14).

On satisfying the boundary conditions (2.3)–(2.7), we obtain independent inhomogeneous algebraic systems with respect to the unknowns $C_i^{(j,s)} \left( i = \overline{1, 6}; j = I, II, III \right)$. Systems will have finite solutions if

$$\Delta_u = -\frac{\chi^{(II,u)} \chi^{(III,u)}}{\tilde{a}_{55}^{II} \tilde{a}_{55}^{III}} cos \chi^{(I,u)} \zeta_1 \neq 0 \qquad (2.16)$$

$$\zeta_1 = h_1/h, \quad \left( u, v, w; \tilde{a}_{55}^i, \tilde{a}_{44}^i, \frac{\Delta^i}{\Delta_{12}^i} \right)$$

The solutions for displacements are expressed as follows:
for the first layer we have

$$u^{(I,s)} = \frac{1}{cos \chi^{(I,u)} \zeta_1} \left( B_{13}^{(u,s)} cos \chi^{(I,u)} \zeta + B_{11}^{(u,s)} sin \chi^{(I,u)} (\zeta - \zeta_1) \right)$$
$$+ \overline{u}^{(I,s)}(\zeta), \quad (u, v, w) \qquad (2.17)$$

for the second layer

$$u^{(II,s)} = \frac{1}{\tilde{a}_{55}^I \chi^{(II,u)}} \left( \tilde{a}_{55}^I \left( B_{13}^{(u,s)} - B_{12}^{(u,s)} \right) \chi^{(II,u)} cos \chi^{(II,u)} (\zeta - \zeta_1) \right.$$
$$\left. - \tilde{a}_{55}^{II} sin \chi^{(II,u)} (\zeta - \zeta_1) T_{11}^{(u,s)} \right)$$
$$+ \overline{u}^{(II,s)}(\zeta)$$

$$\left( u, v, w; \tilde{a}_{55}^i, \tilde{a}_{44}^i, \frac{\Delta^i}{\Delta_{12}^i} \right) \qquad (2.18)$$

and for the third layer:

$$u^{(III,s)} = \frac{T_{12}^{(u,s)}}{\tilde{a}_{55}^{I}\chi^{(II,u)}}cos\chi^{(III,u)}(\zeta - \zeta_2) - \frac{T_{13}^{(u,s)}\tilde{a}_{55}^{III}}{\tilde{a}_{55}^{I}\tilde{a}_{55}^{II}\chi^{(III,u)}}sin\chi^{(III,u)}(\zeta - \zeta_2)$$
$$+ \overline{u}^{(III,s)}(\zeta), \quad \left(u, v; \tilde{a}_{55}^{i}, \tilde{a}_{44}^{i}\right) \tag{2.19}$$

$$w^{(III,s)} = \frac{T_{12}^{(w,s)}}{\chi^{(II,w)}\Delta^{I}\Delta_{12}^{II}}cos\chi^{(III,w)}(\zeta - \zeta_2)$$
$$+ \frac{T_{13}^{(w,s)}\Delta^{III}}{\chi^{(III,w)}\Delta^{I}\Delta^{II}\Delta_{12}^{III}}sin\chi^{(III,w)}(\zeta - \zeta_2) + \overline{w}^{(III,s)}(\zeta)$$

where

$$B_{11}^{(u,s)}(\xi, \eta) = \frac{1}{\chi^{(I,u)}}\left(P_u^{(I,s-1)}(\zeta = 0) - \frac{\partial \overline{u}^{(I,s)}(\zeta = 0)}{\partial \zeta}\right), \quad \left(u, v; \tilde{a}_{55}^{i}, \tilde{a}_{44}^{i}\right)$$

$$B_{12}^{(u,s)}(\xi, \eta) = \overline{u}^{(II,s)}(\zeta_1) - \overline{u}^{(I,s)}(\zeta_1), \ B_{13}^{(u,s)} = u^{+(s)}(\zeta_1) - \overline{u}^{(I,s)}(\zeta_1)$$

$$B_{14}^{(u,s)}(\xi, \eta) = \frac{1}{\tilde{a}_{55}^{I}}\left(P_u^{(I,s-1)}(\zeta_1) - \frac{\partial \overline{u}^{(I,s)}(\zeta_1)}{\partial \zeta}\right) - \frac{1}{\tilde{a}_{55}^{II}}\left(P_u^{(II,s-1)}(\zeta_1) - \frac{\partial \overline{u}^{(II,s)}(\zeta_1)}{\partial \zeta}\right)$$

$$B_{15}^{(u,s)}(\xi, \eta) = \frac{1}{\tilde{a}_{55}^{II}}\left(P_u^{(II,s-1)}(\zeta_1) - \frac{\partial \overline{u}^{(II,s)}(\zeta_1)}{\partial \zeta}\right) - \frac{1}{\tilde{a}_{55}^{III}}\left(P_u^{(III,s-1)}(\zeta_1) - \frac{\partial \overline{u}^{(III,s)}(\zeta_1)}{\partial \zeta}\right)$$

$$B_{16}^{(u,s)}(\xi, \eta) = k_1\mu\tilde{\tau}_{33}^{(II,s)}(\zeta_2) + \overline{u}^{(II,s)}(\zeta_2) - \overline{u}^{(III,s)}(\zeta_2)$$

$$T_{11}^{(u,s)}(\xi, \eta) = \tilde{a}_{55}^{I}B_{14}^{(u,s)} - \frac{B_{11}^{(u,s)}\chi^{(I,u)}}{cos\chi^{(I,u)}\zeta_1} + B_{13}^{(u,s)}\chi^{(I,u)}tg\chi^{(I,u)}\zeta_1 \tag{2.20}$$

$$T_{12}^{(u,s)}(\xi, \eta) = \tilde{a}_{55}^{I}\chi^{(II,u)}B_{16}^{(u,s)} + \tilde{a}_{55}^{II}sin\chi^{(II,u)}(\zeta_1 - \zeta_2)T_{11}^{(u,s)}$$
$$\tilde{a}_{55}^{I}\left(B_{13}^{(u,s)} - B_{12}^{(u,s)}\right)\chi^{(II,u)}cos\chi^{(II,u)}(\zeta_1 - \zeta_2)$$

$$T_{13}^{(u,s)}(\xi, \eta) = \tilde{a}_{55}^{I}\tilde{a}_{55}^{II}B_{15}^{(u,s)} + \tilde{a}_{55}^{II}cos\chi^{(II,u)}(\zeta_1 - \zeta_2)T_{11}^{(u,s)}$$
$$+ \tilde{a}_{55}^{I}\left(B_{12}^{(u,s)} - B_{13}^{(u,s)}\right)\chi^{(II,u)}sin\chi^{(II,u)}(\zeta_1 - \zeta_2), \left(u, v; \tilde{a}_{55}^{i}, \tilde{a}_{44}^{i}\right)$$

$$B_{11}^{(w,s)}(\xi, \eta) = \frac{\Delta^{I}}{\chi^{(I,w)}\Delta_{12}^{I}}T_1^{(I,s)}(\zeta = 0) - \frac{1}{\chi^{(I,w)}}\frac{\partial \overline{w}^{(I,s)}(\zeta = 0)}{\partial \zeta}$$

$$B_{12}^{(w,s)}(\xi, \eta) = \overline{w}^{(II,s)}(\zeta_1) - \overline{w}^{(I,s)}(\zeta_1), \ B_{13}^{(w,s)} = w^{+(s)}(\zeta_1) - \overline{w}^{(I,s)}(\zeta_1)$$

$$B_{14}^{(w,s)}(\xi, \eta) = T_1^{(II,s)}(\zeta_1) - T_1^{(I,s)}(\zeta_1) + \frac{\Delta_{12}^{II}}{\Delta^{II}}\frac{\partial \overline{w}^{(II,s)}(\zeta_1)}{\partial \zeta} - \frac{\Delta_{12}^{I}}{\Delta^{I}}\frac{\partial \overline{w}^{(I,s)}(\zeta_1)}{\partial \zeta}$$

$$B_{15}^{(w,s)}(\xi, \eta) = \overline{w}^{(III,s)}(\zeta_2) - \overline{w}^{(II,s)}(\zeta_2)$$

$$B_{16}^{(w,s)}(\xi, \eta) = T_1^{(III,s)}(\zeta_2) - T_1^{(II,s)}(\zeta_2) + \frac{\Delta_{12}^{III}}{\Delta^{III}} \frac{\partial \overline{w}^{(III,s)}(\zeta_2)}{\partial \zeta} - \frac{\Delta_{12}^{II}}{\Delta^{II}} \frac{\partial \overline{w}^{(II,s)}(\zeta_2)}{\partial \zeta}$$

$$T_{11}^{(w,s)}(\xi, \eta) = \Delta^I B_{14}^{(w,s)} - \frac{B_{11}^{(w,s)} \chi^{(I,w)} \Delta_{12}^I}{\cos \chi^{(I,w)} \zeta_1} + B_{13}^{(w,s)} \chi^{(I,w)} \Delta_{12}^I tg \chi^{(I,w)} \zeta_1$$

$$T_{12}^{(w,s)}(\xi, \eta) = \Delta^{II} \sin \chi^{(II,w)}(\zeta_1 - \zeta_2) T_{11}^{(w,s)} - \chi^{(II,w)} \Delta^I \Delta_{12}^{II} B_{15}^{(w,s)}$$
$$- \Delta^I \Delta_{12}^{II} \left( B_{12}^{(w,s)} - B_{13}^{(w,s)} \right) \chi^{(II,w)} \cos \chi^{(II,w)}(\zeta_1 - \zeta_2)$$

$$T_{13}^{(w,s)}(\xi, \eta) = \Delta^I \Delta_{12}^{II} \left( B_{13}^{(w,s)} - B_{12}^{(w,s)} \right) \chi^{(II,w)} \sin \chi^{(II,w)}(\zeta_1 - \zeta_2)$$
$$- \Delta^I \Delta^{II} B_{16}^{(w,s)} - \Delta^{II} \cos \chi^{(II,w)}(\zeta_1 - \zeta_2) T_{11}^{(w,s)}$$

$$T_1^{(j,s)}(\xi, \eta, \zeta) = \frac{1}{\Delta^j} \left( \Delta_2^j P_{2\tau}^{(j,s-1)}(\zeta) + \Delta_3^j P_{3\tau}^{(j,s-1)}(\zeta) - \Delta_{12}^j P_w^{(j,s-1)}(\zeta) \right)$$

$$\zeta_2 = (h_1 + h_2)/h, \quad j = I, II, III$$

$$u^{+(0)} = \frac{U^+}{R}, \quad u^{+(s)} = 0, s > 0, \quad (u, v, w)$$

The stresses may now be calculated from (2.12).

## 2.3 Numerical Calculation

The shell effect will appear from the s = 1 approximation. But since the Lithospheric plates are modeled as a package of orthotropic plates, therefore, numerical calculations are made for the s = 0 approximation. If we restrict ourselves to the first approximation (s = 0), then for the components of the displacement vector in dimensional form we obtain

$$U^{(I)} = \frac{U^+}{\cos \chi^{(I,u)} \zeta_1} \cos \chi^{(I,u)} \zeta, \quad (U, V, W) \tag{2.21}$$

$$U^{(II)} = U^+ \cos \chi^{(II,u)}(\zeta - \zeta_1) - U^+ \frac{\tilde{a}_{55}^{II} \chi^{(I,u)}}{\tilde{a}_{55}^I \chi^{(II,u)}} tg \chi^{(I,u)} \zeta_1 \sin \chi^{(II,u)}(\zeta - \zeta_1)$$

$$\left( U, V, W; \tilde{a}_{55}^i, \tilde{a}_{44}^i, \frac{\Delta^i}{\Delta_{12}^i} \right)$$

$$U^{(III)} = \left( -\frac{k_1 W^+}{\Delta^I \Delta^{II}} (\Delta^I \Delta_{12}^{II} \chi^{(II,w)} \sin \chi^{(II,w)}(\zeta_1 - \zeta_2) \right.$$
$$\left. - \Delta^{II} \Delta_{12}^I \chi^{(I,w)} tg \chi^{(I,w)} \zeta_1 \cos \chi^{(II,w)}(\zeta_1 - \zeta_2) \right)$$
$$+ U^+ \cos \chi^{(II,u)}(\zeta_1 - \zeta_2) + U^+ \frac{\tilde{a}_{55}^{II} \chi^{(I,u)}}{\tilde{a}_{55}^I \chi^{(II,u)}} tg \chi^{(I,u)} \zeta_1 \sin \chi^{(II,u)}(\zeta_1 - \zeta_2))$$

$$\times \cos\chi^{(III,u)}(\zeta - \zeta_2) - \frac{\tilde{a}_{55}^{III}}{\tilde{a}_{55}^{I}\tilde{a}_{55}^{II}\chi^{(III,u)}}$$

$$\left(\tilde{a}_{55}^{I}U^+\chi^{(II,u)}\sin\chi^{(II,u)}(\zeta_1 - \zeta_2) - \tilde{a}_{55}^{II}U^+\chi^{(I,u)}tg\chi^{(I,u)}\zeta_1\cos\chi^{(II,u)}(\zeta_1 - \zeta_2)\right)$$

$$\times \sin\chi^{(III,u)}(\zeta - \zeta_2), \quad \left(U, V; \tilde{a}_{55}^{i}, \tilde{a}_{44}^{i}\right)$$

$$W^{(III)} = \frac{W^+}{\Delta^I\Delta_{12}^{II}\chi^{(II,w)}}\left(\Delta^I\Delta_{12}^{II}\chi^{(II,w)}\cos\chi^{(II,w)}(\zeta_1 - \zeta_2)\right.$$

$$\left. + \Delta^{II}\Delta_{12}^{I}\chi^{(I,w)}tg\chi^{(I,w)}\zeta_1\sin\chi^{(II,w)}(\zeta_1 - \zeta_2)\right)$$

$$\times \cos\chi^{(III,w)}(\zeta - \zeta_2) + \frac{W^+\Delta^{III}}{\Delta^I\Delta^{II}\Delta_{12}^{III}\chi^{(III,w)}}\left(\Delta^I\Delta_{12}^{II}\chi^{(II,w)}\sin\chi^{(II,w)}(\zeta_1 - \zeta_2)\right.$$

$$\left. - \Delta^{II}\Delta_{12}^{I}\chi^{(I,w)}tg\chi^{(I,w)}\zeta_1\cos\chi^{(II,w)}(\zeta_1 - \zeta_2)\right)\sin\chi^{(III,w)}(\zeta - \zeta_2)$$

Below are graphs (Fig. 2.1) of amplitudes of oscillations at time $t = t_0$.

For calculations, a three-layered cylindrical shell with the following geometrical parameters was taken: R = 6000 km, $h_1$ = 5 km, $h_2$ = 10 km and $h_3$ = 20 km; proportionality coefficients are equal to $k_1 = 10^{-12}$, $k_2 = 1.5*10^{-12}$ and elastic characteristics of layers: Sedimentary layer: $E_1 = 55*10^9 \cdot$ Pa, $\vartheta_1 = 0.184$, $G_1 = 23.2*10^9 \cdot$ Pa, $r_1 = 2050 \cdot$ kg/m$^3$; Granite layer: $E_2 = 74.83*10^9 \cdot$ Pa, $\vartheta_2 = 0.21$, $G_2 = 30.82 * 10^9 \cdot$ Pa, $r_2 = 2610 \cdot$ kg/m$^3$; Basalt layer: $E_3 = 75.11*10^9 \cdot$ Pa, $\vartheta_3 = 0.27$, $G_3 = 29.22*10^9 \cdot$ Pa, $r_3 = 2910 \cdot$ kg/m$^3$. Frequency of forced vibration is equal to $\Omega = 10$. Measurement data at a fixed time $t = t_0$: $U^+ = 0.01$ m, $V^+ = 0.02$ m, $W^+ = -0.03$ m.

The equalities $\cos\chi^{(I,u)}\zeta_1 = 0$, $(u, v, w)$ under conditions (2.16) coincide with the resonance conditions for a single-layer shell in the classical setting [9], that is, when the upper front surface is free, and the lower surface is reported to move harmoniously in time (it is enough to go to the same parameters). We also note that these conditions correspond to thickness resonances in the vicinity of which the asymptotic degenerates [13, 14].

Having the values of stresses and displacements, the accumulated potential energy of deformation can be determined by the well-known formula

$$E = \frac{1}{2}\int_V \left(\sigma_{xx}\varepsilon_{xx} + \sigma_{yy}\varepsilon_{yy} + \sigma_{zz}\varepsilon_{zz} + \sigma_{xy}\varepsilon_{xy} + \sigma_{xz}\varepsilon_{xz} + \sigma_{yz}\varepsilon_{yz}\right)dv \quad (2.22)$$

and by the formula [1]

$$\lg E = 11.8 + 1.5M \quad (2.23)$$

one can determine the magnitude of the expected earthquake.
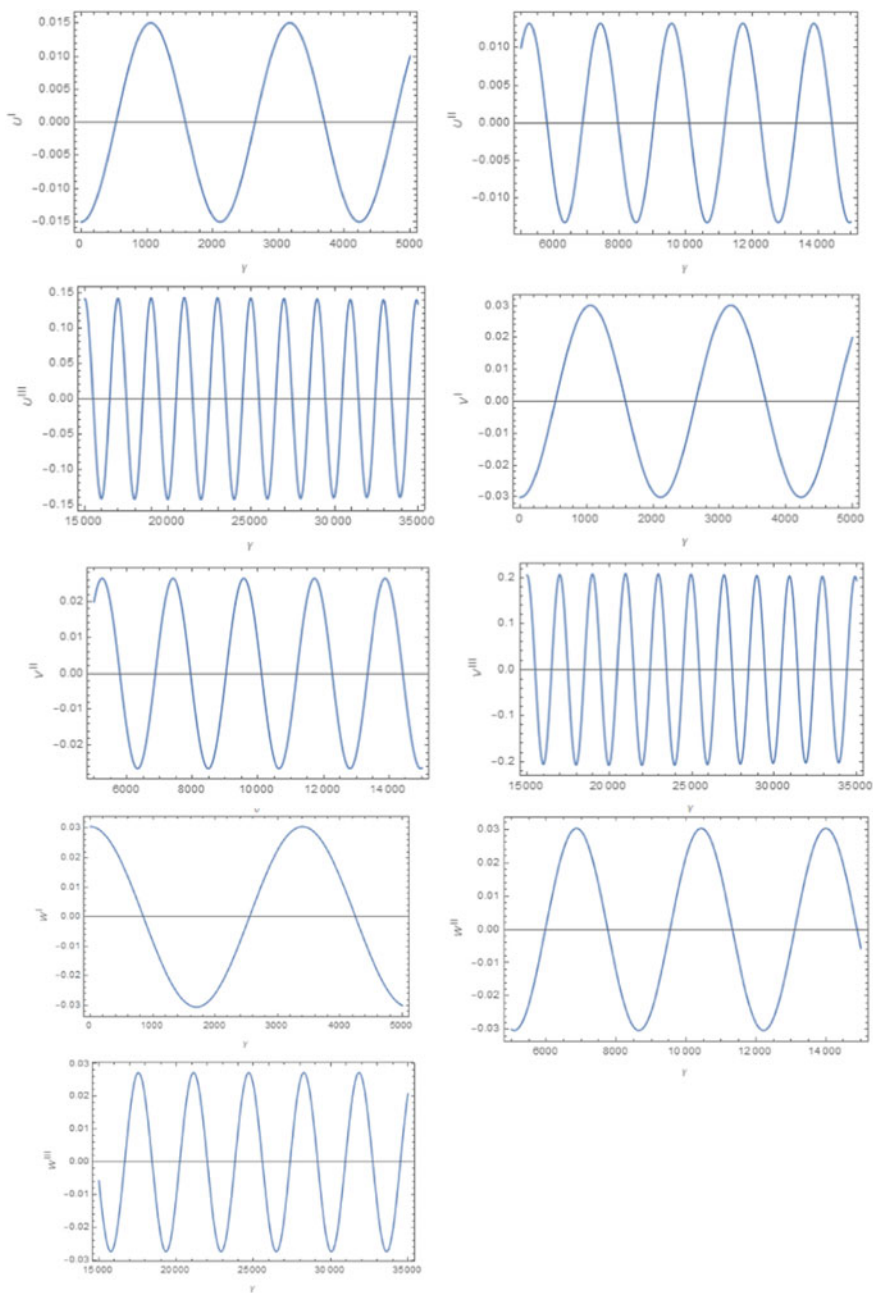
Fig. 2.1 Numerical calculation

## 2.4   Conclusion

The dynamic problem for a three-layered shell is solved when the upper face surface is free, the conditions of ideal contact are satisfied between the first and second layers, and there is a separation between the second and third layers of the shell. The values of the displacement vector components are taken from the contact surface between the first and second layers, as data from inclinometers and other measuring equipment.

The resonance conditions are derived. It is shown that the resonance conditions of a three-layered shell when the values of the displacement vector components are taken from the contact surface between the first and second layers depend only on the parameters of the first layer. Moreover, they coincide with the resonance conditions for a single-layer shell in the classical formulation of the problem, when the upper face surface is free, and the lower surface is reported a movement that changes harmoniously in time.

The components of stresses and displacement vectors are determined, and it is shown that the parameters of all layers affect the stress–strain state of a layered package.

It is shown that the separation between the second and third layers affects only the stress components and the displacement vector of the third layer.

Having carried out regular measurements of the values of the displacements of the points of the contact surface, it is possible, using [15] and the formulas derived above, to trace the change in the stress–strain state of the package in time, to identify the places of occurrence of critical states leading to stratification and global destruction (earthquake).

Having the values of stresses and displacements, the accumulated potential energy of deformation can be determined by the formula (2.22), and by the formula (2.23), the magnitude of the expected earthquake.

## References

1. Kasahara K (1981) Earthquake mechanics. Cambridge University Press, p 261
2. Rikitake T (1976) Earthquake prediction. Elsevier, Amsterdam, p 357p
3. Aghalovyan LA (2015) Asymptotic theory of anisotropic plates and shells. Singapore-London. World Scientific Publishing, p 376
4. Aghalovyan LA (2015) On some classes of 3D boundary-value problems of statics and dynamics of plates and shells. Shell and membrane theories in mechanics and biology. Springer International Publishing, Switzerland, pp 1–23

5. Borodich FM, Galanov BA, Perepelkin NV, Prikazchikov DA (2019) Adhesive contact problems for a thin elastic layer: asymptotic analysis and the JKR theory. Math Mech Solids 24(5):1405–1424

6. Kaplunov J, Prikazchikov D, Sultanova L (2018) Justification and refinement of Winkler-Fuss hypothesis. Z Angew Math Phys 69(3):80

7. Aghalovyan LA, Aghalovyan ML, Tagvoryan VV (2018) On solutions of dynamic three-dimensional problems of the elasticity theory for earthquake modeling. Proc NAS RA Mech 71(4):17–29

8. Ghulghazaryan LG, Hambardzumyan PR (2020) The dynamic three-dimensional problem of the theory of elasticity of a two-layer plate in the presence of viscous resistance. Reports of NAS RA. 2020, vol 120, no 3, pp 181–190

9. Aghalovyan LA, Ghulghazaryan LG, Kaplunov JD, Prikazchikov DA (2020) 3D dynamic analysis of layered elastic shells. Math Methods Physico-Mech Fields 63(4):96–108

10. Aghalovyan LA, Ghulghazaryan LG (2009) Non-classical boundary-value problems of the forced vibrations of orthotropic shells. Int Sci J Appl Mech 45(8):105–122

11. Aghalovyan LA, Ghulghazaryan LG (2018) Forced vibrations of two-layered shells on the case of viscous resistance. IOP J Phys Conf Ser 991(012):002

12. Ghulghazaryan LG, Khachatryan LV (2018) Forced vibrations of a two-layer orthotropic shell with an incomplete contact between layers. Mech Compos Mater 53(6):821–826

13. Kaplunov JD (1990) High-frequency stress-strain states of small variability in elastic thin shells. Proceedings of the AS SSSR. Mechanics of solid body, № 5, pp 147–157

14. Kaplunov JD, Kossovich LYu, Nolde EV (1998) Dynamics of thin walled elastic bodies. Academic Press, p 225

15. Aghalovyan LA, Aghalovyan ML (2012) Monitoring of stress-strain state of plate-like packet of base-foundation constructions on the base of the data of seismic stations and GPS systems. In: Proceedings of the 5th European conference on structural control–EACS 2012. Genoa. Italy, 18–20 June. 2012. Paper N # 069, pp 1–8

16. Goldenveizer AL (1976) Theory of elastic thin shells (in Russian), Nauka, Moscow, pp 512

# Chapter 3
# On Some Methods Analysing Reinforced Materials and Structures

Holm Altenbach

**Abstract**  With respect to the demands of lightweight structural engineering classical structural materials are more and more substituted by fibre and particle-reinforced materials in advanced, but also in ordinary structures. The aim of lightweight structural engineering is to save raw materials, costs and energy in the manufacture, use and recycling of a product. Especially with moving masses, lightweight structures can reduce operating costs or increase the payload. Laminate and sandwich structures are typical lightweight elements with rapidly expanding applications in various industrial fields. In the past, these structures were used primarily in the aircraft and aerospace industries. Now, they have also found applications in civil and mechanical engineering, in the automotive industry, in shipbuilding, in the sport goods industries, etc. Recently, polymers reinforced with short glass fibres (with a length of 0.1–1 mm, a diameter that, as a rule, does not exceed one-tenth of their length, and a volume content of fibres of 15–45%) have been widely used in modern engineering. A great quantity of thin-walled structural elements operating under loads is manufactured by injection moulding. Elements of modelling these materials are discussed. For sufficiently high loading every material suffers some sort of gradual or abrupt mechanical failure (damage or plastic collapse). Its specific form depends on the material internal atomistic, molecular and/or topological structure. Composite materials, by definition, involve at least two distinct materials (phases) which increase the number of various failure possibilities. Further complication related to the failure of composite materials is associated with the presence of interphases. In the paper, a personal view of the author on these problems is given and advantages and disadvantages are presented.

**Keywords**  Reinforced materials · Laminate theories · Particle reinforcement

H. Altenbach (✉)
Fakultät für Maschinenbau, Lehrstuhl für Technische Mechanik, Institut für Mechanik,
Otto-von-Guericke-Universität, Magdeburg, Germany
e-mail: holm.altenbach@ovgu.de

## 3.1   Preliminary Remarks

The focus of the Euromech Colloquium 626 was on the mechanics of high-contrast elastic composites. These materials are characterized by strong inhomogeneity in the advanced composite structure, widely used in modern engineering as lightweight structures. Especially with moving masses (road and rail vehicles, elevators, robot arms, machine components, etc.), lightweight structures can reduce operating costs or increase the payload. In modern applications, lightweight structures are combined with smart structures. This allows us to adapt the structure to the changes in the surroundings and to optimize the behaviour.

In the following, questions about some theoretical models are briefly presented. The starting point is continuum mechanics, which means the discrete structure is ignored. It is obvious that technological applications, including, but not restricted to manufacturing and design of photovoltaic elements, laminated glass, lightweight vehicles, energy harvesting devices and bio-composites, will be presented.

High-contrast composites are metamaterials, which means materials designed to have a property that is not found in naturally occurring materials. Let us start with the definition of high-contrast composites.

**Definition 3.1** (*High-contrast composite*) That is, a heterogeneous material which, at a microscopic level, consists of a periodically perforated matrix whose cavities are occupied by a filling with different physical properties.

This type of composite materials is discussed, for example, in [15].

For accounting for the reinforcement and other heterogeneities of materials and structures, we have two approaches:

- The local description and simulation which yield high computational effort or
- the application of homogenization approaches with lower computational effort.

However, there are several open questions:

- How the properties can be accounted for in the averaged sense?
- The influence of periodicity versus uncertainties is not clear.

The classical approaches are based on the classification of composites shown in Fig. 3.1. Based on this classification, several methods of analysis can be taken into account.

## 3.2   Simplest Models

Let us start with the fibre-matrix relations in the case of unidirectional (UD) reinforced long-fibre composites. In fibre-reinforced composite materials, fibres act as a load-carrying medium and the matrix acts as a load-transporting medium [29]. In particle-reinforced composite materials, particles act as a load-carrying medium and the matrix acts again as a load-transporting medium.
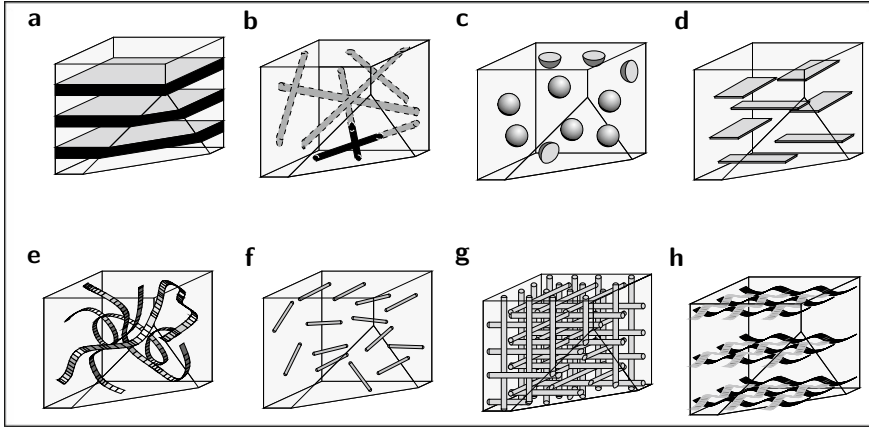
**Fig. 3.1** Classification of composites [12]: **a** laminate, **b** irregular reinforcement, **c** reinforcement with particles, **d** reinforcement with plate strapped particles, **e** random arrangement of continuous fibres, **f** irregular reinforcement with short fibres, **g** spatial reinforcement and **h** reinforcement with surface

One of the most important factors which determines the mechanical behaviour of a composite material is the proportion of the matrix and the fibres/particles expressed by their volume or their weight fraction. In the following, we limit ourselves to long-fibre reinforcement. Then one has the following relations:

- *Description based on the volume fraction*
  The volume of the composite material $V$ is

$$V = V_f + V_m$$

  with the volume of the fibres $V_f$ and the volume of the matrix $V_m$. The volume fractions can be introduced as

$$v_f = \frac{V_f}{V}, \qquad v_m = \frac{V_m}{V}$$

  with the volume fraction of the fibres $v_f$ and the volume fraction of the matrix $v_m v_m$. Finally, we have $v_f + v_m = 1$.
- Alternatively, the *description based on the mass fraction* can be introduced

$$m_f = \frac{M_f}{M}, \qquad m_m = \frac{M_m}{M}$$

with $m_f + m_m = 1$.

Let us estimate the density of the composite

$$\rho = \frac{M}{V} = \frac{M_f + M_m}{V} = \frac{\rho_f V_f + \rho_m V_m}{V} = \rho_f v_f + \rho_m v_m.$$

The mass fractions are easier to measure in material manufacturing, but volume fractions appear in the theoretical equations for effective moduli. Therefore, it is helpful to have simple expressions for shifting from one fraction to the other.

The equations can be easily extended to multi-phase composites

$$v_1 + v_2 + v_3 + \ldots = 1$$

with $v_i$ as the volume fraction of the $i$th phase. This representation can be used even in the case of porosity

$$v_f + v_m + v_{por} = 1$$

which results in

$$v_{por} = 1 - v_f + v_m = 1 - \frac{m_f}{\rho_f} - \frac{m_m}{\rho_m}.$$

Based on these simple mixture rules, the other effective properties of a single layer can be estimated [12]. Let us assume for the UD long-fibre reinforced composites:

- The bond between fibres and matrix is perfect and no friction is considered.
- The fibres are continuous, homogeneous and parallel aligned in each ply.
- They are packed regularly, i.e. the space between fibres is uniform.
- Fibre and matrix materials are linear elastic, they follow approximately Hooke's law and each elastic modulus is constant.
- Voids are ignored.

The rule of mixtures starting from the iso-strain assumption and the inverse rule of mixtures starting from the iso-stress assumption are based on the statement that the composite property is the weighted mean of the properties or the inverse properties of each constituent multiplied by its volume fraction. In the first case, we have the upper-bound effective property, and in the second, the lower bound. These bounds are related to Voigt [36] and Reuss [31]. Examples of such effective properties are as follows:

- The effective longitudinal modulus of elasticity (the strains of the fibres, matrix and composite in the loading direction are the same)

$$E_L = E_f v_f + E_m v_m = E_f v_f + E_m(1 - v_f) = E_f \phi + E_m(1 - \phi)$$

with Young's modulus of the fibres $E_f$, Young's modulus of the matrix $E_m$, the volume fraction of the fibres $v_f$ and the volume fraction of the matrix $v_m$;

- The effective transverse modulus of elasticity (the stress resultant, respectively, the stress is equal for all phases)

$$\frac{1}{E_T} = \frac{v_f}{E_f} + \frac{1 - v_f}{E_m} = \frac{v_f}{E_f} + \frac{v_m}{E_m}$$

or

$$E_T = \frac{E_f E_m}{(1 - v_f)E_f + v_f E_m}.$$

In a similar manner, effective Poisson's ratio, the effective in-plane shear modulus (LT-plane) and the effective in-plane shear modulus (TT-plane) can be computed [12]. The predicted values of $E_L$ are in good agreement with experimental results since effective Young's modulus in fibre direction is dominated by the fibre modulus $E_f$. The maximum fibre volume fraction $v_{f\,max}$ is less than 1. The value depends on the fibre arrangements:

- square or layer-wise fibre packing

$$v_{f\,max} = 0.785,$$

- hexagonal fibre packing

$$v_{f\,max} = 0.907.$$

For real UD-laminae, we have $v_{f\,max} \approx 0.50-0.65$. Since $E_f \gg E_m$, the approximate value of longitudinal Young's modulus is

$$E_L \approx E_f v_f.$$

The predicted values of $E_T$ are as usual not in good agreement with experimental results. In this and similar cases, improved formulas for effective moduli of composites can be suggested. The most popular improvements are based on the Halpin-Tsai method [see, for example, 18], which is a typical semi-empirical approach.

Not only in the classical laminate theory, but also in the nonclassical laminate theories (for example, first-order shear deformation theory), the stiffness parameters of the laminate can be estimated as

- sums of weighted properties (for example, laminates),
- as integrals of weighted properties (for example, functional graded materials) and
- sometimes special expressions (for example, for the shear correction).

Typical predictions are presented in Altenbach [3, 4] and Altenbach and Eremeyev [5]. This approach can be easily extended to viscoelastic systems [2, 6].

### 3.3  Particle-Reinforced Composites

The most common particle-reinforced composite is concrete. Here we have a mixture of gravel and sand usually strengthened by the addition of small rocks or sand. Polymers are often reinforced, for example, with short glass fibres. This material is often produced by injection moulding. The particles and the matrix are isotropic materials; however, their combination can result in a quasi-homogeneous anisotropic material. In [32], the flow-induced orientations of particles during the injection moulding process are discussed. It was established that a rough layered structure can be obtained with different orientations of the glass fibres: in the mid the orientation is orthogonal to the flow direction, close to the cavity walls the orientation is in the flow direction and between "both layers" a chaotic orientation can be established. This kind of anisotropy should be taken into account for global behaviour predictions of structures made of particle-reinforced plastics.

The prediction of the orientation is widely discussed in the literature. One approach is based on the theory of dilute suspensions [1, 13]. If $\boldsymbol{\omega}$ is the angular velocity of a single particle, an evolution equation for the fibre microstructure can be developed. Another approach is based on the micropolar theory of concentrated suspensions [8, 17]. Here $\boldsymbol{\omega}$, $\boldsymbol{J}$ (tensor of inertia) and $\boldsymbol{Q}$ (rotation tensor) are field quantities and a constitutive equation for skew-symmetric part of $\boldsymbol{\sigma}$ (rotary interactions between fluid and suspended particles) could be established. To verify the corresponding assumptions, studies of the particle motion in homogeneous flow fields are helpful.

Maybe the first paper in this direction was published by Jeffery [22]. He discussed the rotation of an ellipsoid of revolution in a Newtonian fluid. The obtained shear flow yields a periodic orbit. The slender particle results in particle alignment parallel to the streamlines. Later, Bretherton [14] generalized Jeffery's formula for the angular velocity to axisymmetric particles of various shapes. In both Jeffery's and Bretherton's works, the particle inertia and inertia effects of the fluid flow were ignored.

Considering experimental results, some disagreements with the theoretical results can be established. The particle dynamics in flow fields are presented accounting for the fluid inertia, but inertialess particles are assumed [23, 35]. Introducing the particle rotation under the influence of rotary inertia, it can be shown that long-time stable orbits do no longer exist [10]. In the case of shear flow, a slender particle may jump over stable alignment [11]. The approximate solution is limited to numerical values for initial angular velocity and particle inertia.

The aim of our further studies was the detailed analysis of the particle rotation in the shear flow. To this end, the governing equations of rigid body dynamics for the slender particle in a homogeneous flow field were deduced, the hydrodynamic moment exerted on the particle was assumed in the form as proposed by Jeffery [22], the shear flow equations of motion are reduced to a single second-order ordinary differential equation with respect to the angle of rotation about a fixed axis, and the phase portrait analysis of this equation was performed. Conclusions about the

influence of inertia and the stability of fibre alignment were made and the combined analysis of particle orientation and stiffness distribution was presented. In addition to Altenbach et al. [8, 11], the main results of our investigations are published in Altenbach et al. [7, 9] and Renner et al. [30].

## 3.4 Spherical Inhomogeneity with Interphase

One of the main problems in the description of real composites with reinforcements is the randomness in composites. Special attention must be paid to the interphase, since it is not present in the initial state. Only when the matrix and reinforcement material are brought together, the interphase is formed. The randomness in the microstructure of the composite then also has a particular effect on the interphase. To make matters worse, the properties of the interphase are very difficult to determine. At the same time, the failure of the composite is determined to a particular extent by the interphase. The local geometric arrangements and the damage are related to the randomness and the problem of modelling such materials is a big challenge.

One of the modelling approaches is based on the energy equivalent inhomogeneity concept. The basic ideas are presented, for example, in Hashin [19, 20] using the spring layer model of interphase in context with the composite cylinder or the composite sphere models. However, only the equivalent inhomogeneity bulk modulus could be evaluated. In Shen and Li [34] and Sevostianov and Kachanov [33], the so-called "differential approach" was used to define equivalent inhomogeneity. Here, Mori-Tanaka's estimate and Hashin's lower bound were used. In [16], equivalent inhomogeneity properties are obtained by using Eshelby's equivalence principle. The properties depend on the properties of the matrix. A detailed description on some previous works, related to the model presented below, is given in Nazarenko et al. [25–28] and Nazarenko and Stolarski [24].

Let us assume the inhomogeneity as shown in Fig. 3.2.

In accordance with [21], the energy of the inhomogeneity/interphase system can be presented as follows:

$$E = \frac{1}{2} \int_{V_i} \boldsymbol{\varepsilon}_i \cdot\cdot \boldsymbol{C}_i \cdot\cdot \boldsymbol{\varepsilon}_i \mathrm{d}V_i + E_{\text{int}} \tag{3.1}$$

with

$$E_{\text{int}} = \frac{1}{2} \int_{\Omega_{\text{int}}} \boldsymbol{\varepsilon}_{\text{int}} \cdot\cdot \boldsymbol{C}_{\text{int}} \cdot\cdot \boldsymbol{\varepsilon}_{\text{int}} \mathrm{d}\Omega_{\text{int}}.$$

The equivalent system is presented by the energy

$$E = \frac{1}{2} V_{\text{eq}} \boldsymbol{\varepsilon}_{\text{eq}} \cdot\cdot \boldsymbol{C}_{\text{eq}} \cdot\cdot \boldsymbol{\varepsilon}_{\text{eq}} = \frac{1}{2} \boldsymbol{\varepsilon}_{\text{eq}} \cdot\cdot \tilde{\boldsymbol{C}}_{\text{eq}} \cdot\cdot \boldsymbol{\varepsilon}_{\text{eq}}. \tag{3.2}$$
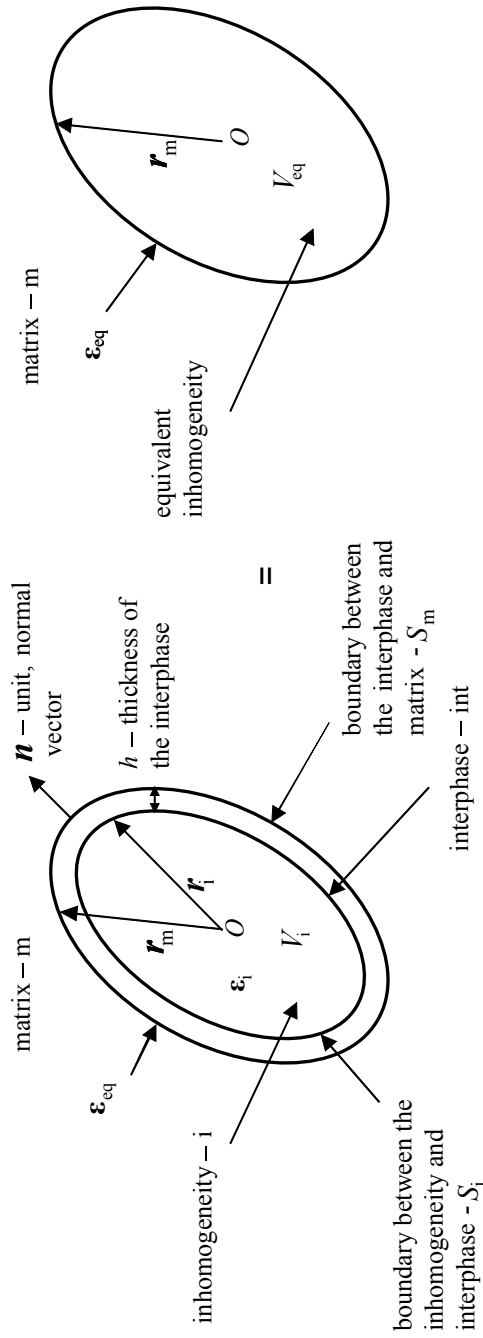
**Fig. 3.2** Schematic illustration of inhomogeneity with interphase: real inhomogeneity (left) and equivalent inhomogeneity (right)

$\boldsymbol{\varepsilon}_{\text{int}}, \boldsymbol{\varepsilon}_{\text{eq}}, \boldsymbol{\varepsilon}_{\text{i}}$ are the strain tensors within the inhomogeneity, interphase and the equivalent inhomogeneity (prescribed). $\boldsymbol{C}_{\text{i}}, \boldsymbol{C}_{\text{int}}, \boldsymbol{C}_{\text{eq}}$ are the stiffness tensor of the inhomogeneity, interphase and equivalent inhomogeneity, respectively.

The minimization of the potential energy (3.1)

$$\delta E = 0$$

and

$$\boldsymbol{\varepsilon}_{\text{i}} = \boldsymbol{T}_{\text{i}} \cdot\cdot \boldsymbol{\varepsilon}_{\text{eq}}, \qquad \boldsymbol{\varepsilon}_{\text{int}} = \boldsymbol{T}_{\text{int}} \cdot\cdot \boldsymbol{\varepsilon}_{\text{eq}}$$

with $\boldsymbol{T}_{\text{i}}, \boldsymbol{T}_{\text{int}}$ are fourth-order tensors resulting in the energy of the system at equilibrium

$$E = \frac{1}{2}\boldsymbol{\varepsilon}_{\text{eq}} \cdot\cdot \left( \int\limits_{V_{\text{i}}} \boldsymbol{T}_{\text{i}}^{\text{T}} \cdot\cdot \boldsymbol{C}_{\text{i}} \cdot\cdot \boldsymbol{T}_{\text{i}} \mathrm{d}V_{\text{i}} + \int\limits_{\Omega_{\text{int}}} \boldsymbol{T}_{\text{int}}^{\text{T}} \cdot\cdot \boldsymbol{C}_{\text{int}} \cdot\cdot \boldsymbol{T}_{\text{int}} \mathrm{d}\Omega_{\text{int}} \right) \cdot\cdot \boldsymbol{\varepsilon}_{\text{eq}}$$

and the stiffness tensor of the equivalent inhomogeneity can be expressed as

$$\widetilde{\boldsymbol{C}}_{\text{eq}} = \int\limits_{V_{\text{i}}} \boldsymbol{T}_{\text{i}}^{\text{T}} \cdot\cdot \boldsymbol{C}_{\text{i}} \cdot\cdot \boldsymbol{T}_{\text{i}} \mathrm{d}V_{\text{i}} + \int\limits_{\Omega_{\text{int}}} \boldsymbol{T}_{\text{int}}^{\text{T}} \cdot\cdot \boldsymbol{C}_{\text{int}} \cdot\cdot \boldsymbol{T}_{\text{int}} \mathrm{d}\Omega_{\text{int}}.$$

Numerical examples are presented in Nazarenko et al. [25, 27, 28] and Nazarenko and Stolarski [24].

## 3.5 Summary and Outlook

There is a number of open questions that need to be investigated in the future:

- the correctness of the assumption of a periodicity in the composite material,
- the uncertainties in the model based on statistical distributions of matrix and reinforcement in the composite material,
- continuum versus discrete approach,
- the correctness of molecular dynamics modelling and
- the assumptions concerning the perfect and real contact conditions.

There is a greater need for research here in the coming years. Questions of failure in particular have not been finally clarified to this day. There are numerous approaches and also experimental results. Unfortunately, there is still now no comprehensive theoretical basis to describe the failure without contradiction.

# References

1. Advani SG, Tucker CL (1987) The use of tensors to describe and predict fiber orientation in short fiber composites. J Rheol 31(8):751–784. https://doi.org/10.1122/1.549945
2. Al'tenbakh Kh (1988) Determination of the reduced properties of multilayer viscoelastic sheets. Mech Compos Mater 24(1):52–59. https://doi.org/10.1007/BF00611335
3. Altenbach H (2000) An alternative determination of transverse shear stiffnesses for sandwich and laminated plates. Int J Solids Struct 37(25):3503–3520. https://doi.org/10.1016/S0020-7683(99)00057-8
4. Altenbach H (2000) On the determination of transverse shear stiffnesses of orthotropic plates. Zeitschrift für angewandte Mathematik und Physik ZAMP 51(4):629–649. https://doi.org/10.1007/s000330050021
5. Altenbach H, Eremeyev VA (2008) Direct approach-based analysis of plates composed of functionally graded materials. Arch Appl Mech 78(10):775–794. https://doi.org/10.1007/s00419-007-0192-3
6. Altenbach H, Eremeyev VA (2008) On the analysis of viscoelastic plates made of functionally graded materials. ZAMM-Zeitschrift für angewandte Mathematik und Mechanik 88(5):332–341. https://doi.org/10.1002/zamm.200800001
7. Altenbach H, Naumenko K, Lvov GI, Pilipenko SN (2003) Numerical estimation of the elastic properties of thin-walled structures manufactured from short-fiber-reinforced thermoplastics. Mech Compos Mater 39(3):221–234. https://doi.org/10.1023/A:1024566026411
8. Altenbach H, Naumenko K, Zhilin PA (2003) A micro-polar theory for binary media with application to phase-transitional flow of fiber suspensions. Continuum Mech Thermodyn 15(6):539–570. https://doi.org/10.1007/s00161-003-0133-5
9. Altenbach H, Naumenko K, Pylypenko S (2005) On the numerical prediction of the anisotropic elastic properties in thin-walled structures made from short fiber reinforced plastics. Comput Assist Mech Eng 12(4):87–97. https://doi.org/10.1023/A:1024566026411
10. Altenbach H, Naumenko K, Pylypenko S, Renner B (2007) Influence of rotary inertia on the fiber dynamics in homogeneous creeping flows. ZAMM-Zeitschrift für Angewandte Mathematik und Mechanik 87(2):81–93. https://doi.org/10.1002/zamm.200610303
11. Altenbach H, Brigadnov I, Naumenko K (2009) Rotation of a slender particle in a shear flow: influence of the rotary inertia and stability analysis. ZAMM-Zeitschrift für Angewandte Mathematik und Mechanik 89(10):823–832. https://doi.org/10.1002/zamm.200900249
12. Altenbach H, Altenbach J, Kissing W (2018) Mechanics of composite structural elements, 2nd edn. Springer. https://doi.org/10.1007/978-981-10-8935-0
13. Bay RS, Tucker III CL (1992) Fiber orientation in simple injection moldings. Part I: theory and numerical methods. Polym Compos 13(4):317–331. https://doi.org/10.1002/pc.750130409
14. Bretherton FP (1962) The motion of rigid particles in a shear flow at low Reynolds number. J Fluid Mech 14:284–304. https://doi.org/10.1017/S002211206200124X
15. Davoli E, Kružík M, Pagliari V (2021) Homogenization of high-contrast composites under differential constraints. arXiv:2104.11306
16. Duan H, Yi X, Huang Z, Wang J (2007) A unified scheme for prediction of effective moduli of multiphase composites with interface effects. Part I: theoretical framework. Mech Mater 39(1):81–93. https://doi.org/10.1016/j.mechmat.2006.02.009

17. Eringen AC (1991) Continuum theory of dense rigid suspensions. Rheol Acta 30(1):23–32. https://doi.org/10.1007/BF00366791
18. Halpin JC, Kardos JL (1976) The halpin-tsai equations: a review. Polym Eng Sci 16(5):344–352. https://doi.org/10.1002/pen.760160512
19. Hashin Z (1990) Thermoelastic properties of fiber composites with imperfect interface. Mech Mater 8(4):333–348. https://doi.org/10.1016/0167-6636(90)90051-G
20. Hashin Z (1991) The spherical inclusion with imperfect interface. J Appl Mech 58(2):444–449. https://doi.org/10.1115/1.2897205
21. Hill R (1963) Elastic properties of reinforced solids: Some theoretical principles. J Mech Phys Solids 11(5):357–372. https://doi.org/10.1016/0022-5096(63)90036-X
22. Jeffery GB (1922) The motion of ellipsoidal particles immersed in a viscous fluid. Proc R Soc Lond Ser A Contain Papers Math Phys Character 102(715):161–179. https://doi.org/10.1098/rspa.1922.0078
23. Leal LG (1980) Particle motions in a viscous fluid. Annu Rev Fluid Mech 12(1):435–476. https://doi.org/10.1146/annurev.fl.12.010180.002251
24. Nazarenko L, Stolarski H (2016) Energy-based definition of equivalent inhomogeneity for various interphase models and analysis of effective properties of particulate composites. Compos B Eng 94:82–94. https://doi.org/10.1016/j.compositesb.2016.03.015
25. Nazarenko L, Bargmann S, Stolarski H (2015) Energy-equivalent inhomogeneity approach to analysis of effective properties of nanomaterials with stochastic structure. Int J Solids Struct 59:183–197. https://doi.org/10.1016/j.ijsolstr.2015.01.026
26. Nazarenko L, Stolarski H, Altenbach H (2016) Effective properties of short-fiber composites with Gurtin-Murdoch model of interphase. Int J Solids Struct 97–98:75–88. https://doi.org/10.1016/j.ijsolstr.2016.07.041
27. Nazarenko L, Stolarski H, Altenbach H (2017) A model of cylindrical inhomogeneity with spring layer interphase and its application to analysis of short-fiber composites. Compos Struct 160:635–652. https://doi.org/10.1016/j.compstruct.2016.10.024
28. Nazarenko L, Stolarski H, Altenbach H (2018) On modeling and analysis of effective properties of carbon nanotubes reinforced materials. Compos Struct 189:718–727. https://doi.org/10.1016/j.compstruct.2018.01.027
29. Palanikumar K (2012) Analyzing surface quality in machined composites. In: Hocheng H (ed) Machining technology for composite materials, Woodhead Publishing Series in Composites Science and Engineering, Woodhead Publishing, pp 154–182. https://doi.org/10.1533/9780857095145.1.154
30. Renner B, Altenbach H, Naumenko K (2005) Numerical treatment of finite rotation for cylindrical particle. Tech Mech 25(3/4):151–161
31. Reuss A (1929) Berechnung der Fließgrenze von Mischkristallen auf Grund der Plastizitätsbedingung für Einkristalle. Z Angew Math Mech 9(1):49–58. https://doi.org/10.1002/zamm.19290090104
32. Saito M, Kukula S, Kataoka Y, Miyata T (2000) Practical use of statistically modified laminate model for injection moldings. Mater Sci Eng A 285(1):280–287. https://doi.org/10.1016/S0921-5093(00)00646-8
33. Sevostianov I, Kachanov M (2007) Effect of interphase layers on the overall elastic and conductive properties of matrix composites. applications to nanosize inclusion. Int J Solids Struct 44(3):1304–1315. https://doi.org/10.1016/j.ijsolstr.2006.06.020
34. Shen L, Li J (2005) Homogenization of a fibre/sphere with an inhomogeneous interphase for the effective elastic moduli of composites. Proc R Soc A Math Phys Eng Sci 461(2057):1475–1504. https://doi.org/10.1098/rspa.2005.1447
35. Subramanian G, Koch DL (2005) Inertial effects on fibre motion in simple shear flow. J Fluid Mech 535:383–414. https://doi.org/10.1017/S0022112005004829
36. Voigt W (1910) Lehrbuch der Kristallphysik (mit Ausschluss der Kristalloptik). Springer, Wiesbaden. https://doi.org/10.1007/978-3-663-15884-4

# Chapter 4
# High-Contrast Multi-layered Plates. Statics, Dynamics and Buckling

**Claude Boutin**

**Abstract** This paper deals with the mechanical behavior of multi-layered plates whose constituents show strong contrasts in mechanical properties. A typical example of such High-Contrast Stratified (HCS) plates is laminated glass panels. The study is conducted within the theoretical framework of dimension reduction methods using an asymptotic approach. This procedure allows to move from the 3D description, which takes into account the interface conditions and the high contrast, to the equivalent 2D description of the plate. The developments are based on previous works carried out by asymptotic treatment of strong local formulations. The paper first presents the explicit bi-torsors or tri-laplacian model of rigid two-layer HCS plates. It then focuses on the specific characteristics of these plates in terms of wave propagation, buckling and the effect of a viscoelastic core layer. These results are generalized to HCS plates composed of 3 then $2p$ (or $2p + 1$) rigid layers. It is shown that the out-of-plane behavior is governed by a $(p + 1)$-torsors model (or $(p + 2)$-Laplacian) and that the in-plane behavior is also enriched by $p - 1$ (or $p$) additional kinematic variables. The perspectives of this work are discussed in the conclusion.

## 4.1 Introduction

This paper deals with the mechanical behavior of stratified plates whose constituents show strong contrasts in mechanical properties. A typical example of such High-Contrast Stratified (HCS) plates is laminated glass panels.

Composite plates of moderate contrast are widely used in engineering for their mechanical performance. The disparities in the behavior of the layers result in a distribution of stress within the plate and in internal kinematics that differ from those observed in homogeneous plates. Indeed, the significant deformations localized in the less rigid layers combines with the lower deformations of the more rigid layers. Thus, an internal equilibrium is established that involves the shear effects of the soft

C. Boutin (✉)

Ecole Nationale des Travaux Publics de l'Etat, Université de Lyon, CNRS UMR 5513, Vaulx-en-Velin, France
e-mail: claude.boutin@entpe.fr

layers and the bending effects of the stiff layers. Various "zig-zag" internal kinematics models have been developed to account for these phenomena and reference is made to [6] or [7] for a comparative analysis of these generalised models of plates or beams.

These particular mechanisms are even more pronounced in HCS plates, and this situation requires a specific analysis. In this field, the precursory works on the behavior of beams carried out by a phenomenological approach are due to [9, 16]. Subsequently, the numerical studies as well as the theoretical and phenomenological modelling of glass beams [19], and plates [10] have also accounted explicitly for the strong contrast.

The present article lies in the context of dimension reduction methods using an asymptotic approach. This procedure allows to move from the explicit 3D description of the constituents and their interface conditions to an equivalent 2D plate description. The pioneering works of [8] on homogeneous plates has demonstrated the relevance of this method. By combining the homogenization method [1, 18] with this approach, substantial developments have been made e.g. [5, 15] for periodic plates with moderate contrasts.

The aim here is to take up this theoretical framework by introducing the strong contrast hypothesis in the asymptotic formulation. The developments are based on previous works carried out by asymptotic treatment of strong formulations [3, 20]. In the same spirit, a parallel approach based on energy and weak formulations has been developed in [2, 17].

The paper is organized as follows. Section 4.2 exposes the main aspects of the HCS plate model with two stiff layers. Section 4.3 focuses on the specific features of these plates in terms of wave propagation, buckling and effect of a viscoelastic central layers. Section 4.3 presents a generalization to HCS plates made of 3 and then $n$ stiff layers. Some perspectives are discussed in the conclusion.

## 4.2 The HCS Plate Model

The elaboration of the model is a direct application of the asymptotic methods dedicated to the formulation of plate theories. Starting from the 3D isotropic elasticity of the constituents, the condition of perfect contact between the different layers and the geometric condition of small thickness, the effective plate model is obtained by recursive resolution of the local problems at successive orders. For conciseness, only the main steps of the procedure are indicated here. More details one the asymptotic derivation of the HCS plates may be find in Boutin and Viverge [3], Viverge et al. [20].

### 4.2.1 Notations

The studied stratified plate of surface $S$ is made of two skins $S \times \Omega^+$ and $S \times \Omega^-$ made of the same stiff material, of thickness $h^+$ and $h^-$, perfectly connected to a
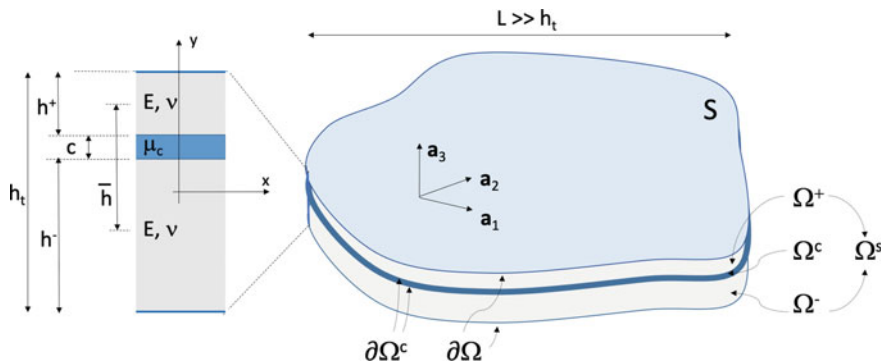
**Fig. 4.1** HCS plate with two stiff layers. Notations

soft central layer $S \times \Omega^c$ of thickness $c$ (see Fig. 4.1); $S \times \Omega^s = S \times (\Omega^+ \cup \Omega^-)$ denotes the two skins of thickness $h^s = h^+ + h^-$ and $S \times \Omega = S \times (\Omega^+ \cup \Omega^c \cup \Omega^-)$ denotes the whole plate of total thickness $h^t = h^s + c$. The distance between the mean planes of the stiff layers is $\bar{h} = c + h^s/2$. All these dimensions are assumed of the same order of magnitude. In contrast, the characteristic in-plane size $L$ of the plate is significantly larger than the thickness $h$.

The external boundaries of $\Omega$ are denoted $\partial\Omega$ while $\partial\Omega^c$ stands for the boundaries of $\Omega^c$.

Both soft and stiff layers are linear isotropic materials. $E$ and $\nu$ denote the Young modulus and the Poisson coefficient of the stiff layers ($\lambda$, $\mu$ the Lamé coefficients) and $E_0 = E(1 - \nu^2)$ stands for the apparent plate modulus ; $\mu_c$ is the shear rigidity of the soft layer. Furthermore, one assume that the density of both layers are of the same order of magnitude.

The bending inertia of each stiff layer reads $I_+ = \frac{(h^+)^3}{12}, I_- = \frac{(h^-)^3}{12}$ ; $I_2 = I_+ + I_-$ is that of both stiff layers and the global bending inertia is $\mathscr{I}_2 = I_2 + \bar{h}^2(\frac{1}{h^+} + \frac{1}{h^-})^{-1}$.

Herein the orientation is specified using the reference orthonormal frame where $\{\underline{a}_1, \underline{a}_2\}$ and $\underline{a}_3$ are respectively the in-plane and the out-of-plane directions. By convention, since we are looking for a 2D model:

- $\underline{x} = x_1\underline{a}_1 + x_2\underline{a}_2$ stands for the in-plane position
- except when specified all the differential operators act in the $\{\underline{a}_1, \underline{a}_2\}$ plane, e.g.

$$\underline{\nabla} = \frac{\partial}{\partial x_1}\underline{a}_1 + \frac{\partial}{\partial x_2}\underline{a}_2 \quad ; \quad \operatorname{div}(\underline{u}) = \frac{\partial u_1}{\partial x_1} + \frac{\partial u_2}{\partial x_2}$$

$\underline{\underline{e}}(\underline{u})$ is the in-plane strain tensor $\underline{\underline{e}}(\underline{v})_{ij} = (\frac{\partial u_i}{\partial x_j} + \frac{\partial u_j}{\partial x_i})/2 \quad (i, j) = (1, 2)$, etc . . .

- $\underline{\underline{\mathscr{E}}}$ is the in-plane differential operator ($\underline{\underline{I}}$ is the 2D identity tensor):

$$\underline{\underline{\mathscr{E}}}(\underline{u}) = (1 - \nu)\underline{\underline{e}}(\underline{u}) + \nu\mathrm{div}(\underline{u})\underline{\underline{I}} \qquad (4.1)$$

## *4.2.2  In-Plane/Out-of-Plane Splitted Formulation*

In the plate, the in-plane evolutions of the variables occurs according to $L$ while their variation across the plate thickness arise according to $h_t$. Consequently, the appropriate dimensionless space variables are ($\frac{x_1}{L}, \frac{x_2}{L}, \frac{x_3}{h_t}$). Equivalently, the suited physical space variables are $(\underline{x}, y)$, where $y = \frac{L}{h_t}x_3 = \varepsilon^{-1}x_3$. Hence the gradient of a quantity $Q$ expressed with the variables $(\underline{x}, y)$ reads:

$$\underline{\nabla}^{3D} Q = (\underline{\nabla} + \varepsilon^{-1}\frac{\partial}{\partial y}\underline{a}_3)Q(\underline{x}, y).$$

The in-plane and out-of-plane splitting also applies to the physical quantities. The displacement $\underline{u}$ in decomposes into the in-plane displacement $u_1\underline{a}_1 + u_2\underline{a}_2$ and $w\underline{a}_3$ the out-of-plane deflection

$$\underline{u} = u_1\underline{a}_1 + u_2\underline{a}_2 + w\underline{a}_3$$

Similarly, the strain and stress tensors are split in reduced tensors, namely, the 2D in-plane tensor, the out of plane vector (index $_T$) and the normal scalar (index $_N$):

$$\underline{\underline{e}}^{3D} = \underline{\underline{e}} + (\underline{e}_T \otimes \underline{a}_3 + \underline{a}_3 \otimes \underline{e}_T) + e_N\underline{a}_3 \otimes \underline{a}_3$$

$$\underline{\underline{\sigma}}^{3D} = \underline{\underline{\sigma}} + (\underline{\sigma}_T \otimes \underline{a}_3 + \underline{a}_3 \otimes \underline{\sigma}_T) + \sigma_N\underline{a}_3 \otimes \underline{a}_3$$

Hence, the balance equation $\underline{\mathrm{div}}(\underline{\underline{\sigma}}^{3D}) = \underline{0}$ in $\Omega$ and the continuity conditions of stress vector and displacement on the internal interfaces $\partial\Omega^c$, i.e., $[\underline{\sigma}.\underline{a}_3] = \underline{0}$; $[\underline{u}] = \underline{0}$ and of vanishing stress vector on the external faces $\partial\Omega$, i.e., $\underline{\sigma}.\underline{a}_3 = \underline{0}$ on $\Gamma$ rewritten with the scaled variables $(x_\alpha, y)$ and the reduced stress tensors separate into:

– a scalar out-of-plane balance (along $\underline{a}_3$):

$$\begin{cases} \varepsilon^{-1}\partial_y\sigma_N + \mathrm{div}(\underline{\sigma}_T) = 0 & \text{in } \ \Omega \\ [\sigma_N] = 0; \quad [w] = 0 & \text{on } \ \partial\Omega^c \\ \qquad\qquad\qquad \sigma_N = 0 & \text{on } \ \partial\Omega \end{cases} \qquad (4.2)$$

– a vectorial in-plane balance (within the plane $(\underline{a}_1, \underline{a}_2)$):

$$
\begin{cases}
\varepsilon^{-1}\partial_y \underline{\sigma}_T + \underline{\mathrm{div}}(\underline{\underline{\sigma}}) = \underline{0} & \text{in} \quad \Omega \\
[\underline{\sigma}_T] = \underline{0} \ ; \quad [\mathrm{u}_\alpha \underline{a}_\alpha] = \underline{0} & \text{on} \quad \partial\Omega^c \\
\underline{\sigma}_T = \underline{0} & \text{on} \quad \partial\Omega
\end{cases}
\qquad (4.3)
$$

Note that these equations are written for zero volume forces $\underline{f}(\underline{x}, y) + f(\underline{x}, y)\underline{a}_3$. The latter will be introduced at the proper level after deriving the leading order description free of loading.

### 4.2.3  Scaling of Highly Contrasted Stratified Plates

In order to account for the physical characteristics of the contrasted plates it is necessary to rescale the variables and parameters.

– First, the plate is assumed to be loaded by negligible tangential forces, so that:

$$
(\underline{\underline{\sigma}}.\underline{a}_3).\underline{a}_i = \mu\left(\frac{\partial w}{\partial x_i} + \frac{\partial \mathrm{u}_i}{\partial x_3}\right) = 0 \quad \text{on} \quad \partial\Omega \quad ; \quad i = 1, 2
$$

According to the in-plane and out-of-plane characteristic sizes of variations of the displacement, the dimensional analysis yields $\partial w/\partial x_\alpha = O(w/L)$ and $\partial \mathrm{u}_i/\partial x_3 = O(\mathrm{u}_i/h)$. Therefore, the zero shear stress on $\partial\Omega$ imposes that $O(\mathrm{u}_i) = (h_t/L)O(w) = O(\varepsilon w)$. Consequently, the in-plane components of the displacement are re-expressed as $\mathrm{u}_i = \varepsilon u_\alpha$ so that $O(u_i) = O(w)$ and $\underline{u} = \varepsilon(u_i \underline{a}_i) + w\underline{a}_3$.
– Second, the bending of the stiff layers interacts with the shear of the soft layer. Such a coupling emerges when the transverse forces in both constituents contribute at the same order of magnitude to the transverse balance of the plate [3]. From dimensional analysis, the shear force in the soft layer is $T_c = O(c\mu_c w/L)$, while the shear force in the stiff skins that are bended is $T_s = O(M/L) = O(Eh_t^3 w/L^3)$. Then, the requirement $T_c = O(T_s)$ yields:

$$
\frac{\mu_c}{E} = O\left(\frac{h_t}{c}\left(\frac{h}{L}\right)^2\right) = O(\varepsilon^2)
$$

Hence, the (3D) stress tensors in the soft layer are rescaled in the form $\varepsilon^2 \underline{\underline{\sigma}}_c$.

Now, the out-of plane set (4.2) and the in-plane set (4.3) involves terms in odd and even power of $\varepsilon$, respectively. Consequently, expressing $u_\alpha$ and $w$ as asymptotic expansions in power of $\varepsilon$, the consecutive terms of these expansions are systematically offset by $\varepsilon^2$. Thus, the displacement $\underline{\mathbf{u}} = \varepsilon\underline{u} + w\underline{u}_3$ is expanded in the form:

$$
\varepsilon\underline{u}(x, y) = \varepsilon\underline{u}^1(x, y) + \varepsilon^3\underline{u}^3(x, y) + \cdots \quad ; \quad w(x, y) = w^0(x, y) + \varepsilon^2 w^2(x, y) + \cdots
$$

This scaling yields in both stiff and soft layers, to the following expansions of the reduced strain tensors

$$\mathrm{e}_N = \varepsilon^{-1}\mathrm{e}_N^{-1} + \varepsilon \mathrm{e}_N^1 + \ldots \quad \underline{\mathrm{e}}_T = \underline{\mathrm{e}}_T^0 + \varepsilon^2 \underline{\mathrm{e}}_T^2 + \ldots \quad \underline{\underline{\mathrm{e}}} = \varepsilon \underline{\underline{\mathrm{e}}}^1 + \ldots$$

while, from the contrasted constitutive law, the reduced stress tensors read:

$$\begin{cases} \text{in } \Omega \quad \sigma_N = \varepsilon^{-1}\sigma_N^{-1} + \varepsilon\sigma_N^1 + \ldots ; & \underline{\sigma}_T = \underline{\sigma}_T^0 + \varepsilon^2 \underline{\sigma}_T^2 \ldots ; & \underline{\underline{\sigma}} = \varepsilon \underline{\underline{\sigma}}^1 + \ldots \\ \text{in } \Omega_c \quad \sigma_{cN} = \varepsilon\sigma_{cN}^1 + \ldots & ; \quad \underline{\sigma}_{cT} = \varepsilon^2 \underline{\sigma}_{cT}^2 + \ldots ; & \underline{\underline{\sigma}}_c = O(\varepsilon^3) \end{cases}$$

The asymptotic plate model is derived by introducing expansions (4.4) in the sets (4.2) and (4.3). Separating the terms of different order leads to a series of problems to be solved whose only the main results are presented here.

It is important to note here that the considered normalization reflects the local physics which leads to the model developed in the following parts. It will be noticed in particular that in the framework of the selected normalization the internal resonance phenomena (i.e. in the thickness of the layers) cannot appear. However, other normalizations are possible to describe other local physics which will lead to different models. The particular situations and the corresponding normalizations that lead to internal resonance phenomena are studied in detail in [14].

### 4.2.4 Kinematics at the Leading Order

The first steps of the resolution show that:

– the out-of-plane deflection $w^0$ is identical in the whole thickness of $\Omega$, i.e.,:

$$w^0(\underline{x}, y) = W(\underline{x}) \tag{4.4}$$

– the in-plane displacement $\underline{u}^1$ combines three $\underline{x}$-dependent kinematic descriptors:

  • the gradient of deflection of the whole plate $\underline{\nabla}W(\underline{x})$
  • the homogeneous in-plane displacement identical in the two stiff layers $\underline{U}(\underline{x})$,
  • the half of the interface sliding vector between the stiff layers $\underline{D}(\underline{x})$.

Each descriptor is associated with a $y$-dependent shape function, and $\underline{u}^1(\underline{x}, y)$ reads:

$$\underline{u}^1(\underline{x}, y) = -\phi_W(y)\underline{\nabla}W(\underline{x}) + \phi_U(y)\underline{U}(\underline{x}) + \phi_D(y)\underline{D}(\underline{x}) \tag{4.5}$$

The shape functions $\phi_W, \phi_U, \phi_D$ defined in $\Omega$ are determined by the structure of the laminate. Taking the origin of $y$ at the middle of the central layer, one has:

$$\phi_W(y) = y + \delta \; ; \; \phi_U = 1 \; ; \; \phi_D = \left\{ \frac{2h^+}{h^s}, \frac{2y}{c} - \delta', -\frac{2h^-}{h^s} \right\} \text{ in } \{\Omega^+, \Omega^c, \Omega^-\}$$

$$\delta = \frac{c(h^+ - h^-)}{2h^s} \qquad \delta' = \frac{(h^s - c)(h^+ - h^-)}{ch^s}$$

which, in the case of symmetric laminates, simplifies into:

$$\phi_W = y; \quad \phi_U = 1; \quad \phi_D = \{1, \frac{2y}{c}, -1\}$$

In (4.5) the term $-\phi_W \underline{\nabla} W + \phi_U \underline{U}$ corresponds to the classical Kirchhoff kinematics of homogeneous plates, while $\phi_D \underline{D}$ is the additional kinematics induced by the presence of the soft layer. Instead of $\underline{D}$ one may consider the differential in-plane displacement $\underline{d}(x)$ between the middle planes of the stiff layers, i.e.,:

$$\underline{d} = \underline{D} - \frac{\overline{h}}{2} \underline{\nabla} W$$

that enables to defines the rotation vector $\underline{\alpha}(x)$ induced by the differential extension of the two glass layers:

$$\underline{\alpha} = -\frac{2}{h}\underline{d} = \underline{\nabla} W - \frac{2}{h}\underline{D} \tag{4.6}$$

### 4.2.5   Strain and Stress State at the Leading Order

In the stiff layers $\Omega_s$ the strain and stress tensors at the leading order, namely $\underline{e}^1$ and $\underline{\sigma}^1$ are explicitly determined from $\underline{u}^1(x, y)$ (recall that the out-of-plane reduced tensors (index $_T$) are nul at this order). Thus:

$$\underline{e}^1(\underline{x}, y) = -\phi_W \underline{e}(\underline{\nabla} W) + \phi_U \underline{e}(\underline{U}) + \phi_D \underline{e}(\underline{D}) \; ; \; e_N^1(\underline{x}, y) = \frac{\lambda}{\lambda + 2\mu} \text{tr}(\underline{e}^1) \tag{4.7}$$

$$\underline{\sigma}^1(\underline{x}, y) = E_0[(1 - v)\underline{e}^1 + v\text{tr}(\underline{e}^1)\underline{I}] \; ; \; \sigma_N^1(\underline{x}, y) = 0 \tag{4.8}$$

Hence, using the operator $\underline{\mathscr{E}}$ defined in (4.1):

$$\underline{\text{div}}(\underline{\sigma}^1) = E_0\underline{div}\big(-\phi_W \underline{\mathscr{E}}(\underline{\nabla} W) + \phi_U \underline{\mathscr{E}}(\underline{U}) + \phi_D \underline{\mathscr{E}}(\underline{D})\big) \tag{4.9}$$

The soft layer $\Omega_c$ experiences at the leading order a uniform shear strain $\underline{e}_{Tc}^2$ and stress $\underline{\sigma}_{Tc}^2$ that read:

$$\underline{e}_{Tc}^2(\underline{x}) = \frac{1}{2}\frac{\partial\phi_D}{\partial y}\underline{D}(\underline{x}) = \frac{1}{c}\underline{D}(\underline{x}) \quad ; \quad \underline{\sigma}_{Tc}^2 = 2\mu_c \underline{e}_{Tc}^2(\underline{x}) = 2\frac{\mu_c}{c}\underline{D}(\underline{x}) \tag{4.10}$$

**Table 4.1** Integrated products of the shape functions related to the three kinematic descriptors

| $\Phi_{AB}$ | $\phi_U$ | $\phi_W$ | $\phi_D$ |
|---|---|---|---|
| $\phi_U$ | $h^s$ | 0 | 0 |
| $\phi_W$ | 0 | $\mathscr{I}_2 = I_2 + \overline{h}^2 h^*$ | $2(\mathscr{I}_2 - I_2)/\overline{h}$ |
| $\phi_D$ | 0 | $2(\mathscr{I}_2 - I_2)/\overline{h}$ | $4(\mathscr{I}_2 - I_2)/\overline{h}^2$ |

$\overline{h} = h + c$; $\quad h^* = (\frac{1}{h^+} + \frac{1}{h^-})^{-1}$

### 4.2.6 Balance Equations at the Leading Order

The overall balances related to the three kinematic descriptors are established by multiplying the in-plane balance Eq. (4.3a) at order $\varepsilon^2$ i.e. $\underline{\sigma_T}^2_{,y} + \underline{div}_x(\underline{\underline{\sigma}}^1) = \underline{0}$, by each shape functions $\phi_A$, $A = \{W, U, D\}$, and integrating over the plate thickness accounting for the boundary conditions (4.3-b,-c). This gives:

$$\int_\Omega \phi_A(y)\underline{\sigma_T}^2_{,y}\mathrm{d}y + \int_\Omega \phi_A(y)\underline{div}_x(\underline{\underline{\sigma}}^1)\mathrm{d}y = \underline{0}$$

Accounting for (4.9) and (4.10), after integrating by part the integral involving $\underline{\sigma_T}^2$, these equations read:

$$E_0\underline{div}\big(-\Phi_{WA}\underline{\underline{\mathscr{E}}}(\nabla W) + \Phi_{UA}\underline{\underline{\mathscr{E}}}(\underline{U}) + \Phi_{DA}\underline{\underline{\mathscr{E}}}(\underline{D})\big) = \int_\Omega \frac{\partial\phi_A}{\partial y}\underline{\sigma_T}^2\mathrm{d}y$$

in which $\Phi_{AB} = \int_{\Omega_s} \phi_A(y)\phi_B(y)\mathrm{d}y$ where $\{A, B\} = \{W, U, D\}$, is the crossed product of the shape functions in the stiff layers integrated value over their thickness. Their values are displayed on Table 4.1. With regards to the last integral, note that we have:

$$\frac{\partial\phi_W}{\partial y} = 1; \quad \frac{\partial\phi_U}{\partial y} = 0; \quad \frac{\partial\phi_D}{\partial y} = \{0, \frac{2}{c}, 0\} \text{ in } \{\Omega^+, \Omega^c, \Omega^-\}$$

– **In-plane balance equation**. Considering the uniform shape function $\phi_U$ for the integration, leads to:
$$E_0\underline{div}(\underline{\underline{\mathscr{E}}}(\underline{U})) = \underline{0}$$

Thus, as in homogeneous plates, the in-plane displacement $\underline{U}$, uniform within the thickness of the plate, is driven by the classic 2D equation which involves the mechanical parameters of the stiff layers only. In presence of a loading $\underline{f}(\underline{x}, y)$ the in-plane balance equation becomes:

$$E_0\underline{div}(\underline{\underline{\mathscr{E}}}(\underline{U})) = -\underline{F}(\underline{x}); \quad \underline{F}(\underline{x}) = \int_\Omega \underline{f}(\underline{x}, y)\mathrm{d}y \qquad (4.11)$$

For instance, in dynamic regime at frequency $f = \omega/2\pi$, $F(\underline{x}) = \rho_m h_t \omega^2 \underline{U}(\underline{x})$ where $\rho_m$ is the mean density of the stiff and soft layers, $\rho_m = \frac{h^s}{h_t}\rho + \frac{c}{h_t}\rho_c$.

– **Overall momentum balance**. Using the shape function $\phi_W$ for the integration, yields:

$$E_0 \underline{\mathrm{div}}\big( -\Phi_{WW}\underline{\underline{\mathscr{E}}}(\nabla W) + \Phi_{WD}\underline{\underline{\mathscr{E}}}(\underline{D})\big) = \int_\Omega \underline{\sigma_T}^2 \mathrm{dy}$$

i.e., denoting by $\underline{T}(\underline{x}) = \int_\Omega \underline{\sigma_T}^2 \mathrm{dy}$ the overall shear force:

$$E_0 \underline{\mathrm{div}}\big( -\mathscr{I}_2\underline{\underline{\mathscr{E}}}(\nabla W) + (2/\bar{h})\big(\mathscr{I}_2 - I_2\big)\underline{\underline{\mathscr{E}}}(\underline{D})\big) = \underline{T}$$

and introducing the rotation vector $\underline{\alpha} = \nabla_{\underline{x}}W - 2\underline{D}/\bar{h}$ one obtains:

$$-E_0(\mathscr{I}_2 - I_2)\underline{\mathrm{div}}(\underline{\underline{\mathscr{E}}}(\underline{\alpha})) - E_0 I_2 \underline{\mathrm{div}}(\underline{\underline{\mathscr{E}}}(\nabla W)) = \underline{T} \qquad (4.12)$$

– **Inner momentum balance**. It is derived through the shape function $\phi_D$ related to the sliding. The corresponding equation reads:

$$E_0 \underline{\mathrm{div}}\big( -\Phi_{WD}\underline{\underline{\mathscr{E}}}(\nabla W) + \Phi_{DD}\underline{\underline{\mathscr{E}}}(\underline{D})\big) = \int_{\Omega_c} \frac{2}{c}\underline{\sigma_T}^2 \mathrm{dy} = \frac{\mu_c}{c}4\underline{D}$$

that is also, after multiplying by $\bar{h}/2$:

$$E_0(\mathscr{I}_2 - I_2)\underline{\mathrm{div}}\big(\underline{\underline{\mathscr{E}}}\big( -\nabla W + 2\underline{D}/\bar{h}\big)\big) = \frac{\mu_c \bar{h}}{c}2\underline{D}$$

Introducing the rotation vector $\underline{\alpha} = \nabla_{\underline{x}}W - 2\underline{D}/\bar{h}$ one derives a second equation that couples the gradient of deflection $\nabla_{\underline{x}}W$ and the rotation vector $\underline{\alpha}$:

$$-E_0\big(\mathscr{I}_2 - I_2\big)\underline{\mathrm{div}}\big(\underline{\underline{\mathscr{E}}}(\underline{\alpha})\big) + \mu_c \frac{\bar{h}^2}{c}\big(\underline{\alpha} - \nabla W\big) = \underline{0} \qquad (4.13)$$

– **Overall shear balance**. Finally integrating the out-of-plane local balance (4.2a) at order $\varepsilon^2$ i.e. $\sigma_{N,y}^3 + \mathrm{div}_x(\underline{\sigma_T}^2) = 0$, over the whole thickness gives the driving equation of the overall shear force $\underline{T}$. In absence of external loading it reads: $\mathrm{div}(\underline{T}) = 0$. In presence of an out-of-plane loading $f(\underline{x}, y)\underline{a}_3$ it becomes:

$$\mathrm{div}(\underline{T}) = F(\underline{x}); \quad F(\underline{x}) = \int_\Omega f(\underline{x}, y)\mathrm{dy} \qquad (4.14)$$

In dynamic regime at frequency $f = \omega/2\pi$, $F(\underline{x}) = -\rho_m h_t \omega^2 W(\underline{x})$.

### *4.2.7 Synthesis*

For a better physical insight, the above results can be recast by introducing two torsors related to the out-of-plane behavior and a stress tensor related to the in-plane behavior, namely:

– the inner shear force within the soft layer averaged on the whole plate thickness $\underline{Q}$, dual of the sliding vector $\underline{D}$,
– the inner momentum symmetric tensor $\underline{\underline{M}}$ dual of the rotation vector $\nabla W$,
– the overall momentum symmetric tensor $\underline{\underline{\mathscr{M}}}$ dual of the rotation vector $\underline{\alpha}$,
– the overall transverse forces $\underline{T} = T\underline{a}_3$ dual of the deflexion $\underline{W} = W\underline{a}_3$,
– the 2D stress tensor $\underline{\underline{\Sigma}}$, dual of the in-plane strain $\underline{e}(U)$.

Then, considering a harmonic regime at pulsation $\omega$, the constitutive laws and the governing equations of the flexural behavior of the plate are re-written as follows:

$$
\begin{cases}
\underline{\underline{M}} = E_0 I_2 \underline{\underline{\mathscr{E}}}(\nabla W) \\
\underline{\underline{\mathscr{M}}} = E_0(\mathscr{I}_2 - I_2)\underline{\underline{\mathscr{E}}}(\underline{\alpha}) \\
\underline{Q} = K(\nabla W - \underline{\alpha}) = \mu_c \frac{\overline{h}^2}{c}(2\underline{D}/\overline{h})
\end{cases}
\quad , \quad
\begin{cases}
\operatorname{div}(\underline{T}) = -\omega^2 \rho_m h_t W \\
\underline{T} = -\underline{\operatorname{div}}(\underline{\underline{M}}) - \underline{\operatorname{div}}(\underline{\underline{\mathscr{M}}}) \\
\underline{Q} = -\underline{\operatorname{div}}(\underline{\underline{\mathscr{M}}})
\end{cases}
\tag{4.15}
$$

and for the in-plane behavior:

$$
\underline{\underline{\Sigma}} = E_0 \underline{\underline{\mathscr{E}}}(\underline{U}); \quad \underline{\operatorname{div}}(\underline{\underline{\Sigma}}) = -\omega^2 \rho_m \underline{U}
\tag{4.16}
$$

Note that the uniform in-plane displacement $\underline{U}$ is not coupled with $\underline{\alpha}$ nor $W$, while these two latter variables are coupled and define the flexural behavior of the plate.

## 4.3   Features of High-Contrast Stratified Plates

The set (4.15) shows that the classical in-plane and the out-of-plane behaviors are uncoupled. The bi-torsor description $\{(\underline{T}, \underline{\underline{\mathscr{M}}}) ; (\underline{Q}, \underline{\underline{M}})\}$ reflects straightforwardly the physical mechanisms within the plate. The out-of-plane load $F$ equilibrate the variations of the overall shear force $\underline{T}$. The latter $\underline{T}$ balances the variation of the proper bending moments of the two layers $\underline{\underline{M}}$ and the overall moment $\underline{\underline{\mathscr{M}}}$. Furthermore $\underline{\underline{\mathscr{M}}}$ results from the opposite normal forces in the upper and lower layers required to balance the inner shear force $\underline{Q}$ which comes from the central layer submitted to the sliding of the two stiff layers.

Such HCS plate model is consistent with several other approaches. For stratified beams, [9, 16] propose the same local and global physical mechanisms. The analysis performed in [10, 17] yield the same understanding of the phenomena. In fact, the assumptions considered in these works are validated by the asymptotic method. Note also that a similar bi-torsor formalism has been established for reticulated framed beams [13].

   It is worth mentioning that the HCS model encompasses the classical plate models as limit cases:

- very soft ($\mu \to 0$) central layer yields $\underline{Q} \to 0$ that corresponds to the bi-layer Kirchhoff plate of inertia $I_2$,
- very stiff ($\mu \to \infty$) central layer imposes $\nabla W - \underline{\alpha} \to 0$ that gives a monolithic Kirchhoff plate of inertia $\mathscr{I}_2$,
- when the overall bending effect dominates, $|\underline{\alpha}| \ll |\nabla W|$, a Reissner-Mindlin model is recovered,
- when the inner bending dominates, $|\nabla W| \ll |\underline{\alpha}|$, one obtains a Shear-Bending Sandwich model.

### 4.3.1   Criteria of Relevant Model

The criteria of transition from the general description to degenerated descriptions can be specified approximately through a dimensional analysis. The argument consists in using the fact that the description in only valid at the leading order. Consequently when an effect is $O(\varepsilon)$ compared to dominating effects it can be neglected.

To perform this analysis let us first establish the tri-Laplacian equation that governs the deflection $W$. Noticing that $\mathrm{div}\underline{\mathrm{div}}(\underline{\mathscr{E}}(\cdot)) = \mathrm{div}(\triangle(\cdot))$ and eliminating the rotation $\underline{\alpha}$ from (4.15) yields:

$$E_0 I_2 E_0(\mathscr{I}_2 - I_2)\triangle^3 W - E_0\mathscr{I}_2 K\triangle^2 W - E_0(\mathscr{I}_2 - I_2)\rho_t h_t \omega^2 \triangle W + K\rho_t h_t \omega^2 W = 0 \tag{4.17}$$

Incidentally, one also establishes that $\triangle W$ and $\mathrm{div}(\underline{\alpha})$ are related by:

$$K(\triangle w - \mathrm{div}(\underline{\alpha})) = -E_0(\mathscr{I} - I)\mathrm{div}(\triangle(\underline{\alpha})) \tag{4.18}$$

Introducing the characteristic size $\mathscr{L}$ of variation of $W$ gives the order of magnitude $O(\triangle^k W) = O(W/(\mathscr{L})^{2k})W^{*(2k)}$, where the dimensionless terms $W^{*(2k)}$ are O(1) by construction (in statics $\mathscr{L}$ is either of the order of $L$ or related to the load distribution, in dynamics $2\pi\mathscr{L}$ is the wave length of the modes). Therefore in order of magnitude the plate model established under the assumption:

$$\varepsilon = \frac{h_t}{\mathscr{L}} \ll 1$$

follows the dimensionless equation:

$$E_0 I_2 E_0(\mathscr{I}_2 - I_2)\frac{W^{*(6)}}{\mathscr{L}^6} - E_0\mathscr{I}_2 K\frac{W^{*(4)}}{\mathscr{L}^4} - E_0(\mathscr{I}_2 - I_2)\rho_m h_t \omega^2 \frac{W^{*(2)}}{\mathscr{L}^2} + K\rho_m h_t \omega^2 W^* = O(\varepsilon)$$

or equivalently, introducing the dimensionless structural numbers $C$, $\beta$, and the dynamic parameter $\chi$:

$$CbW^{*(6)} - (\beta + 1)W^{*(4)} - \chi W^{*(2)} + \tfrac{\chi}{C}W^* = O(\varepsilon)$$
$$C = \frac{E_0(\mathscr{I}_2 - I_2)}{K\mathscr{L}^2}; \quad \beta = \frac{I_2}{\mathscr{I}_2 - I_2} < 1; \quad \chi = \frac{\omega^2 \rho_m h_t}{K\mathscr{L}^2} \tag{4.19}$$

The complete description in dynamics is reached when $C$, $\beta$, are all $O(1)$. Now, according to the values of the dimensionless numbers compared to $\varepsilon$ powers, (4.19) degenerate into simplified forms. For instance a Reissner-Mindlin plate is recovered when $C = O(1)$ and $\beta = O(\varepsilon)$, etc. This approach results in the mapping (Fig. 4.2) that gives the validity domain of the possible behaviors according to the two parameters $p$ and $q$ defined by:

$$C = \varepsilon^p \quad ; \quad \beta = \varepsilon^q, \ q \geq 0 \tag{4.20}$$

Furthermore, a given plate is characterized by the dimensionless parameters $\beta$ and $\gamma = \frac{E_0(\mathscr{I}_2 - I_2)}{K h_t{}^2} = C\epsilon^{-2}$, that are *fixed and known* whatever $\mathscr{L}$ is. Consequently the parameters $p$ and $q$ determining the possible behaviors of this given plate experiencing different macroscopic $\mathscr{L}$ satisfy the relations:

$$(p - 2)\log(\varepsilon) = \log(\gamma) \ ; \quad q\log(\varepsilon) = \log(\beta) \ \text{ i.e. } \ -(p - 2)\log(\beta) + q\log(\gamma) = 0 \tag{4.21}$$

Thus, in the $(p, q)$ plane, the possible behaviors a given plate necessarily lie on a straight line issuing from point P (p = 2, q = 0). The negative slope of the line is $\log(\beta)/\log(\gamma)$ and lies in between $\{0, -1\}$ (resp. $\{-1, -\infty\}$) when $\beta\gamma < 1$ (resp. $> 1$). Hence, the intrinsic dimensionless parameter:

$$\beta\gamma = \frac{E_0 I_2}{K h_t{}^2}$$

is an essential number that determines the possible behaviors of the plate.

The position on the line (hence, the relevant model) moves away from P as $\mathscr{L}$ is decreased (smaller size of plate, "shorter" variations of loading or higher modes). This corresponds to the well known size effect related to slenderness in plate theory. Recall finally that the relevancy of this approach is conditioned by the assumption $\varepsilon = \frac{h_t}{\mathscr{L}} \ll 1$.

It is interesting to note that although the internal kinematics differ markedly from those of homogeneous plates, the degenerate models correspond to classical or generalized homogeneous plate formulations. For example, the Reissner-Mindlin model for thick homogeneous plates is described by the same set of equilibrium equations as the degenerate model for thin HCS plates when $|\alpha| \ll |\nabla W|$. However, the parameters of the constitutive laws are fundamentally different.
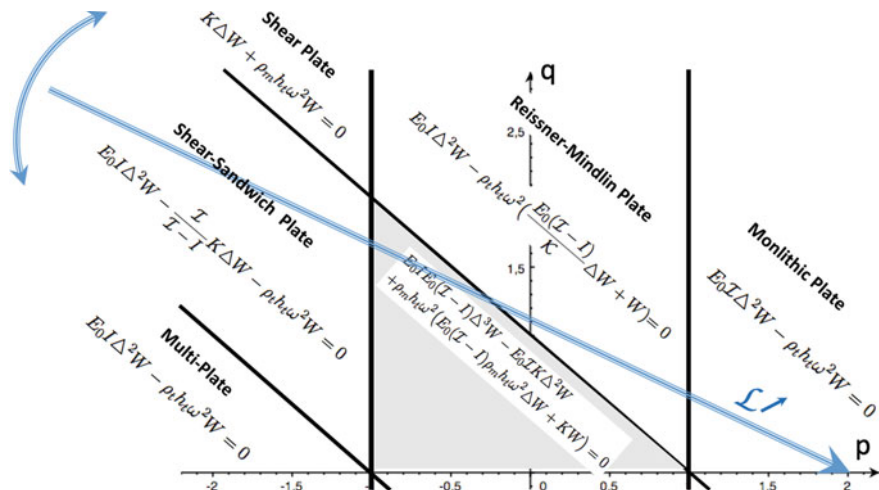
**Fig. 4.2** The possible HCS plates with two or three stiff layers behaviors according to values of $p$ and $q$ defined in (4.20). In each domain the governing equation in harmonic regime is indicated ($\mathscr{I}$ and $I$ stand for $\mathscr{I}_2$ and $I_2$ for two stiff layers and for $\mathscr{I}_3$ and $I_3$ for three stiff layers). The complete model arises in the gray triangle. According to $\mathscr{L}$, the possible behaviors of a given plate characterized by the dimensionless number $b$ and $c$ lies on the blue triple straight line $-(p - 2)\log(\beta) + q\log(c) = 0$

## 4.3.2  Energy Balance and Boundary Conditions

In-plane and out-of plane energy balances can be established independently considering either the energy developed by the in-plane displacement $\underline{U}$ or by the deflection $W$.

The in-plane energy $\int_S \underline{F}.\underline{U}ds$ can be expressed form the balance Eq. (4.16) and integration by part. One obtains the classical formula:

$$\int_S \underline{F}.\underline{U}ds = +E_0 \int_S \mathbf{E}_\nu(\underline{U})ds + \int_{\partial S} \underline{\underline{\Sigma}}.\underline{n}.\underline{U}dl \qquad (4.22)$$

in which $\mathbf{E}_\nu(.) = (1 - \nu)\|\underline{e}(.)\|^2 + \nu\mathrm{div}(.)^2$.

Now, the deflection energy $\int_S F.Wds$ can be transformed using the balance Eq. (4.15) and twice integrations by parts. This gives:

$$\int_S Fwds = K \int_S |\nabla w - \underline{\alpha}|^2 ds + E_0 I_2 \int_S \mathbf{E}_\nu(\nabla w)ds + E_0(\mathscr{I}_2 - I_2) \int_S \mathbf{E}_\nu(\underline{\alpha})ds$$

$$+ \int_{\partial S} \left\{ \underline{T}.\underline{n}w + (\underline{\underline{M}}.\underline{n})\underline{\alpha} + (\underline{M}.\underline{n})\nabla w \right\} dl \qquad (4.23)$$

On the right hand side, one recognizes in the integrals over $\partial S$ the deformation energy due (i) to the shear of the central layer, (ii) to the inner bending of each layer and (iii) to the overall bending of the plate. The integrals over $\partial S$ express the energy provided at the border. They disclose the boundary conditions to be used for the plate, which can be expressed either with the forces and momentum $\underline{T}$, $\underline{\underline{\mathscr{M}}}$ and $\underline{\underline{M}}$ or with the kinematic variables $W$, $\underline{\alpha}$, and $\underline{\nabla}W$. For instance:

- at a free border: $\underline{T}.\underline{n} = 0$ and $\underline{\underline{\mathscr{M}}}.\underline{n} = \underline{\underline{M}}.\underline{n} = \underline{0}$
- on a strictly clamped border, i.e., without sliding: $W = 0$ and $\underline{\nabla}w = \underline{\alpha} = \underline{0}$
- on a simply supported border: $W = 0$ and $\underline{\underline{\mathscr{M}}}.\underline{n} = \underline{\underline{M}}.\underline{n} = \underline{0}$.

### 4.3.3 Flexural Waves

The flexural waves propagating along the $x$-axis (or any other direction because of the in-plane isotropy of the plate), induces a deflection:

$$W(x, t) = W_0 \exp(kx) \exp(i\omega t)$$

where $k$ is the frequency dependent real or complex wave number. This expression introduced in the Tri-Laplacian equation (4.17) provides the dispersion equation:

$$E_0 I_2 E_0 (\mathscr{I}_2 - I_2)k^6 - E_0 \mathscr{I}_2 K k^4 - E_0 (\mathscr{I}_2 - I_2)\rho_m h_t \omega^2 k^2 + K\rho_m h_t \omega^2 = 0 \quad (4.24)$$

Introducing the following parameters:

$$a = \frac{\mathscr{I}_2}{\mathscr{I}_2 - I_2} \quad ; \quad A = \frac{K}{E_0 I_2} \quad ; \quad \varpi = \frac{\rho_m h_t \omega^2}{K} \quad (4.25)$$

Equation (4.24) is rewritten as the following cubic equation of unknown $k^2$:

$$(k^2)^3 - aA(k^2)^2 - A\varpi k^2 + (a - 1)A^2\varpi = 0 \quad (4.26)$$

Hence, consistently with the existence of three degrees of freedom $(W, \nabla W, \alpha)$, there are three types of bending waves characterized by the three roots $k_1^2, k_2^2, k_3^2$ of (4.26). Through the Cardan's method it can be shown that as $a - 1$, $A$ and $\varpi$ are positive the three roots are reals, one negative, two positive, i.e. $k_1^2 < 0 < k_2^2 < k_3^2$. Hence there is a single propagative flexural wave and two evanescent waves. Furthermore, a good approximation of $k_1^2$ can be established using Padé approximant based and the low and high frequency limits, see [4]:

$$-k_1^2 \approx \omega \sqrt{\frac{\rho_t h_t}{E_0 I_2}} \left(1 - \frac{1 + \frac{1}{2}\tilde{\omega}}{1 + \tilde{\omega} + \frac{\tilde{\omega}^2}{1 + \sqrt{I_2/\mathscr{I}_2}}} \left(1 - \sqrt{\frac{I_2}{\mathscr{I}_2}}\right)\right) \quad (4.27)$$

where:

$$\tilde{\omega} = \frac{\omega}{\omega_0}; \quad \omega_0 = \frac{1}{1 + \sqrt{I_2/\mathscr{I}_2}} \left( \frac{\mathscr{I}_2}{\mathscr{I}_2 - I_2} \right)^2 \frac{K}{\sqrt{E_0 I_2 \rho_m h_t}}$$

from which the two positives roots can be calculated using the exact relations:

$$k_p^2 = \frac{aA - k_1^2}{2} \left( 1 \mp \sqrt{1 - 4\left(1 - \frac{k_1^2}{(a-1)A}\right)^{-1} \left(1 - \frac{aA}{k_1^2}\right)^{-1}} \right); \quad p = 2, 3 \quad (4.28)$$

For each type of bending wave $W \exp(k_p x)$, the overall rotation $\alpha \exp(k_p x)$ and sliding $D \exp(k_p x)$, are deduced from (4.6) and (4.18). Thus the associated in-plane displacements $u(x, y)$ reads:

$$u(x, y) = k_p \left( \phi_W(y) - \phi_D(y)\bar{h} \frac{k_p^2}{(a-1)A - k_p^2} \right) W \exp(k_p x) \quad (4.29)$$

Thus, for the progressive $k_1$-wave $\alpha$ and $D$ are in phase quadrature with the deflection $W$, while, for the evanescent $k_2$ and $k_3$-waves, $\alpha$ and $D$ are respectively in phase and in opposition of phase with $W$. Furthermore, the inner kinematics of the plate differ for the three waves and varies with the frequency for a given type of wave.

### 4.3.4 Buckling

Consider a rectangular plate of length $L$ along $\underline{a}_1$, and width $2B$ along $\underline{a}_2$. This plate has a free boundary on the border $x_2 = \pm B$, while it is loaded by a normal force $P\underline{a}_1$ on the border $x_1 = \pm L/2$. Under buckling, the total moment induced by the load is

$$-PW(x_1) = M(x_1) + \mathscr{M}(x_1)$$

where $W$ is the buckled deflection. Hence, the balance Eq. (4.15a, b) expressed in 1D and statics ($\omega = 0$) imposes that the overall shear force is such that:

$$T = \frac{d(M + \mathscr{M})}{dx_1} = -P\frac{dW}{dx_1} \quad , \quad \frac{dT}{dx_1} = -P\frac{d^2W}{dx_1^2}$$

Then, eliminating the rotation $\alpha$ in (4.15) provides the 1D tri-Laplacian equation (4.17) in which $\rho_m h_t \omega^2 W$ is replaced by $-PW^{(2)}$, that is:

$$E_0 I_2 E_0 (\mathscr{I}_2 - I_2) W^{(6)} - E_0 \mathscr{I}_2 K W^{(4)} + E_0 (\mathscr{I}_2 - I_2) P W^{(4)} - K P W^{(2)} = 0$$
$$(4.30)$$

Pinned-pinned boundary conditions:

$$M(\pm L/2) = 0 \quad ; \quad W(\pm L/2) = 0$$

enables to derive a closed-form solution. Indeed these conditions are fulfilled by a cosinusoïdal deflection:

$$W = W_0 \cos(\pi x_1/L)$$

Introducing this expression into (4.30) leads to the critical buckling load:

$$\left(\frac{\pi}{L}\right)^2 E_0 I_2 < P_{cr} = \left(\frac{\pi}{L}\right)^2 E_0 \frac{I_2 E_0 (\mathscr{I}_2 - I_2)(\pi/L)^2 + \mathscr{I}_2 K}{E_0 (\mathscr{I}_2 - I_2)(\pi/L)^2 + K} < \left(\frac{\pi}{L}\right)^2 E_0 \mathscr{I}_2$$

(4.31)

As expected, $P_{cr}$ lies in between the critical buckling loads of a bi-layer and a mono-lithic Kirchhoff plate of respective bending inertia $I_2$ and $\mathscr{I}_2$. For other boundary conditions, the determination of the critical load require to identify the buckled shape respecting both the boundary conditions and (4.30).

### 4.3.5   Plates with Soft Viscoelastic Layer

The HCS model is directly applicable to plates with viscoelastic constituents provided that the variables are expressed in the frequency domain, and the elastic parameters are replaced by the complex-valued coefficients at a given frequency. The time domain response can be obtained by inverse Fourier transform. It is also possible to work directly in the time domain. In this case the equilibrium equations remain unchanged while the constitutive laws involve convolution products. These express the non-locality in time induced by the viscoelastic behavior, which is manifested by memory effects.

    The case of a soft viscoelastic core layer between rigid elastic layers is of practical importance because many soft materials used for example to bond rigid layers are not strictly elastic. The typical example is laminated glass, where the shear modulus of the viscoelastic core layer can vary over several orders of magnitude as a function of temperature and frequency. In that case, one has:

$$\underline{Q}(t) = K(t) * \left(\underline{\nabla}_{\underline{x}} W - \underline{\alpha}\right)(t) \quad \text{with} \quad K(t) = \bar{h}^2/c \int_{-\infty}^{\infty} \exp^{(-i\omega t)} \mu_c(\omega \tau_\theta) d\omega$$

The time dependence in the constitutive law implies memory effects in the plate behavior, such as creep and relaxation, see [12] for analyzing creep response of three points bending experiments. It should be noted that, since the viscoelasticity of the

central layer combines with the elastic bending of the stiff layers, the time response of the plate cannot be reduced to a purely rheological feature (i.e., as if the plate were made of a specific viscoelastic material) because the spatial variations are also involved, [3]. Moreover, since the shear modulus $\mu_c$ varies then the dimensionless parameter $\gamma = \frac{E_0(\mathscr{I}_2 - I_2)}{K h_t^2}$ is not a constant. Therefore, in the $(p, q)$ map the possible behaviors are not restricted to a straight line.

Regarding flexural waves, analytical developments similar to those in Sect. 4.3.3 apply but the roots of the dispersion Eq. (4.26) becomes complexe. As a result, the progressive bending wave is attenuated and the evanescent waves exhibit spatial oscillations. Accordingly, the variables $(W, \alpha, D)$ describing the kinematics of the three modes of the plate are all out phase and their ratio varies with frequency.

It should also be noted that the critical buckling load becomes time dependent, and takes different values for instantaneous loading and for slow monotonic loading.

## 4.4  Generalization to Multi-layered Contrasted Plates

### 4.4.1  Plates with Three Stiff Layers

Consider now a plate made of three layers ($\Omega^s = \Omega^+ \cup \Omega^0 \cup \Omega^-$) made of the same stiff material, and two layers ($\Omega^c = \Omega^{c+} \cup \Omega^{c-}$) made of the same soft material. To simplify the expressions (but this not a restriction of the method) one assume here that the three stiff layers are identical of thickness $h$, and the two soft layers are identical of thickness $c$ so that the total thickness is $h_t = 3h + 2c$ (Fig. 4.3).

Following the same procedure, one establishes that the whole system experiences a deflection $W^0(\underline{x})$, and that each of the three stiff layers follows the classical Kirchhoff kinematics, and can slide on each other. More precisely the in plane fields in the stiff layers can be decomposed as follows:
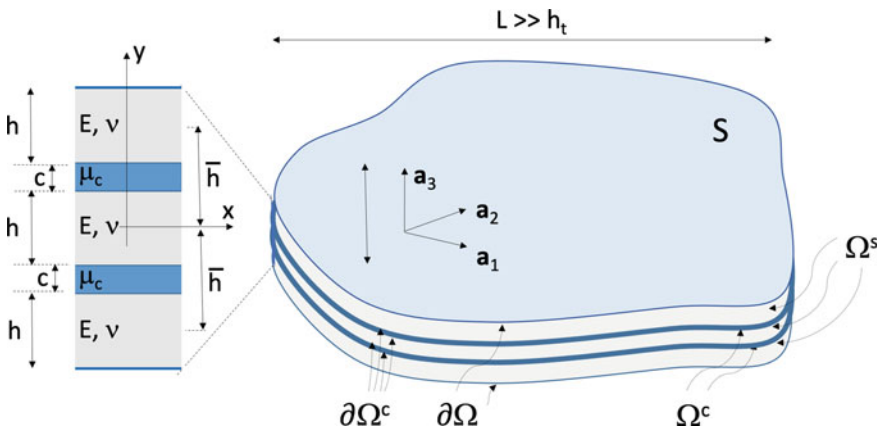


**Fig. 4.3** HCS Plate with three stiff layers. Notations

**Table 4.2** Integrated products of the shape functions of the three stiff layers plate

| $\Phi_{AB}$ | $\phi_U$ | $\phi_W$ | $\phi_D$ | $\phi_S$ |
|---|---|---|---|---|
| $\phi_U$ | $3h$ | $0$ | $0$ | $0$ |
| $\phi_W$ | $0$ | $\mathscr{I}_3 = I_3 + 2\overline{h}^2 h$ | $(\mathscr{I}_3 - I_3)/\overline{h}$ | $0$ |
| $\phi_D$ | $0$ | $(\mathscr{I}_3 - I_3)/\overline{h}$ | $(\mathscr{I}_3 - I_3)/\overline{h}^2$ | $0$ |
| $\phi_S$ | $0$ | $0$ | $0$ | $6h$ |

$I_3 = 3I = 3h^3/12$ ; $\overline{h} = h + c$

$$\begin{cases} \underline{u}^1 = -y\underline{\nabla}_x W + \underline{U}(x) + \underline{D}(x) + \underline{S}(x) & \text{in } \ \Omega^+ \\ \underline{u}^1 = -y\underline{\nabla}_x W + \underline{U}(x) + 0 - 2\underline{S}(x) & \text{in } \ \Omega^0 \\ \underline{u}^1 = -y\underline{\nabla}_x W + \underline{U}(x) - \underline{D}(x) + \underline{S}(x) & \text{in } \ \Omega^- \end{cases} \tag{4.32}$$

or also:

$$\underline{u}^1(\underline{x}, y) = -\phi_W(y)\underline{\nabla}W(\underline{x}) + \phi_U(y)\underline{U}(\underline{x}) + \phi_D(y)\underline{D}(\underline{x}) + \phi_S(y)\underline{S}(\underline{x}) \tag{4.33}$$

where the shape functions defined in $\Omega$ describe:

– the homogeneous in-plane displacement, $\phi_U = 1$,
– linear Kirchhoff 's kinematics, $\phi_W = y$,
– the continuous antisymmetric in-plane displacement, $\phi_D = \{1, 0, -1\}$ in $\{\Omega^+, \Omega^0, \Omega^-\}$, and $\phi_D$ varies linearly in the soft layers, i.e. $\frac{\partial \phi_D}{\partial y} = \frac{1}{c}$ in $\Omega^c$ ,
– the continuous symmetric in-plane displacement with $\phi_S = \{1, -2, 1\}$ in $\{\Omega^+, \Omega^0, \Omega^-\}$, and $\phi_S$ varies linearly in the soft layers, i.e. $\frac{\partial \phi_D}{\partial y} = \{\frac{3}{c}, -\frac{3}{c}\}$ in $\{\Omega^{c+}, \Omega^{c-}\}$.

The overall rotation $\underline{\alpha}$ is in that case defined by:

$$\underline{\alpha} = \underline{\nabla}(W) - \underline{D}\frac{1}{h + c}$$

#### 4.4.1.1 Governing Equations

Four overall balances are established by multiplying the local in-plane balance (4.3) at the order $\varepsilon^2$ by each of the four shape function and integrating them over the whole plate thickness. In addition, as previously, the overall shear balance is obtained by a direct integration of (4.2) at the order $\varepsilon^3$. The shape functions are such that their integrated crossed products $\Phi_{AB}$ may be null which, in that case, results in uncoupled terms. The values presented in Table 4.2 shows that the in-plane displacements $\underline{U}$ and $\underline{S}$ are independent and uncoupled variables, while the out-of-plane deflection $W$ and the in-plane sliding displacements $\underline{D}$ are coupled.

From this procedure the following set of equations is derived:

$$
\begin{cases}
E_0\underline{\mathrm{div}}(\underline{\underline{\mathscr{E}}}((\underline{U})) = -\underline{F}(\underline{x}) \\
-E_0(\mathscr{I}_3 - I_3)\underline{\mathrm{div}}(\underline{\underline{\mathscr{E}}}(\underline{\alpha})) - E_0 I_3\underline{\mathrm{div}}(\underline{\underline{\mathscr{E}}}(\nabla W)) = \underline{T} \\
-E_0(\mathscr{I}_3 - I_3)\underline{\mathrm{div}}(\underline{\underline{\mathscr{E}}}(\underline{\alpha})) + \mu_c\frac{2\overline{h}^2}{c}(\nabla W - \underline{\alpha}) = \underline{0} \\
E_0\underline{\mathrm{div}}(\underline{\underline{\mathscr{E}}}(\underline{S})) - 3\frac{\mu_c}{h.c}\underline{S} = -\underline{\widetilde{F}}(\underline{x}) \\
\mathrm{div}(\underline{T}) = -F(\underline{x})
\end{cases} \tag{4.34}
$$

where:

$$
\underline{F}(\underline{x}) = \int_\Omega \underline{f}(\underline{x}, y)\mathrm{d}y; \quad F(\underline{x}) = \int_\Omega f(\underline{x}, y)\mathrm{d}y; \quad \underline{\widetilde{F}}(\underline{x}) = \int_\Omega \underline{f}(\underline{x}, y)\phi_S(y)\mathrm{d}y
$$

The description splits into three independent sets:

- **Out-of-plane behavior** The set (4.34b, c, e) corresponds to a bi-torsor description, identical to (4.15) with similar constitutive laws except that the parameters $(\mathscr{I}_2, I_2, K)$ are modified into $\mathscr{I}_3, I_3, K_{c2}$:

$$
\begin{cases}
\underline{M} = E_0 I_3\underline{\underline{\mathscr{E}}}(\nabla W) \\
\underline{\underline{\mathscr{M}}} = E_0(\mathscr{I}_3 - I_3)\underline{\underline{\mathscr{E}}}(\underline{\alpha}) \\
\underline{Q} = K_{c2}(\nabla W - \underline{\alpha}) = \mu_c\frac{\overline{h}^2}{2c}(2\underline{D}/\overline{h})
\end{cases}
,\quad
\begin{cases}
\mathrm{div}(\underline{T}) = -\omega^2\rho_m h_t W \\
\underline{T} = -\underline{\mathrm{div}}(\underline{M}) - \underline{\mathrm{div}}(\underline{\underline{\mathscr{M}}}) \\
\underline{Q} = -\underline{\mathrm{div}}(\underline{\underline{\mathscr{M}}})
\end{cases} \tag{4.35}
$$

- **Homogeneous in-plane behavior** Equation (4.34a) is the same as (4.16).
- **Inhomogeneous in-plane behavior** An new differential in-plane behavior appears (4.34b) governed by the following differential set acting on $\underline{S}(\underline{x})$:

$$
\underline{\mathrm{div}}_x(\underline{\underline{\Xi}}) - 3\frac{\mu_c}{h}\frac{\underline{S}}{c} = \underline{\widetilde{F}}(\underline{x}) \quad ; \quad \underline{\underline{\Xi}} = E_0\underline{\underline{\mathscr{E}}}(\underline{S}) \tag{4.36}
$$

Since the $\Phi_{US} = 0$, $\underline{\widetilde{F}}(\underline{x}) = 0$ in presence of a uniform (in the thickness) in-plane body force. However, in dynamics, the inertial forces in harmonic regime $\rho\omega^2\phi_S(y)\underline{S}$ are not homogenous. Then the balance involves an inertial term characterized by an effective density $R$:

$$
\underline{\mathrm{div}}_x(\underline{\underline{\Xi}}) - 3\frac{\mu_c}{h}\frac{\underline{S}}{c} = -R\omega^2\underline{S} \quad ; \quad R = \int_\Omega \rho(y)\phi_S^2\mathrm{d}y \tag{4.37}
$$

### 4.4.1.2 Flexural Waves and Buckling

These results show that the features of the flexural waves and of the homogeneous in-plane waves in a three stiff layers plate are identical (with different parameters) than that of the two layer plate. However, in addition to the usual in-plane shear and compressional waves new modes arises which involves the inhomogeneous symmetric field $\underline{S}$. Their governing equation is of Helmholtz type complemented by a linear

term. Hence, the corresponding waves presents a cut-off frequency below which the wave reduces to a boundary layer with an exponential decay.

Note in addition, that the critical load for buckling can be expressed in the same way as (4.31) provided that the parameters $(\mathcal{I}_2, I_2, K)$ are replaced by $(\mathcal{I}_3, I_3, K_{c2})$ (this change must also be made for $a$, $A$ and $\varpi$).

### 4.4.2  Plates with n Stiff Layers

Consider now multi-layer laminates made of $n > 3$ stiff layers assumed here identical of thickness $h$, as well as the $n - 1$ soft layers of thickness $c$ in between them. The stiff and soft domain are respectively:

$$\text{if } n = 2p, \ \Omega^s = \cup_i \Omega^i, \ i \in [-p, p], \ i \neq 0 \ \ ; \ \ \Omega^c = \cup_j \Omega^{cj}, \ j \in [-p+1, p-1]$$
$$\text{if } n = 2p+1, \ \Omega^s = \cup_i \Omega^i, \ i \in [-p, p] \ \ ; \ \ \Omega^c = \cup_j \Omega^{cj}, \ j \in [-p, p], \ j \neq 0$$

The same procedure can be applied, and we focus here on the structure of the description.

As previously in such laminate, the whole plate experiences a common deflection $W(\underline{x})$, and each of the $n$ stiff layers follows the classical Kirchhoff kinematics and can slide on each other. Consequently, the in-plane fields in the stiff layers can be decomposed into:

- the Kirchhoff 's linear displacement related to $\underline{\nabla}W$ of shape function $\phi_W = y$,
- the homogeneous in-plane displacement $\underline{U}$ associated with the uniform shape function $\phi_U = 1$,
- a set of $p$ anti-symmetric in-plane displacements of zero mean average over $\Omega^s$ characterized by their amplitude $\underline{D}_q$, $q \in [1, p]$ and their anti-symmetric shape function $\phi_{D_q}(y)$,
- a set of $p'$ ($p'$ stands either for $p - 1$ or $p$ according to $n = 2p$ or $n = 2p+1$) symmetric in-plane displacements of zero mean average over $\Omega$, each characterized by the amplitude $\underline{S}_m$, $m \in [1, p']$ and the symmetric shape function $\phi_{S_m}$.

From these considerations, we deduce that:

$$\underline{\text{div}}(\underline{\underline{\sigma}}^1) = E_0 \underline{\text{div}}\left(-\phi_W \underline{\underline{\mathcal{E}}}(\underline{\nabla}W) + \phi_U \underline{\underline{\mathcal{E}}}(\underline{U}) + \Sigma_{q=1}^p \phi_{D_q} \underline{\underline{\mathcal{E}}}(\underline{D_q}) + \Sigma_{m=1}^{p'} \phi_{S_m} \underline{\underline{\mathcal{E}}}(\underline{S_m})\right)$$

(4.38)

and

$$\underline{\sigma}_{Tc}^2 = \mu_c \left(\Sigma_{q=1}^p \frac{\partial \phi_{D_q}}{\partial y} \underline{D_q} + \Sigma_{m=1}^{p'} \frac{\partial \phi_{S_m}}{\partial y} \underline{S_m}\right)$$

(4.39)

Reporting these expressions in the $n + 1$ equations obtained with the different shape functions $\phi_A(y)$, i.e.:

$$\int_\Omega \phi_A(y)\underline{\mathrm{div}}_x(\underline{\underline{\sigma}}^1)\mathrm{d}y = \int_\Omega \frac{\partial \phi_A}{\partial y}\underline{\sigma_T}^2\mathrm{d}y \tag{4.40}$$

together with the out-of-plane local balance $\sigma_N{}^3{}_{,y} + \mathrm{div}_x(\underline{\sigma_T}^2) = F(\underline{x})$ integrated over the whole thickness, yields the govering equations.

Now, for a better physical insight, is possible and convenient to choose the anti-symmetric modes $\{\phi_{D_q}\}$ such that they constitue an orthogonal basis in the sense that

$$\forall q \neq r \quad \Phi_{D_q D_r} = \int_{\Omega_s} \phi_{D_q}\phi_{D_r}\mathrm{d}y = 0 \quad ; \quad \Psi_{D_q D_r} = \int_{\Omega_c} \frac{\partial \phi_{D_q}}{\partial y}\frac{\partial \phi_{D_r}}{\partial y}\mathrm{d}y \neq 0$$

The inequality indicates that the orthogonality cannot not be satisfied for both the functions and their derivatives. Similarly, one chooses the symmetric fields $\{\phi_{S_m}\}$ of zero mean value in such a way that they form an orthogonal basis and then:

$$\forall m \neq l \quad \Phi_{S_m S_l} = \int_{\Omega_s} \phi_{S_m}\phi_{S_l}\mathrm{d}y = 0 \quad \Psi_{S_m S_l} = \int_{\Omega_c} \frac{\partial \phi_{S_m}}{\partial y}\frac{\partial \phi_{S_l}}{\partial y}\mathrm{d}y \neq 0$$

By construction, we have also the following relations:

$$\Phi_{UW} = 0, \text{ and }, \forall D_q, S_m : \Phi_{U D_q} = \Phi_{U S_m} = \Phi_{S_m D_q} = \Phi_{W S_m} = 0 \quad ; \quad \Phi_{W D_q} \neq 0$$

Using shape functions thus defined we obtain three uncoupled subsets of equations.

### 4.4.2.1   Structure of the Governing Equations

- **Homogeneous in-plane behavior**: The orthogonality of $\phi_U$ with all the other shape functions makes the homogeneous in-plane behavior is unchanged and governed by the usual in-plane balance equation.

$$E_0\underline{\mathrm{div}}(\underline{\underline{\mathscr{E}}}(\underline{U})) = -\underline{F}(\underline{x})$$

- **Out-of-plane behavior**: The shape functions $\phi_{D_q}$, $q = 1, p$, are uncoupled each other but coupled with $\phi_W$. Consequently the out-of plane behavior is governed by the $p$ kinematic descriptors $\underline{D}_q$ together with $W$ and $\underline{\nabla}W$. Using respectively the shape function $\phi_W$ and $\phi_{D_q}$ the for the integration yields, where $\underline{T}(\underline{x})$ is the overall shear force:

$$E_0 \underline{\mathrm{div}}\big( -\varPhi_{WW}\underline{\underline{\mathscr{E}}}(\nabla W) + \Sigma_{q=1}^p \varPhi_{WD_q}\underline{\underline{\mathscr{E}}}(\underline{D}_q)\big) = \underline{T}$$

$$E_0 \underline{\mathrm{div}}\big( -\varPhi_{WD_q}\underline{\underline{\mathscr{E}}}(\nabla W) + \varPhi_{D_q D_q}\underline{\underline{\mathscr{E}}}(\underline{D}_q)\big) = \mu_c \Sigma_{q=1}^p \Psi_{D_p D_q}\underline{D}_p$$

Defining for each $\underline{D}_q$ a corresponding apparent rotation $\underline{\alpha}_q$ by:

$$\underline{\alpha}_q = \nabla W - \frac{\varPhi_{D_q D_q}}{\varPhi_{WD_q}} \underline{D}_q$$

enables to re-writte the governing equations in a form that generalizes that identified for the two- and three- stiff layers plates and involves $p+1$ torsors $\big(\underline{T}, \underline{\underline{M}}, \{\underline{Q}_q, \underline{\underline{M}}_q\}\big)$:

$$\begin{cases} \mathrm{div}_{\underline{x}}(\underline{T}) = -F(\underline{x}) \\ \quad \underline{T} = -\underline{\mathrm{div}}_{\underline{x}}(\underline{\underline{M}}) - \sum_{q=1}^p \underline{\mathrm{div}}_{\underline{x}}(\underline{\underline{\mathscr{M}}}_q) \\ \quad Q_q = -\underline{\mathrm{div}}_{\underline{x}}(\underline{\underline{\mathscr{M}}}_q) \end{cases} \tag{4.41}$$

with the fully determined constitutive laws:

$$\begin{cases} \underline{T}_q = K_q\big(\nabla_{\underline{x}} W - \underline{\alpha}_q\big) & ; & K_q = \mu_c \dfrac{\varPhi_{WD_q}^2}{\varPhi_{D_q D_q}^2}\Psi_{D_p D_q} \\ \underline{\underline{M}} = E_0 I \underline{\underline{\mathscr{E}}}(\nabla W) & ; & I = \varPhi_{WW} - \Sigma_{q=1}^p \dfrac{\varPhi_{WD_q}^2}{\varPhi_{D_p D_q}} \\ \underline{\underline{\mathscr{M}}}_q = E_0 \mathscr{I}_q \underline{\underline{\mathscr{E}}}(\underline{\alpha}_q) & ; & \mathscr{I}_q = \dfrac{\varPhi_{WD_q}^2}{\varPhi_{D_p D_q}} \end{cases} \tag{4.42}$$

- **Inhomogeneous In-plane behavior**: The symmetric non-homogeneous displacements of zero mean value associated to $\underline{S}_m$, $m = 1$, $p'$, are orthogonal each other and also orthogonal to both the homogeneous and the antisymmetric fields. Thus introducing (4.38) and (4.39) into (4.40) provides:

$$E_0 \underline{\mathrm{div}}\big(\underline{\underline{\mathscr{E}}}(\underline{S}_l)\big) - \mu_c \Sigma_{m=1}^{p'} \frac{\Psi_{S_m S_l}}{\varPhi_{S_m S_l}}\underline{S}_m = -\underline{\widetilde{F}}_l(\underline{x}) \quad , \quad \underline{\widetilde{F}}_l(\underline{x}) = \int_\Omega \underline{f}(\underline{x}, y)\phi_{S_l}(y)\mathrm{d}y$$

This define the coupled set of $p'$ equations that governs the $p'$ non-homogeneous in-plane symmetric fields.

Emphasis that the above description lies on the symmetric/antisymmetric decoupling. This geometric argument, and therefore the differential set of equations, applies for any stratified plate whatever the thickness of the layers provided that they are symmetrically distributed.

#### 4.4.2.2   Waves and Buckling

Eliminating the $p$ rotations in (4.41) and (4.42) shows that the deflection $W$ is governed by a $(p + 2)$-Laplacian equation. This implies that a plate with $n = 2p$ or $2p + 1$ stiff layers presents $p + 2$ flexural modes consistently with the $p + 2$ degrees of freedom $(W, \nabla W, \alpha_q)$, q = 1, p. All these modes involves anti-symmetrical shapes through the thickness. A detailed analysis of the dispersion equation would be required to determine the evanescent or propagative nature of theses modes. As regard to in-plane waves, there is $2p$ modes corresponding to $p$ shear and $p$ compressional waves. Among them one distinguishes the classic waves with uniform shape within the thickness and the non conventional waves of non uniform symmetric shapes in the thickness.

The critical load for buckling can be determined as previously by expressing that the total momentum is $M + \sum_{q=1}^{p} \mathscr{M}_q = -PW$. Then after eliminating the $\alpha_q$ an equation similar to the dispersion equation in 1D where $\rho_t h_t \omega^2 W$ is replaced by $-PW^{(2)}$ is obtained. However, for $n > 3$, the classical pinned-pinned boundary conditions $M(\pm L/2) = 0$ and $W(\pm L/2) = 0$ are not sufficient and must be complemented by $2(p - 1)$ conditions involving $D_q$ or $\alpha_q$. Different values of the critical load will be obtained depending on the choice of the complementary conditions.

### 4.5   Conclusion

The concise description of HCS plates grasp the physics in a simple and closed analytical form that encompasses in a same framework, symmetric and non-symmetric plates, viscoelastic constituents, dynamic behavior and buckling. This formulation overcomes the numerical issues of Finite Element models that face difficulties to manage the contrasted mechanical and geometrical parameters in elasto-statics and, a fortiori, in visco-elasto-dynamics. It also circumvent the intrinsic limitations of the semi-empirical approaches based on effective stiffness in statics that are not applicable for dynamics.

The proper physical account of the global and local mechanisms of shear and bending open several possibilities—not developed in this work—among which:

- identify the local state of strain and stress within the constituents, and then evaluate the strength of HCS plate under dynamics/transient loadings,
- determine the damping due to the internal dissipation within the visco-elastic central layer,
- assess in the case of thermo-sensible constituents the influence of the temperature on the dynamic properties.

The proposed approach can be implemented either to calculate the actual behavior of industrial laminated panels or to optimise the design (including the choice of the viscoelastic properties of the central layer) for specific purposes related either to the strength or to the acoustic performance (transmission loss) of stratified panels.

Another area of application concerns composite structures with flexible discrete connections, as illustrated by the study of reticulated beams [13]. Let us conclude by pointing out that these results are only valid under the following conditions:

- the thickness is sufficiently small compared to the characteristic size $\mathscr{L}$ (theoretically infinitely small, in practice less than one fifth of $\mathscr{L}$),
- the contrast in properties only affects the stiffness.

This is the case of laminated glass for which a series of vibrational and creep experiments [4–20] showed very good agreement with the theoretical results of the HCS plate model. Nevertheless, as demonstrated in [14], other models are possible for contrasted plates if one additionally introduces contrasts on the thicknesses of the layers and on their densities.

# References

1. Auriault J-L, Boutin C, Geindreau C (2009) Homogenization of coupled phenomena in heterogenous media. ISTE and Wiley
2. Berdichevsky VL (2010) An asymptotic theory of sandwich plates. Int J Eng Sci 48:383–404
3. Boutin C, Viverge K (2016) Generalized plate model for highly contrasted laminates. Eur J Mech A Solids 55:149–166
4. Boutin C, Viverge K, Hans S (2020) Dynamics of contrasted stratified elastic and viscoelastic plates-application to laminated glass. Compos Part B, 21. https://doi.org/10.1016/j.compositesb.2020.108551
5. Caillerie D (1984) Thin elastic and periodic plates. Math Meth Appl Sci 6:159–191
6. Carrera E, Ciuffreda A (2005) Bending of composites and Sandwich plates subjected to localized lateral loading: a comparison of various theories. Compos Struct 68:185–202
7. Challamel N (2013) Variational formulation of gradient or/and nonlocal higher-order shear elasticity beams. Compos Struct 105:351–368
8. Ciarlet PG, Destuynder P (1979) A justification of the two-dimensional linear plate model. J Mec 18:315–344
9. DiTaranto RA (1965) Theory of the vibratory bending for elastic and viscoelastic layered finite length beams. J Appl Mech 32:881–886
10. Foraboschi P (2012) Analytical model for laminated-glass plate. Compos Part B 43:2094–2106
11. Foraboschi P (2014) Three-layered plate: elasticity solution. Compos Part B 60:764–776
12. Galuppi L, Royer-Carfagni G (2012) Laminated beams with viscoelastic interlayer. Int J Solids Struct 49(18):2637–2645
13. Hans S, Boutin C (2008) Dynamics of discrete framed structures: an unified homogenized description. J Mech Mater Struct 3(9):1709–1739
14. Kaplunov J, Prikazchikov DA, Prikazchikova LA (2017) Dispersion of elastic waves in a strongly inhomogeneous three-layered plate. Int J Solids Struct 113–114:169–179
15. Lewinsky T, Telega JJ (2000) Plates, laminates and shells-asymptotic analysis and homogenization. World Scientific, Singapore, London
16. Mead DJ, Markus S (1969) The forced vibration of a three-layer, damped Sandwich beam with arbitrary boundary conditions. J Sound Vib 10–2:163–175
17. Naumenko K, Eremeyev VA (2014) A layer-wise theory for laminated glass and photovoltaic panels. Compos Struct 112:283–291

18. Sanchez-Palencia E (1980) Non homogeneous media and vibration theory. Springer, Berlin
19. Schulze SH, Pander M, Naumenko K, Altenbach H (2012) Analysis of laminated glass beams for photovoltaic applications. Int J Solids Struct 49(15):2027–2036
20. Viverge K, Boutin C, Sallet F (2016) Model of highly contrasted plates versus experiments on laminated glass. Int J Solids Struct 102–103:238–258

# Chapter 5
# Universal Representation of Dynamic Frequency Spectra for Canonical Generalised Quasicrystalline-Generated Waveguides

**Z. Chen, A. K. M. Farhat, and M. Gei**

**Abstract** An effective way to describe the sequence of stop and pass bands in a one-dimensional phononic waveguide is represented by the 'flow' line reported onto the plot of the relevant $\pi$-periodic reduced torus. In this chapter, these concepts are introduced for silver-mean quasicrystalline-generated elastic waveguides. Results are obtained for canonical configurations for which the dynamic frequency spectra are periodic. Application to finite-size waveguides is also illustrated. As the silver-mean sequence is one of the generalised Fibonacci sequences, the illustrated method can be easily extended to other quasicrystalline substitution rules.

## 5.1 Introduction

The study of elastodynamics of the class of two-phase periodic, one-dimensional waveguides whose elementary cells are generated through a quasicrystalline sequence has recently gained considerable attention. In a couple of early papers, Gei [1] and Morini and Gei [2] have provided the basic theory underlying the topic and introduced the fundamental tool of Kohmoto's invariant through which the main features of the problem can be explained: in particular, recursivity of traces of transmission matrices that govern the dynamic properties, self-similarity of the frequency spectra and the determination of the associated scaling factor, etc. The theory has been also applied to periodic media composed of laminae [3, 4] arranged according to the

Z. Chen · A. K. M. Farhat

School of Engineering, Cardiff University, The Parade, Cardiff CF24 3AA, U.K.
e-mail: chenz51@cardiff.ac.uk

A. K. M. Farhat
e-mail: farhatak@cardiff.ac.uk

M. Gei (✉)
Department of Engineering and Architecture, University of Trieste, via A. Valerio 6/1, 34127 Trieste, Italy
e-mail: massimiliano.gei@dia.units.it

Fibonacci chain (that is a quasicrystalline sequence), to show the capability of these composites to display negative refraction of antiplane shear waves.

Recently, Gei et al. [5] have defined the concept of *canonical* configurations for one-dimensional quasicrystalline-generated periodic waveguides for which, among several properties, the frequency spectra are periodic being the period a multiple of a particular frequency—the *canonical* frequency—that depends on the geometric and mechanical properties of the constituents of the elementary cell.

A further study [6] has shown how to employ the method of the dynamic flow on the *reduced torus*, proposed in elastodynamics by Shmuel and Band [7], to describe in an universal way the sequence of stop and pass bands for the same type of waveguides introduced in [1, 2]. A relevant application of this approach is that optimisation of the widths of stop bands becomes a simple graphical exercise when the reduced torus is adopted.

The goal of this note is to extend the latter concept to the case of silver-mean quasicrystalline-generated rods that are an example of waveguides obtained through a generalised Fibonacci sequence.

## 5.2 Wave Propagation in Silver-Mean Quasicrystalline Waveguides

We introduce a particular class of infinite, one-dimensional, two-component quasicrystalline phononic rods consisting of a repeated elementary cell in which two distinct phases, say $L$ and $S$, are arranged according to the so-called *Silver-Mean* sequence, that is an example of *generalised Fibonacci* sequence. The repetition of the fundamental cell implies global periodicity along the axis and then the possibility of applying the Floquet-Bloch technique to investigate the propagation of harmonic elastic waves along the longitudinal axis of the rod. Each element of the class, denoted by $\mathscr{F}_i$ $(i = 0, 1, 2, \dots)$, where the index $i$ is the *order*, is constructed following the recursive rule

$$\mathscr{F}_i = \mathscr{F}_{i-1}^2 \mathscr{F}_{i-2}, \tag{5.1}$$

where the initial condition is $\mathscr{F}_0 = S$ and $\mathscr{F}_1 = L$ (in Fig. 5.1, elementary cells representing $\mathscr{F}_2$, $\mathscr{F}_3$ and $\mathscr{F}_4$ are sketched). Each cell $\mathscr{F}_i$ is composed of $\tilde{n}_i$ elements, where $\tilde{n}_i = 2\tilde{n}_{i-1} + \tilde{n}_{i-2}$ $(i \geq 2)$ and $\tilde{n}_0 = \tilde{n}_1 = 1$. The limit $\tilde{n}_{i+1}/\tilde{n}_i$ for $i \to \infty$ corresponds to the *silver-mean ratio* $(1 + \sqrt{2}) \cong 2.414$.[1]

Consider now the geometrical and physical properties of phases $L$ and $S$. The lengths of the two elements are indicated, respectively, with $l_L$ and $l_S$, while $A_J$, $E_J$ and $\varrho_J$ $(J \in \{L, S\}$ here and henceforth) denote cross-section area, Young's modulus and mass density per unit volume of each element, respectively. For both

---

[1] In general, all sequences that follow the rule $\mathscr{F}_i = \mathscr{F}_{i-1}^m \mathscr{F}_{i-2}$ $(m \geq 1)$ are quasicrystalline; see the discussion in [2].
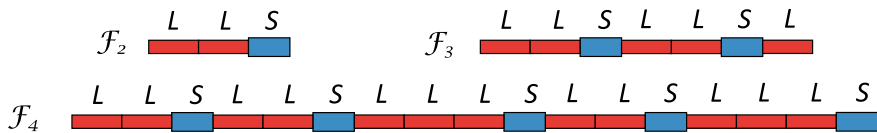
**Fig. 5.1** Sketch of elementary cells for silver-mean phononic rods whose elements of the sequence are $\mathscr{F}_2$, $\mathscr{F}_3$ and $\mathscr{F}_4$

segments, we define the displacement function along the rod $u(z)$ and the axial force $N(z) = EAu'(z)$, where $z$ is the longitudinal coordinate. The governing equation of longitudinal harmonic axial waves in each phase is

$$u''_J(z) + Q_J\,\omega^2 u_J(z) = 0, \tag{5.2}$$

where $\omega$ is the circular frequency and $Q_J = \varrho_J/E_J$. The general solution to Eq. (5.2) is

$$u_J(z) = C_J \sin(\sqrt{Q_J}\,\omega z) + D_J \cos(\sqrt{Q_J}\,\omega z), \tag{5.3}$$

where $C_J$ and $D_J$ are constants.

To obtain the dispersion diagram of the periodic rod, displacement and axial force at the right-hand boundary of the elementary cell, respectively, $u_r$ and $N_r$, have to be identified in terms of those at the left-hand boundary, respectively, $u_l$ and $N_l$, as

$$U_r = T_i U_l, \tag{5.4}$$

where $U_j = [u_j\ N_j]^T$ ($j = r, l$) and $T_i$ is the 2 × 2 transmission matrix of the cell $\mathscr{F}_i$. The latter is the result of the product $T_i = \prod_{p=1}^{\tilde{n}_i} T^J$, where $T^J$ is the transmission matrix relating quantities across a single element that can be found explicitly in [2]. $T_i$ is unimodular (det $T_i = 1$) and follows, from Eq. (5.1), the recursion rule $T_{i+1} = T_{i-1} T_i^2$ ($i > 0$), with $T_0 = T^S$ and $T_1 = T^L$.

Periodicity allows the Floquet-Bloch condition to be applied to the problem, namely $U_r = \exp(iK)U_l$, so that, by combining this with Eq. (5.4), the dispersion equation

$$\cos K = x_i/2 \tag{5.5}$$

is achieved, where $x_i = \mathrm{tr} T_i$. The solution to Eq. (5.5) provides the complete Floquet-Bloch spectrum and allows the definition stop-/pass-band pattern of each waveguide at varying index $i$. Waves propagate when $|x_i| < 2$, stop bands correspond to the ranges of frequencies where $|x_i| > 2$, whereas $|x_i| = 2$ characterises standing waves.

## 5.3   Universal Representation of the Frequency Spectrum

To achieve the goal of this article, it is instrumental to introduce the following functions of the circular frequency $\omega$, i.e.

$$\zeta_S(\omega) = l_S\sqrt{Q_S}\,\omega, \quad \zeta_L(\omega) = l_L\sqrt{Q_L}\,\omega. \tag{5.6}$$

General recursive relations for the traces of unimodular transfer matrices of generalised Fibonacci chains have been derived in terms of Chebyshev polynomials of the first and second kind. Specialising these expressions to the silver-mean case, it turns out that

$$\begin{cases} x_i = x_{i-1}t_i - x_{i-2}, \\ t_{i+1} = x_i x_{i-1} - t_i, \end{cases} \quad (i \geq 2), \tag{5.7}$$

where $t_i = \mathrm{tr}(\boldsymbol{T}_{i-2}\boldsymbol{T}_{i-1})$. Through the new set of variables

$$\tilde{x}_i = t_{i+2}, \; \tilde{y}_i = x_{i+1}, \; \tilde{z}_i = x_i \tag{5.8}$$

and its substitution into expression (5.7), the following nonlinear discrete map determining the evolution of $x_i$ and $t_i$ is obtained

$$\mathscr{T} : \mathbb{R}^3 \to \mathbb{R}^3, \; \mathscr{T}(\tilde{x}_i, \tilde{y}_i, \tilde{z}_i) = (\tilde{x}_{i+1}, \tilde{y}_{i+1}, \tilde{z}_{i+1}) = \left(\tilde{x}_i\tilde{y}_i^2 - \tilde{y}_i\tilde{z}_i - \tilde{x}_i, \; \tilde{x}_i\tilde{y}_i - \tilde{z}_i, \; \tilde{y}_i\right), \tag{5.9}$$

where the initial conditions are given by

$$\tilde{z}_0 = x_0 = 2\cos\zeta_S, \quad \tilde{y}_0 = x_1 = 2\cos\zeta_L, \quad \tilde{x}_0 = t_2 = 2\cos\zeta_L\cos\zeta_S - \beta\sin\zeta_L\sin\zeta_S. \tag{5.10}$$

In Eq. (5.10), the impedance mismatch $\beta$ takes the form

$$\beta = \frac{A_L^2 E_L^2 Q_L + A_S^2 E_S^2 Q_S}{A_L E_L A_S E_S \sqrt{Q_L Q_S}}. \tag{5.11}$$

The generic trace $x_i$ can be derived through successive iterations of the expressions in Eq. (5.7) by assuming (5.10) as initial conditions[2] which include $2\pi$-periodic functions of their arguments. Therefore, $x_i$ is also a $2\pi$-periodic function of both $\zeta_L$ and $\zeta_S$ as it is defined through sums and products of functions with the same period. This implies that we can consider each $x_i$ as a function of a two-dimensional torus of edge length $2\pi$, whose toroidal and poloidal coordinates correspond to $\zeta_S$ and $\zeta_L$, respectively. More in detail, the toroidal domain, independent of $l_L$ and $l_S$, is composed of two complementary subspaces that are associated with $|x_i(\zeta_S, \zeta_L)| < 2$ (pass band) and $|x_i(\zeta_S, \zeta_L)| > 2$ (stop band). The two regions are separated by lines in

---

[2] For instance, it turns out that $x_2 = 2\cos(2\zeta_L)\cos(\zeta_S) - \beta\sin(2\zeta_L)\sin(\zeta_S)$.

which $|x_i(\zeta_S, \zeta_L)| = 2$ (standing-wave solution). The measures of the two subregions are univocally determined by the value of $\beta$.

Equation (5.5) shows that $|x_i(\zeta_S, \zeta_L)|$ is invariant under the transformation

$$\zeta_S \to \zeta_S + n\pi, \quad \zeta_L \to \zeta_L + m\pi \quad (n, m \in \mathbb{N}), \tag{5.12}$$

so that the map on the torus can be equivalently represented on a reduced $\pi$-periodic torus (the *reduced torus*) that is a—flat—square whose edges are still described by coordinates $\zeta_S$ and $\zeta_L$, both ranging now between 0 and $\pi$.

Examples of stop- and pass-band domains within the corresponding reduced tori are displayed, for $\beta = 2.5$, in Figs. 5.2, 5.3 and 5.5 for cells $\mathscr{F}_2$, $\mathscr{F}_3$ and $\mathscr{F}_4$, respectively, in particular stop-band regions are coloured in light blue.

The sequence of stop bands and pass bands of a silver-mean waveguide of any arbitrary order can be studied by analysing the linear 'flow' parametrised by map $(\zeta_S(\omega), \zeta_L(\omega))$ on the reduced torus, where $\omega$ is the time-like parameter. Note that in this parametrisation the lengths of the two phases come into play and contribute to the inclination of the trajectory together with quantities $\sqrt{Q_J}$. Thanks to conditions (5.12), the 'flow' lines are subdivided into ordered sequences of segments within the reduced torus. The starting point of a segment depends on the final point of the previous one. As $\omega > 0$, the initial point of each trajectory is the origin. Two examples of trajectory are the black lines sketched in Figs. 5.2 and 5.3. However, an additional piece of theory is required to fully capture the information conveyed by the plots.



**Fig. 5.2** Flow lines on the reduced torus for a canonical silver-mean phononic rod whose elementary cell is $\mathscr{F}_2$ and $\beta = 2.5$. Solid line: $l_S/l_L = 1$, $A_S/A_L = 1/2$, $Q_S/Q_L = 1$ ($\mathscr{C}_1 = 1$); dashed line: $l_S/l_L = 2$, $A_S/A_L = 1/2$, $Q_S/Q_L = 1$ ($\mathscr{C}_3 = 2$). Coloured dots mark the extremes of the stop bands
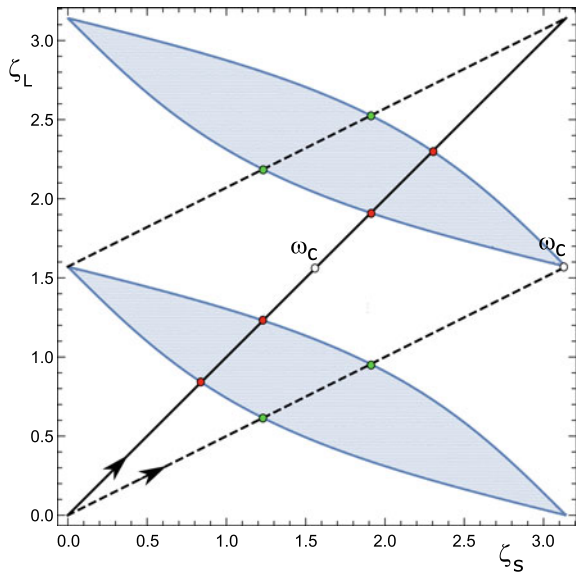
**Fig. 5.3** Flow lines on the reduced torus for a canonical silver-mean phononic rod whose elementary cell is $\mathscr{F}_3$ and $\beta = 2.5$. Solid line: $l_S/l_L = 1$, $A_S/A_L = 1/2$, $Q_S/Q_L = 1$ ($\mathscr{C}_1 = 1$); dashed line: $l_S/l_L = 2$, $A_S/A_L = 1/2$, $Q_S/Q_L = 1$ ($\mathscr{C}_3 = 2$)
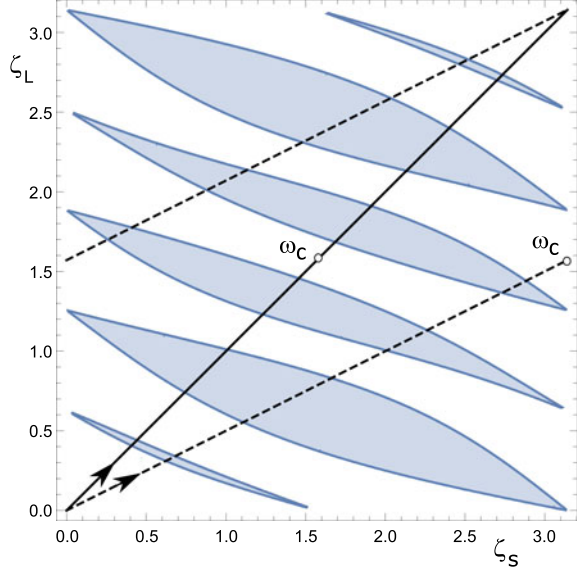


## 5.4 Canonical Configurations

In [8], the notions of *canonical configuration* and *canonical frequency* for silver-mean periodic waveguides have been proposed. For the problem analysed in this note, the most important feature of a canonical waveguide is that the frequency spectrum is *periodic*, and the period of the sequence of stop and pass bands matches twice the canonical frequency ($\omega_\mathscr{C}$ from now on).

A silver-mean canonical waveguide is such when the ratio $\mathscr{C} = l_S/l_L\sqrt{Q_S/Q_L}$ is a rational number, namely

$$\mathscr{C}_1 = \frac{1+2j}{1+2k} \quad \text{or} \quad \mathscr{C}_2 = \frac{1+2j}{2q} \quad \text{or} \quad \mathscr{C}_3 = \frac{2q}{1+2k} \quad (j, k \in \mathbb{N}, q \in \mathbb{N}^+) \quad (5.13)$$

where the separation in three distinct ratios (or families) comes from the detailed analysis reported in [8]. We note that family no. 1 encompasses odd/odd ratios, while odd/even and even/odd ratios are associated with family nos. 2 and 3, respectively, and it is important to remark that indices $j$, $k$ and $q$ in (5.13) are such that fractions on the right-hand sides are in the lowest terms.

The corresponding canonical frequencies are

$$\omega_{\mathscr{C}_1} = \omega_{\mathscr{C}_3} = \frac{\pi}{2l_L\sqrt{Q_L}}(1+2k), \quad \omega_{\mathscr{C}_2} = \frac{\pi}{l_L\sqrt{Q_L}}q \quad (k \in \mathbb{N}, q \in \mathbb{N}^+), \quad (5.14)$$

where $k$, $q$ coincide with the analogous indices selected in the relevant condition among those listed in (5.13).

The periodicity of the frequency spectrum of canonical waveguides is evident on the reduced torus as the trajectory becomes, in turn, periodic. This means that at $\omega = 2\omega_{\mathscr{C}}$ the point of the 'flow' coincides with that of coordinate $(\pi, \pi)$ and for $\omega > 2\omega_{\mathscr{C}}$ the trajectory repeats itself starting from the origin. This occurs each time a frequency multiple of $2\omega_{\mathscr{C}}$ is reached.

## 5.5 Results

The reduced torus in Fig. 5.2 is for an elementary cell constructed adopting $\mathscr{F}_2$ and for the set of parameters $A_S/A_L = 1/2$, $E_S/E_L = 1$, $Q_S/Q_L = 1$; therefore, the impedance mismatch parameter is $\beta = 2.5$. Two flow lines are sketched—in black— namely, the solid one is for $l_S/l_L = 1$ whereas the dashed one describes the ratio $l_S/l_L = 2$; therefore, the former associated rod belongs to the first family of canonical waveguides (cfr. (5.13)) being $\mathscr{C}_1 = 1$ ($j = k = 0$), whereas the latter belongs to the third family ($\mathscr{C}_3 = 2, q = 1, \ k = 0$).

The solid line is the diagonal of the square (reduced torus) and represents the whole trajectory for the former structure in the interval $\omega \in [0, 2\omega_{\mathscr{C}}]$ (here $l_L \sqrt{Q_L} \omega_{\mathscr{C}} = \pi/2$); hence, for frequencies just greater than the threshold $2\omega_{\mathscr{C}}$, the trajectory runs along the same segment re-starting from the origin. For the latter canonical configuration, the trajectory in the period $[0, 2\omega_{\mathscr{C}}]$ is composed of two segments (dashed) (where, again, $l_L \sqrt{Q_L} \omega_{\mathscr{C}} = \pi/2$). In both cases, the point at which $\omega = \omega_{\mathscr{C}}$ is depicted with a white circle.

For both cases, when at a given frequency the point of the flow lies in the white region, the frequency itself sits in a pass band; conversely, when the point is in the light-blue domain, the frequency is in a stop band. The limit of the stop bands is marked with coloured dots.

Figure 5.3 reports the same information (all parameters match those of the previous figure), but the reduced torus is for an elementary cell $\mathscr{F}_3$. It is clear now that the distribution of stop and pass bands is remarkably different as the light-blue subregions are in a greater number with respect to that in Fig. 5.2. This makes more involved the computation of the number of stop bands for any canonical configuration associated with the same value of $\beta$; however, the reduced torus proved to be an exceptional tool to understand how the sequence of stop and pass bands evolves for a given canonical configuration in a period. As a further example showing the increasing complexity for high-order elementary cells, the reduced torus for $\mathscr{F}_4$ is sketched in Fig. 5.5.

In order to give the reader an additional insight into the diagrams illustrated in Figs. 5.2 and 5.3, we consider two finite waveguides composed of six elementary cells $\mathscr{F}_2$ and $\mathscr{F}_3$, respectively. They join two semi-infinite, identical outer media whose elastic properties match those of phase $L$ (the common schematic is depicted in Fig. 5.4a)). We expect the system to be able to transmit (resp. reflect) a signal whose frequency belongs to a pass band (resp. stop band). To this end, transmission coefficient $T_c$ and reflection coefficient $R_c = 1 - T_c$ can be calculated following the method presented in [9]. The reflection coefficients for the two problems at hand

(a)



(b)



(c)



(d)
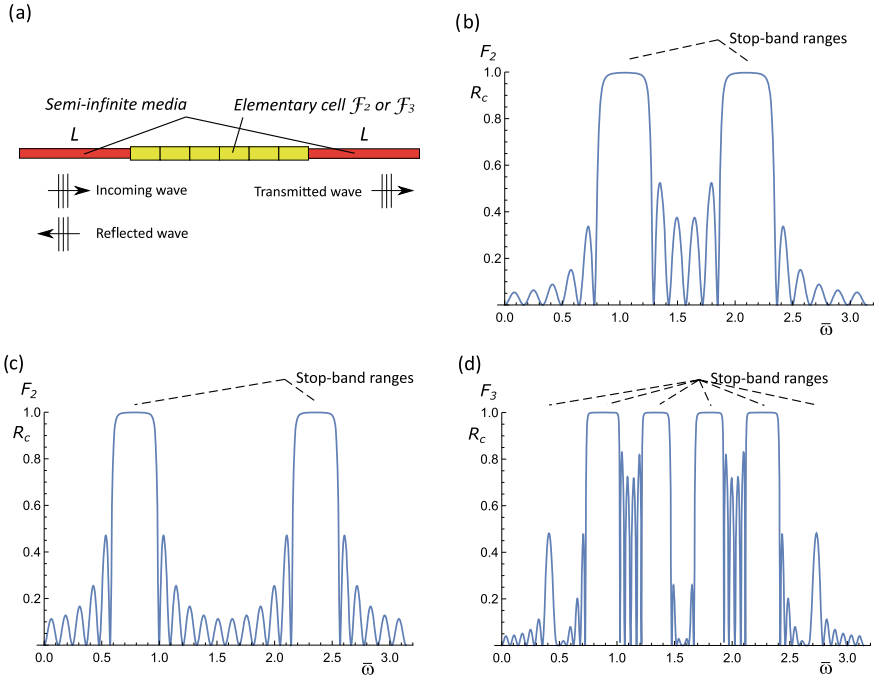


**Fig. 5.4** Reflection of axial waves in a finite-sized silver-mean phononic waveguide ($\beta = 2.5$ in all analysed cases): **a** schematic of the device; **b** plot of the reflection coefficient $R_c$ for elementary cell $\mathscr{F}_2$ ($l_S/l_L = 1$, $A_S/A_L = 1/2$, $Q_S/Q_L = 1$, $\mathscr{C}_1 = 1$) for a dimensionless frequency in the interval $[0, 2\,l_L\sqrt{Q_L}\,\omega_\mathscr{C}\,]$; **c** plot of $R_c$ for elementary cell $\mathscr{F}_2$ ($l_S/l_L = 2$, $A_S/A_L = 1/2$, $Q_S/Q_L = 1$, $\mathscr{C}_3 = 2$) in the interval $[0, 2\,l_L\sqrt{Q_L}\,\omega_\mathscr{C}\,]$; **d** plot of $R_c$ for elementary cell $\mathscr{F}_3$ ($l_S/l_L = 1$, $A_S/A_L = 1/2$, $Q_S/Q_L = 1$, $\mathscr{C}_1 = 1$) in the interval $[0, 2\,l_L\sqrt{Q_L}\,\omega_\mathscr{C}\,]$

are displayed in Fig. 5.4. On the one hand, for cell $\mathscr{F}_2$, the whole—dimensionless—frequency domain $[0, 2\,l_L\sqrt{Q_L}\,\omega_\mathscr{C}]$ represented in Fig. 5.2 is analysed in Fig. 5.4b and c for the two length ratii. On the other hand, Fig. 5.4d describes the case of cell $\mathscr{F}_3$ (Fig. 5.3) with $l_S/l_L = 2$. Note that the two peaks in Fig. 5.4c are more distant from each other than those in Fig. 5.4b and this is consistent with the information obtained following the two flow lines in Fig. 5.2.

In all diagrams, it is evident that $R_c$ approaches 1 (i.e. total reflection) in the frequency ranges that correspond to stop bands, thus confirming that the model of infinite, periodic waveguide provides an excellent estimation of frequencies at which waves cannot propagate. Only for the two outer stop bands of Fig. 5.4d the match is not very good because six cells in the finite-size waveguide are not enough as it is well known that narrow stop bands require a high number of elements to be correctly captured by such a waveguide. For the same reason, the function $R_c(\omega)$ is oscillatory and not null in the corresponding pass bands.

In closing the section, a natural question may arise when thinking about the reduced-torus representation: what is the key information conveyed by the white and

**Fig. 5.5** Reduced torus for a canonical silver-mean phononic rod whose elementary cell is $\mathscr{F}_4$ and $\beta = 2.5$
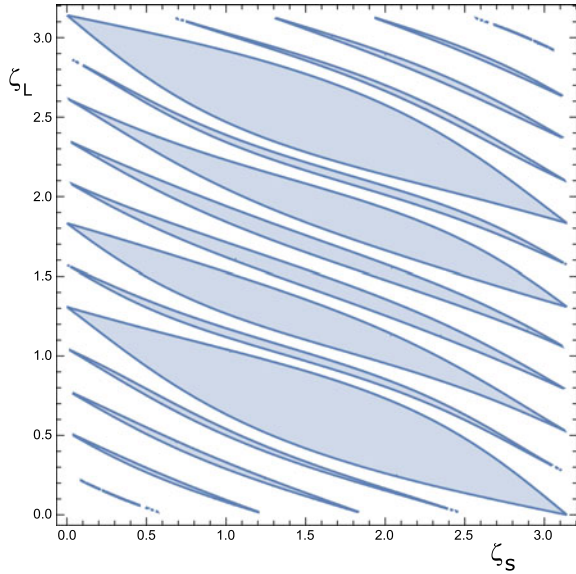
light-blue regions in the square when the structure is 'non-canonical', namely when $\mathscr{C}$ is irrational? In this case, the spectrum is not periodic, the flow lines are 'open' and cover ergodically the whole square at increasing frequency. Consequently, the flow trajectories on the torus consist of an infinite number of parallel segments which, in turn, cover the whole square domain. Therefore, for the frequency spectrum, we can define the 'stop-band density' that is given by the ratio between the area of the light-blue subdomain and that of the square, i.e. $\pi^2$. Since the measure of stop-band domain is determined only by the parameter $\beta$, which is independent of the ratio $l_S/l_L$, for non-canonical bars the stop-band density does not depend on the ratio between lengths of the phases (Fig. 5.5).

## 5.6 Conclusions

Through the adoption of the silver-mean Fibonacci sequence, we have extended to generalised quasicrystalline-generated waveguides the method to represent the layout of stop and pass bands by flow lines on the square domain of the reduced torus. The reduced torus is an effective graphical way to display pass-band and stop-band regions for a set of configurations sharing the same impedance mismatch parameter. Specific results reported in the note are given for canonical configurations, for which the frequency spectra are periodic; as a consequence, the relevant trajectories on the reduced torus at varying frequencies are periodic and are composed of a finite number of segments. For non-canonical configurations, the trajectories cover ergodically the

whole domain and it can be shown that the stop-band density does not depend on the ratio between lengths of the phases. Finite-size waveguides are also studied and the values of the reflection coefficient confirm the reliability of the Floquet-Bloch method. The tool of the reduced torus can be profitably employed for optimisation problems such as maximisation of the widths of stop bands.

# References

1. Gei M (2010) Int J Solids Struct 47:3067
2. Morini L, Gei M (2018) J Mech Phys Solids 119:83
3. Morini L, Eyzat Y, Gei M (2019) J Mech Phys Solids 124:282
4. Chen Z, Morini L, Gei M (2022) Phil Trans R Soc A, art n 20210401
5. Gei M, Chen Z, Bosi F, Morini L (2020) Appl Phys Lett 116, art n 241903
6. Morini L, Tetik ZG, Shmuel G, Gei M (2019) Phil Trans R Soc A 378, art n 20190240
7. Shmuel G, Band R (2016) J Mech Phys Solids 92:127
8. Farhat AKM, Morini L, Gei M (2022) J Sound Vib 553, art n 116679
9. Lekner J (1994) J Opt Soc Am A 11:2892

# Chapter 6
# Overall Properties for Elastic Micropolar Heterogeneous Laminated Composites with Centro-symmetric Constituents

**Yoanh Espinosa-Almeyda, Victor Yanes, Reinaldo Rodríguez-Ramos, Federico J. Sabina, Frédéric Lebon, César F. Sánchez-Valdés, and Héctor Camacho-Montes**

**Abstract**  In this work, the effective properties of multi-phase periodic laminated Cosserat composite are computed by means of the two-scale asymptotic homogenization method (AHM). The statements of the local problems and the formulas of the associated effective properties are explicitly described. In addition, the case of centro-symmetric laminated Cosserat with isotropic constituents is studied and the corresponding effective coefficients are given in terms of the engineering constants. Numerical results for different periodic centro-symmetric bi-laminated Cosserat composites are reported and analyzed.

Y. Espinosa-Almeyda · C. F. Sánchez-Valdés · H. Camacho-Montes
Instituto de Ingeniería y Tecnología, Universidad Autónoma de Ciudad Juárez, Av. Del Charro
450 Norte Cd. Juárez, Chihuahua CP 32310, México
e-mail: yoanhealmeyda1209@gmail.com; yoanh.espinosa@uacj.mx

C. F. Sánchez-Valdés
e-mail: cesar.sanchez@uacj.mx

H. Camacho-Montes
e-mail: hcamacho@uacj.mx

V. Yanes
Facultad de Física, Universidad de La Habana, San Lázaro y L, Vedado, La Habana
CP 10400, Cuba

R. Rodríguez-Ramos (✉)
Facultad de Matemática y Computación, Universidad de La Habana, San Lázaro y L,
Vedado, La Habana CP 10400, Cuba
e-mail: reinaldo@matcom.uh.cu; rerora2006@gmail.com

F. J. Sabina
Instituto de Investigaciones en matemáticas Aplicadas y Sistemas, Universidad Nacional
Autónoma de México, Apartado Postal 20-126, Alcaldía, Álvaro Obregón,
CDMX 01000, México
e-mail: fjs@mym.iimas.unam.mx

F. Lebon
Laboratoire de Mecanique et d'Acoustique, Universite Aix-Marseille, CNRS,
CS 40006 Centrale Marseille, Marseille Cedex 13 13453, France
e-mail: lebon@lma.cnrs-mrs.fr

## 6.1 Introduction

In the field of microstructured materials, the knowledge of the structure-properties relationship and its effects, in a priori way, is important to guarantee a better functionality in some engineering applications. To know how much the physical and geometrical characteristics of the microstructure, the size and coupling effects, and the constituent materials affect the macroscopic material response, by means of macro-micro-mechanical models, have permitted an improvement of the properties of these materials. The generalized continuum theories that include additional kinematic degrees of freedom, as in micropolar or Cosserat continuum with coupled stresses and micromorphic continuum, have been suitable approaches for modeling the effects within the material (see, for instance, Refs. [1, 5, 6, 9, 25]). Cosserat continuum models have been implemented in different branches related to continuum mechanics. One of them, in which the present work is framed, is the characterization of the underlying heterogeneous microstructure of composite materials. For example, the Cosserat continuum has been used for fiber-reinforced materials [4, 35], foams [33, 37], cellular [38], and bone structures [18, 21], among others.

Regarding the modeling and simulation of heterogeneous micropolar or Cosserat media, some works based on multiscale homogenization schemes have been reported. For example: In Forest's works [10, 12], alternative homogenization schemes are proposed to determine the effective moduli of 2D Cauchy medium. Also, the development of an effective generalized continuum model replacing a heterogeneous Cauchy medium by a homogeneous Cosserat continuum is described. In [14], an asymptotic analysis is implemented to analyze a linear elastic Cosserat media with periodic microstructure, taking into account the hierarchy of the characteristic size of the microstructure, of the intrinsic Cosserat length of the components and of the composite material. Likewise, effective generalized continuum [11, 13] and discrete Cosserat media [34] were analyzed following the ideas given in [14]. In these mentioned works, the macroscopic generalized stress and strain are related to the displacements, strains, and stresses defined inside the representative volume element of the composite material. Liu and Hu [20] derived analytical expressions of the Eshelby tensor for an isotropic micro-stretch medium with spherical inclusions using Green's function technique. Riahi and Curran [30, 31] studied 2D and 3D Cosserat continuum with a layered-like microstructure by a finite element scheme, and Li et al. [19] employed a generalized Hill's lemma for micro-macro homogenization modeling of heterogeneous gradient-enhanced Cosserat continuum. On the other hand, various homogenization procedures are implemented for heterogeneous Cosserat elastic composite materials, see, for instance, [3, 15, 16, 29, 40].

Since the Cosserat work in 1909 [5], the couple-stress elasticity field remains quite active due to its ability to account for the effects of the microstructure, as can be seen in the aforementioned papers. Despite this fact, one of the main problems of the application of this theory consists of the insufficient data on the values of additional material constants, even for isotropic materials. Regarding this point, contributions aiming at the analytical determination of such constants have been developed, which

is not the aim of the present work. For example, the estimation of the 5-constant Toupin-Mindlin gradient elasticity for polycrystalline materials has been carried out in [22]. For the cubic case of Mindlin's anisotropic gradient elasticity theory, the 3 elastic and the 11 gradient-elastic constants are found for Aluminum and Copper from atomistic potentials and ab-into calculations [28]. In this sense, further research is needed to focus on the determination of the Cosserat material constants.

The main aim of this work is that using the two-scale asymptotic homogenization (AHM) [2, 27, 41], the statements of the local problems, the homogenized problem, as well as, the analytical formulas of the effective properties for a Cosserat laminated medium are reported. The effective coefficients have been written explicitly in terms of the engineering constants for a Cosserat laminated medium where each layer is isotropic. This is a novelty of the work. In particular, the case of centro-symmetric laminated Cosserat with isotropic constituents is provided. Examples of centro-symmetric bi-laminated composites with isotropic constituents are analyzed. The numerical results are shown and discussed. Finally, the influence of the volume fraction and phase permutation on the Cosserat effective moduli is investigated. This is another important contribution of the present investigation.

## 6.2  Mathematical Formulation for Micropolar Media

A periodic laminated Cosserat composite in a domain $\Omega$ with an infinitely smooth boundary surface $\partial\Omega$ is considered at the Cartesian coordinate system $\{x_1, x_2, x_3\}$, as can be seen in Fig. 6.1a. The region $\Omega$ is characterized by a parallelepiped generated by repetitions of the periodic cell Y, in which the layered direction is along the $x_3$-axis.

The transversal section of the periodic cell $Y = \{(y_1, y_2, y_3) \in \mathbb{R}^3 : 0 \le y_i \le l_i\}$, in the normal plane $Oy_2y_3$ at the microscale level $\{y_1, y_2, y_3\}$, is assumed by a bi-laminated composite (see, Fig. 6.1c) where $l_i$ is the cell length in the $y_i$-direction. Here, $S_\gamma$ is the region occupied by the layer $\gamma$ of volume $V_\gamma$ ($\gamma = 1, 2$), such as $Y = S_1 \cup S_2$, $S_1 \cap S_2 = \emptyset$, and $V_1 + V_2 = 1$. The contact region $\Gamma$ between the layers is defined perfect, see, for instance, [32].
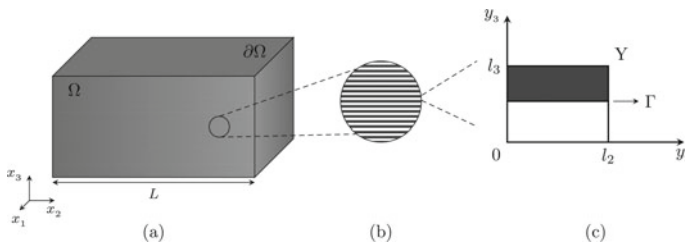


**Fig. 6.1**  **a** Heterogeneous Cosserat composite $\Omega$; **b** blow-up of periodic laminated structure; **c** the cross-section of the periodic laminated structure Y at the plane $Oy_2y_3$

The heterogeneous finite micropolar structure $\Omega$ responds to a linear system of partial differential equations through the static governing linear and angular equilibrium equations

$$\left(C_{ijmn}e_{nm} + B_{ijmn}\psi_{nm}\right)_{,j} + f_i = 0,$$
$$\left(B_{ijmn}e_{nm} + D_{ijmn}\psi_{nm}\right)_{,j} + \varepsilon_{ijk}\left(C_{kjmn}e_{nm} + B_{kjmn}\psi_{nm}\right) + g_i = 0, \quad (6.1)$$

in terms of the asymmetric strain ($e_{nm}$) and the couple strain ($\psi_{nm}$) tensors, with $i, j, k, m, n = 1, 2, 3$. Here, $C_{ijmn}$, $D_{ijmn}$ and $B_{ijmn}$ are the elastic, torque, and coupling moduli, respectively. They are supposed to be infinitely differentiable and rapidly oscillating functions, with 45, 45, and 81 components, respectively. Also, they satisfy the symmetry conditions $C_{ijmn} = C_{mnij}$ and $D_{ijmn} = D_{mnij}$, and only depend on the coordinate $x_3$. $\varepsilon_{ijk}$ is the Levi-Civita tensor, $f_i$ are the body force components, and $g_i$ represent the moment components.

The system, Eq. (6.1), together with the boundary conditions on $\partial\Omega$

$$\begin{aligned} u_i \mid_{\partial\Omega_1} = 0, \quad & \left(C_{ijmn} \, e_{nm} + B_{ijmn} \, \psi_{nm}\right) n_j \mid_{\partial\Omega_2} = F_i, \\ \omega_i \mid_{\partial\Omega_3} = 0, \quad & \left(B_{ijmn} \, e_{nm} + D_{ijmn} \, \psi_{nm}\right) n_j \mid_{\partial\Omega_4} = G_i, \end{aligned} \quad (6.2)$$

represent the static boundary value problem associated with the linear theory of micropolar elasticity whose coefficients are rapidly oscillating. In Eq. (6.2), the subsets $\partial\Omega_1$, $\partial\Omega_2$, $\partial\Omega_3$, and $\partial\Omega_4$ are disjoint and satisfy that $\partial\Omega = \partial\Omega_1 \cup \partial\Omega_2 \cup \partial\Omega_3 \cup \partial\Omega_4$. Also, $F_i$ and $G_i$ are the surface force and torque components, respectively; $n_j$ is the unit outer normal vector to $\partial\Omega$ and $f_{m,j} = \partial f_m / \partial x_j$. Foundations of the micropolar and generalized coupled stress theories are found in Refs. [1, 6, 7, 9, 23, 24, 26, 39].

Furthermore, the linear constitutive equations are defined by

$$\sigma_{ji} = C_{ijmn} \, e_{nm} + B_{ijmn} \, \psi_{nm}, \qquad \mu_{ji} = B_{ijmn} \, e_{nm} + D_{ijmn} \, \psi_{nm}, \quad (6.3)$$

where $\sigma_{ji}$ and $\mu_{ji}$ represent the components of the force stress and the couple stress, respectively. The tensors of second-order $e_{nm}$ and $\psi_{nm}$ are given by

$$e_{nm} = u_{m,n} + \varepsilon_{mns} \, \omega_s, \qquad \psi_{nm} = \omega_{m,n}, \quad (6.4)$$

where $u_i$ is the displacement vector field and $\omega_i$ is the microrotation vector field, independent of the displacement field.

In addition to Eqs. (6.1)–(6.4), the perfect contact condition over $\Gamma$ are considered, i.e., the displacement, stress, microrotation, and couple stress are continuous across $\Gamma$, such as

$$[[u_i]] = 0, \qquad [[\omega_i]] = 0, \qquad [[\sigma_{ji} \, n_j]] = 0, \qquad [[\mu_{ji} \, n_j]] = 0. \quad (6.5)$$

where $[[f]] = f^{(1)} - f^{(2)}$.

## 6.3  Method of Solution: Local Problems and Effective Properties for Laminated Composites

The two-scale asymptotic homogenization method (AHM) [2, 27, 36] is applied to solve the system Eqs. (6.1)–(6.5) in order to find the overall properties of the above considered periodic laminate medium through the asymptotic expansions as in Ref. [41]. The two scales $\mathbf{x} = \{x_1, x_2, x_3\}$ and $\mathbf{y} = \{y_1, y_2, y_3\}$ describe the macroscopic (global) behavior of the composite and the heterogeneities at microscopic (local) level over Y, respectively. They are related by $\mathbf{y} = \mathbf{x}/\varepsilon$, where $\varepsilon$ is a small geometric parameter defined by the ratio between the characteristic dimension of the periodic cell ($l$) and the representative length of the laminate composite ($L$), see, for instance, Fig. 6.1. Details about the AHM procedure developed into micropolar laminated composites are shown in Ref. [41] and are omitted here.

In this framework, the mathematical statement of the $_{pq}\mathcal{L}^1$ and $_{pq}\mathcal{L}^2$ ($p, q = 1, 2, 3$) local problems over the unit cell Y are now defined, as can be see below

The $_{pq}\mathcal{L}^1$ Local problems

$$\left(C_{i3pq} + C_{i3m3\ pq}N'_m + C_{i3mn}\ \varepsilon_{mnk\ pq}V_k + B_{i3m3\ pq}V'_m\right)' = 0, \quad \text{in Y}, \tag{6.6}$$

$$\left(B_{i3pq} + B_{i3m3\ pq}N'_m + B_{i3mn}\ \varepsilon_{mnk\ pq}V_k + D_{i3m3\ pq}V'_m\right)' = 0, \quad \text{in Y}, \tag{6.7}$$

$$[[_{pq}N_m]] = 0, \quad [[_{pq}V_m]] = 0, \text{ on } \Gamma, \tag{6.8}$$

$$[[(C_{i3m3\ pq}N'_m + C_{i3mn}\ \varepsilon_{mnk\ pq}V_k + B_{i3m3\ pq}V'_m)\ n_i]] = -[[C_{i3pq}]]n_3, \text{ on } \Gamma, \tag{6.9}$$

$$[[(B_{i3m3\ pq}N'_m + B_{i3mn}\ \varepsilon_{mnk\ pq}V_k + D_{i3m3\ pq}V'_m)\ n_i]] = -[[B_{i3pq}]]n_3, \text{ on } \Gamma, \tag{6.10}$$

$$\langle_{pq}N_m\rangle_Y = 0, \quad \langle_{pq}V_m\rangle_Y = 0. \tag{6.11}$$

The $_{pq}\mathcal{L}^2$ local problems

$$\left(B_{i3pq} + C_{i3m3\ pq}U'_m + C_{i3mn}\ \varepsilon_{mnk\ pq}M_k + B_{i3m3\ pq}M'_m\right)' = 0, \text{ in Y}, \tag{6.12}$$

$$\left(D_{i3pq} + B_{i3m3\ pq}U'_m + B_{i3mn}\ \varepsilon_{mnk\ pq}M_k + D_{i3m3\ pq}M'_m\right)' = 0, \text{ in Y}, \tag{6.13}$$

$$[[_{pq}U_m]] = 0, [[_{pq}M_m]] = 0, \text{ on } \Gamma, \tag{6.14}$$

$$[[(C_{i3mn\ pq}U'_m + C_{i3mn}\ \varepsilon_{mnk\ pq}M_k + B_{i3m3\ pq}M'_m)\ n_i]] = -[[B_{i3pq}]]n_3, \text{ on } \Gamma, \tag{6.15}$$

$$[[(B_{i3m3\ pq}U'_m + B_{i3mn}\ \varepsilon_{mnk\ pq}M_k + D_{i3m3\ pq}M'_m)\ n_i]] = -[[D_{i3pq}]]n_3, \text{ on } \Gamma, \tag{6.16}$$

$$\langle_{pq}U_m\rangle_Y = 0, \quad \langle_{pq}M_m\rangle_Y = 0. \tag{6.17}$$

where $f'_m \equiv \mathrm{d}f_m/\mathrm{d}y_3$, the brackets $\langle f \rangle$ is the volume average of $f$ on Y, i.e., $\langle f \rangle = \frac{1}{|Y|}\int_V f\,\mathrm{d}V$, and $i, j, k, m, n = 1, 2, 3$. In both local problems (Eqs. (6.6)–(6.17)), the unknown functions $_{pq}N_m$, $_{pq}U_m$, $_{pq}V_m$, and $_{pq}M_m$ only depend on $y_3$ as well. They represent the local $pq$-displacements ($_{pq}N_m$ and $_{pq}U_m$) and the local $pq$-microrotations ($_{pq}V_m$ and $_{pq}M_m$) associate to the $_{pq}\mathcal{L}^1$ and $_{pq}\mathcal{L}^2$ local problems. Therefore, they need to be computed in order to find the effective properties of the Cosserat laminated composite.

Once the $_{pq}\mathcal{L}^1$ and $_{pq}\mathcal{L}^2$ local problems are solved, the associated effective properties for a periodic laminate Cosserat composite are found as

$$C_{ijpq}^* = \left\langle C_{ijpq} + C_{ijm3} \left( {_{pq}N_m'} + \varepsilon_{m3k} \, {_{pq}V_k} \right) + B_{ijm3} \, {_{pq}V_m'} \right\rangle_Y, \qquad (6.18)$$

$$B_{ijpq}^* = \left\langle B_{ijpq} + C_{ijm3} \left( {_{pq}U_m'} + \varepsilon_{m3k} \, {_{pq}M_k} \right) + B_{ijm3} \, {_{pq}M_m'} \right\rangle_Y, \qquad (6.19)$$

$$B_{ijpq}^* = \left\langle B_{ijpq} + B_{ijm3} \left( {_{pq}N_m'} + \varepsilon_{m3k} \, {_{pq}V_k} \right) + D_{ijm3} \, {_{pq}V_m'} \right\rangle_Y, \qquad (6.20)$$

$$D_{ijpq}^* = \left\langle D_{ijpq} + B_{ijm3} \left( {_{pq}U_m'} + \varepsilon_{m3k} \, {_{pq}M_k} \right) + D_{ijm3} \, {_{pq}M_m'} \right\rangle_Y. \qquad (6.21)$$

Notice that the effective coefficients (Eqs. (6.18)–(6.21)) are functions of the local functions $_{pq}N_m'$, $_{pq}V_m'$, $_{pq}U_m'$ and $_{pq}M_m'$, the material properties and the volume of the constituents on the periodic unit cell Y.

On the other hand, the statement of the homogenized static problem, on equivalent domain $\overline{\Omega}$, from Eqs. (6.1)–(6.5) is defined by the system

$$C_{ijpq}^* \left( u_{p,q}^{(0)} + \varepsilon_{pqk} \, \omega_k^{(0)} \right)_{,j} + B_{ijpq}^* \, \omega_{p,qj}^{(0)} + f_i = 0, \qquad (6.22)$$

$$B_{ijpq}^* \left( u_{p,q}^{(0)} + \varepsilon_{pqk} \, \omega_k^{(0)} \right)_{,j} + D_{ijpq}^* \, \omega_{p,q}^{(0)} +$$

$$\varepsilon_{ijl} \left[ C_{ljpq}^* \left( u_{p,q}^{(0)} + \varepsilon_{pqk} \, \omega_k^{(0)} \right) + B_{ljpq}^* \, \omega_{p,q}^{(0)} \right] + g_i = 0, \qquad (6.23)$$

where $u_p^{(0)}$ and $\omega_p^{(0)}$ are the new homogenized solution which represent the first corrections of $u_m$ and $\omega_m$, respectively, and the effective coefficients $C_{ijpq}^*$, $B_{ijpq}^*$ and $D_{ijpq}^*$ are defined as in Eqs. (6.18)–(6.21).

The completeness of problem (Eqs. (6.22) and (6.23)) is given by the homogenized boundary conditions

$$u_p^{(0)} \big|_{\partial\overline{\Omega}_1} = 0, \quad \sigma_{ji}^{(0)} \, n_j \big|_{\partial\overline{\Omega}_2} = F_i^{(0)}, \quad \omega_p^{(0)} \big|_{\partial\overline{\Omega}_3} = 0, \quad \mu_{ji}^{(0)} \, n_j \big|_{\partial\overline{\Omega}_4} = G_i^{(0)}, \quad (6.24)$$

where $F_i^{(0)}$ and $G_i^{(0)}$ are infinitely differential functions on the boundary surface $\partial\overline{\Omega} = \partial\overline{\Omega}_1 \cup \partial\overline{\Omega}_2 \cup \partial\overline{\Omega}_3 \cup \partial\overline{\Omega}_4$.

## 6.4 Effective Coefficients of Centro-symmetric Multi-laminated Cosserat Media with Isotropic Constituents

Let us consider a centro-symmetric multi-laminated Cosserat composite. For centro-symmetric material, the coupling moduli ($B_{ijmn}$) are null since the symmetry condition $B_{ijmn} = B_{mnij}$ is not satisfied. Therefore, the stresses and the coupled stresses are not related to the microcurvature and strains, respectively. Also, the material prop-

erties $C_{ijmn}$ and $D_{ijmn}$ have the same material representation. More details about centro-symmetric Cosserat materials are shown in [7, 8, 42].

Taking into account $B_{ijmn} = 0$ into Eqs. (6.18)–(6.21) and following the ideas reported in [15, 41], it can be proved for centro-symmetric micropolar laminated composites that $B^*_{ijmn} \equiv 0$ and the non-null effective properties $C^*_{ijmn}$ (Eq. 6.18) and $D^*_{ijmn}$ (Eq. 6.21) are re-written as follows:

$$C^*_{ijpq} = \left\langle C_{ijpq} + C_{ijm3}\, C^{-1}_{m3l3} \left( \left\langle C^{-1}_{l3k3} \right\rangle^{-1} \left\langle C^{-1}_{k3d3}\, C_{d3pq} \right\rangle - C_{l3pq} \right) \right\rangle_{\mathrm{Y}}, \quad (6.25)$$

$$D^*_{ijpq} = \left\langle D_{ijpq} + D_{ijm3}\, D^{-1}_{m3l3} \left( \left\langle D^{-1}_{l3k3} \right\rangle \left\langle D^{-1}_{k3d3}\, D_{d3pq} \right\rangle - D_{l3pq} \right) \right\rangle_{\mathrm{Y}}. \quad (6.26)$$

In addition, assuming that each constituent possess isotropic symmetry, $C_{ijmn}$ and $D_{ijmn}$ ($i, j, m, n = 1, 2, 3$) are defined by only six independent constants ($C_{1122}$, $C_{1212}$, $C_{1221}$, $D_{1122}$, $D_{1212}$, and $D_{1221}$) through the formulas

$$\begin{aligned}
C_{ijmn} &= C_{1122}\delta_{ij}\delta_{mn} + C_{1212}\delta_{im}\delta_{jn} + C_{1221}\delta_{in}\delta_{jm}, \\
D_{ijmn} &= D_{1122}\delta_{ij}\delta_{mn} + D_{1212}\delta_{m}\delta_{jn} + D_{1221}\delta_{in}\delta_{jm},
\end{aligned} \quad (6.27)$$

where $\delta_{ij}$ is the Kronecker delta tensor. Also, the restrictions related to the positive-definite quadratic form of the internal energy are satisfied as

$$\begin{aligned}
C_{1212} + C_{1221} > 0, \quad C_{1212} - C_{1221} > 0, \quad 3C_{1122} + C_{1212} + C_{1221} > 0, \\
D_{1212} + D_{1221} > 0, \quad D_{1212} - D_{1221} > 0, \quad 3D_{1122} + D_{1212} + D_{1221} > 0, \quad (6.28)
\end{aligned}$$

where $C_{1111} = C_{1122} + C_{1212} + C_{1221}$ and $D_{1111} = D_{1122} + D_{1212} + D_{1221}$, see, for instance, [7, 8, 26]. Linear isotropic equations associated with the micropolar elasticity theory can be found in [17].

Again, replacing Eq. (6.27) into Eqs. (6.25) and (6.26), and taking into account the relationships between the stiffness and torque moduli and the engineering constants, for isotropic materials,

$$\begin{aligned}
C_{1111} &= \frac{{}_sE}{{}_sA}\,({}_s\nu - 1), \quad C_{1122} = \frac{{}_sE}{{}_sA}\,{}_s\nu, \quad C_{1212} = \frac{{}_sE}{(1 + {}_s\nu)(1 + {}_s\zeta)}, \\
D_{1111} &= \frac{{}_tE}{{}_tA}\,({}_t\nu - 1), \quad D_{1122} = \frac{{}_tE}{{}_tA}\,{}_t\nu, \quad D_{1212} = \frac{{}_tE}{(1 + {}_t\nu)(1 + {}_t\zeta)}, \quad (6.29)
\end{aligned}$$

with ${}_sA = 2\,{}_s\nu^2 + {}_s\nu - 1$ and ${}_tA = 2\,{}_t\nu^2 + {}_t\nu - 1$, we obtain the analytical expressions of the non-null effective properties $C^*_{ijpq}$ and $D^*_{ijpq}$ for centro-symmetric laminated Cosserat composites with isotropic constituents, as follows:

$$C^*_{1111} = C^*_{2222} = \left\langle \frac{{}_sE}{1-{}_s\nu^2} \right\rangle + \left\langle \frac{{}_s\nu}{1-{}_s\nu} \right\rangle^2 \left\langle \frac{2\,{}_s\nu^2 + {}_s\nu - 1}{{}_sE({}_s\nu-1)} \right\rangle^{-1},$$

$$C^*_{3333} = \left\langle \frac{2\,{}_s\nu^2 + {}_s\nu - 1}{{}_sE({}_s\nu-1)} \right\rangle^{-1}, \quad C^*_{1122} = \left\langle \frac{{}_sE\,{}_s\nu}{1-{}_s\nu^2} \right\rangle + \left\langle \frac{{}_s\nu}{1-{}_s\nu} \right\rangle^2 \left\langle \frac{2\,{}_s\nu^2 + {}_s\nu - 1}{{}_sE({}_s\nu-1)} \right\rangle^{-1},$$

$$C^*_{1133} = C^*_{2233} = \left\langle \frac{{}_s\nu}{1-{}_s\nu} \right\rangle \left\langle \frac{2\,{}_s\nu^2 + {}_s\nu - 1}{{}_sE({}_s\nu-1)} \right\rangle^{-1}, \quad C^*_{1221} = \left\langle \frac{{}_sE\,{}_s\zeta}{(1+{}_s\nu)(1+{}_s\zeta)} \right\rangle,$$

$$C^*_{1212} = C^*_{2121} = \left\langle \frac{{}_sE}{(1+{}_s\nu)(1+{}_s\zeta)} \right\rangle, \quad C^*_{1313} = C^*_{2323} = \left\langle \frac{(1+{}_s\nu)(1+{}_s\zeta)}{{}_sE} \right\rangle^{-1},$$

$$C^*_{3232} = C^*_{3131} = \left\langle \frac{{}_sE(1-{}_s\zeta)}{1+{}_s\nu} \right\rangle + \left\langle {}_s\zeta^2 \right\rangle \left\langle \frac{(1+{}_s\nu)(1+{}_s\zeta)}{{}_sE} \right\rangle^{-1},$$

$$C^*_{1331} = C^*_{2332} = \left\langle \frac{{}_sE\,{}_s\zeta}{(1+{}_s\nu)(1+{}_s\zeta)} \right\rangle \left\langle \frac{(1+{}_s\nu)(1+{}_s\zeta)}{{}_sE} \right\rangle^{-1}, \tag{6.30}$$

and

$$D^*_{1111} = D^*_{2222} = \left\langle \frac{{}_tE}{1-{}_t\nu^2} \right\rangle + \left\langle \frac{{}_t\nu}{1-{}_t\nu} \right\rangle^2 \left\langle \frac{2\,{}_t\nu^2 + {}_t\nu - 1}{{}_tE({}_t\nu-1)} \right\rangle^{-1},$$

$$D^*_{3333} = \left\langle \frac{2\,{}_t\nu^2 + {}_t\nu - 1}{{}_tE({}_t\nu-1)} \right\rangle^{-1}, \quad D^*_{1122} = \left\langle \frac{{}_tE\,{}_t\nu}{1-{}_t\nu^2} \right\rangle + \left\langle \frac{{}_t\nu}{1-{}_t\nu} \right\rangle^2 \left\langle \frac{2\,{}_t\nu^2 + {}_t\nu - 1}{{}_tE({}_t\nu-1)} \right\rangle^{-1},$$

$$D^*_{1133} = D^*_{2233} = \left\langle \frac{{}_t\nu}{1-{}_t\nu} \right\rangle \left\langle \frac{2\,{}_t\nu^2 + {}_t\nu - 1}{{}_tE({}_t\nu-1)} \right\rangle^{-1}, \quad D^*_{1221} = \left\langle \frac{{}_tE\,{}_t\zeta}{(1+{}_t\nu)(1+{}_t\zeta)} \right\rangle,$$

$$D^*_{1212} = D^*_{2121} = \left\langle \frac{{}_tE}{(1+{}_t\nu)(1+{}_t\zeta)} \right\rangle, \quad D^*_{1313} = D^*_{2323} = \left\langle \frac{(1+{}_t\nu)(1+{}_t\zeta)}{{}_tE} \right\rangle^{-1},$$

$$D^*_{3232} = D^*_{3131} = \left\langle \frac{{}_tE(1-{}_t\zeta)}{1+{}_t\nu} \right\rangle + \left\langle {}_t\zeta^2 \right\rangle \left\langle \frac{(1+{}_t\nu)(1+{}_t\zeta)}{{}_tE} \right\rangle^{-1},$$

$$D^*_{1331} = D^*_{2332} = \left\langle \frac{{}_tE\,{}_t\zeta}{(1+{}_t\nu)(1+{}_t\zeta)} \right\rangle \left\langle \frac{(1+{}_t\nu)(1+{}_t\zeta)}{{}_tE} \right\rangle^{-1}, \tag{6.31}$$

where ${}_sE$ is the classical Young's modulus, ${}_s\nu$ is Poisson's ratio, ${}_s\zeta$ is the shear-strain ratio, ${}_tE$ is the torsional Young's modulus, ${}_t\nu$ is the twist Poisson's ratio, and ${}_t\zeta$ represents the twist shear-strain ratio. The subscripts $s$ and $t$ mean that the engineering constants results from the compliance $S_{ijmn} = C^{-1}_{ijmn}$ and torque compliance $T_{ijmn} = D^{-1}_{ijmn}$ matrices, respectively. The duality between the terminologies applied in classical and micropolar elasticity theories are reported in [17]. In Eqs. (6.30) and (6.31), the symbol $\langle f \rangle$ denotes the Voigt's average of the property $f$, so that, in case of a bi-laminated composite, $\langle f \rangle = f^{(1)}V_1 + f^{(2)}V_2$ where $V_1$ and $V_2$ are the volume fractions per unit length occupied by the layer 1 and 2, respectively; such as $V_1 + V_2 = 1$, see Fig. 6.1c.

In addition, for isotropic materials, it should also be noted that the engineering and material moduli are related by

$$\begin{aligned}
{}_sE &= \frac{\mu\,(3\lambda + 2\nu)}{\lambda + \nu}, & {}_s\nu &= \frac{\lambda}{2\,(\lambda + \nu)}, & {}_s\zeta &= 1 - \frac{2\alpha}{\alpha + \nu}, \\
{}_tE &= \frac{\gamma\,(3\beta + 2\gamma)}{\beta + \gamma}, & {}_t\nu &= \frac{\beta}{2\,(\beta + \gamma)}, & {}_t\zeta &= 1 - \frac{2\varepsilon}{\varepsilon + \gamma}.
\end{aligned} \tag{6.32}$$

where $\lambda$, $\nu$, $\alpha$ are the Lamé coefficient, Lamé shear modulus, Cosserat couple modulus, and $\gamma$, $\beta$, $\varepsilon$ are the Cosserat twist coefficients.

From Eqs. (6.30) and (6.31), we can observe that the homogenized material belongs to an orthotropic symmetry class restricted with the invariance of stiffness and torques under rotations of 90° about the unitary vector in the $x_3-$direction, with eighteen independent effective properties. The material symmetry groups and their matricial representations for polar-elastic continuum are reported in [8]. In addition, it can be mention that the effective coefficients (Eq. 6.30) reproduce the same ones reported by [27] (see Eq. 1.19, page 147) when $C_{1212} = C_{1221}$. Therefore, the Cauchy classical elasticity problem is a particular case of the present model.

## 6.5 Numerical Results

In this section, numerical simulations were conducted for different periodic centrosymmetric bi-laminated Cosserat composites (layer 1/layer 2) using Eqs. (6.30)–(6.32). The constituent materials are given in Table 6.1 and taken from [17]. Also, the influence of the volume fraction and phase permutation on the Cosserat effective moduli is investigated.

Figures 6.2 and 6.3 show the effective elastic and torque properties as a function of $V_1$ volume fraction for three different homogenized bi-laminate Cosserat composites made of SyF/PUF, SyF/PMIF-WF51, and SyF/PMIF-WF110. In Fig. 6.2, it can be seen that the highest values of all the elastic moduli $C^*_{ijpq}$ are obtained when a SyF/PUF composite is considered, whereas the lowest values are for a SyF/PMIF-WF51 composite, inside of the whole interval. Also, the elastic moduli $C^*_{ijpq}$ are monotonic increasing functions where the more noticeable growth occurs for almost all moduli when $V_1$ tends to 1. From Fig. 6.3, it can be observed that the torque moduli $D^*_{1111}$, $D^*_{3333}$, $D^*_{1212}$, $D^*_{1221}$, $D^*_{1313}$, and $D^*_{1331}$ for the SyF/PUF composite are

**Table 6.1** Constituent material properties

| Material properties | $\lambda$ (MPa) | $\mu$ (MPa) | $\alpha$ (MPa) | $\beta$ (N) | $\gamma$ (N) | $\varepsilon$ (N) |
|---|---|---|---|---|---|---|
| Syntactic foam (SyF) (hollow glass spheres in epoxy resin) | 2097 | 1033 | 114.8 | –2.91 | 4.364 | –0.133 |
| Dense polyurethane foam (PUF) | 762.7 | 104 | 4.333 | –26.65 | 39.98 | 4.504 |
| PMIF-WF51[a] | 6.00 | 30 | 1.25 | –5.83 | 8.75 | 27.6 |
| PMIF-WF110[b] | 487.4 | 75 | 0.7576 | –13.52 | 20.28 | 16.47 |

[a]Polymethacrylimide foam grade WF51 and
[b]Polymethacrylimide foam grade WF110
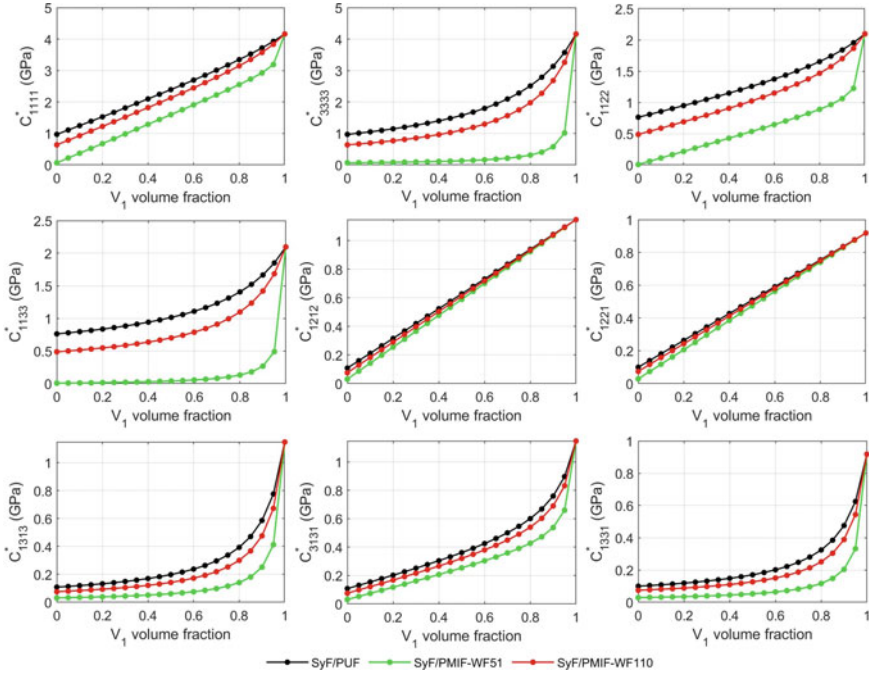
**Fig. 6.2** Effective elastic moduli as a function of $V_1$ volume fraction for three bi-laminated Cosserat composites with isotropic constituents: SyF/PUF, SyF/PMIF-WF51, and SyF/PMIF-WF110

strengthened, whereas $D_{1122}^*$ and $D_{1133}^*$ are for the SyF/PMIF-WF51 composite. In addition, the moduli $D_{1111}^*$, $D_{3333}^*$, $D_{1212}^*$, $D_{1221}^*$, $D_{1313}^*$, and $D_{3131}^*$ are decreasing and $D_{1133}^*$ is increasing in the $V_1$ whole interval. $D_{1122}^*$ reaches minimum values when $V_1 \approx 0.1$ for the SyF/PUF and SyF/PMIF-WF110 configurations. $D_{1331}^*$ decreases for SyF/PUF and increases for the other two configurations.

Figures 6.4 and 6.5 illustrate the effective elastic and torque properties as a function of $V_1$ volume fraction for three different homogenized bi-laminate Cosserat composites made of PUF/SyF, PUF/PMIF-WF51 and PUF/PMIF-WF110 layer combinations. In Fig. 6.4, for the elastic moduli $C_{ijpq}^*$, the PUF/SyF composite always have higher moduli than those of the other two composites (PUF/PMIF-WF51 and PUF/PMIF-WF110). The lower values are obtained for the PUF/PMIF-WF51 composite. A similar behavior is reported in Fig. 6.2. Also, the elastic moduli $C_{ijpq}^*$ decreases for a PUF/SyF composite with the increase of the $V_1$ volume fraction. For PUF/PMIF-WF51 and PUF/PMIF-WF110, the elastic moduli $C_{ijpq}^*$ are monotonic increasing functions. In Fig. 6.5, we observed that the torque moduli $D_{1111}^*$, $D_{3333}^*$, $D_{1212}^*$, $D_{1313}^*$, and $D_{3131}^*$ for a PUF/PMIF-WF110 composite got strength-
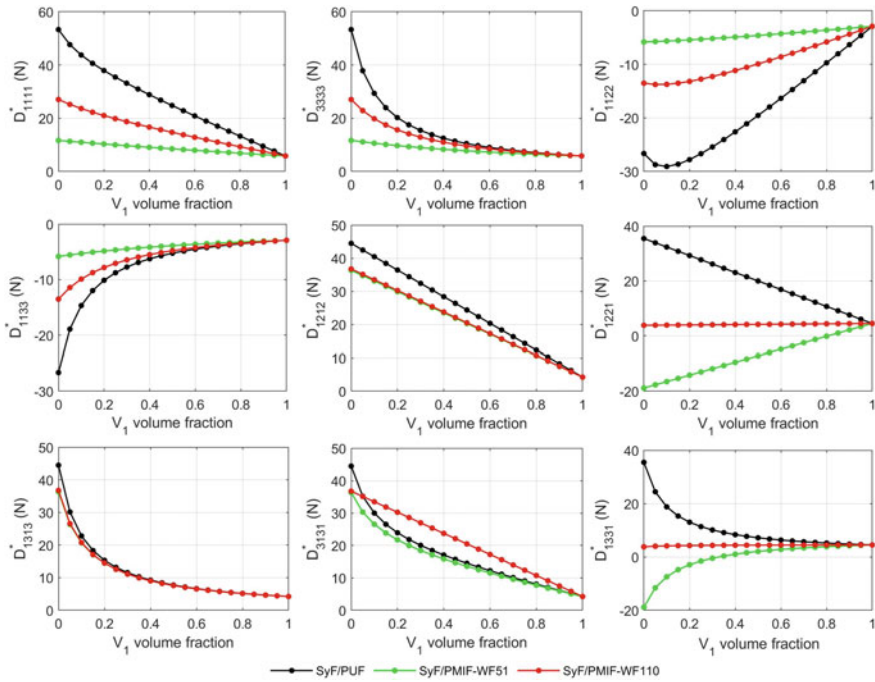
**Fig. 6.3** Effective torque moduli as a function of $V_1$ volume fraction for three bi-laminated Cosserat composites with isotropic constituents: SyF/PUF, SyF/PMIF-WF51, and SyF/PMIF-WF110

ened, whereas $D^*_{1133}$ and $D^*_{1221}$ does as well for the PUF/SyF composite. Also, the torque moduli $D^*_{1111}$, $D^*_{3333}$, $D^*_{1212}$, $D^*_{1221}$, $D^*_{1313}$, and $D^*_{1331}$ increases and $D^*_{1122}$ and $D^*_{1133}$ decreases as a function of $V_1$ volume fraction. For PUF/PMIF-WF51 and PUF/PMIF-WF110 composites, the $D^*_{3131}$ moduli exhibit a minimum value for $V_1$ volume fraction equal to 0.45 and 0.35, respectively, while PUF/SyF is always an increasing function.

## 6.6 Conclusions

In the present work, the problem of a heterogeneous micropolar medium is studied. The statement of the problem is proposed for this type of media, and the asymptotic homogenization formalism is applied based on the asymptotic expansion in terms of the small parameter. As a consequence, the local problems and the analytical expressions for the effective coefficients are derived. A case study of a laminated medium formed by two isotropic layers perpendicular to a preferential axis is developed and the effective coefficients are derived from the solution of local problems, which are expressed as functions of engineering constants. Numerical results are
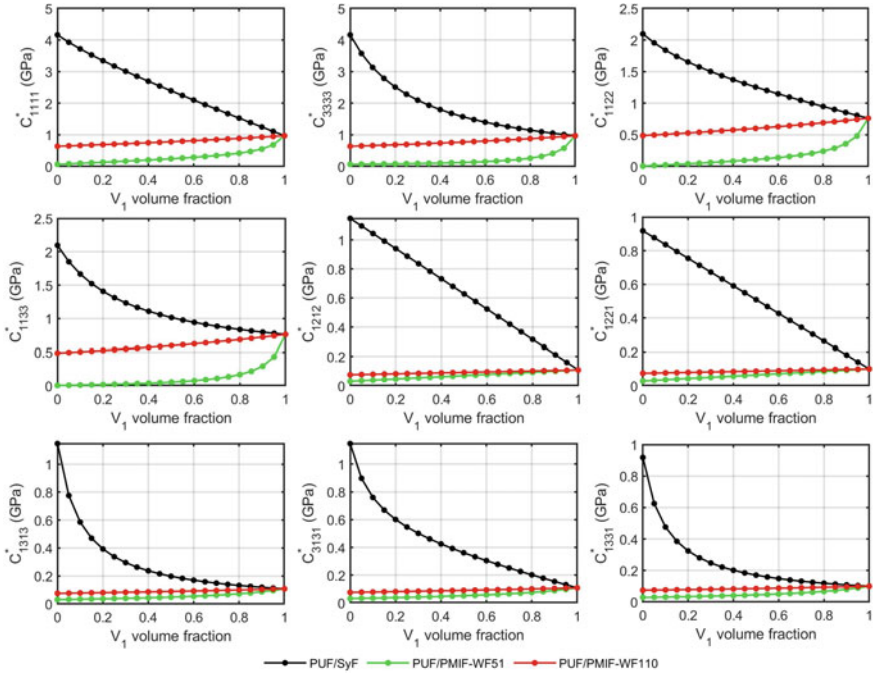
**Fig. 6.4** Effective elastic moduli as a function of $V_1$ volume fraction for three bi-laminated Cosserat composites with isotropic constituents: PUF/SyF, PUF/PMIF-WF51 and PUF/PMIF-WF110

reported and discussed. The overall behavior is affected (strengthened or weakened) by different constituents' selection in the composites. The larger strengthening for the elastic moduli $C^*_{ijpq}$ are obtained for the SyF/PUF and PUF/SyF composites. The torque moduli $D^*_{ijpq}$ are highly sensitive to the selection of constituents. The proposed numerical results serve to validate other models and experimental results.
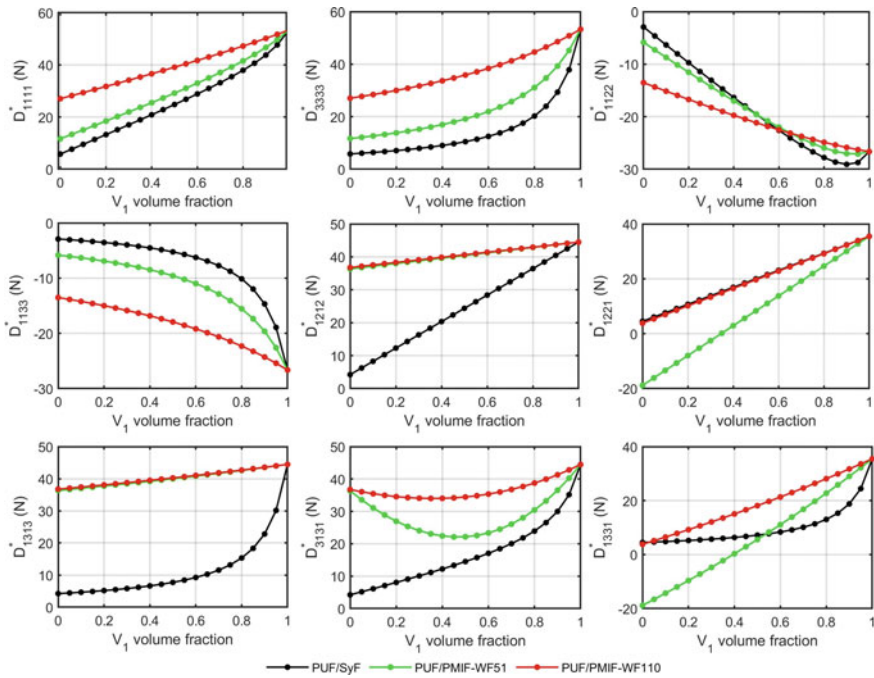
**Fig. 6.5** Effective torque moduli as a function of $V_1$ volume fraction for three bi-laminated Cosserat composites with isotropic constituents: PUF/SyF, PUF/PMIF-WF51 and PUF/PMIF-WF110

# References

1. Altenbach H, Eremeyev VA (2013) Generalized continua from the theory to engineering applications. CISM International Centre for Mechanical Sciences. Springer, Vienna
2. Bakhvalov N, Panasenko G (1989) Homogenization: averaging process in periodic media. In: Mathematics and its applications (Soviet Series), 1 ed. Moscow, Lenin Hills
3. Bigoni D, Drugan W (2006) Analytical derivation of cosserat moduli via homogenization of heterogeneous elastic materials. J Appl Mech 74(4):741–753
4. Bleyer J (2018) Multiphase continuum models for fiber-reinforced materials. J Mech Phys Solids 121:198–233
5. Cosserat E, Cosserat F (1909) Théorie des corps déformables [in French]. A. Hermann et fils, Paris
6. Erigen AC (1966) Linear theory of micropolar elasticity. J Math Mech 15(6):909–923
7. Eringen A (1999) Microcontinuum field theories I: foundations and solids, 1 ed. Springer
8. Eremeyev V, Pietraszkiewicz W (2012) Material symmetry group of the non-linear polar-elastic continuum. Int J Solids Struct 49(14):1993–2005
9. Eremeyev V, Lebedev L, Altenbach H (2013) Foundations of micropolar mechanics. Springer, Vienna
10. Forest S (1998) Mechanics of generalized continua: construction by homogenization. J Phys IV 8:39–48
11. Forest S (2002) Homogenization methods and mechanics of generalized continua-part 2. Theor Appl Mech 28–29:113–144

12. Forest S, Sab K (1998) Cosserat overall modeling of heterogeneous media. Mech Res Commun 25(4):449–454
13. Forest S, Trinh D (2011) Generalized continua and non-homogeneous boundary conditions in homogenisation methods. J Appl Math Mech ZAMM 91(2):90–109
14. Forest S, Padel F, Sab K (2001) Asymptotic analysis of heterogeneous Cosserat media. Int J Solids Struct 38:4585–4608
15. Gorbachev VI, Emel'yanov AN (2014) Homogenization of the equations of the Cosserat theory of elasticity of inhomogeneous bodies. Mech Solids 49(1):73–82
16. Gorbachev VI, Emel'yanov AN (2021) Homogenization of problems of Cosserat theory of elasticity of composites. Additional materials. In: International scientific symposium in problems of mechanics of deformable solids dedicated to A. A. Il'yushin on the occasion of His 100th Birthday [in Russian], vol 49, no 1, pp 81–88
17. Hassanpour S, Heppler GR (2017) Micropolar elasticity theory: a survey of linear isotropic equations, representative notations, and experimental investigations. Math Mech Solids 22:224–242
18. Lakes R (1995) On the torsional properties of single osteons. J Biomech 28:1409–1410
19. Li X, Zhang J, Zhang X (2011) Micro-macro homogenization of gradient-enhanced Cosserat media. Eur J Mech A Solids 30:362–372
20. Liu X, Hu G (2004) Inclusion problem of microstretch continuum. Int J Eng Sci 42(8–9):849–860
21. Liu S, Su W (2009) Effective couple-stress continuum model of cellular solids and size effects analysis. Int J Solids Struct 46:2787–2799
22. Malyi VI (2021) Theoretical determination of the five physical constants of the Toupin-Mindlin gradient elasticity for polycrystalline materials. In: Abramyan A, Andrianov I, Gaiko V (eds) Nonlinear dynamics of discrete and continuous systems. Advanced structured materials, vol 139. Springer Nature, pp 145–154
23. Maugin G (2013) Continuum mechanics through the twentieth century. A concise historical perspective, 1 ed. Springer, Dordrecht
24. Maugin GA, Metrikine A (2013) Mechanics of generalized continua: one hundred years after the Cosserats, 1st edn. Springer, New York
25. Nowacki W (1974) The linear Theory of Micropolar Elasticity. In: Nowacki W, Olszak W (eds) Micropolar elasticity. Springer, Vienna, pp 1–43
26. Nowacki W (1986) Theory of asymmetric elasticity, 1 ed. Pergamon-Press
27. Pobedrya B (1984) Mechanics of composite materials, 1st edn. Izd-vo MGU, Moscow [in Russian]
28. Po G, Admal NC, Lazar M (2019) The green tensor of Mindlin's anisotropic first strain gradient elasticity. Mater Theory 3(3)
29. Reda H, Alavi SE, Nasimsobhan M, Ganghoffer JF (2021) Homogenization towards chiral Cosserat continua and applications to enhanced Timoshenko beam theories. Mech Mater 155:103728
30. Riahi A, Curran JH (2009) Full 3d finite element Cosserat formulation with application in layered structures. Appl Math Modell 33:3450–3464
31. Riahi A, Curran JH (2010) Comparison of the Cosserat continuum approach with finite element interface models in a simulation of layered materials. Trans A Civ Eng 17(1):39–52
32. Rodríguez-Ramos R, Sabina FJ, Guinovart-Díaz R, Bravo-Castillero J (2001) Closed-form expressions for the effective coefficients of a fiber-reinforced composite with transversely isotropic constituents I. Elastic and square symmetry. Mech Mater 33:223–235
33. Rueger Z, Ha C, Lakes R (2016) Experimental Cosserat elasticity in open-cell polymer foam. Philos Mag 96:93–111
34. Sab K, Pradel F (2009) Homogenisation of periodic Cosserat media. Int J Comput Appl 34(1):60–71
35. Sakhaei AH, Erland S, Dodwell TJ (2020) A finite deformation Cosserat continuum model for uncured carbon fibre composites. Mech Mater 151:103611. (46:2787–2799, (2009))
36. Sanchez-Palencia E (1985) Homogenization techniques for composite media, 1 ed. Springer

37. Skrzat A, Eremeyev V (2020) On the effective properties of foams in the framework of the couple stress theory. Contin Mech Thermodyn 32:1779–1801
38. Tekoglu C, Onck PR (2005) Size effects in the mechanical behavior of cellular materials. J Mater Sci 40:5911–5917
39. Toupin R (1962) Elastic materials with couple-stresses. Arch Ration Mech Anal 11:385–414
40. Trovalusci P, Ostoja-Starzewski M, Laura De Bellis M, Murrali A (2015) Scale-dependent homogenization of random composites as micropolar continua. Euro J Mech A/Solids 49:396–407
41. Yanes V, Sabina FJ, Espinosa-Almeyda Y, Otero JA, RodrÍguez-Ramos R (2022) Asymptotic homogenization approach applied to Cosserat heterogeneous media. In: Andrianov I, Gluzman S, Mityushev V (eds) Mechanics and physics of structured media: asymptotic and integral equations methods of Leonid Filshtinsky. Academic Press. (In Press)
42. Zheng QS, Spencer AJM (1993) On the canonical representation for Kronecker powers of orthogonal tensors with application to material symmetry problems. Int J Eng Sci 31(4):617–635

# Chapter 7
# Free Localized Vibrations of a Thin Elastic Composite Panel

**Gurgen Ghulghazaryan and Lusine Ghulghazaryan**

**Abstract** Free boundary and interfacial vibrations of a composite cylindrical panel with free edges comprised of two finite orthotropic thin cylindrical panels with different elastic properties and full contact along the generators are studied. Starting from the formulation of the classical theory of orthotropic cylindrical shells, dispersion relations and asymptotic approximations for eigenfrequencies of interfacial and boundary vibrations of such composite cylindrical panels are derived. An algorithm for separating the interfacial and boundary vibrations is presented. Asymptotic connections between the dispersion relations of the problem at hand and the analogous problems for a composite rectangular plate are established. Examples of cylindrical panel with different widths of constituents are considered, and approximate values of dimensionless eigenfrequencies are obtained.

**Keywords** Cylindrical panel · Boundary and interfacial vibrations · Full contact

## 7.1 Introduction

Investigation of free vibrations of composite cylindrical panels plays an important role in the studies of dynamics of deformable solids. Such studies contribute to the development of the theory itself and are also required for the practical needs of different branches of engineering and industry, e.g. construction, instrument-engineering, seismic surveys, etc. [1]. In many cases the objects of investigations are finite thin-walled composite cylindrical panels. For such structures, attention is often attracted to free vibrations localized near the edges of the panels, i.e. edge

G. Ghulghazaryan (✉) · L. Ghulghazaryan
Armenian State Pedagogical University, Yerevan, Armenia
e-mail: ghulghazaryangurgen08@aspu.am

L. Ghulghazaryan
e-mail: ghulghazaryanlusine08@aspu.am

L. Ghulghazaryan
Institute of Mechanics of NAS RA, Yerevan, Armenia

vibrations, as well as vibrations localized near the interface of material properties, i.e. interfacial vibrations.

It is known that, at the free edge of an orthotropic plate planar and flexural vibrations can occur independently of each other [1–4]. When the plate is bent, these types of vibration are coupled, giving two new types of vibrations localized at the free edge: predominantly tangential and predominantly bending vibrations. Moreover, for thin cylindrical elastic panel the transformation of one type of vibration into the other occurs at the free edge of the panel. For this transformation of vibrations complex distribution picture of frequencies of natural vibrations occur, depending on the geometrical and mechanical parameters of the finite and infinite cylindrical panels [4–15]. By increasing the number of free edges of a cylindrical panel, this picture becomes more complex, see [15–18] and also [28, 29]. Therefore, investigation of edge resonance phenomena in composite plates and cylindrical panels with free edges is among the most challenging problems in the theory of vibrations of plates and shells [8]. These difficulties can be resolved by using a combination of analytical and asymptotic theories, as well as by numerical methods.

For studies of free interfacial vibrations, the reader is referred to contributions [16–18]. Transverse vibrations occurring along the contact line of two semi-infinite plates and concentrated close to it are studied in [16]. The plane interfacial vibrations near the interface of two joined semi-strips with different elastic properties are investigated in [17]. We also mention important contributions to edge and interfacial vibrations in shells, using special asymptotic methods, [5–8], see also a review paper [9].

In the present paper, free interfacial and edge vibrations of a composite cylindrical panel with free edges, consisting of finite orthotropic cylindrical panels with different elastic properties and longitudinal section of material properties are studied. On the line of material interface, the full contact conditions are imposed. Such type of structural elements are important components of modern constructions; therefore, an issue of free vibrations of such elements is important and deserves attention.

The dispersion relations which determine the appropriate frequencies of interfacial and edge vibrations of the considered composite cylindrical panel with free edges are derived. An asymptotic link between the dispersion relations of the considered problem and the analogous problem for a plate with free edges, composed of orthotropic plates with different elastic properties is established. The derived dispersion relations and related asymptotic formulas can be used for controlling the spectrum of frequencies of the formulated problem by varying the geometry of the panel and mechanical properties of materials. In particular, one can control the spectrum by shifting either the origin of the spectrum or the points of condensation from the undesirable resonance region.

1. **Statement of the Problem and Basic Equations.** Let the generatrices of the cylindrical panel be orthogonal to the edge of the panel. On the middle surface of the panel, the curvilinear coordinates $(\alpha, \beta)$ are introduced, where $\alpha(0 \leq \alpha \leq l)$ and $\beta(-s^{(2)} \leq \beta \leq s^{(1)})$ are the oriented length of the generatrix and the length of the arc of the directing circle, respectively. $l$ is the length of the cylindrical panel (Fig. 7.1). $\beta = 0$ corresponds to the interface between materials with

**Fig. 7.1** The interface between materials with different properties
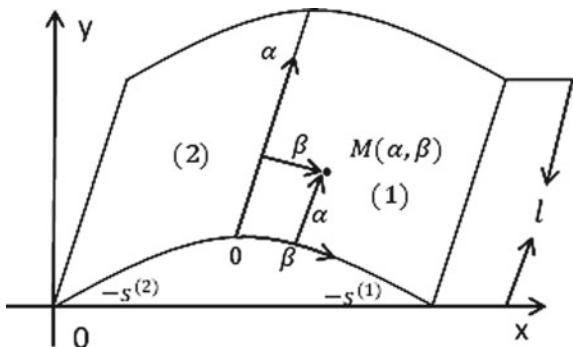


different properties. All the values corresponding to the right panel ($0 \leq \beta \leq s^{(1)}$) on (Fig. 7.1) are marked with superscript (1). Similarly, for the left panel ($-s^{(2)} \leq \beta \leq 0$) superscript (2) is used.

As the initial equations describing vibrations of the left and right sides cylindrical panels, we will use the equations corresponding to the classical theory of orthotropic cylindrical shells written in the curvilinear coordinates for given $\alpha$ and $\beta$ (Fig. 7.1) [19]:

$$-B_{11}^{(r)} \frac{\partial^2 u_1^{(r)}}{\partial \alpha^2} - B_{66}^{(r)} \frac{\partial^2 u_1^{(r)}}{\partial \beta^2} - \left(B_{12}^{(r)} + B_{66}^{(r)}\right) \frac{\partial^2 u_2^{(r)}}{\partial \alpha \partial \beta} + \frac{B_{12}^{(r)}}{R} \frac{\partial u_3^{(r)}}{\partial \alpha} = \rho^{(r)} \omega^2 u_1^{(r)},$$

$$-\left(B_{12}^{(r)} + B_{66}^{(r)}\right) \frac{\partial^2 u_1^{(r)}}{\partial \alpha \partial \beta} - B_{66}^{(r)} \frac{\partial^2 u_2^{(r)}}{\partial \alpha^2} - B_{22}^{(r)} \frac{\partial^2 u_2^{(r)}}{\partial \beta^2} + \frac{B_{22}^{(r)}}{R} \frac{\partial u_3^{(r)}}{\partial \beta} - \frac{\mu^4}{R^2} X$$

$$\left(4B_{66}^{(r)} \frac{\partial^2 u_2^{(r)}}{\partial \alpha^2} + B_{22}^{(r)} \frac{\partial^2 u_2^{(r)}}{\partial \beta^2}\right) - \frac{\mu^4}{R} \left(B_{22}^{(r)} \frac{\partial^3 u_3^{(r)}}{\partial \beta^3} + \left(B_{12}^{(r)} + 4B_{66}^{(r)}\right) \frac{\partial^3 u_3^{(r)}}{\partial \alpha^2 \partial \beta}\right)$$

$$= \rho^{(r)} \omega^2 u_2^{(r)},$$

$$\mu^4 \left(B_{11}^{(r)} \frac{\partial^4 u_3^{(r)}}{\partial \alpha^4} + 2\left(B_{12}^{(r)} + 2B_{66}^{(r)}\right) \frac{\partial^4 u_3^{(r)}}{\partial \alpha^2 \partial \beta^2} + B_{22}^{(r)} \frac{\partial^4 u_3^{(r)}}{\partial \beta^4}\right) + \frac{\mu^4}{R} \left(B_{22}^{(r)} \frac{\partial^3 u_2^{(r)}}{\partial \beta^3}\right)$$

$$+\left(B_{12}^{(r)} + 4B_{66}^{(r)}\right) \frac{\partial^3 u_2^{(r)}}{\partial \alpha^2 \partial \beta}\right) - \frac{B_{12}^{(r)}}{R} \frac{\partial u_1^{(r)}}{\partial \alpha} - \frac{B_{22}^{(r)}}{R} \frac{\partial u_2^{(r)}}{\partial \beta} + \frac{B_{22}^{(r)}}{R^2} u_3^{(r)} = \rho^{(r)} \omega^2 u_3^{(r)},$$

$$r = 1, 2. \tag{7.1}$$

Here $u_1^{(r)}$, $u_2^{(r)}$ and $u_3^{(r)} (r = 1, 2)$ are projections of the displacement vector on the directions $\alpha$, $\beta$ and on the normal to the median surface of the shell, respectively; R is the radius of the directing circumference of the median surface; $\mu^4 = h^2/12$ ($h$ is shell thickness); $\omega$ is the angular frequency, $\rho^{(r)} (r = 1, 2)$ are densities of materials; $B_{ij}^{(r)} (r = 1, 2)$ are elasticity coefficients. The boundary conditions for orthotropic cantilever cylindrical panel have the form [19]

$$T_2^{(1)}\Big|_{\beta=0} = T_2^{(2)}\Big|_{\beta=0}, \ S_{21}^{(1)}\Big|_{\beta=0} = S_{21}^{(2)}\Big|_{\beta=0}, \ N_2^{(1)} + \frac{\partial H^{(1)}}{\partial \alpha}\Big|_{\beta=0} = N_2^{(2)} + \frac{\partial H^{(2)}}{\partial \alpha}\Big|_{\beta=0},$$

$$M_2^{(1)}\Big|_{\beta=0} = M_2^{(2)}\Big|_{\beta=0}, \ u_1^{(1)}\Big|_{\beta=0} = u_1^{(2)}\Big|_{\beta=0}, \ u_2^{(1)}\Big|_{\beta=0} = u_2^{(2)}\Big|_{\beta=0}$$

$$u_3^{(1)}\Big|_{\beta=0} = u_3^{(2)}\Big|_{\beta=0}, \ \frac{\partial u_3^{(1)}}{\partial \beta}\Big|_{\beta=0} = \frac{\partial u_3^{(2)}}{\partial \beta}\Big|_{\beta=0}. \tag{7.2}$$

$$T_2^{(r)}\Big|_{\beta=(-1)^{r-1}s^{(r)}} = S_{21}^{(r)}\Big|_{\beta=(-1)^{r-1}s^{(r)}} = N_2^{(r)} + \frac{\partial H^{(r)}}{\partial \alpha}\Big|_{\beta=(-1)^{r-1}s^{(r)}} =$$

$$M_2^{(r)}\Big|_{\beta=(-1)^{r-1}s^{(r)}} = 0, r = 1, 2. \tag{7.3}$$

$$T_1^{(r)}\Big|_{\alpha=0,l} = S_{12}^{(r)} + \frac{H^{(r)}}{R}\Big|_{\alpha=0,l} = N_1^{(r)} + \frac{\partial H^{(r)}}{\partial \beta}\Big|_{\alpha=0,l} = M_1^{(r)}\Big|_{\alpha=0,l} = 0, r = 1, 2.$$

$$T_1^{(r)} = hB_{11}^{(r)}\left[\frac{\partial u_1^{(r)}}{\partial \alpha} + \frac{B_{12}^{(r)}}{B_{11}^{(r)}}\left(\frac{\partial u_2^{(r)}}{\partial \beta} - \frac{u_3^{(r)}}{R}\right)\right],$$

$$T_2^{(r)} = hB_{22}^{(r)}\left[\frac{B_{12}^{(r)}}{B_{22}^{(r)}}\frac{\partial u_1^{(r)}}{\partial \alpha} + \frac{\partial u_2^{(r)}}{\partial \beta} - \frac{u_3^{(r)}}{R}\right], \tag{7.4}$$

$$M_1^{(r)} = \frac{h^3}{12}B_{11}^{(r)}\left[\frac{\partial^2 u_3^{(r)}}{\partial \alpha^2} + \frac{B_{12}^{(r)}}{B_{11}^{(r)}}\left(\frac{\partial^2 u_3^{(r)}}{\partial \beta^2} + \frac{1}{R}\frac{\partial u_2^{(r)}}{\partial \beta}\right)\right],$$

$$M_2^{(r)} = \frac{h^3}{12}B_{22}^{(r)}\left[\frac{B_{12}^{(r)}}{B_{22}^{(r)}}\frac{\partial^2 u_3^{(r)}}{\partial \alpha^2} + \frac{\partial^2 u_3^{(r)}}{\partial \beta^2} + \frac{1}{R}\frac{\partial u_2^{(r)}}{\partial \beta}\right],$$

$$S_{12}^{(r)} + \frac{H^{(r)}}{R} = hB_{66}^{(r)}\left[\frac{\partial u_1^{(r)}}{\partial \beta} + \frac{\partial u_2^{(r)}}{\partial \alpha} + \frac{h^2}{3R}\left(\frac{\partial^2 u_3^{(r)}}{\partial \alpha \partial \beta} + \frac{1}{R}\frac{\partial u_2^{(r)}}{\partial \alpha}\right)\right],$$

$$S_{21}^{(r)} = hB_{66}^{(r)}\left(\frac{\partial u_1^{(r)}}{\partial \beta} + \frac{\partial u_2^{(r)}}{\partial \alpha}\right), \tag{7.5}$$

$$N_1^{(r)} + \frac{\partial H^{(r)}}{\partial \beta} = \frac{h^3}{12}B_{11}^{(r)}\left[\frac{\partial^3 u_3^{(r)}}{\partial \alpha^3} + \frac{B_{12}^{(r)} + 4B_{66}^{(r)}}{B_{11}^{(r)}}\left(\frac{\partial^3 u_3^{(r)}}{\partial \beta^2 \partial \alpha} + \frac{1}{R}\frac{\partial^2 u_2^{(r)}}{\partial \alpha \partial \beta}\right)\right],$$

$$N_2^{(r)} + \frac{\partial H^{(r)}}{\partial \alpha} = \frac{h^3}{12}B_{22}^{(r)}\left[\frac{\partial^3 u_3^{(r)}}{\partial \beta^3} + \frac{B_{12}^{(r)} + 4B_{66}^{(r)}}{B_{22}^{(r)}}\frac{\partial^3 u_3^{(r)}}{\partial \alpha^2 \partial \beta} + \frac{1}{R}\frac{\partial^2 u_2^{(r)}}{\partial \beta^2} + \frac{4B_{66}^{(r)}}{B_{22}^{(r)}}\frac{1}{R}\frac{\partial^2 u_2^{(r)}}{\partial \alpha^2}\right].$$

Relations (7.2) are complete contact conditions at $\beta = 0$. Relations (7.3) and (7.4) are the conditions of free edges at $\beta = -s^{(2)}, s^{(1)}$ and $\alpha = 0, l$, respectively (Fig. 7.1). It can be proved that the problem (7.1)–(7.4) is self–conjugate and has a non–negative discrete spectrum with a limit point at $+\infty$.

The problem (7.1)–(7.4) does not allow separation of variables. Therefore, based on the nonnegative definiteness of the corresponding operator of problem (7.1)–(7.4), for finding natural frequencies and corresponding natural forms a generalized

Kantorovich—Vlasov method of reduction to ordinary differential equations can be applied [21–25].

The eigenfunctions of the problem

$$w^{VIII} = \theta^8 w, \quad w|_{\alpha=0,l} = w'|_{\alpha=0,l} = w''|_{\alpha=0,l} = w'''|_{\alpha=0,l} = 0, 0 \le \alpha \le l \tag{7.6}$$

are used as the basic functions. The problem (7.6) is self-conjugate and positive definite. The eigenfunctions corresponding to the eigenvalues $\theta_m^8, m = \overline{1, \infty}$ of the problem (7.6) have the form.

$$w_m(\theta_m\alpha) = \frac{\Delta_1}{\Delta} x_1(\theta_m\alpha) + \frac{\Delta_2}{\Delta} x_2(\theta_m\alpha) + \frac{\Delta_3}{\Delta} x_3(\theta_m\alpha) + x_4(\theta_m\alpha), 0 \le \alpha \le l.$$

$$x_1(\theta_m\alpha) = ch(\theta_m\alpha) - ch\frac{\theta_m\alpha}{\sqrt{2}}cos\frac{\theta_m\alpha}{\sqrt{2}} - sh\frac{\theta_m\alpha}{\sqrt{2}}sin\frac{\theta_m\alpha}{\sqrt{2}}, \tag{7.7}$$

$$x_2(\theta_m\alpha) = sh(\theta_m\alpha) - \sqrt{2}ch\frac{\theta_m\alpha}{\sqrt{2}}sin\frac{\theta_m\alpha}{\sqrt{2}}, x_3(\theta_m\alpha) = sin(\theta_m\alpha)$$

$$- \sqrt{2}sh\frac{\theta_m\alpha}{\sqrt{2}}cos\frac{\theta_m\alpha}{\sqrt{2}}, x_4(\theta_m\alpha) = cos(\theta_m\alpha) - ch\frac{\theta_m\alpha}{\sqrt{2}}cos\frac{\theta_m\alpha}{\sqrt{2}}$$

$$+ sh\frac{\theta_m\alpha}{\sqrt{2}}sin\frac{\theta_m\alpha}{\sqrt{2}}, \quad m = \overline{1, \infty}. \tag{7.8}$$

In above

$$\Delta = \begin{vmatrix} x_1(\theta_m\alpha) & x_2(\theta_m\alpha) & x_3(\theta_m\alpha) \\ x_1'(\theta_m\alpha) & x_2'(\theta_m\alpha) & x_3'(\theta_m\alpha) \\ x_1''(\theta_m\alpha) & x_2''(\theta_m\alpha) & x_3''(\theta_m\alpha) \end{vmatrix},$$

$$\Delta_1 = -\begin{vmatrix} x_4(\theta_m\alpha) & x_2(\theta_m\alpha) & x_3(\theta_m\alpha) \\ x_4'(\theta_m\alpha) & x_2'(\theta_m\alpha) & x_3'(\theta_m\alpha) \\ x_4''(\theta_m\alpha) & x_2''(\theta_m\alpha) & x_3''(\theta_m\alpha) \end{vmatrix},$$

$$\Delta_2 = -\begin{vmatrix} x_1(\theta_m\alpha) & x_4(\theta_m\alpha) & x_3(\theta_m\alpha) \\ x_1'(\theta_m\alpha) & x_4'(\theta_m\alpha) & x_3'(\theta_m\alpha) \\ x_1''(\theta_m\alpha) & x_4''(\theta_m\alpha) & x_3''(\theta_m\alpha) \end{vmatrix},$$

$$\Delta_3 = -\begin{vmatrix} x_1(\theta_m\alpha) & x_2(\theta_m\alpha) & x_4(\theta_m\alpha) \\ x_1'(\theta_m\alpha) & x_2'(\theta_m\alpha) & x_4'(\theta_m\alpha) \\ x_1''(\theta_m\alpha) & x_2''(\theta_m\alpha) & x_4''(\theta_m\alpha) \end{vmatrix}.$$

Also, these functions form an orthogonal basis in the Hilbert space $L_2[0, l]$ with their first and second derivatives [25]. Here $\theta_m, m = \overline{1, \infty}$, are the positive zeros of the Wronskian of functions (7.8) at the point $\alpha = l$.

Let us introduce the designations

$$\beta'_m = \int_0^l \left(\mathrm{w}'_m(\theta_m\alpha)\right)^2 d\alpha \ \Big/ \int_0^l \left(\mathrm{w}_m(\theta_m\alpha)\right)^2 d\alpha,$$

$$\beta''_m = \int_0^l \left(\mathrm{w}''_m(\theta_m\alpha)\right)^2 d\alpha \ \Big/ \int_0^l \left(\mathrm{w}'_m(\theta_m\alpha)\right)^2 d\alpha. \tag{7.9}$$

In formulas (7.8) and (7.9), derivatives are taken with respect to $\theta_m\alpha$ and $\beta'_m \to 1, \beta''_m \to 1 \, at \, m \to +\infty$.

2. **Derivation and Analysis of Characteristic Equations.** In the first, second, and third equations of system (7.1), the angular frequency $\omega$ is formally replaced by $\omega_1$, $\omega_2$, and $\omega_3$, respectively. The solution of system (7.1) is sought in the form.

$$\left(u_1^{(r)}, u_2^{(r)}, u_3^{(r)}\right) = \left(u_m^{(r)} \mathrm{w}'_m(\theta_m\alpha), v_m^{(r)} \mathrm{w}_m(\theta_m\alpha), \mathrm{w}_m(\theta_m\alpha)\right)$$

$$\times \exp\!\left((-1)^r \chi^{(r)}\theta_m\beta + \chi^{(r)}\theta_m s^{(r)}\right), r = 1, 2; m = \overline{1, \infty}. \tag{7.10}$$

Here, $\mathrm{w}_m(\theta_m\alpha)$, $m = \overline{1, \infty}$, are determined from formula (7.7) and $u_m^{(r)}$, $v_m^{(r)}$ and $\chi^{(r)}$ are undetermined constants. In this case, conditions (7.4) are satisfied automatically. Let us insert Eq. (7.10) into Eq. (7.1). The equations found are scalarly multiplied by the vector-function

$$\left(\mathrm{w}'_m(\theta_m\alpha), \mathrm{w}_m(\theta_m\alpha), \mathrm{w}_m(\theta_m\alpha), \mathrm{w}'_m(\theta_m\alpha), \mathrm{w}_m(\theta_m\alpha), \mathrm{w}_m(\theta_m\alpha)\right) \tag{7.11}$$

and then integrated between the limits from $0$ to $l$. From the first two pairs of equations we deduce

$$\left(c_m^{(r)} + \varepsilon_m^2 a^2 g_m^{(r)} d_m^{(r)}\right) u_m^{(r)}$$

$$= \varepsilon_m \left\{ a_m^{(r)} + a^2 \frac{B_{22}^{(r)}\left(B_{12}^{(r)} + B_{66}^{(r)}\right)}{B_{11}^{(r)} B_{66}^{(r)}} \left(\chi^{(r)}\right)^2 l_m^{(r)} + \varepsilon_m^2 a^2 \frac{B_{22}^{(r)} B_{12}^{(r)}}{B_{11}^{(r)} B_{66}^{(r)}} d_m^{(r)} \right\} \tag{7.12}$$

$$\left(c_m^{(r)} + \varepsilon_m^2 a^2 g_m^{(r)} d_m^{(r)}\right) v_m^{(r)} = (-1)^r \varepsilon_m \chi^{(r)} \left\{ b_m^{(r)} - a^2 g_m^{(r)} l_m^{(r)} \right\}, r = 1, 2. \tag{7.13}$$

From the third equation, by taking into account the relations (7.12) and (7.13), we obtain the characteristic equations

$$R_{mm}^{(r)} c_m^{(r)} + \varepsilon_m^2 \{ c_m^{(r)} - b_m^{(r)}\left(\chi^{(r)}\right)^2 + \frac{B_{12}^{(r)}}{B_{22}^{(r)}} \beta'_m a_m^{(r)} + a^2 (R_{mm}^{(r)} g_m^{(r)} d_m^{(r)}$$

$$+ 2b_m^{(r)} l_m^{(r)}\left(\chi^{(r)}\right)^2) + \varepsilon_m^2 a^2 d_m^{(r)}\left(b_m^{(r)} - \frac{B_{12}^{(r)}}{B_{22}^{(r)}} \beta'_m\right) - a^4\left(\chi^{(r)}\right)^2 g_m^{(r)}\left(l_m^{(r)}\right)^2\} = 0,$$

$$r = 1, 2; m = \overline{1, \infty} \tag{7.14}$$

$$a_m^{(r)} = -\left( \frac{B_{12}^{(r)}}{B_{11}^{(r)}} \left(\chi^{(r)}\right)^2 + \frac{B_{12}^{(r)}}{B_{11}^{(r)}} \beta_m' - \frac{B_{12}^{(r)}}{B_{11}^{(r)}} \left(\eta_{2m}^{(r)}\right)^2 \right),$$

$$b_m^{(r)} = \frac{B_{22}^{(r)}}{B_{11}^{(r)}} \left(\chi^{(r)}\right)^2 + \frac{B_{22}^{(r)}}{B_{11}^{(r)}} \left(\eta_{1m}^{(r)}\right)^2 - B_1^{(r)}, \quad a^2 = \mu^4 \theta_m^2,$$

$$c_m^{(r)} = \frac{B_{22}^{(r)}}{B_{11}^{(r)}} \left(\chi^{(r)}\right)^4 - B_2^{(r)} \left(\chi^{(r)}\right)^2 + \left( \frac{B_{22}^{(r)}}{B_{11}^{(r)}} \left(\eta_{1m}^{(r)}\right)^2 + \frac{B_{66}^{(r)}}{B_{11}^{(r)}} \left(\eta_{2m}^{(r)}\right)^2 \right) \left(\chi^{(r)}\right)^2$$

$$+ \left( \beta_m' - \left(\eta_{2m}^{(r)}\right)^2 \right) \left( \beta_m'' - \frac{B_{66}^{(r)}}{B_{11}^{(r)}} \left(\eta_{1m}^{(r)}\right)^2 \right), \quad d_m^{(r)} = \left(\chi^{(r)}\right)^2 - \frac{4 B_{66}^{(r)}}{B_{11}^{(r)}} \beta_m',$$

$$g_m^{(r)} = \frac{B_{22}^{(r)}}{B_{11}^{(r)}} \left(\chi^{(r)}\right)^2 + \frac{B_{22}^{(r)}}{B_{11}^{(r)}} \left(\eta_{1m}^{(r)}\right)^2 - \frac{B_{22}^{(r)}}{B_{66}^{(r)}} \beta_m'', \quad l_m^{(r)} = \left(\chi^{(r)}\right)^2 - \frac{B_{12}^{(r)} + 4 B_{66}^{(r)}}{B_{22}^{(r)}} \beta_m',$$

$$(7.15)$$

$$R_{mm}^{(r)} = a^2 \left( \left(\chi^{(r)}\right)^4 - \frac{2\left( B_{12}^{(r)} + 2 B_{66}^{(r)} \right)}{B_{22}^{(r)}} \beta_m' \left(\chi^{(r)}\right)^2 + \frac{B_{11}^{(r)}}{B_{22}^{(r)}} \beta_m' \beta_m'' \right) - \frac{B_{66}^{(r)}}{B_{22}^{(r)}} \left(\eta_{3m}^{(r)}\right)^2,$$

$$\left(\eta_{im}^{(r)}\right)^2 = \frac{\rho^{(r)} \omega_i}{B_{66}^{(r)} \theta_m^2}, i = 1, 2, 3; , \quad \varepsilon_m = \frac{1}{R \theta_m}.$$

$$B_1^{(r)} = \frac{B_{11}^{(r)} B_{11}^{(r)} \beta_m'' - \left(B_{12}^{(r)}\right)^2 \beta_m' - B_{12}^{(r)} B_{66}^{(r)} \beta_m'}{B_{11}^{(r)} B_{66}^{(r)}},$$

$$B_2^{(r)} = \frac{B_{11}^{(r)} B_{11}^{(r)} \beta_m'' - \left(B_{12}^{(r)}\right)^2 \beta_m' - 2 B_{12}^{(r)} B_{66}^{(r)} \beta_m'}{B_{11}^{(r)} B_{66}^{(r)}}$$

Let $\chi^{(r)}(j = 1, 2, 3, 4)$, be pairwise different roots of the Eq. (7.14) with nonnegative real parts and $\chi_{j+4}^{(r)} = -\chi_j^{(r)}$, $j = 1, 2, 3, 4$. Let $\left(u_{1j}^{(r)}, u_{2j}^{(r)}, u_{3j}^{(r)}\right)$, , be nontrivial solutions of type (7.10) of system (7.1) at $\chi^{(r)} = \chi_j^{(r)}$, $j = 1, 2, \ldots, 8$, respectively. The solution of the problem (7.1)–(7.4) is sought for in the form

$$u_i^{(r)} = \sum_{j=1}^{8} u_{ij}^{(r)} w_j^{(r)}, i = 1, 2, 3; r = 1, 2. \tag{7.16}$$

Let us insert Eq. (7.16) into the boundary conditions (7.2)−(7.4). As a result, we obtain the system of equations

$$\sum_{j=1}^{8} \frac{M_{ij}^{(1)} \exp\left(\chi_j^{(1)} \theta_m s^{(1)}\right) w_j^{(1)}}{c_{mj}^{(1)} + \varepsilon_m^2 a^2 g_{mj}^{(1)} d_{mj}^{(1)}} - \sum_{j=1}^{8} \frac{c M_{ij}^{(2)} \exp\left(\chi_j^{(2)} \theta_m s^{(2)}\right) w_j^{(2)}}{c_{mj}^{(2)} + \varepsilon_m^2 a^2 g_{mj}^{(2)} d_{mj}^{(2)}}, i = \overline{1, 4};$$

$$\sum_{j=1}^{8} \frac{M_{ij}^{(1)} \exp\left(\chi_j^{(1)} \theta_m s^{(1)}\right) w_j^{(1)}}{c_{mj}^{(1)} + \varepsilon_m^2 a^2 g_{mj}^{(1)} d_{mj}^{(1)}} - \sum_{j=1}^{8} \frac{c M_{ij}^{(2)} \exp\left(\chi_j^{(2)} \theta_m s^{(2)}\right) w_j^{(2)}}{c_{mj}^{(2)} + \varepsilon_m^2 a^2 g_{mj}^{(2)} d_{mj}^{(2)}}, i = \overline{5, 8};$$

$$(7.17)$$

$$\sum_{j=1}^{8} \frac{M_{ij}^{(1)} w_j^{(1)}}{c_{mj}^{(1)} + \varepsilon_m^2 a^2 g_{mj}^{(1)} d_{mj}^{(1)}} = 0, i = \overline{9, 12}; \sum_{j=1}^{8} \frac{M_{ij}^{(2)} w_j^{(2)}}{c_{mj}^{(2)} + \varepsilon_m^2 a^2 g_{mj}^{(2)} d_{mj}^{(2)}}, i = \overline{13, 16};$$

$$M_{1j}^{(r)} = \left(\chi_j^{(r)}\right)^2 b_{mj}^{(r)} - \frac{B_{12}^{(r)}}{B_{22}^{(r)}} \beta_m' a_{mj}^{(r)} - c_{mj}^{(r)} - a^2 l_{mj}^{(r)} b_{mj}^{(r)} \left(\chi_j^{(r)}\right)^2$$

$$- \varepsilon_m^2 a^2 g_{mj}^{(r)} \left(b_{mj}^{(r)} - \frac{B_{12}^{(r)}}{B_{22}^{(r)}} \beta_m'\right), M_{2j}^{(r)} = \frac{B_{66}^{(r)}}{B_{11}^{(r)}} \chi_j^{(r)} \{a_{mj}^{(r)} + b_{mj}^{(r)}$$

$$+ a^2 l_{mj}^{(r)} \left[\frac{B_{22}^{(r)} B_{12}^{(r)}}{B_{11}^{(r)} B_{66}^{(r)}} \left(\chi_j^{(r)}\right)^2 + \frac{B_{22}^{(r)}}{B_{66}^{(r)}} \beta_m'' - \frac{B_{22}^{(r)}}{B_{11}^{(r)}} \left(\eta_{1m}^{(r)}\right)^2\right]$$

$$+ \varepsilon_m^2 a^2 \frac{B_{22}^{(r)} B_{12}^{(r)}}{B_{11}^{(r)} B_{66}^{(r)}} d_{mj}^{(r)}\},$$

$$M_{3j}^{(r)} = \left(\left(\chi_j^{(r)}\right)^2 - \frac{B_{12}^{(r)}}{B_{22}^{(r)}} \beta_m'\right) c_{mj}^{(r)} + \varepsilon_m^2 \left[b_{mj}^{(r)} \left(\chi_j^{(r)}\right)^2 + 4a^2 \frac{B_{66}^{(r)} B_{12}^{(r)}}{\left(B_{22}^{(r)}\right)^2} g_{mj}^{(r)} \left(\beta_m'\right)^2\right]$$

$$M_{4j}^{(r)} = \chi_j^{(r)} \left(l_{mj}^{(r)} c_{mj}^{(r)} + \varepsilon_m^2 b_{mj}^{(r)} d_{mj}^{(r)}\right), c = \frac{B_{22}^{(2)}}{B_{22}^{(1)}}, \qquad (7.18)$$

$$M_{5j}^{(r)} = a_{mj}^{(r)} + a^2 \beta_m' \frac{B_{22}^{(r)} (B_{12}^{(r)} + B_{66}^{(r)})}{B_{11}^{(r)} B_{66}^{(r)}} l_{mj}^{(r)} \left(\chi_j^{(r)}\right)^2 + \varepsilon_m^2 a^2 \frac{B_{22}^{(r)} B_{12}^{(r)}}{B_{11}^{(r)} B_{66}^{(r)}} d_{mj}^{(r)},$$

$$M_{6j}^{(r)} = \chi_j^{(r)} \left(b_{mj}^{(r)} - a^2 g_{mj}^{(r)} l_{mj}^{(r)}\right), M_{7j}^{(r)} = c_{mj}^{(r)} + \varepsilon_m^2 a^2 g_{mj}^{(r)} d_{mj}^{(r)},$$

$$M_{8j}^{(r)} = \chi_j^{(r)} \left(c_{mj}^{(r)} + \varepsilon_m^2 a^2 g_{mj}^{(r)} d_{mj}^{(r)}\right);$$

$$M_{9j}^{(1)} = M_{1j}^{(1)}, M_{10j}^{(1)} = M_{2j}^{(1)}, M_{11j}^{(1)} = M_{3j}^{(1)}, M_{12j}^{(1)} = M_{4j}^{(1)}, j = \overline{1, 8};$$

$$M_{13j}^{(2)} = M_{1j}^{(2)}, M_{14j}^{(2)} = M_{2j}^{(2)}, M_{15j}^{(2)} = M_{3j}^{(2)}, M_{16j}^{(2)} = M_{4j}^{(2)}, j = \overline{1, 8}.$$

The superscript $j$ means that the corresponding function is taken at $\chi^{(r)} = \chi_j^{(r)}$. In order for the system (7.17) to possess a nontrivial solution, it is necessary and sufficient that

$$\Delta = exp\left(-\sum_{r=1}^{2} \sum_{j=1}^{4} z_j^{(r)}\right) Det \left\| T_{ij} \right\|_{i,j=1}^{4} = 0, m = \overline{1, \infty} \qquad (7.19)$$

$$T_{11} = \left\| M_{ij}^{(1)} \right\|_{i,j=1}^{4}, \ T_{12} = \left\| (-1)^{i-1} M_{ij}^{(1)} \exp\left( z_j^{(1)} \right) \right\|_{i,j=1}^{4},$$

$$T_{13} = -c \left\| M_{ij}^{(2)} \right\|_{i,j=1}^{4}, \ T_{14} = \left\| (-1)^{i} M_{ij}^{(2)} \exp\left( z_j^{(2)} \right) \right\|_{i,j=1}^{4},$$

$$T_{21} = \left\| M_{ij}^{(1)} \right\|_{i=5,j=1}^{8,4}, \ T_{22} = \left\| (-1)^{i-1} M_{ij}^{(1)} \exp\left( z_j^{(1)} \right) \right\|_{i=5,j=1}^{8,4},$$

$$T_{23} = -\left\| M_{ij}^{(2)} \right\|_{i=5,j=1}^{8,4}, \ T_{24} = \left\| (-1)^{i} M_{ij}^{(2)} \exp\left( z_j^{(2)} \right) \right\|_{i=5,j=1}^{8,4},$$

$$T_{31} = T_{12}, T_{32} = T_{11}, T_{33} = 0, T_{34} = 0;$$

$$T_{41} = 0, \ T_{42} = 0, \ T_{43} = T_{14}, \ T_{44} = T_{13}; \ z_j^{(r)} = -\theta_m \chi_j^{(r)} s^{(r)}. \tag{7.20}$$

Performing elementary operations with columns of determinant (7.19), we obtain

$$\Delta = exp\left( -\sum_{r=1}^{2}\sum_{j=1}^{4} z_j^{(r)} \right) \left( K^{(1)} \right)^2 \left( K^{(2)} \right)^2 Det \left\| t_{ij} \right\|_{i,j=1}^{4} = 0, m = \overline{1, \infty}; \tag{7.21}$$

$$K^{(r)} = \left( \chi_1^{(r)} - \chi_2^{(r)} \right)\left( \chi_1^{(r)} - \chi_3^{(r)} \right)\left( \chi_1^{(r)} - \chi_4^{(r)} \right)\left( \chi_2^{(r)} - \chi_3^{(r)} \right)\left( \chi_2^{(r)} - \chi_4^{(r)} \right)$$
$$\left( \chi_3^{(r)} - \chi_4^{(r)} \right) r = 1, 2. \tag{7.22}$$

$$t_{11} = \left\| m_{ij} \right\|_{i,j=1}^{4}, t_{12} = \left\| m_{ij} \right\|_{i=1,j=5}^{4,8}, t_{13} = c\left\| m_{ij} \right\|_{i=1,j=9}^{4,12}, t_{14} = c\left\| m_{ij} \right\|_{i=1,j=13}^{4,16};$$

$$t_{21} = \left\| m_{ij} \right\|_{i=5,j=1}^{8,4}, t_{22} = \left\| m_{ij} \right\|_{i,j=5}^{8}, t_{23} = c\left\| m_{ij} \right\|_{i=5,j=9}^{8,12}, t_{24} = c\left\| m_{ij} \right\|_{i=5,j=13}^{8,16};$$

$$t_{31} = t_{12}, t_{32} = t_{11}, t_{33} = 0, t_{34} = 0; T_{41} = 0, t_{42} = 0, t_{43} = t_{14}, t_{44} = t_{13}.$$

Expressions for $m_{ij}$ can be obtained in a similar way as in [24, 25].

It follows from (7.21) that the Eq. (7.19) are equivalent to the following

$$\nabla = Det \left\| t_{ij} \right\|_{i,j=1}^{4} = 0, m = \overline{1, \infty} \tag{7.23}$$

Taking into account the relations between $\eta_{1m}^{(r)}$, $\eta_{2m}^{(r)}$ and $\eta_{3m}^{(r)}$, we conclude that Eqs. (7.23) determine frequencies of the interfacial and boundary types of corresponding vibrations. At $\eta_{1m}^{(r)} = \eta_{2m}^{(r)} = \eta_{3m}^{(r)} = \eta_m^{(r)}$ the Eqs. (7.14) are the characteristic equations of system (7.1), and Eqs. (7.23) at $\theta = \theta_m, m \in N$ the dispersion equations of problem (7.1)−(7.4).

In Sect. 7.50, we will study the asymptotic behavior of the dispersion relations (7.23) at $\varepsilon_m = 1/(\theta_m R) \to 0$ (transition to a rectangular composed plate with free edges or to vibrations localized at the free edges and at the interface of materials with different properties of the cylindrical panel) and at $\theta_m s^{(r)} \to \infty$ transition to a wide enough cylindrical panel or to vibrations localized at the free edges and at the

interface of materials with different properties of the cylindrical panel). To verify the reliability of the asymptotic relations found in Sect. 7.5, we will investigate the free planar and flexural vibrations of a rectangular composed plate in the next sections.

3. **Planar vibrations of a composite rectangular plate with free edges.** Free inter-facial and edge vibrations of a rectangular plate composed of finite thin elastic orthotropic rectangular plates with different elastic coefficients are considered. Let us introduce rectilinear oriented orthogonal coordinates $(\alpha, \beta)$ on the mid-plane, where $0 \leq \alpha \leq l, -s_0^{(2)} \leq \beta \leq s_0^{(1)}$. The line $\beta = 0$ corresponds to the interface of material properties. All values related to the right plate $0 \leq \beta \leq s_0^{(1)}$ are indicated by superscript (1), and to the left plate $-s_0^{(2)} \leq \beta \leq 0$ by (2), respectively. As the initial equations, the equations of small planar vibrations of the left and right plates are used, which correspond to the classical theory of orthotropic plates [19].

$$-B_{11}^{(r)} \frac{\partial^2 u_1^{(r)}}{\partial \alpha^2} - B_{66}^{(r)} \frac{\partial^2 u_1^{(r)}}{\partial \beta^2} - \left(B_{12}^{(r)} + B_{66}^{(r)}\right) \frac{\partial^2 u_2^{(r)}}{\partial \alpha \partial \beta} = \rho^{(r)} \omega^2 u_1^{(r)}, \qquad (7.24)$$

$$-\left(B_{12}^{(r)} + B_{66}^{(r)}\right) \frac{\partial^2 u_1^{(r)}}{\partial \alpha \partial \beta} - B_{66}^{(r)} \frac{\partial^2 u_2^{(r)}}{\partial \alpha^2} - B_{22}^{(r)} \frac{\partial^2 u_2^{(r)}}{\partial \beta^2} = \rho^{(r)} \omega^2 u_2^{(r)}, r = 1, 2.$$

Here $\alpha (0 \leq \alpha \leq l)$ and $\beta(-s_0^{(2)} \leq \beta \leq s_0^{(1)})$ are the orthogonal rectilinear coordinates of a point of the mid-plane; $u_1^{(r)}, u_2^{(r)} (r = 1, 2)$ are the projections of the displacements vector in the directions $\alpha$ and $\beta$, respectively; $B_{ik}^{(r)}, i, k = 1, 2, 6(r = 1, 2)$, are coefficients of elasticity; $\omega$- is the natural frequency; $\rho^{(r)} (r = 1, 2)$–are the density of the materials. The boundary conditions are written as

$$T_2^{(1)}\Big|_{\beta=0} = T_2^{(2)}\Big|_{\beta=0}, \ S_{21}^{(1)}\Big|_{\beta=0} = S_{21}^{(2)}\Big|_{\beta=0},$$

$$u_1^{(1)}\Big|_{\beta=0} = u_1^{(2)}\Big|_{\beta=0}, \ u_2^{(1)}\Big|_{\beta=0} = u_2^{(2)}\Big|_{\beta=0}, \qquad (7.25)$$

$$T_2^{(r)}\Big|_{\beta=(-1)^{r-1}s_0^{(r)}} = 0, \ S_{21}^{(r)}\Big|_{\beta=(-1)^{r-1}s_0^{(r)}} = 0, r = 1, 2. \qquad (7.26)$$

$$T_1^{(r)}\Big|_{\alpha=0,l} = 0, \ S_{12}^{(r)}\Big|_{\alpha=0,l} = 0, r = 1, 2. \qquad (7.27)$$

$$T_1^{(r)} = h B_{11}^{(r)} \left[\frac{\partial u_1^{(r)}}{\partial \alpha} + \frac{B_{12}^{(r)}}{B_{11}^{(r)}} \frac{\partial u_2^{(r)}}{\partial \beta}\right], \ T_2^{(r)} = h B_{22}^{(r)} \left[\frac{B_{12}^{(r)}}{B_{22}^{(r)}} \frac{\partial u_1^{(r)}}{\partial \alpha} + \frac{\partial u_2^{(r)}}{\partial \beta}\right], \quad (7.28)$$

$$S_{21}^{(r)} = S_{12}^{(r)} = h B_{66}^{(r)} \left[\frac{\partial u_1^{(r)}}{\partial \beta} + \frac{\partial u_2^{(r)}}{\partial \alpha}\right].$$

The relations (7.25) describe the full contact conditions at $\beta = 0$. Relations (7.26) and (7.27) are the conditions of free edges at $= -s_0^{(2)}, s_0^{(1)}$ and $\alpha = 0, l$, respectively, see Fig. 7.2. The problem (7.24)−(7.27) does not allow the separation of variables. The differential operator corresponding to this problem is self-conjugate and nonnegative definite. Therefore, the generalized Kantorovich-Vlasov method of reduction to ordinary differential equations can be used to find vibration eigenfrequencies and eigenmodes [21–25]. The solution of system (7.24) is sought for in the form

$$\left(u_1^{(r)}, u_2^{(r)}\right) = \left(u_m^{(r)} w_m'(\theta_m \alpha), v_m^{(r)} w_m(\theta_m \alpha)\right) \exp\left((-1)^r y^{(r)} \theta_m \beta + y^{(r)} \theta_m s_0^{(r)}\right),$$
$$r = 1, 2; m = \overline{1, \infty}. \tag{7.29}$$

Here $w_m(\theta_m \alpha)$ are determined from formula (7.7) and $u_1^{(r)}, u_2^{(r)}, y^{(r)}$ are undetermined constants. In this case, the conditions (7.27) are satisfied automatically. Let us insert (7.29) into Eq. (7.24). As a result, we obtain the system of equations

$$\left(\frac{B_{66}^{(r)}}{B_{11}^{(r)}}\left(y^{(r)}\right)^2 - \beta_m'' + \frac{B_{66}^{(r)}}{B_{11}^{(r)}}\left(\eta_m^{(r)}\right)^2\right)u_m^{(r)} + (-1)^r y^{(r)} \frac{B_{12}^{(r)} + B_{66}^{(r)}}{B_{11}^{(r)}} v_m^{(r)} = 0, \quad (7.30)$$

$$(-1)^r y^{(r)} \frac{B_{12}^{(r)} + B_{66}^{(r)}}{B_{22}^{(r)}} \beta_m' u_m^{(r)} - \left(\left(y^{(r)}\right)^2 - \frac{B_{66}^{(r)}}{B_{22}^{(r)}}\beta_m' + \frac{B_{66}^{(r)}}{B_{22}^{(r)}}\left(\eta_m^{(r)}\right)^2\right)v_m^{(r)} = 0,$$

$$r = 1, 2,$$

where $\eta_m^{(r)}, \beta_m', \beta_m''$ are defined in (7.15) and (7.9), respectively. Equating the determinant of system (7.30) to zero, the following characteristic equation of the system (7.24) is found:

$$c_m^{(r)} = \frac{B_{22}^{(r)}}{B_{11}^{(r)}}\left(y^{(r)}\right)^4 - B_2^{(r)}\left(y^{(r)}\right)^2 + \frac{B_{22}^{(r)} + B_{66}^{(r)}}{B_{11}^{(r)}}\left(\eta_m^{(r)}\right)^2\left(y^{(r)}\right)^2$$
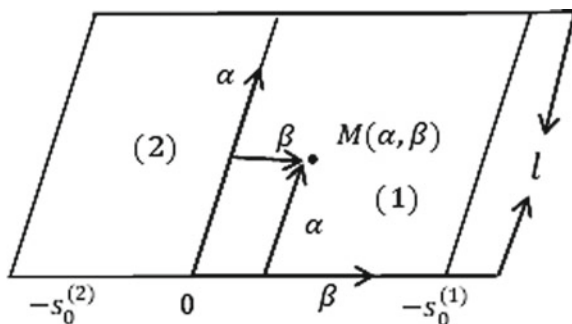


**Fig. 7.2** Kantorovich-Vlasov method of reduction to ordinary differential equations can be used to find vibration eigenfrequencies and eigenmodes

$$+ \left( \beta'_m - \left( \eta_m^{(r)} \right)^2 \right) \left( \frac{B_{22}^{(r)}}{B_{11}^{(r)}} \beta''_m - \frac{B_{66}^{(r)}}{B_{11}^{(r)}} \left( \eta_m^{(r)} \right)^2 \right),$$

$$r = 1, 2; m = \overline{1, \infty}. \tag{7.31}$$

Let $y_1^{(r)}$, $y_2^{(r)} (r = 1, 2)$ be various roots of Eq. (7.31) with nonnegative real parts and $y_{j+2}^{(r)} = -y_j^{(r)} (j = 1, 2)$. As a solution of Eq. (7.30) for $y_j^{(r)} \left( j = \overline{1,4} \right)$ we take

$$u_{mj}^{(r)} = \left( y_j^{(r)} \right)^2 - \frac{B_{66}^{(r)}}{B_{22}^{(r)}} \beta'_m + \frac{B_{66}^{(r)}}{B_{22}^{(r)}} \left( \eta_m^{(r)} \right)^2, \quad v_{mj}^{(r)} = (-1)^r y^{(r)} \frac{B_{12}^{(r)} + B_{66}^{(r)}}{B_{22}^{(r)}} \beta'_m \tag{7.32}$$

The solution of the problem (7.24)−(7.27) can be presented in the form

$$u_1^{(r)} = \sum_{j=1}^{4} u_{mj}^{(r)} w'_m (\theta_m \alpha) \exp \left( (-1)^r y_j^{(r)} \theta_m \beta + y_j^{(r)} \theta_m s_0^{(r)} \right) w_j^{(r)}, \tag{7.33}$$

$$u_2^{(r)} = \sum_{j=1}^{4} v_{mj}^{(r)} w_m (\theta_m \alpha) \exp \left( (-1)^r y_j^{(r)} \theta_m \beta + y_j^{(r)} \theta_m s_0^{(r)} \right) w_j^{(r)}, r = 1, 2.$$

Let us insert Eq. (7.33) into boundary conditions (7.25) and (7.26). As a result, we arrive at the following system of equations

$$\sum_1^4 R_{1j}^{(1)} \exp \left( y_j^{(1)} \theta_m s_0^{(1)} \right) w_j^{(1)} - c \sum_1^4 R_{1j}^{(2)} \exp \left( y_j^{(2)} \theta_m s_0^{(2)} \right) w_j^{(2)} = 0,$$

$$\sum_1^4 R_{2j}^{(1)} \exp \left( y_j^{(1)} \theta_m s_0^{(1)} \right) w_j^{(1)} + c \sum_1^4 R_{2j}^{(2)} \exp \left( y_j^{(2)} \theta_m s_0^{(2)} \right) w_j^{(2)} = 0,$$

$$\sum_1^4 R_{3j}^{(1)} \exp \left( y_j^{(1)} \theta_m s_0^{(1)} \right) w_j^{(1)} - \sum_1^4 R_{3j}^{(2)} \exp \left( y_j^{(2)} \theta_m s_0^{(2)} \right) w_j^{(2)} = 0,$$

$$\sum_1^4 R_{4j}^{(1)} \exp \left( y_j^{(1)} \theta_m s_0^{(1)} \right) w_j^{(1)} + \sum_1^4 R_{4j}^{(2)} \exp \left( y_j^{(2)} \theta_m s_0^{(2)} \right) w_j^{(2)} = 0,$$

$$\sum_1^4 R_{1j}^{(r)} w_j^{(r)} = 0, \sum_1^4 R_{2j}^{(r)} w_j^{(r)} = 0, r = 1, 2. \tag{7.34}$$

$$R_{1j}^{(r)} = \frac{B_{66}^{(r)}}{B_{22}^{(r)}} \left( \left( y_j^{(r)} \right)^2 + \frac{B_{12}^{(r)}}{B_{22}^{(r)}} \left( \beta'_m - \left( \eta_m^{(r)} \right)^2 \right) \right),$$

$$R_{2j}^{(r)} = \frac{B_{66}^{(r)}}{B_{22}^{(r)}} y_j^{(r)} \left( \left(y_j^{(r)}\right)^2 + \frac{B_{12}^{(r)}}{B_{22}^{(r)}} \beta_m' + \frac{B_{66}^{(r)}}{B_{22}^{(r)}} \left(\eta_m^{(r)}\right)^2 \right),$$

$$R_{3j}^{(r)} = \left(y_j^{(r)}\right)^2 - \frac{B_{66}^{(r)}}{B_{22}^{(r)}} \left( \beta_m' - \left(\eta_m^{(r)}\right)^2 \right),$$

$$R_{4j}^{(r)} = y_j^{(r)} \frac{B_{12}^{(r)} + B_{66}^{(r)}}{B_{22}^{(r)}}, c = \frac{B_{22}^{(2)}}{B_{22}^{(1)}}, r = 1, 2. \tag{7.35}$$

Equating the determinant $\Delta_e$ of system (7.34) to zero and performing elementary operations with columns of the determinant, we obtain the dispersion equations

$$\Delta_e = \left(y_2^{(1)} - y_1^{(1)}\right)^2 \left(y_2^{(2)} - y_1^{(2)}\right)^2 exp\left( \theta_m \sum_{r=1}^{2} s_0^{(r)} \left(y_1^{(r)} + y_2^{(r)}\right) \right)$$

$$Det \left\| e_{ij} \right\|_{i,j=1}^{8} = 0, m = \overline{1, \infty}. \tag{7.36}$$

$$e_{11} = \frac{B_{66}^{(1)}}{B_{22}^{(1)}} \left( \left(y_j^{(1)}\right)^2 + \frac{B_{12}^{(1)}}{B_{22}^{(1)}} \left( \beta_m' - \left(\eta_m^{(1)}\right)^2 \right) \right), e_{12} = \frac{B_{66}^{(1)}}{B_{22}^{(1)}} \left(y_1^{(1)} + y_2^{(1)}\right),$$

$$e_{13} = e_{11} exp\left(z_1^{(1)}\right), e_{14} = e_{12} exp\left(z_2^{(1)}\right) + e_{11}\left[z_1^{(1)} z_2^{(1)}\right],$$

$$e_{15} = \frac{B_{66}^{(2)}}{B_{22}^{(2)}} \left( \left(y_j^{(2)}\right)^2 + \frac{B_{12}^{(2)}}{B_{22}^{(2)}} \left( \beta_m' - \left(\eta_m^{(2)}\right)^2 \right) \right),$$

$$e_{16} = -c \frac{B_{66}^{(2)}}{B_{22}^{(2)}} \left(y_1^{(2)} + y_2^{(2)}\right), e_{17} = c e_{15} exp\left(z_1^{(2)}\right),$$

$$e_{18} = e_{16} exp\left(z_2^{(2)}\right) + e_{15}\left[z_1^{(2)} z_2^{(2)}\right];$$

$$e_{21}^{(1)} = \frac{B_{66}^{(1)}}{B_{22}^{(1)}} y_1^{(1)} \left( \left(y_1^{(1)}\right)^2 + \frac{B_{12}^{(1)}}{B_{22}^{(1)}} \beta_m' + \frac{B_{66}^{(1)}}{B_{22}^{(1)}} \left(\eta_m^{(1)}\right)^2 \right),$$

$$e_{22}^{(1)} = \frac{B_{66}^{(1)}}{B_{22}^{(1)}} \left( y_1^{(1)} y_2^{(1)} + B^{(1)} - \left(\eta_m^{(1)}\right)^2 \right),$$

$$e_{23} = -e_{21} exp\left(z_1^{(1)}\right), e_{24} = -e_{22} exp\left(z_2^{(1)}\right) - e_{21}\left[z_1^{(1)} z_2^{(1)}\right],$$

$$e_{25}^{(1)} = \frac{B_{66}^{(2)}}{B_{22}^{(2)}} y_1^{(2)} \left( \left(y_1^{(2)}\right)^2 + \frac{B_{12}^{(2)}}{B_{22}^{(2)}} \beta_m' + \frac{B_{66}^{(2)}}{B_{22}^{(2)}} \left(\eta_m^{(2)}\right)^2 \right),$$

$$e_{26}^{(1)} = \frac{B_{66}^{(2)}}{B_{22}^{(2)}} \left( y_1^{(2)} y_2^{(2)} + B^{(2)} - \left(\eta_m^{(2)}\right)^2 \right), e_{27} = -e_{25} exp\left(z_1^{(2)}\right),$$

$$e_{28} = -e_{26} exp\left(z_2^{(2)}\right) - e_{25}\left[z_1^{(2)} z_2^{(2)}\right]; \tag{7.37}$$

$$e_{31} = \left(y_1^1\right)^2 - \frac{B_{66}^{(1)}}{B_{22}^{(1)}}\left(\beta_m' - \left(\eta_m^{(1)}\right)^2\right), e_{32} = y_1^{(1)} + y_2^{(1)}, e_{33} = e_{31}exp\left(z_1^{(1)}\right),$$

$$e_{34} = e_{32}exp\left(z_2^{(1)}\right) + e_{31}\left[z_1^{(1)}z_2^{(1)}\right], e_{35} = -\left(\left(y_1^2\right)^2 - \frac{B_{66}^{(2)}}{B_{22}^{(2)}}\left(\beta_m' - \left(\eta_m^{(2)}\right)^2\right)\right),$$

$$e_{36} = -\left(y_1^{(2)} + y_2^{(2)}\right), e_{37} = e_{35}exp\left(z_1^{(2)}\right), e_{38} = e_{36}exp\left(z_2^{(2)}\right) + e_{35}\left[z_1^{(2)}z_2^{(2)}\right];$$

$$e_{41} = y_1^{(1)}\frac{B_{12}^{(1)} + B_{66}^{(1)}}{B_{22}^{(1)}}, e_{42} = \frac{B_{12}^{(1)} + B_{66}^{(1)}}{B_{22}^{(1)}}, e_{43} = -e_{41}exp\left(z_1^{(1)}\right),$$

$$e_{44} = -e_{42}exp\left(z_2^{(1)}\right) - e_{41}\left[z_1^{(1)}z_2^{(1)}\right],$$

$$e_{45} = y_1^{(2)}\frac{B_{12}^{(2)} + B_{66}^{(2)}}{B_{22}^{(2)}}, e_{46} = \frac{B_{12}^{(2)} + B_{66}^{(2)}}{B_{22}^{(2)}},$$

$$e_{47} = -e_{45}exp\left(z_1^{(2)}\right), e_{48} = -e_{46}exp\left(z_2^{(2)}\right) - e_{45}\left[z_1^{(2)}z_2^{(2)}\right];$$

$$e_{51} = e_{13}, e_{52} = e_{14}, e_{53} = e_{11}, e_{54} = e_{12}, e_{55} = e_{56} = e_{57} = e_{58} = 0,$$

$$e_{61} = e_{23}, e_{62} = e_{24}, e_{63} = e_{21}, e_{64} = e_{22}, e_{65} = e_{66} = e_{67} = e_{68} = 0,$$

$$e_{71} = e_{72} = e_{73} = e_{74} = 0, e_{75} = e_{17}, e_{76} = e_{18}, e_{77} = e_{15}, e_{78} = e_{16},$$

$$e_{81} = e_{82} = e_{83} = e_{84} = 0, e_{85} = e_{27}, e_{86} = e_{28}, e_{87} = e_{25}, e_{88} = e_{26};$$

$$z_j^{(r)} = -y_j^{(r)}\theta_m s_0^{(r)}, \left[z_1^{(r)}z_2^{(r)}\right] = -\frac{\theta_m s_0^{(r)}\left(exp\left(z_2^{(r)}\right) - exp\left(z_1^{(r)}\right)\right)}{\left(z_2^{(r)} - z_1^{(r)}\right)}, j = 1, 2; r = 1, 2.$$

Equation (7.36) are equivalent to the following

$$Det\left\|e_{ij}\right\|_{i,j=1}^8 = 0, m = \overline{1, \infty}. \tag{7.38}$$

For $\theta_m s_0^{(1)} \to \infty$ and $\theta_m s_0^{(2)} \to \infty$ the set of Eq. (7.38) have the form

$$Det\left\|e_{ij}\right\|_{i,j=1}^8 =$$
$$\left(\frac{B_{66}^{(1)}}{B_{22}^{(1)}}\right)^2 \left(\frac{B_{66}^{(2)}}{B_{22}^{(1)}}\right)^2 \frac{B_{12}^{(1)} + B_{66}^{(1)}}{B_{22}^{(1)}} \frac{B_{12}^{(2)} + B_{66}^{(2)}}{B_{22}^{(2)}} K_2^{(1)}\left(\eta_m^{(1)}\right)K_2^{(2)}\left(\eta_m^{(2)}\right)L\left(\eta_m^{(1)}, \eta_m^{(2)}\right) +$$
$$\sum_{r=1}^2\sum_{j=1}^2 O\left(exp\left(z_j^{(r)}\right)\right) = 0, m = \overline{1, \infty} \tag{7.39}$$
$$L\left(\eta_m^{(1)}, \eta_m^{(2)}\right) = \frac{B_{12}^{(1)} + B_{66}^{(1)}}{B_{11}^{(1)}} \frac{B_{12}^{(2)} + B_{66}^{(2)}}{B_{11}^{(2)}}\left\{\left(\frac{B_{66}^{(1)}}{B_{22}^{(1)}}\right)^2 K_2^{(1)}\left(\eta_m^{(1)}\right)Q^{(2)}\left(\eta_m^{(2)}\right)\right.$$

$$+ \left(\frac{B_{22}^{(2)}}{B_{22}^{(1)}}\right)^2 \left(\frac{B_{66}^{(2)}}{B_{22}^{(1)}}\right)^2 K_2^{(2)}\left(\eta_m^{(2)}\right) Q^{(1)}\left(\eta_m^{(1)}\right)\Bigg\}$$

$$+ \frac{B_{22}^{(2)}}{B_{22}^{(1)}}\left[\left(l_{11}^{(1)}l_{22}^{(2)}+l_{21}^{(1)}l_{12}^{(2)}\right)\left(l_{32}^{(1)}l_{41}^{(2)}+l_{31}^{(1)}l_{42}^{(2)}\right)\right.$$

$$+ \left(l_{11}^{(2)}l_{22}^{(1)}+l_{21}^{(2)}l_{12}^{(1)}\right)\left(l_{32}^{(2)}l_{41}^{(1)}+l_{31}^{(2)}l_{42}^{(1)}\right) - \left(l_{11}^{(1)}l_{21}^{(2)}+l_{11}^{(2)}l_{21}^{(1)}\right)$$

$$\left.\left(l_{32}^{(1)}l_{42}^{(2)}+l_{31}^{(2)}l_{42}^{(1)}\right) - \left(l_{12}^{(1)}l_{22}^{(2)}+l_{12}^{(2)}l_{22}^{(1)}\right)\left(l_{31}^{(1)}l_{41}^{(2)}+l_{31}^{(2)}l_{41}^{(1)}\right)\right], \qquad (7.40)$$

$$K_2^{(r)}\left(\eta_m^{(r)}\right) = \left(\beta_m' - \left(\eta_m^{(r)}\right)^2\right)\left(\frac{B_{11}^{(r)}B_{22}^{(r)}\beta_m'' - \left(B_{12}^{(r)}\right)^2 \beta_m'}{B_{11}^{(r)}B_{66}^{(r)}} - \left(\eta_m^r\right)^2\right) - \left(\eta_m^r\right)^2 y_1^{(r)}y_2^{(r)},$$

$$Q^{(r)}\left(\eta_m^{(r)}\right) = y_1^{(r)}y_2^{(r)} + \frac{B_{66}^{(r)}}{B_{22}^{(r)}}\left(\beta_m' - \left(\eta_m^{(r)}\right)^2\right)$$

$$\frac{l_{11}^{(r)}}{=} \frac{B_{66}^{(r)}}{B_{22}^{(r)}}\left(\left(y_j^{(r)}\right)^2 + \frac{B_{12}^{(r)}}{B_{22}^{(r)}}\left(\beta_m' - \left(\eta_m^{(r)}\right)^2\right)\right), \quad \frac{l_{12}^{(r)}}{=} \frac{B_{66}^{(r)}}{B_{22}^{(r)}}\left(y_1^{(r)} + y_2^{(r)}\right),$$

$$\frac{l_{21}^{(r)}}{=} \frac{B_{66}^{(r)}}{B_{22}^{(r)}}y_1^{(r)}\left(\left(y_1^{(r)}\right)^2 + \frac{B_{12}^{(r)}}{B_{22}^{(r)}}\beta_m' + \frac{B_{66}^{(r)}}{B_{22}^{(r)}}\left(\eta_m^{(r)}\right)^2\right),$$

$$l_{22}^{(r)} = \frac{B_{66}^{(r)}}{B_{22}^{(r)}}\left(y_1^{(r)}y_2^{(r)} + B^{(r)} - \left(\eta_m^{(r)}\right)^2\right)$$

$$l_{31}^{(r)} = \left(y_1^r\right)^2 - \frac{B_{66}^{(r)}}{B_{22}^{(r)}}\left(\beta_m' - \left(\eta_m^{(r)}\right)^2\right), \quad l_{32}^{(r)} = y_1^{(r)} + y_2^{(r)},$$

$$l_{41}^{(r)} = y_1^{(r)}\frac{B_{12}^{(r)} + B_{66}^{(r)}}{B_{22}^{(r)}}, \quad l_{42}^{(r)} = \frac{B_{12}^{(r)} + B_{66}^{(r)}}{B_{22}^{(r)}}; r = 1, 2.$$

It follows from (7.39) that for $\theta_m s_0^{(1)} \to \infty$ and $\theta_m s_0^{(2)} \to \infty$ the set of equations from (7.38) splits into sets of equations

$$K_2^{(1)}\left(\eta_m^{(1)}\right) = 0, m = \overline{1, \infty}; \; K_2^{(2)}\left(\eta_m^2\right) = 0, m = \overline{1, \infty};$$
$$L\left(\eta_m^{(1)}, \eta_m^{(2)}\right) = 0, m = \overline{1, \infty}. \qquad (7.41)$$

The first and second sets of equations from (7.41) are analogs of the Rayleigh equation, which determine the frequencies of the edge oscillations of the generators $\beta = s_0^{(1)}, -s_0^{(2)}$ and the third set of equations from (7.41) is an analog of Stoneley's dispersion relations, which determines the frequencies of the interface planar vibrations at the interface line of material properties $\beta = 0$.

4. **Bending vibrations of composite rectangular plate with free edges**. Existence of free bending interface and edge vibrations of a rectangular plate composed of

thin elastic orthotropic rectangular plates with different elastic properties is investigated. We introduce rectilinear orthogonal coordinates $(\alpha, \beta)$ on the middle plane of a rectangular plate, where, $0 \leq \alpha \leq l$, $-s_0^{(2)} \leq \beta \leq s_0^{(1)}$. The straight line $\beta = 0$ corresponds to the interface of material properties. All values related to the right plate $0 \leq \beta \leq s_0^{(1)}$ are indicated by the superscript (1), and to the left plate $-s_0^{(2)} \leq \beta \leq 0$ by (2), respectively. As the initial equations, the equations of small bending vibrations of the left and right plates are used, which correspond to the classical theory of orthotropic plates [19].

$$\mu^4 \left( B_{11}^{(r)} \frac{\partial^4 u_3^{(r)}}{\partial \alpha^4} + 2\left( B_{12}^{(r)} + 2B_{66}^{(r)} \right) \frac{\partial^4 u_3^{(r)}}{\partial \alpha^2 \partial \beta^2} + B_{22}^{(r)} \frac{\partial^4 u_3^{(r)}}{\partial \beta^4} \right)$$
$$= \rho^{(r)} \omega^2 u_3^{(r)}, r = 1, 2. \tag{7.42}$$

Here $u_3^{(r)}, r = 1, 2$ are the normal components of the displacement vector of the right and left plates; $B_{ij}^{(r)}, r = 1, 2$—elasticity coefficients; $\omega$–angular frequency; $\rho^{(r)}, r = 1, 2$—the density of materials; $\mu^4 = h^2/12$ ($h$–plate thickness). The following boundary conditions are considered.

$$M_2^{(1)} \Big|_{\beta=0} = M_2^{(2)} \Big|_{\beta=0}, \ N_2^{(1)} + \frac{\partial H^{(1)}}{\partial \alpha} \Big|_{\beta=0} = N_2^{(2)} + \frac{\partial H^{(2)}}{\partial \alpha} \Big|_{\beta=0},$$
$$u_3^{(1)} \Big|_{\beta=0} = u_3^{(2)} \Big|_{\beta=0}, \ \frac{\partial u_3^{(1)}}{\partial \beta} \Big|_{\beta=0} = \frac{\partial u_3^{(2)}}{\partial \beta} \Big|_{\beta=0}; \tag{7.43}$$

$$N_2^{(r)} + \frac{\partial H^{(r)}}{\partial \alpha} \Big|_{\beta=(-1)^{r-1}s^{(r)}} = 0, \ M_2^{(r)} \Big|_{\beta=(-1)^{r-1}s^{(r)}} = 0, r = 1, 2. \tag{7.44}$$

$$N_1^{(r)} + \frac{\partial H^{(r)}}{\partial \beta} \Big|_{\alpha=0,l} = 0, \ M_1^{(r)} \Big|_{\alpha=0,l} = 0, r = 1, 2. \tag{7.45}$$

$$M_1^{(r)} = \frac{h^3}{12} B_{11}^{(r)} \left[ \frac{\partial^2 u_3^{(r)}}{\partial \alpha^2} + \frac{B_{12}^{(r)}}{B_{11}^{(r)}} \frac{\partial^2 u_3^{(r)}}{\partial \beta^2} \right], M_2^{(r)} = \frac{h^3}{12} B_{22}^{(r)} \left[ \frac{B_{12}^{(r)}}{B_{22}^{(r)}} \frac{\partial^2 u_3^{(r)}}{\partial \alpha^2} + \frac{\partial^2 u_3^{(r)}}{\partial \beta^2} \right],$$

$$N_1^{(r)} + \frac{\partial H^{(r)}}{\partial \beta} = \frac{h^3}{12} B_{11}^{(r)} \left[ \frac{\partial^3 u_3^{(r)}}{\partial \alpha^3} + \frac{B_{12}^{(r)} + 4B_{66}^{(r)}}{B_{11}^{(r)}} \frac{\partial^3 u_3^{(r)}}{\partial \beta^2 \partial \alpha} \right],$$

$$N_2^{(r)} + \frac{\partial H^{(r)}}{\partial \alpha} = \frac{h^3}{12} B_{22}^{(r)} \left[ \frac{\partial^3 u_3^{(r)}}{\partial \beta^3} + \frac{B_{12}^{(r)} + 4B_{66}^{(r)}}{B_{22}^{(r)}} \frac{\partial^3 u_3^{(r)}}{\partial \alpha^2 \partial \beta} \right], r = 1, 2. \tag{7.46}$$

Here relations (7.43) are complete contact conditions at $\beta = 0$. Relations (7.44) and (7.45) are the conditions of free edges at $\beta = s_0^{(1)}, -s_0^{(2)}$ and $\alpha = 0, l$, where $l$ is the length of the plate, respectively (Fig. 7.2.) Problem (7.42)−(7.45) does not

allow separation of variables. The differential operator corresponding to problem (7.42)−(7.45) is self-conjugate and nonnegative definite. Therefore, the generalized Kantorovich-Vlasov method of reduction to ordinary differential equations can be used to find vibration eigenfrequencies and eigenmodes [25]. The solution of system (7.42) is sought in the form

$$
u_3^{(r)} = w_m(\theta_m \alpha) \exp\left((-1)^r y^{(r)} \theta_m \beta + y^{(r)} \theta_m s_0^{(r)}\right),
$$
$$
r = 1, 2; m = \overline{1, \infty}. \tag{7.47}
$$

Here $w_m(\theta_m \alpha)$ defined in (7.7), $y^{(r)}, r = 1, 2$ are undetermined coefficients. In this case, conditions (7.45) are satisfied automatically. We substitute (7.47) into (7.42). As a result, we obtain the characteristic equations

$$
R_{mm}^{(r)} = a^2 \left( \left(y^{(r)}\right)^4 - \frac{2\left(B_{12}^{(r)} + 2B_{66}^{(r)}\right)}{B_{22}^{(r)}} \beta_m'\left(y^{(r)}\right)^2 + \frac{B_{11}^{(r)}}{B_{22}^{(r)}} \beta_m' \beta_m'' \right)
$$
$$
- \frac{B_{66}^{(r)}}{B_{22}^{(r)}} \left(\eta_m^{(r)}\right)^2 = 0, \quad r = 1, 2; m = \overline{1, \infty}, \tag{7.48}
$$

where $a^2, \eta_m^{(r)}, \beta_m', \beta_m''$ are defined in (7.15), (7.9).

Let $y_3^{(r)}, y_4^{(r)}$ be the different roots of Eq. (7.48) with positive real parts and $y_{j+2}^{(r)} = -y_j^{(r)} j = 3, 4$. We seek solutions to problem (7.42)−(7.45) in the form

$$
u_3^{(r)} = \sum_{j=1}^{4} w_m(\theta_m \alpha) \exp\left((-1)^r y_j^{(r)} \theta_m \beta + y_j^{(r)} \theta_m s_0^{(r)}\right) w_j^{(r)},
$$
$$
r = 1, 2; m = \overline{1, \infty}. \tag{7.49}
$$

We substitute (7.49) into the boundary conditions (7.43)−(7.44). As a result, we arrive at the system of equations

$$
\sum_{3}^{6} P_{1j}^{(1)} \exp\left(y_j^{(1)} \theta_m s_0^{(1)}\right) w_j^{(1)} - c \sum_{3}^{6} P_{1j}^{(2)} \exp\left(y_j^{(2)} \theta_m s_0^{(2)}\right) w_j^{(2)} = 0,
$$

$$
\sum_{3}^{6} P_{2j}^{(1)} \exp\left(y_j^{(1)} \theta_m s_0^{(1)}\right) w_j^{(1)} + c \sum_{3}^{6} P_{2j}^{(2)} \exp\left(y_j^{(2)} \theta_m s_0^{(2)}\right) w_j^{(2)} = 0,
$$

$$
\sum_{3}^{6} \exp\left(y_j^{(1)} \theta_m s_0^{(1)}\right) w_j^{(1)} - \sum_{3}^{6} R_{3j}^{(2)} \exp\left(y_j^{(2)} \theta_m s_0^{(2)}\right) w_j^{(2)} = 0, \tag{7.50}
$$

$$\sum_{3}^{6} y_j^{(1)} \exp\left(y_j^{(1)} \theta_m s_0^{(1)}\right) w_j^{(1)} + \sum_{3}^{6} y_j^{(2)} \exp\left(y_j^{(2)} \theta_m s_0^{(2)}\right) w_j^{(2)} = 0,$$

$$\sum_{3}^{6} P_{1j}^{(r)} w_j^{(r)} = 0, \sum_{3}^{6} P_{2j}^{(r)} w_j^{(r)} = 0, r = 1, 2.$$

$$P_{1j}^{(r)} = \left(y_j^{(r)}\right)^2 - \frac{B_{12}^{(r)}}{B_{22}^{(r)}} \beta_m', P_{2j}^{(r)} = \left(y_j^{(r)}\right)^3 - \frac{B_{12}^{(r)} + 4B_{66}^{(r)}}{B_{22}^{(r)}} \beta_m' y_j^{(r)},$$

$$c = \frac{B_{22}^{(2)}}{B_{22}^{(1)}}, r = 1, 2; j = \overline{3, 6}. \tag{7.51}$$

Equating the determinant of system (7.50) to zero and performing elementary operations on the columns of the determinant, we obtain the dispersion equations

$$\Delta_p = \left(y_4^{(1)} - y_3^{(1)}\right)^2 \left(y_4^{(2)} - y_3^{(2)}\right)^2 \exp\left(\theta_m \sum_{r=1}^{2} s_0^{(r)} \left(y_3^{(r)} + y_4^{(r)}\right)\right)$$

$$Det \left\|b_{ij}\right\|_{i,j=1}^{8} = 0, m = \overline{1, \infty}. \tag{7.52}$$

$$b_{11} = \left(y_3^{(1)}\right)^2 - \frac{B_{12}^{(1)}}{B_{22}^{(1)}} \beta_m', b_{12} = y_3^{(1)} + y_4^{(1)}$$

$$b_{13} = b_{11} \exp\left(z_3^{(1)}\right), b_{14} = b_{12} \exp\left(z_4^{(1)}\right) + b_{11}\left[z_3^{(1)} z_4^{(1)}\right],$$

$$b_{15} = -c\left(\left(y_j^{(2)}\right)^2 - \frac{B_{12}^{(2)}}{B_{22}^{(2)}} \beta_m'\right), b_{16} = -c\left(y_3^{(2)} + y_4^{(2)}\right),$$

$$b_{17} = b_{15} \exp\left(z_3^{(2)}\right), b_{18} = b_{16} \exp\left(z_4^{(2)}\right) + b_{15}\left[z_3^{(2)} z_4^{(2)}\right];$$

$$b_{21} = \left(y_3^{(1)}\right)^3 - \frac{B_{12}^{(1)} + 4B_{66}^{(1)}}{B_{22}^{(1)}} \beta_m' y_3^{(1)}, b_{22} = y_3^{(1)} y_4^{(1)} + \frac{B_{12}^{(1)}}{B_{22}^{(1)}} \beta_m',$$

$$b_{23} = -b_{21} \exp\left(z_3^{(1)}\right), b_{24} = -b_{22} \exp\left(z_4^{(1)}\right) - b_{21}\left[z_3^{(1)} z_4^{(1)}\right],$$

$$b_{25} = c\left(\left(y_3^{(2)}\right)^3 - \frac{B_{12}^{(2)} + 4B_{66}^{(2)}}{B_{22}^{(2)}} \beta_m' y_3^2\right),$$

$$b_{26} = c\left(y_3^{(2)} y_4^{(2)} + \frac{B_{12}^{(2)}}{B_{22}^{(2)}} \beta_m'\right), b_{27} = -b_{25} \exp\left(z_3^{(2)}\right),$$

$$b_{28} = -b_{26} \exp\left(z_4^{(2)}\right) - b_{25}\left[z_3^{(2)} z_4^{(2)}\right]; \tag{7.53}$$

$$b_{31} = 1, b_{32} = 0, , b_{33} = \exp\left(z_3^{(1)}\right), b_{34} = \left[z_3^{(1)} z_4^{(1)}\right],$$

$$b_{35} = -1, b_{36} = 0, b_{37} = -exp\left(z_3^{(2)}\right), b_{38} = -\left[z_3^{(2)} z_4^{(2)}\right];$$

$$b_{41} = y_3^{(1)}, b_{42} = 1, b_{43} = -y_3^{(1)} exp\left(z_3^{(1)}\right), b_{44} = -exp\left(z_4^{(1)}\right) - y_3^{(1)}\left[z_3^{(1)} z_4^{(1)}\right],$$

$$b_{45} = y_3^{(2)}, b_{46} = 1, b_{47} = -y_3^{(2)} exp\left(z_3^{(2)}\right), b_{48} = -b_{46} exp\left(z_4^{(2)}\right) - b_{45}\left[z_3^{(2)} z_4^{(2)}\right];$$

$$b_{51} = b_{13}, b_{52} = b_{14}, b_{53} = b_{11}, b_{54} = b_{12}, b_{55} = b_{56} = b_{57} = b_{58} = 0,$$
$$b_{61} = b_{23}, b_{62} = b_{24}, b_{63} = b_{21}, b_{64} = b_{22}, b_{65} = b_{66} = b_{67} = b_{68} = 0,$$
$$b_{71} = b_{72} = b_{73} = b_{74} = 0, b_{75} = b_{17}, b_{76} = b_{18}, b_{77} = b_{15}, b_{78} = b_{16},$$
$$b_{81} = b_{82} = b_{83} = b_{84} = 0, b_{85} = b_{27}, b_{86} = b_{28}, b_{87} = b_{25}, b_{88} = b_{26};$$

$$z_j^{(r)} = -y_j^{(r)} \theta_m s_0^{(r)}, \left[z_3^{(r)} z_4^{(r)}\right] = -\frac{\theta_m s_0^{(r)}\left(exp\left(z_4^{(r)}\right) - exp\left(z_3^{(r)}\right)\right)}{\left(z_4^{(r)} - z_3^{(r)}\right)},$$

$$j = 3, 4; r = 1, 2 :$$

Equation (7.52) are equivalent to the equations

$$Det \left\|b_{ij}\right\|_{i,j=1}^{8} = 0, m = \overline{1, \infty}. \tag{7.54}$$

For $\theta_m s_0^{(1)} \to \infty$ and $\theta_m s_0^{(2)} \to \infty$ the set of Eq. (7.54) have the form

$$Det \left\|b_{ij}\right\|_{i,j=1}^{8} = -\left(\frac{B_{22}^{(2)}}{B_{22}^{(1)}}\right)^2 G\left(\eta_m^{(1)}, \eta_m^{(2)}\right) K_1^{(1)}\left(\eta_m^{(1)}\right) K_1^{(2)}\left(\eta_m^{(2)}\right)$$

$$+ \sum_{r=1}^{2} \sum_{j=3}^{4} O\left(exp\left(z_j^{(r)}\right)\right) = 0, m = \overline{1, \infty}. \tag{7.55}$$

$$G\left(\eta_m^{(1)}, \eta_m^{(2)}\right) = -K_1^{(1)}\left(\eta_m^{(1)}\right) - c^2 K_1^{(2)}\left(\eta_m^{(2)}\right) + c\left[\left(b_{11}^{(1)} b_{22}^{(2)} + b_{22}^{(1)} b_{11}^{(2)}\right)\right.$$
$$\left. + \left(l_{21}^{(1)} l_{12}^{(2)} + l_{12}^{(1)} l_{21}^{(2)}\right) - \left(y_3^{(1)} + y_3^{(2)}\right)\left(b_{12}^{(1)} b_{22}^{(2)} + b_{22}^{(1)} b_{12}^{(2)}\right)\right], m = \overline{1, \infty} \tag{7.56}$$

$$K_1^{(r)}\left(\eta_m^{(r)}\right) = \left(y_3^{(r)} y_4^{(r)}\right)^2 + \frac{4 B_{66}^{(r)}}{B_{22}^{(r)}} \beta_m' y_3^{(r)} y_4^{(r)} - \left(\frac{B_{12}^{(r)}}{B_{22}^{(r)}}\right)^2 \left(\beta_m'\right)^2, r = 1, 2;$$

$$b_{11}^{(r)} = \left(y_3^{(r)}\right)^2 - \frac{B_{12}^{(r)}}{B_{22}^{(r)}} \beta_m', b_{12}^{(r)} = y_3^{(r)} + y_4^{(r)}, b_{21}^{(r)} = \left(y_3^{(r)}\right)^3 -$$

$$\frac{B_{12}^{(r)} + 4 B_{66}^{(r)}}{B_{22}^{(r)}} \beta_m' y_3^{(r)}, b_{22}^{(r)} = y_3^{(r)} y_4^{(r)} + \frac{B_{12}^{(r)}}{B_{22}^{(r)}} \beta_m';$$

It follows from (7.55) that, for $\theta_m s_0^{(1)} \to \infty$ and $\theta_m s_0^{(2)} \to \infty$, Eq. (7.54) splits into sets of equations

$$G\left(\eta_m^{(1)}, \eta_m^{(2)}\right) = 0, m = \overline{1, \infty}; \ K_1^{(1)}\left(\eta_m^{(1)}\right) = 0, m = \overline{1, \infty};$$

$$K_1^{(2)}\left(\eta_m^2\right) = 0, m = \overline{1, \infty}. \tag{7.57}$$

The first set of equations from (7.57) is a set of dispersion equations of the bending type of the interface vibration of a plate composed of two orthotropic sufficiently wide plates with different elastic properties when the edges are free. The second and third sets of equations from (7.57) are analogs of the Konenkov type equations for the bending vibration of a plate made of the material of the right and left plates, respectively, with free edges [8].

## 5. Asymptotics of dispersion Eq. (7.23) for $\varepsilon_m \to 0$

Using the formulae from Sect. 7.2, we assume that $\eta_1^{(r)} = \eta_2^{(r)} = \eta_3^{(r)} = \eta^{(r)}$, $(r = 1, 2)$. Then, when $\varepsilon_m \to 0$ Eq. (7.14) is transformed into a set of equations

$$c_m^{(r)} = \frac{B_{22}^{(r)}}{B_{11}^{(r)}}\left(\chi^{(r)}\right)^4 - B_2^{(r)}\left(\chi^{(r)}\right)^2 + \frac{B_{22}^{(r)} + B_{66}^{(r)}}{B_{11}^{(r)}}\left(\eta_m^{(r)}\right)^2\left(\chi^{(r)}\right)^2$$

$$+ \left(\beta_m' - \left(\eta_{2m}^{(r)}\right)^2\right)\left(\beta_m'' - \frac{B_{66}^{(r)}}{B_{11}^{(r)}}\left(\eta_{1m}^{(r)}\right)^2\right) r = 1, 2, m = \overline{1, \infty} \tag{7.58}$$

$$R_{mm}^{(r)} = a^2\left(\left(\chi^{(r)}\right)^4 - \frac{2\left(B_{12}^{(r)} + 2B_{66}^{(r)}\right)}{B_{22}^{(r)}}\beta_m'\left(\chi^{(r)}\right)^2 + \frac{B_{11}^{(r)}}{B_{22}^{(r)}}\beta_m'\beta_m''\right) -$$

$$\frac{B_{66}^{(r)}}{B_{22}^{(r)}}\left(\eta_{3m}^{(r)}\right)^2 = 0, r = 1, 2, \ m = \overline{1, \infty} \tag{7.59}$$

which are sets of characteristic equations for the equations of planar and bending vibrations of the left and right rectangular components with two opposite free edges, respectively [10]. The roots of Eqs. (7.58) and (7.59) with positive real parts are denoted by $y_1^{(r)}, y_2^{(r)}$ and $y_3^{(r)}, y_4^{(r)}$ respectively.

In the same way as in [27], it may be proved that under the condition

$$\varepsilon_m \ll 1, y_1^{(r)}, y_j^{(r)} \neq y_i^{(r)}, \quad i \neq j, \tag{7.60}$$

the roots $\left(\chi^{(r)}\right)^2$ of Eq. (7.14) can be represented as

$$\left(\chi_j^{(r)}\right)^2 = \left(y_j^{(r)}\right)^2 + \alpha_{jm}^{(r)}\varepsilon_m^2 + \beta_{jm}^{(r)}\varepsilon_m^4 + \cdots, j = \overline{1, 4}. \tag{7.61}$$

Under conditions (7.60), taking into account relations (7.18), (7.61) and the fact that

$$M_{3j}^{(r)} = M_{4j}^{(r)} = M_{7j}^{(r)} = M_{8j}^{(r)} = O(\varepsilon_m^2),\ j = 1, 2;\ r = 1, 2, \tag{7.62}$$

the set of Eq. (7.23) is reduced to the form

$$Det\,\|t_{ij}\|_{i,j=1}^4 = \left(N^{(1)}\!\left(\eta_m^{(1)}\right) N^{(2)}\!\left(\eta_m^{(2)}\right)\right)^2 \left(K_3^{(1)}\!\left(\eta_m^{(1)}\right) K_3^{(2)}\!\left(\eta_m^{(2)}\right)\right)^2 X$$

$$Det\,\|e_{ij}\|_{i,j=1}^8 \cdot Det\,\|b_{ij}\|_{i,j=1}^8 + O(\varepsilon_m^2) = 0, \quad m = \overline{1,\infty}, \tag{7.63}$$

$$N^{(r)}\!\left(\eta_m^{(r)}\right) = \left(y_1^{(r)} + y_3^{(r)}\right)\!\left(y_1^{(r)} + y_4^{(r)}\right)\!\left(y_2^{(r)} + y_3^{(r)}\right)\!\left(y_2^{(r)} + y_3^{(r)}\right),$$

$$K_3^{(r)}\!\left(\eta_m^{(r)}\right) = \left(\left(\beta_m' - \left(\eta_m^{(r)}\right)^2\right)\!\left(\frac{B_{11}^{(r)}}{B_{22}^{(r)}}\beta_m'' - \frac{B_{66}^{(r)}}{B_{22}^{(r)}}\left(\eta_m^{(r)}\right)^2\right)\!\left(p^{(r)}\right)^2\right.$$

$$+ \left(\frac{B_{11}^{(r)}}{B_{22}^{(r)}}B_2^{(r)} - \frac{B_{22}^{(r)} + B_{66}^{(r)}}{B_{22}^{(r)}}\left(\eta_m^{(r)}\right)^2\right)p^{(r)}q^{(r)} + \left(p^{(r)}\right)^2\right)$$

$$\left(\frac{B_{22}^{(r)}}{B_{22}^{(r)} + B_{66}^{(r)}}\right)^2\!\left(\frac{1}{\beta_m'}\right)^2,$$

$$p^{(r)} = \frac{B_{22}^{(r)}}{B_{11}^{(r)}} + a^2\left(\frac{B_{66}^{(r)}}{B_{11}^{(r)}}\left(\eta_m^{(r)}\right)^2 + \frac{\left(B_{12}^{(r)}\right)^2 + 3B_{12}^{(r)}B_{66}^{(r)} + 4\left(B_{66}^{(r)}\right)^2}{B_{11}^{(r)}B_{66}^{(r)}}\beta_m'\right), \quad (7.64)$$

$$q^{(r)} = \frac{B_{22}^{(r)}}{B_{11}^{(r)}}\left(\eta_m^{(r)}\right)^2 - B_1^{(r)} + a^2\left(\frac{B_{66}^{(r)}}{B_{11}^{(r)}}\left(\eta_m^{(r)}\right)^2 - \beta_m''\right)\!\left(\left(\eta_m^{(r)}\right)^2 + \frac{B_{12}^{(r)} + 3B_{66}^{(r)}}{B_{66}^{(r)}}\beta_m'\right),$$

and determinants $Det\,\|e_{ij}\|_{i,j=1}^8 \cdot Det\,\|b_{ij}\|_{i,j=1}^8$ are defined in (7.38) and (7.54), respectively.

It follows from Eq. (7.63) that, when $\varepsilon_m \to 0$ the set of Eq. (7.23) splits into sets of equations

$$Det\,\|e_{ij}\|_{i,j=1}^8 = 0,\, m = \overline{1,\infty};\ Det\,\|b_{ij}\|_{i,j=1}^8 = 0,$$

$$m = \overline{1,\infty};\ K_3^{(r)}\!\left(\eta_m^{(r)}\right) = 0,\, r = 1, 2;\, m = \overline{1,\infty}. \tag{7.65}$$

The first and second sets of equations from (7.65) are the dispersion equations of planar and bending interface and edge vibrations of a composite plate, respectively. The roots of the third and fourth set of equations correspond to planar vibrations of the components of the cylindrical panel. They appear as a result of using the equation of the corresponding classical theory of orthotropic cylindrical shells.

For $\varepsilon_m \to 0$, $\theta_m s_0^{(1)} \to \infty$ and $\theta_m s_0^{(2)} \to \infty$, relations (7.23) take the form

$$Det \left\| t_{ij} \right\|_{i,j=1}^4 = \left( \frac{B_{66}^{(1)}}{B_{22}^{(1)}} \right)^2 \left( \frac{B_{66}^{(2)}}{B_{22}^{(2)}} \right)^2 \left( \frac{B_{22}^{(2)}}{B_{22}^{(1)}} \right)^2 \frac{B_{12}^{(1)} + B_{66}^{(1)}}{B_{22}^{(2)}} \frac{B_{12}^{(2)} + B_{66}^{(2)}}{B_{22}^{(2)}} X$$

$$\left( N^{(1)}\left( \eta_m^{(1)} \right) N^{(2)}\left( \eta_m^{(2)} \right) \right)^2 \left( K_3^{(1)}\left( \eta_m^{(1)} \right) K_3^{(2)}\left( \eta_m^{(2)} \right) \right)^2 K_1^{(1)}\left( \eta_m^{(1)} \right) K_2^{(1)}\left( \eta_m^{(1)} \right) X$$

$$K_1^{(2)}\left( \eta_m^{(2)} \right) K_2^{(2)}\left( \eta_m^{(2)} \right) L\left( \eta_m^{(1)}, \eta_m^{(2)} \right) G\left( \eta_m^{(1)}, \eta_m^{(2)} \right) + O\left( \varepsilon_m^2 \right)$$

$$+ \sum_{r=1}^2 \sum_{j=1}^4 O\left( exp\left( z_j^{(r)} \right) \right) = 0, m = \overline{1, \infty} \tag{7.66}$$

From (7.66) it follows that for, $\varepsilon_m \to 0, \theta_m s_0^{(1)} \to \infty$ and $\theta_m s_0^{(2)} \to \infty$ the set of Eqs. (7.23) splits into the totality of the equations

$$L\left( \eta_m^{(1)}, \eta_m^{(2)} \right) = 0, m = \overline{1, \infty}; \ G\left( \eta_m^{(1)}, \eta_m^{(2)} \right) = 0, m = \overline{1, \infty};$$

$$K_2^{(r)}\left( \eta_m^{(r)} \right) = 0, m = \overline{1, \infty}; \ K_1^{(r)}\left( \eta_m^{(r)} \right) = 0, m = \overline{1, \infty};$$

$$K_3^{(r)}\left( \eta_m^{(r)} \right) = 0, m = \overline{1, \infty}; r = 1, 2. \tag{7.67}$$

The first and second sets of equations from (7.67) are, respectively, the dispersion equations of the planar and bending interface vibrations for a sufficiently wide composite plate with free edges.

The third and fourth sets of equations from (7.67) are, respectively, analogs to the Rayleigh and Konenkov equations for vibrations of a plate made of material (1) and (2) localized at the free edges.

6.  **Numerical investigation.** Tables 7.1 and 7.2 shows some of the roots of Eqs. (7.41), (7.57) and the dispersion Eqs. (7.38) and (7.54) of planar and bending vibrations for a composite rectangular plate, with free edges, made of boroplastic and special paper with mechanical parameters [19, 30]

$$\underline{Boroplastic} \ \rho^{(1)} = 2.10^3 \frac{kg}{m^3}, E_1^{(1)} = 2.646.10^{11} \frac{N}{m^2}, E_2^{(1)} = 1.323.10^{10} \frac{N}{m^2},$$

$$G^{(1)} = 9.604.10^9 \frac{N}{m^2}, \gamma_1^{(1)} = 0.2, \gamma_2^{(1)} = 0.01; \tag{7.68}$$

$$\underline{Paper} \ \rho^{(2)} = 0.16 \frac{kg}{m^3}, E_1^{(2)} = 2.95281.10^9 \frac{N}{m^2}, E_2^{(2)} = 2.210.10^9 \frac{N}{m^2},$$

$$G^{(2)} = 9.77076.10^8 \frac{N}{m^2}, \gamma_1^{(2)} = \frac{\gamma_2^{(2)} E_1^{(2)}}{E_2^{(2)}}, \gamma_2^{(2)} = 0.23 \tag{7.69}$$

**Table 7.1** Characteristics of the natural frequencies for planar vibrations of a rectangular plate

| N | $\theta_m$ | $K_2^{(1)}\left(\eta_m^{(1)}\right) = 0, L\left(\eta_m^{(1)}, \eta_m^{(2)}\right) = 0$ $K_2^{(2)}\left(\eta_m^{(2)}\right) = 0$ | $Det\,\|e_{ij}\|_{i,j=1}^8 = 0$ |
|---|---|---|---|
| 1 | 1.95473 | | 0.91143 $e^{(1)}$<br>0.92511 $^{ine}$<br>27.5679 $e^{(2)}$ |
| 2 | 2.74891 | 0.98307<br>0.98398<br>32.9634 | 0.98171 $e^{(1)}$<br>0.98311 $^{ine}$<br>30.7910 $e^{(2)}$ |
| 3 | 3.52957 | 1.00099<br>1.00225<br>33.3045 | 0.99965 $e^{(1)}$<br>1.00100 $^{ine}$<br>30.6812 $e^{(2)}$ |
| 4 | 4.27693 | 0.97897<br>0.98012<br>32.6340 | 0.977771 $e^{(1)}$<br>0.997897$^{ine}$<br>30.1650 $e^{(2)}$ |
| 11 | 11.6577 | 0.98580<br>0.98696<br>32.8645 | 0.98436 $e^{(1)}$<br>0.98580 $^{ine}$<br>30.3826 $e^{(2)}$ |
| 15 | 16.0962 | 0.98580<br>0.98696<br>32.8645 | 0.98436 $e^{(1)}$<br>0.98580 $^{ine}$<br>30.3826 $e^{(2)}$ |
| 16 | 17.1935 | 0.98580<br>0.98696<br>32.8645 | 0.98436 $e^{(1)}$<br>0.98580 $^{ine}$<br>30.3826 $e^{(2)}$ |

and geometric parameters: $l = 4, h = \frac{1}{50}, s_0^{(1)} = 15, s_0^{(2)} = 5$. The roots of the dispersion Eqs. (7.41) and (7.57) of planar and bending edge and interface vibrations of a rectangular plate are given.

Note that the connection between $\eta_m^{(1)}$ and $\eta_m^{(2)}$ has the form

$$\eta_m^{(2)} = \frac{\rho^{(2)} B_{66}^{(1)}}{\rho^{(1)} B_{66}^{(2)}} \tag{7.70}$$

Tables 7.3 and 7.4 shows dimensionless characteristics $\eta_{1m}^{(1)}$ of the natural frequencies of interface and edge vibrations for a composite cylindrical panel, made of boroplastic and special paper, with mechanical parameters (7.68), (7.69) and geometric parameters:

$$R = 45, l = 4, h = 1/50, s^{(1)} = 15.2927, s^{(2)} = 5.01035.$$

**Table 7.2** Characteristics of the natural frequencies for bending vibrations of a rectangular plate

| N | $\theta_m$ | $K_1^{(1)}\left(\eta_m^{(1)}\right) = 0,\ G\left(\eta_m^{(1)}, \eta_m^{(2)}\right) = 0$ $K_1^{(2)}\left(\eta_m^{(2)}\right) = 0$ | $Det\,\|b_{ij}\|_{i,j=1}^8 = 0$ |
|---|---|---|---|
| 1 | 1.95473 | 0.04872 0.04874 0.59552 | 0.04872 $b^{(1)}$ 0.04926 $^{inb}$ 0.31068 $b^{(2)}$ |
| 2 | 2.74891 | 0.08576 0.08580 1.04836 | 0.08580 $b^{(1)}$ 0.08638 $^{inb}$ 0.82623 $b^{(2)}$ |
| 3 | 3.52957 | 0.10921 0.10927 1.33494 | 0.10921 $b^{(1)}$ 0.10949 $^{inb}$ 1.11285 $b^{(2)}$ |
| 4 | 4.27693 | 0.12789 0.12795 1.56329 | 0.12789 $b^{(1)}$ 0.12830 $^{inb}$ 1.31165 $b^{(2)}$ |
| 11 | 11.6577 | 0.35363 0.35382 4.32282 | 0.35363 $b^{(1)}$ 0.35410 $^{inb}$ 4.11623 $b^{(2)}$ |
| 15 | 16.0962 | 0.48828 0.488531 5.96867 | 0.48828 $b^{(1)}$ 0.49196 $^{inb}$ 5.80026 $b^{(2)}$ |
| 16 | 17.1935 | 0.52156 0.52183 6.37556 | 0.52156 $b^{(1)}$ 0.52389 $^{inb}$ 6.00390 $b^{(2)}$ |

In Tables 7.1, 7.2, 7.3 and 7.4 after the characteristics of the natural frequencies, the type of interface vibrations is indicated: *ine* is predominantly planar, *inb* is predominantly bending; edge vibrations are: $e^{(r)}$, $r = 1,2-$predominantly planar types, $b^{(r)}$, $r = 1,2-$predominantly bending types, $n^{(r)}$, $r = 1,2-$new types of vibrations corresponding to materials (1) and (2), respectively. Note that the new types of vibrations are predominantly planar types. The latest manifests itself as a result of using the basic equations corresponding to the classical theory of orthotropic cylindrical shells.

In Table 7.3 the case $\eta_{1m}^{(r)} = \eta_{2m}^{(r)} = \eta_m^{(r)}, \eta_{3m}^{(r)} = 0, r = 1, 2$ corresponds to problem (7.1)−(7.4), in which there is no normal component of the inertia force, i.e. we have a predominantly planar type of interface and edge vibrations. Similarly, the case $\eta_{1m}^{(r)} = \eta_{2m}^{(r)} = 0, \eta_{3m}^{(r)} = \eta_m^{(r)}, r = 1, 2$ corresponds predominantly to bending type.

In Table 7.4, the case $\eta_{1m}^{(r)} = \eta_{2m}^{(r)} = \eta_{3m}^{(r)} = \eta_m^{(r)}$ corresponds to the problem (7.1)−(7.4).

**Table 7.3** Characteristics of the natural frequencies for predominantly planar and predominantly bending vibrations of cylindrical panel

| N | $\theta_m$ | $K_3^{(1)}\left(\eta_m^{(1)}\right) = 0$ <br> $K_3^{(2)}\left(\eta_m^{(2)}\right) = 0$ | $\eta_{1m}^{(r)} = \eta_{2m}^{(r)} = \eta_m^{(r)}$ <br> $\eta_{3m}^{(r)} = 0, r = 1, 2$ | $\eta_{1m}^{(r)} = \eta_{2m}^{(r)} = 0$ <br> $\eta_{3m}^{(r)} = \eta_m^{(r)}, r = 1, 2$ |
|---|---|---|---|---|
| 1 | 1.95391 | 4.25538 <br> 41.3822 | $0.91110\, e^{(1)}\ 4.25538\, n^{(1)}$ <br> $0.92492\ ^{ine}$ <br> $30.8139\, e^{(2)}\ 41.4274\, n^{(2)}$ | $0.04987\, b^{(1)}$ <br> $0.05037\ ^{inb}$ <br> $0.31296\, b^{(2)}$ |
| 2 | 2.74776 | 4.94711 <br> 44.7479 | $0.98479\, e^{(1)}\ 4.94711\, n^{(1)}$ <br> $0.99608\ ^{ine}$ <br> $30.8149\, e^{(2)}\ 44.7652\, n^{(2)}$ | $0.08584\, b^{(1)}$ <br> $0.08625\ ^{inb}$ <br> $0.81451\, b^{(2)}$ |
| 3 | 3.52810 | 4.81097 <br> 44.0542 | $1.00349\, e^{(1)}\ 4.81005\, n^{(1)}$ <br> $1.01586\ ^{ine}$ <br> $30.6635\, e^{(2)}\ 43.9950\, n^{(2)}$ | $0.10888\, b^{(1)}$ <br> $0.10965\ ^{inb}$ <br> $1.10953\, b^{(2)}$ |
| 4 | 4.27542 | 4.75564 <br> 43.8201 | $0.98210\, e^{(1)}\ 4.75564\, n^{(1)}$ <br> $0.99330\ ine$ <br> $30.5387\, e^{(2)}\ 43.8119\, n^{(2)}$ | $0.12759\, b^{(1)}$ <br> $0.12803\ inb$ <br> $1.31880\, b^{(2)}$ |
| 11 | 11.6577 | 4.78850 <br> 44.0115 | $0.98696\, e^{(1)}\ 4.78850\, n^{(1)}$ <br> $0.99970\ ^{ine}$ <br> $30.3831\, e^{(2)}\ 44.0155\, n^{(2)}$ | $0.35377\, b^{(1)}$ <br> $0.35430\ ^{inb}$ <br> $4.12242\, b^{(2)}$ |
| 15 | 16.1102 | 4.78555 <br> 44.0396 | $0.98696\, e^{(1)}\ 4.78555\, n^{(1)}$ <br> $0.99970\ ^{ine}$ <br> $30.3822\, e^{(2)}\ 44.0403\, n^{(2)}$ | $0.48841\, b^{(1)}$ <br> $0.50299\ ^{inb}$ <br> $5.80563\, b^{(2)}$ |
| 16 | 17.2065 | 4.78465 <br> 44.0479 | $0.98696\, e^{(1)}\ 4.78465\, n^{(1)}$ <br> $0.99970\ ^{ine}$ <br> $30.3829\, e^{(2)}\ 44.0506\, n^{(2)}$ | $0.52158\, b^{(1)}$ <br> $0.52392\ ^{inb}$ <br> $5.99851\, b^{(2)}$ |

For $\varepsilon_m \to 0$ the interface and edge vibrations of problem (7.1)–(7.4), are splitting on quasi-transverse and quasi tangential vibrations. Meanwhile, the frequencies of this problem tend to the frequencies of a similar problem for a composite plate.

In vibrations of a predominantly tangential type $\eta_{1m}^{(r)} = \eta_{2m}^{(r)} = \eta_m^{(r)}$, $\eta_{3m}^{(r)} = 0, r = 1, 2$, in addition to planar interface and edge vibrations of the Stoneley and Rayleigh type, new vibrations can also appear due to the longitudinal and torsional components of the inertia force [14].

## 7.2 Conclusions

Using the system of equations of dynamic equilibrium of orthotropic cylindrical shells of the corresponding classical theory, dispersion equations are obtained to determine the eigenfrequencies of interfacial and edge vibrations of the composite cylindrical panel with free edges.

**Table 7.4** Characteristics of the natural frequencies of a cylindrical panel

| N | $\theta_m$ | $\eta_{1m}^{(r)} = \eta_{2m}^{(r)} = \eta_{3m}^{(r)} = \eta_m^{(r)}$ |
|---|---|---|
| 1 | 1.95391 | 0.91201 $e^{(1)}$ 0.04986 $b^{(1)}$ 4.25908 $n^{(1)}$ <br> 0.92503 $^{ine}$ 0.05037 $^{inb}$ <br> 30.8092 $e^{(2)}$ 0.31295 $b^{(2)}$ 41.4275 $n^{(2)}$ |
| 2 | 2.74776 | 0.98431 $e^{(1)}$ 0.08621 $b^{(1)}$ 4.94711 $n^{(1)}$ <br> 0.99667 $^{ine}$ 0.086631 $^{inb}$ <br> 30.7821 $e^{(2)}$ 0.81451 $b^{(2)}$ 44.7696 $n^{(2)}$ |
| 3 | 3.52810 | 1.00225 $e^{(1)}$ 0.10932 $b^{(1)}$ 4.81097 $n^{(1)}$ <br> 1.01914 $^{ine}$ 0.10991 $^{inb}$ <br> 30.6693 $e^{(2)}$ 1.10952 $b^{(2)}$ 43.9950 $n^{(2)}$ |
| 4 | 4.27542 | 0.98291 $e^{(1)}$ 0.12803 $b^{(1)}$ 4.75564 $n^{(1)}$ <br> 0.99309 $^{ine}$ 0.12868 $^{inb}$ <br> 30.5395 $e^{(2)}$ 1.33719 $b^{(2)}$ 43.8120 $n^{(2)}$ |
| 11 | 11.6577 | 0.98696 $e^{(1)}$ 0.35351 $b^{(1)}$ 4.78850 $n^{(1)}$ <br> 0.99670 $^{ine}$ 0.35380 $^{inb}$ <br> 30.3831 $e^{(2)}$ 4.11548 $b^{(2)}$ 44.0155 $n^{(2)}$ |
| 15 | 16.1102 | 0.98696 $e^{(1)}$ 0.48828 $b^{(1)}$ 4.78555 $n^{(1)}$ <br> 0.99970 $^{ine}$ 0.49098 $^{inb}$ <br> 30.3822 $e^{(2)}$ 5.79800 $b^{(2)}$ 44.0403 $n^{(2)}$ |
| 16 | 17.2065 | 0.98696 $e^{(1)}$ 0.52160 $b^{(1)}$ 4.78465 $n^{(1)}$ <br> 0.99970 $^{ine}$ 0.52339 $^{inb}$ <br> 30.3829 $e^{(2)}$ 5.98166 $b^{(2)}$ 44.0465 $n^{(2)}$ |

The frequencies of intrinsic interfacial and edge vibrations of a composite cylindrical panel composed of two orthotropic thin elastic cylindrical panels with different elastic coefficients and having full contact along the generators are determined by the set of Eq. (7.23).

The frequencies of natural interface and edge vibrations for the composite rectangular plate with free edges are determined by the sets of Eqs. (7.38) and (7.54).

The existence of interfacial and boundary vibrations depends on the radius of the circle, the length and width of the components of the cylindrical panels and the elastic coefficients.

The obtained asymptotic formulas and numerical analysis show that for large $\theta_m$ or small curvature of the composite panel, all the characteristics of the intrinsic interface and edge vibrations of the cylindrical panel tend to the characteristics of the interface and edge vibrations of the composed rectangular plate, respectively.

The first frequencies of natural vibrations depend on the selected basis functions satisfying the same boundary conditions, and also, when $\varepsilon_m \to 0$ the vibration frequencies at the free generators become independent of the basis functions and the boundary conditions on the ends [29].

Numerical results show that the asymptotic formulas (7.63), (7.66) of the dispersion Eq. (7.23) provide an efficient approximation for finding the eigenfrequencies of problem (7.1)–(7.4).

Further possible generalizations may include accounting for the effects of prestress [31] and elastic foundations [32].

# References

1. Norris AN (1994) Flexural edge waves. J Sound Vib 171(4):571–573
2. Belubekyan VM, Yengibaryan IA (1996) Waves localized along a free edge of a plane with cubic symmetry (in Russian). Izv. Ross. Akad. Nauk Mech. Solids 6:139–143
3. Thompson I, Abrahams ID (1994) On the existence of flexural edge waves on thin orthotropic plates. J. Acoust. Soc. Amer. 112(5):1756–1765
4. Grinchenko VT (2005) Wave motion localization effects in elastic waveguides. Int Appl Mech 41(9):988–994
5. Kaplunov JD, Kossovich LY, Wilde MV (2000) Free localized vibrations of a semi-infinite cylindrical shell. J Acoust Soc Am 107(3):1383–1393
6. Kaplunov JD, Wilde MV (2000) Edge and interfacial vibrations in elastic shells of revolution. Z Angew Math Phys ZAMP 51(4):530-549
7. Kaplunov JD, Wilde MV (2002) Free interfacial vibrations in cylindrical shells. J Acoust Soc Am 111(6):2692–2704
8. Wilde MV, Kaplunov YD, Kossovich LY (2010) Edge and interfacial resonance phenomena in elastic bodies (in Russian), M., Fizmatlit
9. Lawrie JB, Kaplunov J (2012) Edge waves and resonance on elastic structures: an overview. Math Mech Solids 17(1):4–16
10. Mikhasev GI, Tovstik PE (2009) Localized vibrations and waves in thin shells, asymptotic methods (in Russian), M., Fizmatlit
11. Gol'denveizer AL, Lidskii VB, Tovstik PE (1979) Free vibrations of thin elastic shells (in Russian), M., Nauka
12. Ghulghazaryan GR, Ghulghazaryan LG (2006) On vibrations of a thin elastic orthotropic shell with free edges. Prob Prochn PlastichnS 68:150–160
13. Gulgazaryan GR, Gulgazaryan RG, Khachanyan AA (2013) Vibrations of an orthotropic cylindrical panel with various boundary conditions. Int Appl Mech 49(5):534–554
14. Ghulghazaryan GR, Ghulghazaryan RG, Srapionyan DL (2013) Localized vibrations of a thin-walled stracture consisted of orthotropic elastic non-closed cylindrical shells with free and rigid-clamped edge generators. ZAMM Z Math Mech 93(4):269–283
15. Gulgazaryan GR, Gulgazaryan LG, Saakyan RD (2008) The vibrations of a thin elastic orthotropic circular cylindrical shell with free and hinged edges. J Appl Math Mech 72(3):453–465
16. Zilbergleit AS, Suslova EB (1983) Contact flexural waves in thin plates. Sov Phys Acoust 29(2):108–111
17. Gertman IP, Lisitskiy ON (1988) Reflection and transmission of acoustic waves at the interface of separation of two elastic semi-strips. J Appl Mech 52(6):816–820
18. Stoneley R (1924) The elastic waves at the interface of two solids. Proc Roy Soc London A 106:416–429
19. Ambartsumyan SA (1961) The theory of anizotropic shells. Fizmatlit, Moscow, p 384p
20. Kolmogorov AN, Fomin SV (1981) Elements of the theory of functions and functional analysis (in Russian). M., Nauka
21. Vlasov VZ (1932) A new practical method for calculating folfed coverings and shells, Stroit. Prom (11):33–38 and (12):21–26 (1932)

22. Kantorovich LV (1933) A direct method for approximate solution of a problem on the minimum of a double integral. Izv.AH SSSR, Otd Mat Estestv Nauk (5):647–653
23. Prokopov G, Bespalov EI, Sherenkovskii YV (1982) LV Kantorovich method of reduction to ordinary differential equations and a general method for solving multidimensional problems of heat transfer. Inzh Fiz Zhurn 42(6):1007–1013
24. Bespalov EI (2008) To the solution of stationary problems of the theory of gently sloped shells by the generalized Kantorovich-Vlasov method. Prikl Mekh 44(11):99–111
25. Mikhlin SG (1970) Variational methods in mathematical physics (in Russian). M., Nauka
26. Ghulghazaryan GR, Ghulghazaryan LG, Mikhasev G.I (2018) Free interfacial and boundary vibrations of thin elastic circular cylindrical shells with free ends. Izv NAS Armenia, Mech 71(1):61–78
27. Gulgazaryan GR (2004) Vibrations of semi-infinite, orthotropic cylindrical shells of open profile. Intern Appl Mech 40(2):199–212
28. Ghulghazaryan GR (2020) Free vibrations of thin elastic orthotropic cylindrical panel with hinge-mounted end. Izv NAS Armenia, Mech 73(4):29–47
29. Ghulghazaryan GR, Ghulghazaryan LG, Kudish II (2019) Free vibrations of a thin elastic orthotropic cylindrical panel with free edges. Mech Comp Mat 55(5):557–574
30. Ghulghazaryan GR, Lidskii VB (1982) Density of free vibrations frequencies of a thin anisotropic shell with anisotropic layers, Izv. AN.SSSR, Mech Solids (3):171–174
31. Kaplunov JD, Prikazchikov DA, Rogerson GA (2004) Edge vibration of a pre-stressed semi-infinite strip with traction-free edge and mixed face boundary conditions. Z Angew Math Phys ZAMP 55(4):701–719
32. Kaplunov J, Prikazchikov DA, Rogerson GA, Lashab MI (2014) The edge wave on an elastically supported Kirchhoff plate. J Acoust Soc Am 136(4):1487–1490

# Chapter 8
# Detection of a Hidden Sandy Layer in a Stratified Substrate by Dispersion Analysis

Sergey V. Kuznetsov

**Abstract** Dispersion properties of Rayleigh–Lamb waves in a stratified substrate containing several elastic isotropic upper layers, a distant sandy layer and a homogeneous isotropic (bottom) half-space are analyzed by Cauchy sextic formalism. The analysis revealed that the most distant from the free Earth surface sandy layer can not only be detected, but its physical and geometrical properties can also be determined by comparing the corresponding dispersion portraits. A necessary modification of the Weiskopf model for a sandy layer is proposed, accounting for the immanent anisotropy of the sandy layers.

**Keywords** Weiskopf model · Sandy layer · Anisotropy · Cubic symmetry · Rayleigh wave · Dispersion

## 8.1 Introduction

Herein, a stratified substrate containing several elastic *isotropic* upper layers, a sandy *anisotropic* layer and a homogeneous *isotropic* half-space, see Fig. 8.1, is studied in terms of propagation of Rayleigh–Lamb waves.

A natural question on the principal ability of acoustic measurements on identifying the possible presence of a hidden sandy layer displaced beneath other sediment layers is of great importance for finding oil and gas deposits within the upper structure of the Earth's crust [1–13]. While the existing acoustic methods are mostly based on analyzing signals of bulk P and S waves, several approaches use Rayleigh or Rayleigh–Lamb waves; see [1, 5–13].

According to the original Weiskopf model for a sandy medium [14], the experimentally observed shear modulus $\mu$ of a sandy material is smaller than predicted by the known isotropic relation flowing out from Hook's law:

S. V. Kuznetsov (✉)
Ishlinsky Institute for Problems in Mechanics RAS, Moscow, Russia
e-mail: kuzn-sergey@yandex.ru

Institute of Problems of Mechanical Engineering RAS, SPb, Russia

Bauman Moscow State Technical University, Moscow, Russia

**Fig. 8.1** The model for a
stratified substrate with
elastic isotropic layers, a
sandy (anisotropic) layer and
an elastic isotropic
half-space
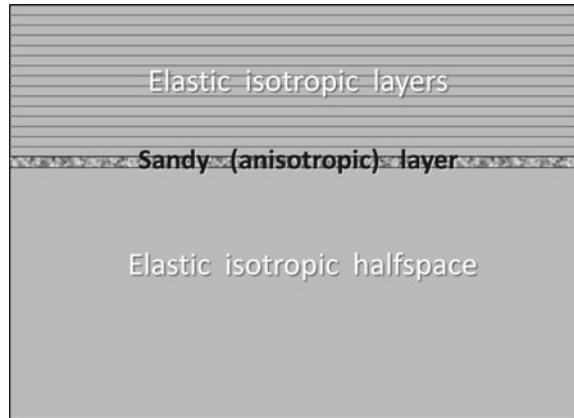


$$\frac{E}{\mu} \equiv \xi \geq 2(1 + \nu), \tag{8.1}$$

where $E$ is Young's modulus; $\xi$ is the "soil constant" [14]; $\nu$ is Poisson's ratio; note
that for isotropic material

$$\xi = 2(1 + \nu), \mu = \frac{E}{2(1 + \nu)} \tag{8.2}$$

In the next section, the constitutive equation for sandy material is studied in
more detail, revealing that the Weiskopf sandy medium is actually anisotropic and
possesses cubic symmetry.

## 8.2  Original Weiskopf Model for Sandy Material

The Weiskopf model utilizing assumption (8.1) was initially proposed for obtaining
more reasonable values for side pressure of sandy soils on retaining walls than
predicted by the than based on Rankine and Coulomb theories [16–18] Boussi-
nesq solution; see also [18–21]. Along with the "soil constant" $\xi$ another parameter
characterizing sandy materials, known as the "sandiness" [14], is introduced:

$$\frac{E}{\mu} = 2\chi(1 + \nu), \tag{8.3}$$

where $\chi \geq 1$ is the "sandiness"; at $\chi = 1$ the medium becomes isotropic. It appears
that the sandiness parameter $\chi$ is more convenient for theoretical studies than the
"soil constant" $\xi$, since the former does not contain Poisson's ratio. In [14], it was
implicitly assumed that another Lame's constant $\lambda$ satisfies the isotropic condition

$$\lambda = \frac{E\nu}{(1+\nu)(1-2\nu)}. \tag{8.4}$$

The constitutive equations for sandy materials in the form of Eqs. (8.1), (8.3) were later on used in studies on analyzing sandy soil pressure on retaining walls and piles [22–28]. Experimental data show that in many sandy soils $2 \leq \chi \leq 3$. Combining Eqs. (8.1) and (8.3) yields the following relation between $\xi$ and $\chi$:

$$\chi = \frac{\xi}{2(1+\nu)}. \tag{8.5}$$

Despite quite a large number of works utilizing Weiskopf equations of state for sandy materials, the problem of the immanent anisotropy of Eqs. (8.1) and (8.3) remains almost unexplored. Meanwhile, since the pioneering work [29], the natural anisotropy of soils due to sedimentation followed by either one-dimensional or anisotropic consolidation over long periods of time should be taken into account, see [30–33], with the particularly important studies of elastic anisotropy of sand [31, 32].

## 8.3 Modified Weiskopf Model

As was pointed out earlier, the original Weiskopf model [14] inevitably leads to elastic anisotropy, since violating any of the conditions (8.3) with $\chi = 1$ or (8.4) the corresponding elasticity tensor $\boldsymbol{C}$ with components

$$\begin{matrix} C_{1111} & C_{1122} & C_{1122} & 0 & 0 & 0 \\ & C_{1111} & C_{1122} & 0 & 0 & 0 \\ & & C_{1111} & 0 & 0 & 0 \\ & & & C_{2323} & 0 & 0 \\ & & & & C_{2323} & 0 \\ & & & & & C_{2323} \end{matrix}, \tag{8.6}$$

where

$$C_{kkkk} = \eta; \ C_{kkmm} = \lambda; \ C_{kmkm} = \mu; \ \mu \neq \frac{1}{2}(\eta - \lambda)$$
$$k = 1, 2, 3; \ m = 1, 2, 3 \tag{8.7}$$

does not satisfy the isotropy condition [34]

$$C_{ijmn} = Q_i^a Q_j^b C_{abde} Q_m^d Q_n^e, \tag{8.8}$$

which should be valid for any orthogonal tensor $\boldsymbol{Q}$.

To ensure the positiveness of the specific mechanical energy, the elasticity tensor should be positive definite

$$\underset{A \in R^3 \otimes R^3, A \neq 0}{\forall A} \quad \boldsymbol{A} \cdot \cdot \boldsymbol{C} \cdot \cdot \boldsymbol{A} > 0 \tag{8.9}$$

It will be further assumed that inequality (8.9) is satisfied.

### 8.3.1 Cubic Anisotropy

The highest symmetry group is compatible with the elasticity tensor Eq. (8.6) and Eq. (8.7) corresponds to cubic symmetry written in the crystallographic axes. For cubic symmetry, the material constants $\eta$ and $\lambda$ can also be represented in terms of two other constants, elastic modulus and Poisson's ratio:

$$\eta = \frac{E(1-\nu)}{(1-2\nu)(1+\nu)}, \lambda = \frac{E\nu}{(1-2\nu)(1+\nu)} \tag{8.10}$$

The positive definite condition (8.9) can also be rewritten in terms of the eigenvalues of the elasticity tensor $\boldsymbol{C}$, yielding

$$\frac{E}{1-2\nu} > 0, \frac{E}{1+\nu} > 0, \mu > 0 \tag{8.11}$$

In addition to conditions (8.11), a natural assumption $E > 1$ will be imposed on the modulus $E$.

### 8.3.2 Relation Between Parameters

With three elastic constants $E$, $\nu$ and $\mu$ and relations, the considered cubic medium becomes identical (along crystallographic axes) with the Weiskopf model, yielding

$$\xi = 2\frac{2\lambda + \eta}{\lambda + \mu}, \chi = \frac{2\lambda + \eta}{3\lambda + 2\mu}. \tag{8.12}$$

Now, with Eq. (8.12) the elastic modulus $\eta$ can be expressed in terms of other elastic moduli and the corresponding soil parameter $\xi$:

$$\eta = \frac{1}{2}\xi(\lambda + \mu) - 2\lambda, \tag{8.13}$$

or sandy parameter $\eta$

$$\eta = \chi(3\lambda + 2\mu) - 2\lambda. \tag{8.14}$$

Equation $(8.14)_2$ will be used for computing elastic constant $\eta$ by varying soil parameter $\chi$ at two other fixed constants $\lambda$ and $\mu$.

## 8.4  Dispersion Equation for Rayleigh–Lamb Waves

Herein, the dispersion equation for Rayleigh–Lamb waves in stratified media with anisotropic layers is obtained by applying Cauchy sextic formalism [35, 36].

The equation of motion for the elastic anisotropic medium has the form

$$div_x \mathbf{C} : \nabla_x \mathbf{u}(\mathbf{x}, t) - \rho \partial_{tt} \mathbf{u}(\mathbf{x}, t) = 0, \tag{8.15}$$

where $\mathbf{u}(\mathbf{x}, t)$ is the displacement field; $\rho$ is the material density; $\mathbf{x}$, t are the spatial variable and time, respectively. The elasticity tensor $\mathbf{C}$ has components defined by expressions, (8.6), (8.7) for a sandy layer and (8.6), (8.10), (8.2) for isotropic upper layers and a half-space.

The harmonic plane wave representation can be written in a form [35, 36]

$$\mathbf{m}(ir\nu \cdot \mathbf{x}) \exp(ir(\mathbf{n} \cdot \mathbf{x} - ct)), \tag{8.16}$$

where $\mathbf{m}(ir\nu \mathbf{x})$ is the vector amplitude; $\nu$ is the unit normal to the free surface; see Fig. 8.1; $r$ is the wave number; $\mathbf{n}$ is the wave normal; $c$ is the phase velocity; $i = \sqrt{-1}$.

Following [35] and substituting representation (8.16) into Eq. (8.15) yields the following equation of motion:

$$\partial_{x'} \mathbf{Y}(x') = \mathbf{G} \cdot \mathbf{Y}(x'), \tag{8.17}$$

where $x' = ir\nu \cdot \mathbf{x}$ and

$$\mathbf{Y}(x') = \begin{pmatrix} \mathbf{m}(x') \\ \mathbf{w}(x') \end{pmatrix}, \mathbf{G} = \begin{pmatrix} \mathbf{0} & \mathbf{I} \\ -\mathbf{A}_1^{-1} \cdot \mathbf{A}_3 & -\mathbf{A}_1^{-1} \cdot \mathbf{A}_2 \end{pmatrix} \tag{8.18}$$

In Eq. (8.18), $\mathbf{w}(x') = \partial_{x'} \mathbf{m}(x')$, $\mathbf{0}$ and $\mathbf{I}$ are zero and unit $3 \times 3$-matrices respectively, and

$$\begin{aligned} \mathbf{A}_1 &= \nu \cdot \mathbf{C} \cdot \nu \\ \mathbf{A}_2 &= \nu \cdot \mathbf{C} \cdot \mathbf{n} + \mathbf{n} \cdot \mathbf{C} \cdot \nu \\ \mathbf{A}_3 &= \mathbf{n} \cdot \mathbf{C} \cdot \mathbf{n} - \rho c^2 \mathbf{I} \end{aligned} \tag{8.19}$$

The following matrix will also be needed for further analysis.

$$A_4 = v \cdot C \cdot n \tag{8.20}$$

The general solution of Eq. (8.17) admits the following representation in the form of the exponential matrix [35].

$$Y(x') = \exp(Gx') \cdot \vec{C}, \tag{8.21}$$

where $\vec{C}$ is the six-dimensional vector defined by the boundary conditions.

Assuming all the alternating layers of the stratified plate have equal thickness $2h$, the traction-free boundary conditions at the upper and bottom faces of the plate can be written in terms of vector $Y$:

$$\begin{cases} t_\nu^{(1)}(x')\big|_{x'=+irh} \equiv \left(A_4^{(1)}; A_1^{(1)}\right) \cdot Y^{(1)}(x')\big|_{x'=+irh} = 0 \\ t_\nu^{(N)}(x')\big|_{x'=-irh} \equiv \left(A_4^{(N)}; A_1^{(N)}\right) \cdot Y^{(N)}(x')\big|_{x'=-irh} = 0 \end{cases} \tag{8.22}$$

In Eq. (8.22), the upper index is referred to the corresponding layer, and the origins of the local coordinate systems are placed at the central lines of each layer.

At the interface between the adjacent layers, the condition of the ideal mechanical contact written in terms of vector $Y$ is as follows [36].

$$Z_{(k+1)} \cdot Y^{(k+1)}(x')\big|_{x'=+irh} = Z_{(k)} \cdot Y^{(k)}(x')\big|_{x'=-irh}$$
$$= k = 1, ..., N-1, \tag{8.23}$$

where $Z_{(k)}$ is the impedance matrix for the corresponding layer:

$$Z_{(k)} = \begin{pmatrix} I & 0 \\ A_4^{(k)} & A_1^{(k)} \end{pmatrix} \tag{8.24}$$

Note that the direction of the unit normal $v$ to the median plane in Eqs. (8.22)–(8.24) remains the same for all the layers.

Defining the unknown vector $\vec{C}$ in Eq. (8.21) by boundary condition (8.22) yields

$$\vec{C} = \exp\left(-irhG^{(1)}\right) \cdot Z_{(1)}^{-1} \cdot \begin{pmatrix} m^{(1)}(+irh) \\ 0 \end{pmatrix} \tag{8.25}$$

where $m^{(1)}(+irh)$ is the unknown amplitude at the upper surface of the first layer. Combining Eqs. (8.21)–(8.25) yields

$$\begin{pmatrix} m^{(1)}(-irh) \\ t_\nu^{(1)}(-irh) \end{pmatrix} = Z_{(1)} \cdot \exp\left(-2irhG^{(1)}\right) \cdot Z_{(1)}^{-1} \cdot \begin{pmatrix} m^{(1)}(+irh) \\ 0 \end{pmatrix} \tag{8.26}$$

Repeating the latter procedure for the subsequent layers results in the following relation:

$$\begin{pmatrix} \boldsymbol{m}^{(N)}(-irh) \\ \boldsymbol{t}_\nu^{(N)}(-irh) \end{pmatrix} = \prod_{k=1}^{N}\Big(Z_{(k)} \cdot \exp\big(-2irh\boldsymbol{G}^{(k)}\big) \cdot \boldsymbol{Z}_{(k)}^{-1}\Big) \cdot$$
$$\begin{pmatrix} \boldsymbol{m}^{(1)}(+irh) \\ \boldsymbol{0} \end{pmatrix} \tag{8.27}$$

Equation (8.27) could be considered as a mapping from the nontrivial vector field of magnitudes $\boldsymbol{m}^{(1)}(+irh)$ to the vanishing field of surface tractions $\boldsymbol{t}_\nu^{(N)}(-irh)$. The condition of existence for such a nontrivial vector field $\boldsymbol{m}^{(1)}(+irh)$ means degeneracy of the considering mapping, yielding

$$\det\left(\begin{pmatrix} \boldsymbol{0} & \boldsymbol{I} \end{pmatrix} \cdot \prod_{k=1}^{N}\Big(\boldsymbol{Z}_{(k)} \cdot \exp\big(-2irh\boldsymbol{G}^{(k)}\big) \cdot \boldsymbol{Z}_{(k)}^{-1}\Big) \cdot \begin{pmatrix} \boldsymbol{I} \\ \boldsymbol{0} \end{pmatrix}\right) = 0 \tag{8.28}$$

Equation (8.28) is the desired dispersion equation for finding roots ensuring the existence of the nontrivial harmonic guided wave in the considered $N$-layered system.

## 8.5 Dispersion Analyses

Dispersion of Rayleigh–Lamb waves propagating in a stratified substrate containing 13 elastic isotropic upper layers, a sandy layer, defined by the modified Weiskopf model, and a homogeneous isotropic bottom half-space, Fig. 8.1, is analyzed by numerically solving dispersion Eq. (8.28). Finding real positive roots of Eq. (8.28) was done with the multiprecision algorithms based on the Advanpix® codes, allowing computations with mantissa having more than 200 decimal digits [37].

### 8.5.1 The Models

Properties of the isotropic layers remained unaltered during computations with varying physical and geometrical properties of the sandy layer. The following dimensionless physical and geometrical parameters of isotropic upper layers were used in the computation

$$E_k = \frac{\exp(k)}{\exp(N-1)}; \; \rho_k = \frac{k}{N-1}; \; \nu_k = 0.25; \; h_k = 1$$
$$k = 1, ..., N-2 \tag{8.29}$$

where $N$ is the total number of layers, including the bottom half-space. Thus, elastic moduli of the upper sedimentary layers exponentially increase, while densities gradually linearly increase; see [38]; Poisson's ratio and thickness of the layers in the numerical experiments are assumed constant.

In computations, the modified Weiskopf model for the sandy layer defined by Eqs. (8.6), (8.10) had the following parameters (in crystallographic axes):

$$E_{N-1} = 1; \rho_{N-1} = 1; \nu_{N-1} = 0.25; \mu_{N-1} = 0.2; h_{N-1} = 1. \tag{8.30}$$

Equation (8.30) yields $\chi = 2$ for the sandiness parameter.

For the isotropic bottom half-space, the following dimensionless parameters corresponding to granite rocks were adopted:

$$E_N = 10; \rho_N = 2; \nu_N = 0.25. \tag{8.31}$$

In the numerical experiments, the overall number of layers $N$ including the bottom half-space was 15.

### 8.5.2 Dispersion Portraits

Dispersion portraits of Rayleigh–Lamb waves in two models were compared, 14 layers were modeled as (i) the sandy layer defined by Eq. (8.5.2), and (ii) an isotropic layer with the following dimensionless elastic parameters:

$$E_{N-1} = 1; \rho_{N-1} = 1; \nu_{N-1} = 0.25; h_{N-1} = 1, \tag{8.32}$$

yielding the shear modulus $\mu_{N-1} = 0.4$.

In these plots, the relative phase velocity and relative circular frequency are defined by

$$\omega^* = \omega h_{N-1} c_{S_N}^{-1} c^* = c c_{S_N}^{-1}, \tag{8.33}$$

where $c$ is the phase velocity and $c_{S_N}$ is the shear bulk wave velocity in the bottom half-space.

$$c_s = \sqrt{\mu_N \rho_T^{-1}}. \tag{8.34}$$

The low-frequency limit shown in Fig. 8.2a and d is known as the second limiting velocity [39]. It can be obtained either by the direct limit at $\omega \to 0$.

$$c_{2,\text{lim}}^{* \frac{\lim^{-1}}{\omega \to 0_{S_N}}}, \tag{8.35}$$
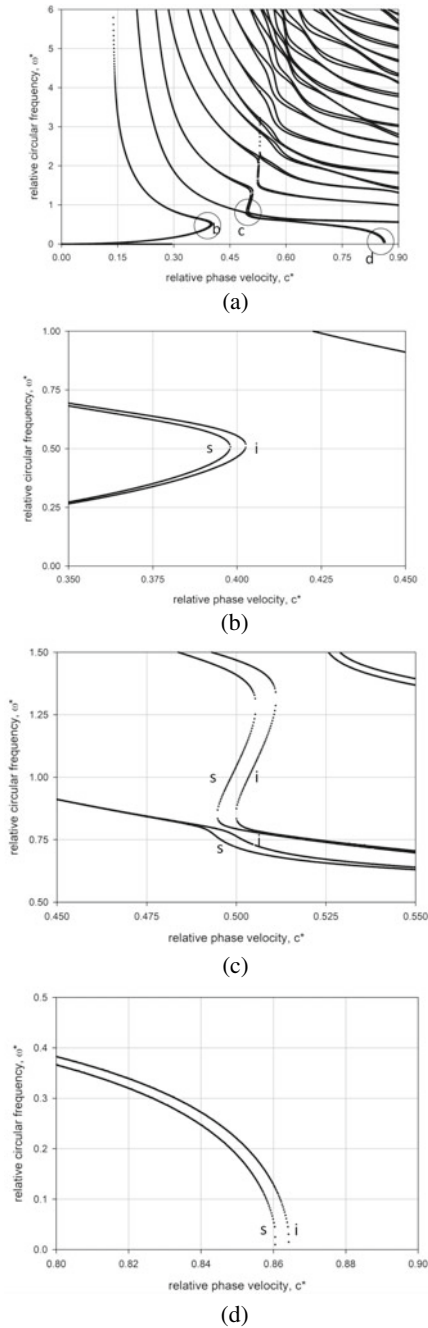
**Fig. 8.2** Dispersion curves for Rayleigh–Lamb waves in a model with a sandy layer (s) and with isotropic layer (i); **a** an overview; **b** near pivot point of the quasi-asymmetric fundamental branch; **c** near branching points of quasi-symmetric fundamental branch (lower curves) and a higher mode (upper curves); **d** near the second limiting velocity

or by the low-frequency asymptotic formulas [40, 41].

Analysis of these two sets of dispersion curves reveals that both quasi-asymmetric ($qA_0$) and quasi-symmetric ($qS_0$) fundamental branches are quite informative for distinguishing sandy layer from isotropic one with the same physical and geometrical properties except for their shear moduli, $\mu_{N-1,sandy} = 0.2$; $\mu_{N-1,isotropic} = 0.4$, Fig. 8.2a, b. Moreover, even at the vanishing frequency, the quasi-symmetric ($qS_0$) fundamental branches of the purely isotropic system and with sandy layer reveal a substantial discrepancy in $c^*_{2,lim}$ values; see Fig. 8.2d. At frequencies $\omega^* \in (0.6; 0.8)$, the fundamental branches $qS_0$ exhibit discrepancy, Fig. 8.2c. Similarly, the higher modes $qA_1$ separate from each other at $\omega^* > 0.8$; see two upper curves in Fig. 8.2c. Thus, the considered dispersion portraits reveal that even a very distant sandy layer can be detected and sorted out from a system containing only isotropic layers.

### 8.5.3   Sandiness Parameter Variation

The plots in Fig. 8.3 show the dispersion portraits plotted at varying sandiness parameter $\chi$ in a range $2 \leq \chi \leq 3$ of the most probable values, according to a number of experimental values for dried compacted sands [15]. Other physical and geometrical properties of the considered system remain the same as given in Eqs. (8.28)–(8.30).

Again, as it was in the preceding analysis, comparing these three sets of dispersion portraits reveals that both quasi-asymmetric ($qA_0$) and quasi-symmetric ($qS_0$) fundamental branches are quite informative; the fundamental branches have sufficient information for not only qualitative determination of the possible presence of the distant sandy layer, but they ensure quantitative information on possible sandiness parameter value; see Fig. 8.3b–d. Moreover, even at the vanishing frequency, the quasi symmetric ($qS_0$) fundamental branch exhibit substantial discrepancy in the $c^*_{2,lim}$ values; see Fig. 8.3d. And at higher frequencies, $\omega^* \in (0.6; 0.8)$, the fundamental quasi-symmetric branch $qS_0$ provides information on the sandiness parameter value; see Fig. 8.3c.

## 8.6   Concluding Remarks

The dispersion analysis of Rayleigh–Lamb waves propagating in a heterogeneous half-space containing a sandy layer modeled as an anisotropic elastic medium with cubic symmetry and an isotropic elastic substrate in a perfect contact is done with the modified Cauchy formalism [35, 36].

It is also proved that the Weiskopf model [15] for a sandy material eventually leads to the anisotropic elasticity with cubic symmetry, and the widely adopted [1–14] Weiskopf assumption on the modified isotropic equations for sandy materials should be substituted by equations of the anisotropic elasticity.

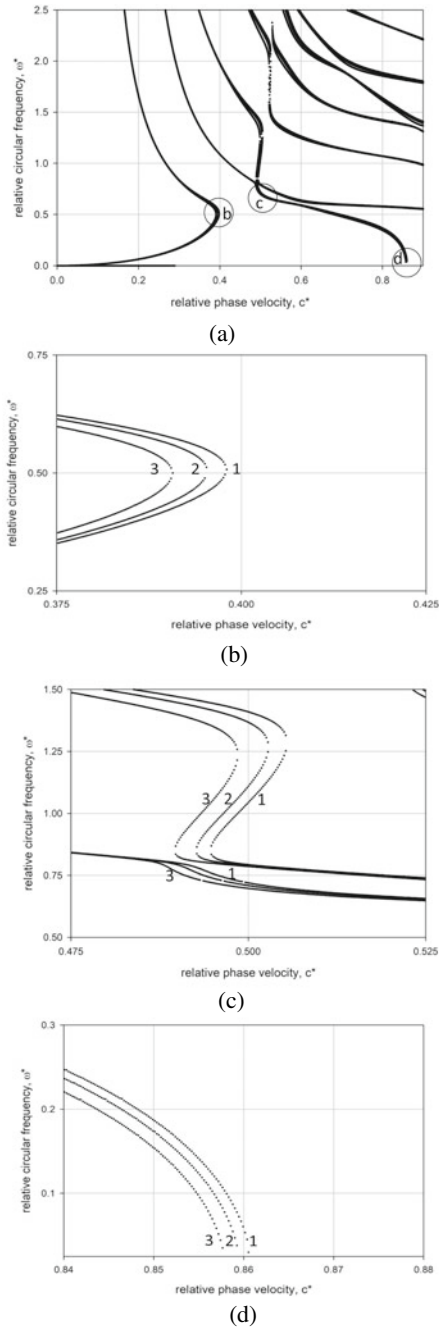**Fig. 8.3** Dispersion curves for Rayleigh–Lamb waves in a model with a sandy layer at the varying sandiness parameter; **a** an overview; **b** near pivot point of the quasi-asymmetric fundamental branch; **c** near branching points of quasi-symmetric fundamental branch (lower curves) and a higher mode (upper curves); **d** near the second limiting velocity: (1) $\chi = 2$; (2) $\chi = 2.5$; (3) $\chi = 3.0$

Several phenomena associated with the substantial discrepancy in the dispersion of Rayleigh–Lamb waves propagating in two systems with (a) an isotropic elastic layer and (b) a sandy layer with varying sandiness parameters modeled by equations of anisotropic elasticity reveal the principle ability to apply acoustic methods for identifying the presence of the distance from the Earth' surface sandy layers and estimating the sandiness parameter value. The performed analysis revealed that both quasi-asymmetric ($qA_0$) and quasi-symmetric ($qS_0$) fundamental branches are quite informative; the fundamental branches have sufficient information for not only qualitative determination of the possible presence of the distant sandy layer, but they also ensure quantitative information on possible sandiness parameter value; see Fig. 8.3b–d. Moreover, even at the vanishing frequency, the quasi-symmetric ($qS_0$) fundamental branch exhibits substantial discrepancy in the $c^*_{2,lim}$ values; see Fig. 8.3d. And at higher frequencies, $\omega^* \in (0.6; 0.8)$, the fundamental quasi-symmetric branch $qS_0$ provides information on the sandiness parameter value; see Fig. 8.3c.

Thus, a clear choice for experimental acoustic mechanics in geotechnical and geophysical applications is the use of different branches of Rayleigh–Lamb waves including both fundamental branches for identifying the presence and properties of the possible presence of the distant sandy layers. For possible applications in the internal Lamb problem, see [42, 43].

# References

1. Sharma MD (2018) Rayleigh wave at the surface of a general anisotropic poroelastic medium: derivation of real secular equation. Proc Roy Soc A 474(2211):1–12
2. Fletcher JB, Erdem J, Seats K, Lawrence J (2016) Tomographic Rayleigh wave group velocities in the Central valley, California, centered on the Sacramento/San Joaquin delta. J Geophys Res Solid Earth 121:2429–2446
3. Asten MW (2006) On bias and noise in passive seismic data fromfinite circular array data processed using SPAC methods. Geophysics 71(6):V153–V162
4. Boschi L, Becker TW, Soldati G, Dziewonski AM (2006) On the relevance of Born theory in global seismic tomography. Geophys Res Lett 33(L06302):1–4
5. García-Jerez A, Seivane H, Navarro M, Martínez-Segura M, Piña-Flores J (2019) Joint analysis of Rayleigh-wave dispersion curves and diffuse-field HVSR for site characterization: The case of El Ejido town (SE Spain). Soil Dyn Earthq Eng 121:102–120
6. Dey S, Gupta AK, Gupta S (1998) Propagation of torsional surface waves in dry sandy medium under gravity. Math Mech Solids 3(2): 229–235
7. Gupta S, Ahmed M (2017) On propagation of Love waves in dry sandy medium sandwiched between fiber-reinforced layer and prestressed porous half-space. Earthq Struc 12(6):619–628
8. Pal PC, Kumar S, Mandal D (2014) Surface wave propagation in sandy layer overlying a liquid saturated porous half-space and lying under a uniform liquid layer. Mech Adv Mater Struct 23(1):59–65
9. Pandit DK, Kundu S (2017) Propagation of Love wave in viscoelastic sandy medium lying over pre-stressed orthotropic half-space. Procedia Eng 173:996–1002

10. Deep S, Sharma V 2020 Love type waves in a dry sandy layer lying over an isotropic elastic halfspace with imperfect interface, J Phys Conf Ser 1531: 012069
11. Gupta S, Ahmed, M (2017) On propagation of Love waves in dry sandy medium sandwiched between fiber-reinforced layer and prestressed porous half-space. Earthq Struct 12(6):619–628
12. Kakar R, Kakar S (2016) Rayleigh wave in an anisotropic heterogeneous crustal layer lying over a gravitational sandy substratum. Geomech Eng 10(2):137–154
13. Dey S, Chandra A (1983) Surface waves in a dry sandy medium under gravity. Acta Geophysica Polonica 31(4):395–404
14. Kumar P, Chattopadhyay A, Singh AK (2021) Propagation of edge wave in homogeneous viscoelastic sandy media. In: Dutta S, Inan E, Dwivedy SK (eds) Advances in Structural Vibration. Lecture Notes in Mechanical Engineering. Singapore: Springer. https://doi.org/10.1007/978-981-15-5862-7_39
15. Weiskopf WH (1945) Stresses in soils under a foundation. J Franklin Inst 239:445–465
16. Lazebnik GE, Tsinker GP (1998) Soil pressure on retaining walls. In: Lazebnik GE, Tsinker GP (eds.) Monitoring of soil-structure interaction. Boston: Springer
17. Yang TH, He HJ (2010) Earth pressure calculation theory considering displacement effects. Rock Soil Mech 31(11):3635–3650
18. Jarquio R (1981) Total lateral surcharge pressure due to strip load. J Geotech Eng ASCE 107(10):1424–1428
19. Steenfelt JS, Hansen B (1983) Discussion of total lateral surcharge pressure due to strip load by R. Jarquio. J. Geotech. Eng, ASCE 109(2): 271–273
20. Cernica JN (1995) Geotechnical engineering: foundation design. John Wiley & Sons Inc., N.Y.
21. Cornforth DH (1964) Some experiments on the influence of strain conditions on the strength of sand. Géotechnique 14(2):143–167
22. Goldstein RV et al (2016) The modified Cam-Clay (MCC) model: cyclic kinematic deviatoric loading. Arch Appl Mech 86:2021–2031
23. Gotoh K, Yamanouchi T (1979) Stress and displacement characteristics of soil mass as Weiskopf's body due to surface load (in Japanese). Soils Foundations 19(1):97–107
24. Misra B, Sen BR (1975) Stresses and displacements in granular materials due to surface load. Int J Eng Sci 13(7/8):743–761
25. Kuznetsov SV (2005) Fundamental and singular solutions of Lamé equations for media with arbitrary elastic anisotropy. Quart Appl Math 63(3):455–467
26. Motta E (1994) Generalized Coulomb active-earth pressure for distanced surcharge. J. Geotech. Eng. ASCE 120(6):1072–1079
27. Georgiadis M, Anagnostopoulos C (1998) Lateral pressure on sheet pile walls due to strip load. J Geotech Geoenvironment Eng 124(1):95–98
28. Georgiadis K, Skordas D, Kamas I, Comodromos E (2020) Heating and cooling induced stresses and displacements in heat exchanger piles in sand. Renew Energy 147(2):2599–2617
29. Wolf K (1935) Ausbreitung der kraft in der halbebene und im halbraum bei anisotropen material. Z Angew Math Mech 15:249–254
30. Barden L (1963) Stresses and displacements in a cross-anisotropic soil. Géotechnique 13(3):198–210
31. Arthur JRF, Menzies BK (1972) Inherent anisotropy in a sand. Geotechnique 22:115–128
32. Meyerhof GG (1978) Bearing capacity of anisotropic cohesionless soils. Canadian Geotech J 15(4):592–595
33. Peng, X. 2011. *Anisotropy of Soil Physical Properties*. In: Gliński J., Horabik J., Lipiec J. (eds) Encyclopedia of Agrophysics. Encyclopedia of Earth Sciences Series. Dordrecht: Springer.
34. Gurtin ME (1973) The linear theory of elasticity. In: Truesdell C. (eds) Linear theories of elasticity and thermoelasticity. Berlin, Heidelberg: Springer
35. Kuznetsov SV (2019) Cauchy formalism for Lamb waves in functionally graded plates. J Vibr Control 25(6):1227–1232. https://doi.org/10.1177/1077546318815376
36. Kuznetsov SV (2019) Abnormal dispersion of Lamb waves in stratified media. Z Angew Math Phys 70:175. https://doi.org/10.1007/s00033-019-1222-z

37. Bailey D, Borwein P, Plouffe S (1997) On the rapid computation of various poly-logarithmic constants. Math Computation AMS 66(218):903–913
38. Turcotte DL, Schubert G (2002) Geodynamics, 2d edn. Cambridge University Press, Cambridge
39. Djeran-Maigre I et al (2008) Solitary SH waves in two-layered traction-free plates. Comptes Rendus Mechanique 336(1–2):102–107. https://doi.org/10.1016/j.crme.2007.11.001
40. Ilyashenko A et al. (2018) SH waves in anisotropic (monoclinic) media. Z Angew Math Phys 69:17. https://doi.org/10.1007/s00033-018-0916-y
41. Kaplunov J, Prikazchikov DA, Prikazchikova LA (2017) Dispersion of elastic waves in a strongly inhomogeneous three-layered plate. Int J Solids Struct 113–114:169–179
42. Kravtsov AV et al (2011) Finite element models in Lamb's problem. Mech Solids 46:952–959. https://doi.org/10.3103/S002565441106015X
43. Kuznetsov SV, Terentjeva EO (2015) Planar internal Lamb problem: Waves in the epicentral zone of a vertical power source. Acoust Phys 61:356–367. https://doi.org/10.1134/S1063771015030112

# Chapter 9
# Tunable Static and Dynamic Responses of Soft Porous Phononic Crystals

**Jian Li, Nan Gao, Ronghao Bao, and Weiqiu Chen**

**Abstract** Phononic crystals (PnCs) have attracted intensive research interests for almost three decades from investigators in different disciplines including physics, mechanics, materials, devices, etc. The particular band structures in PnCs make them perfect candidates for many novel and useful acoustic wave devices. In this chapter, we present two designs of porous periodic structures made of soft materials. One is a soft PnC with criss-crossed elliptical holes subject to tension, and the other is a soft PnC with circular holes, where rigid inclusions can be filled in, under compressive loads. Both PnCs can be seen as a high-contrast elastic composite. Owing to the large and recoverable deformation of soft materials, the external load can be well utilized to change the geometric configuration as well as the effective material properties, so as to tune both the static deformation and the superimposed linear wave propagation in soft PnCs. The finite element method is employed to numerically study the effects of geometry and the inserted rigid inclusions on deformation, buckling mode, post-buckling deformation, and band structure of wave propagation in the soft PnCs subject to external loads. Experiments are also conducted to validate the numerical observations. It is found that either making use of tension or inserting rigid inclusions can enhance the robustness of deformation and wave propagation in the soft porous PnCs. The results shall be beneficial to the design of robust soft PnC-based acoustic wave devices.

**Keywords** Soft porous phononic crystal · Large deformation · Wave propagation · Bandgap · Rigid inclusion

Jian Li and Nan Gao The authors contribute equally to this work.

J. Li · N. Gao · R. Bao (✉) · W. Chen (✉)
Key Laboratory of Soft Machines and Smart Devices of Zhejiang Province and Department of Engineering Mechanics and Soft Matter Research Center, Zhejiang University, Hangzhou 310027, China
e-mail: brh@zju.edu.cn

W. Chen
e-mail: chenwq@zju.edu.cn

W. Chen
State Key Laboratory of CAD and CG, Zhejiang University, Hangzhou 310058, China

## 9.1 Introduction

Materials with periodic meso-/micro-structures or structures with periodicity can exhibit unusual acoustic wave propagation behavior (e.g. bandgap, negative refraction, topological state, etc.) due to the Brag scattering mechanism [1, 2]. These artificial materials are now known as phononic crystals (PnCs). It is noted that different mechanisms (e.g. local resonance, inertial amplification) have also been found that can lead to unprecedented electric, magnetic or/and mechanical properties, and a unified terminology, i.e. metamaterial, has been created to name the various structured materials [3, 4].

The earlier studies all focus on PnCs with a fixed and unchangeable substructure. These PnCs are usually narrow-banded and non-adaptive, which greatly hinders their practical applications. In 2001, Goffaux and Vigneron [5] performed a theoretical study on a tunable PnC, showing that the wave propagation behavior could be changed by simply rotating the solid scatterers in the solid-air acoustic periodic system. Since then, different ideas and methods have been proposed to design multifarious tunable PnCs [6].

Soft materials can undergo large deformation even under a small external stimulus, which is of great superiority in developing novel, reconfigurable, functional devices and robotics. Hyperelastic materials are a special type of soft materials with the outstanding ability to recover its original configuration from the deformed state once the applied load is removed. Thus, hyperelastic materials have been widely applied in various fields such as biomedical devices, flexible displays, and soft robotics. The research group led by Professor Katia Bertoldi of Harvard University has systematically explored the use of hyperelastic materials in tunable PnCs and metamaterials [7–12].

Applying an external stimulus to soft materials can effectively alter the geometric configuration, internal stress distribution, and/or local material properties. Among various kinds of stimuli, mechanical loading is more simple, common and practical to be adopted in practice. Thus, Bertoldi and her collaborators mainly paid their attention to adaptive soft PnCs tuned by mechanical means in general and compressive loads in particular. A compressive load can make a soft PnC deform largely and even buckle. However, there is a great challenge that the large deformation (and buckling as well) of the soft PnCs subject to compressive loads is very sensitive to the initial imperfections that may be introduced during manufacture.

To enhance the robustness of large deformation, we introduce here two designs of soft PnCs with high-contrast elastic properties. One PnC is a soft porous material with periodically arranged criss-crossed elliptical holes [13]. This configuration actually corresponds to the compression-induced buckled state of a soft porous material with periodic circular holes in a square pattern as studied by Bertoldi and Boyce [7]. Further, we adopt a tensile load instead of the compressive one to tune the mechanical behavior of this soft PnC. The other PnC differs from the soft porous PnC with oblique infinite array of circular holes in Bertoldi and Boyce [7] by inserting rigid inclusions into certain holes in a representative volume element (RVE) [14]. We show

numerically and experimentally here that both the two designs enable robust static and dynamic responses of the soft PnCs.

## 9.2  Two Designs

In this section, we show the details of the two designs of soft PnCs with the capability of robust large deformation and wave propagation. Shown in Fig. 9.1a is the in-plane geometry of the first PnC, with square array of criss-crossed elliptical holes [13]. The thickness of the PnC can vary; if it is very thick as compared to the in-plane size, then we adopt the assumption of plane-strain state for simplicity (as in the simulations in Sect. 9.3), and if it is very thin then a plane-stress state is assumed (as in the experiments and the corresponding simulations to be presented in Sect. 9.4). The RVE marked by the black box in Fig. 9.1a is enlarged and given in Fig. 9.1b. $2L_0$ denotes the side length of the square RVE, $a$ and $b$ are the semi-axis lengths of the elliptical hole, i.e. the minor and major axes respectively. Two dimensionless parameters are introduced here for the sake of discussion: $\psi = ab\pi/L_0^2$ is the porosity of the PnC, and $\alpha = b/a$ is the major-to-minor half-axis ratio.

The host material of the PnC is soft and hyperelastic, which is able to withstand large deformation. The whole PnC with holes also can be seen as a high-contrast, two-phase elastic composite by treating the holes as a special material phase. Instead of using compression to tune the mechanical behavior of the PnC as in Refs. [7–9], Gao et al. [13] suggested to use tension, as shown in Fig. 9.2, where the tensile strains $\varepsilon_x$ and $\varepsilon_y$ in the $x$ and $y$ directions are defined as

$$\varepsilon_i = \frac{u_i}{2L_0} \quad (i = x, y), \tag{9.1}$$



(a)                                              (b)
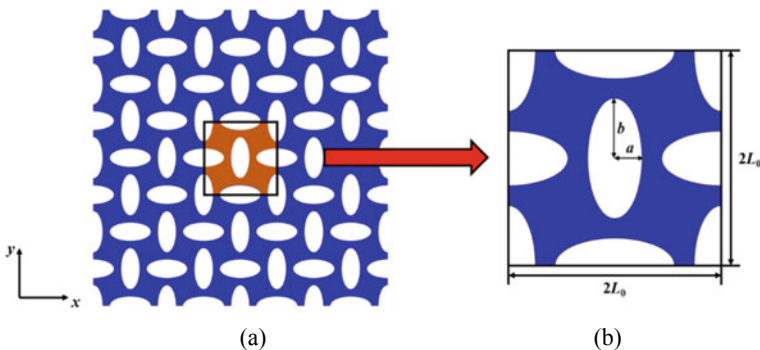
**Fig. 9.1**  The first soft PnC: **a** The pattern of criss-crossed elliptical holes; and **b** the RVE. $2L_0$ is the side length of the RVE, while $a$ and $b$ are the minor and major axes of the elliptical hole, respectively. (Reproduced with permission from Gao et al. [13]. Copyright 2018 by Springer Nature)

(a)                                                        (b)
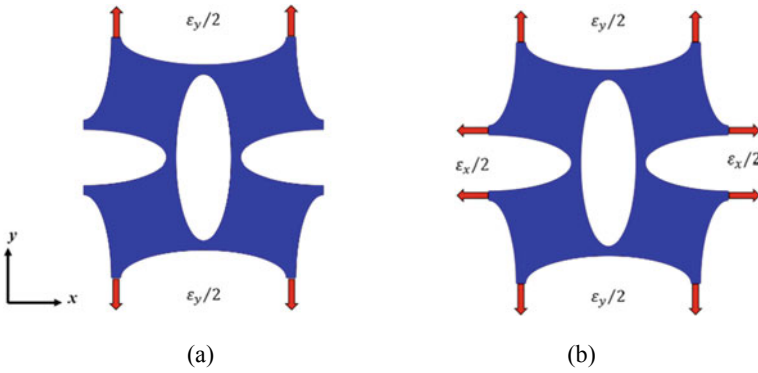
**Fig. 9.2** Tension as a tuning means: **a** Uniaxial tension; and **b** biaxial tension. $\varepsilon_x$ and $\varepsilon_y$ are the tensile strains in the $x$ and $y$ directions, respectively. (Reproduced with permission from Gao et al. [13]. Copyright 2018 by Springer Nature)

with $u_i$ being the displacement component.

Figure 9.3 displays the top view of the second hyperelastic PnC [14]. In contrast to the first PnC, we assume at the very beginning that it is very thick and its static and dynamic responses are approximately in a plane-strain state. The RVE is chosen to be a rectangular block with eight circular holes, into which rigid inclusions can be inserted in different patterns. Shown in Fig. 9.2b are eight typical patterns of the inserted rigid inclusions with the number of inclusions ranging from 1 to 8, respectively. In this design, inserting rigid inclusions is used to tune the mechanical behavior of the PnC, which also can be seen as a high-contrast, three-phase elastic composite when rigid inclusions are present as a third material phase.



(a)                                                        (b)
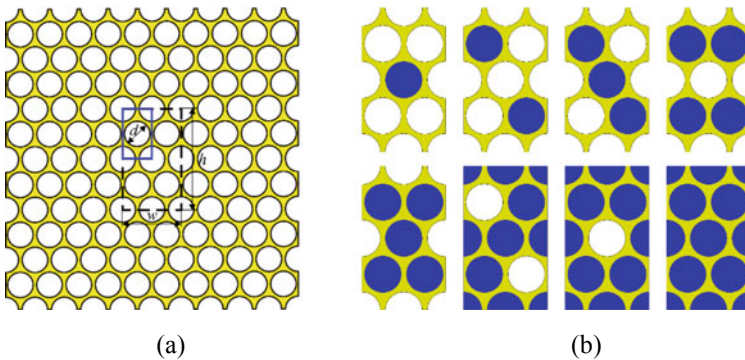
**Fig. 9.3** The second soft PnC: **a** The unit cell (solid line) and the RVE (dashed line); and **b** eight patterns of inserted rigid inclusions. $d$ is the diameter of the circular hole and $w$ and $h$ are the width and height of the RVE, respectively. (Reproduced with permission from Li et al. [14]. Copyright 2019 by Elsevier)

For the second PnC, the porosity $\psi$, which also represents the main geometric feature of the structure, is expressed as

$$\psi = \frac{2\pi d^2}{wh},\tag{9.2}$$

where $d$ is the diameter of the circular hole, and $w$ and $h$ are the width and height of the RVE, respectively.

## 9.3  Simulations

The structure of the first or second PnC is simple but not as regular as a uniform rectangular or circular plate for instance. Moreover, the host material exhibits nonlinear hyperelastic characteristics. Thus, it is very difficult, if not impossible, to derive the analytical solutions even in the static deformation case. Thus, we will adopt the finite element method (FEM) to carry out the simulations for both the static and dynamic responses. The dynamic responses here are specifically referred to the linear wave propagation which is superimposed on the statically deformed configuration.

### 9.3.1  Material Model and Basic Equations

The host material is hyperelastic and its mechanical behavior is assumed to be characterized by the compressible neo-Hookean model, with the energy density function given by:

$$W = C_0\big(\bar{I}_1 - 3\big) + \frac{K_0}{2}(J-1)^2\tag{9.3}$$

where $C_0 = \mu_0/2$, with $\mu_0$ being the initial shear modulus, $K_0$ is the initial bulk modulus, $\bar{I}_1$ is the first deviatoric strain invariant, and $J = \det(\boldsymbol{F})$ is the local volume change or volume ratio. Here $\boldsymbol{F}$ is the deformation gradient, which is a basic measure of deformation of the body of interest.

The first Piola–Kirchhoff (PK) stress $\boldsymbol{S}$ can be obtained from the energy density function as

$$\boldsymbol{S} = \frac{\partial W}{\partial \boldsymbol{F}}.\tag{9.4}$$

The Cauchy stress then can be obtained from the first PK stress by the relation $\boldsymbol{\sigma} = J^{-1}\boldsymbol{S}\boldsymbol{F}^T$.

In the absence of body forces, the dynamic equilibrium equation may be written as

$$Div\,\boldsymbol{S} - \rho_0 \frac{D^2\boldsymbol{\chi}}{Dt^2} = \boldsymbol{0},\tag{9.5}$$

where $\rho_0$ is the material density in the initial (reference) configuration, $\boldsymbol{\chi}(X, t)$ is a mapping function, giving the current position vector $\boldsymbol{x}$ of a material particle originally at $X$ in the initial configuration (i.e. $\boldsymbol{x} = \boldsymbol{\chi}(X)$), $D/Dt$ is the material time derivative, and Div is the divergence operator with respect to the initial configuration. (In this chapter, the operator with the first character capital denotes that it is for the initial configuration, while that with a lower-case first character is for the current configuration.)

For static deformation analysis, the inertial term in Eq. (9.5) shall be discarded. For the linear elastic wave that is superimposed on the static finite deformation of the hyperelastic body, the above governing equations could be simplified and linearized. These new equations for the incremental motion are readily obtained from Eqs. 9.4 and 9.5 through linear perturbation [15], and are given by in the current configuration

$$\text{div}\,\dot{\boldsymbol{S}}_0 - \rho \frac{\partial^2\boldsymbol{u}}{\partial t^2} = \boldsymbol{0}\tag{9.6}$$

where $\boldsymbol{u}(x, t) = \dot{\boldsymbol{x}} = \dot{\boldsymbol{\chi}}(X, t)$ is the incremental displacement vector, and $\rho = J^{-1}\rho_0$ is the current material density. Here, an overdot indicates an incremental quantity and the subscript 0 denotes a "push forward" version, and hence $\dot{\boldsymbol{S}}_0$ is the "push forward" incremental first PK stress, which obeys the following approximate linear constitutive relations

$$\dot{\boldsymbol{S}}_0 = \boldsymbol{A}_0 : grad\,\boldsymbol{u},\tag{9.7}$$

where $\boldsymbol{A}_0$ is the fourth-order effective moduli tensor, with its components given by

$$A_{0ijks} = J^{-1}F_{j\alpha}F_{s\beta}A_{i\alpha k\beta},\tag{9.8}$$

where $\boldsymbol{A} = \partial^2 W(\boldsymbol{F})/\partial\boldsymbol{F}\partial\boldsymbol{F}$. The Einstein summation convention is adopted throughout this paper.

Equation (9.6) can be further written in the frequency domain for a harmonic wave for which all physical variables have a common factor $e^{-i\omega t}$, with $\omega$ being the circular frequency.

### 9.3.2 Finite Deformation and Linear Wave Propagation Analysis

Both uniaxial and biaxial loadings are considered here for illustration, as shown in Fig. 9.2 for the first soft PnC for example. For the biaxial loading, we can express the deformation gradient tensor as

$$\boldsymbol{F} = (1 + \varepsilon_x)\boldsymbol{e}_x \otimes \boldsymbol{e}_x + \left(1 + \varepsilon_y\right)\boldsymbol{e}_y \otimes \boldsymbol{e}_y, \tag{9.9}$$

where $\boldsymbol{e}_x$ and $\boldsymbol{e}_y$ are the base vectors in the Cartesian coordinates, and $\varepsilon_x$ and $\varepsilon_y$ denote the macroscopic nominal strains in the $x$ and $y$ directions, respectively, which may be described as [16]

$$\varepsilon_x = \lambda \cos \theta, \, \varepsilon_y = \lambda \sin \theta \tag{9.10}$$

where $\lambda$ ($\lambda \geq 0$) denotes the loading parameter, and $\theta$ is the loading path angle, which is related to the ratio between $\varepsilon_x$ and $\varepsilon_y$. For example, $\theta = \pi/4$ and $\theta = 5\pi/4$ correspond to the equi-biaxial tension and compression, respectively.

It should be noted that for the uniaxial loading, say $\varepsilon_x \neq 0$ in the $x$ direction, the nominal strain in the $y$ direction also doesn't vanish. Actually, $\varepsilon_y$ should be determined from the corresponding free boundary condition.

As mentioned earlier, for the soft PnCs, we employ the FEM to simulate their static and dynamic responses via the commercial software platform ABAQUS. To do so, we first consider the RVE, which is taken from the infinite periodic structure as shown in Fig. 9.1 or 9.3. Then, we apply to the boundary of the RVE the periodic conditions for the finite deformation analysis and the Bloch conditions for the linear wave propagation analysis, respectively.

In the finite deformation analysis, two virtual nodes are introduced to model the deformation of the RVE along the two periodic directions (i.e. $x$ and $y$ directions as indicated in Fig. 9.2), while the periodic boundary conditions are used to establish the coupling and constraint equations through the motion of each virtual node [14]. Due to the holes existing in the two PnCs, buckling usually happens when they deform to a certain extent under compression [7, 8]. To determine the corresponding critical loads, a linear theory for the incremental field similar to that for linear wave propagation should be adopted. Then the eigenvalue buckling analysis in Abaqus could be invoked conveniently to obtain the critical loads and the corresponding buckling modes. The post-buckling deformation of the structure is also of interest because it can lead to a more significant change in the geometry and effective material properties of the PnCs. The post-buckling deformation can be numerically induced by introducing a reasonable geometrical imperfection corresponding to a certain buckling mode using the modified pseudo arc-length method (i.e. Riks algorithm) in Abaqus [17].

In order to investigate the propagation of linear elastic waves in a two-dimensional (either plane-strain or plane-stress) infinite periodic structure, a primitive unit cell should be defined by a set of base vectors $\boldsymbol{a}_i$ ($i = 1, 2$) and the corresponding reciprocal lattice vectors $\boldsymbol{b}_j$ ($j = 1, 2$), which satisfy

$$\boldsymbol{a}_i \cdot \boldsymbol{b}_j = 2\pi \delta_{ij}, \tag{9.11}$$

where $\delta_{ij}$ is the Kronecker delta. The location of a point $\boldsymbol{x}$, may be rewritten as

$$\boldsymbol{x} = \boldsymbol{r} + \boldsymbol{x}_0, \tag{9.12}$$

where $r = n_i a_i$ with $n_i$ being integers, and $x_0$ denotes the relative position within the primitive unit cell. Thus, for a periodic function $f(x)$, we have

$$f(x) = f(r + x_0) = f(x_0) \tag{9.13}$$

For the elastic wave propagating in a periodic structure, we shall employ the following Bloch conditions [18]:

$$\kappa(r + x_0) = \kappa(x_0)e^{i(k \cdot r)} = \kappa(x_0)e^{i(k_0 \cdot r)}, \tag{9.14}$$

where $\kappa$ is the amplitude vector of any physical quantity (e.g. displacement, stress) and $k$ is the wave vector specified in the reciprocal space, which can be expressed as

$$k = m_i b_i + k_0 \tag{9.15}$$

Here $m_i$ are integers, and $k_0$ is the wave vector in the primitive lattice.

To obtain the dispersion relation or band structure, which is actually the relation between the circular frequency $\omega$ and the Bloch wave number vector $k_0$ (with two components, i.e. the wave numbers), we can consider only those values of $k_0$ located on the boundary of the irreducible first Brillouin zone (see Fig. 9.4), which will be called the reduced wave vector (but still denoted as $k$ for simplicity) later. It should be noted that, the resulting eigenvalue problem is actually complex-valued, caused by the Bloch conditions in Eq. (9.14). Thus, following Åberg and Gudmundson [19], we take two instances with identical mesh and material properties, representing the real and imaginary parts of the corresponding fields respectively, to overcome this particular difficulty.
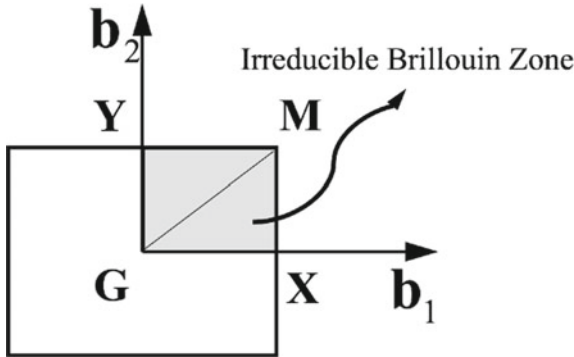


**Fig. 9.4** The first Brillouin zone and the irreducible Brillouin zone (grey area, bounded by the boundary GXMYG) for a rectangular primitive unit cell as in the second PnC. When the primitive unit cell is square (as for the first PnC before loading), the irreducible Brillouin zone can be further reduced by half, which is bounded by the boundary GXMG. $b_j$ are the reciprocal lattice vectors of the primitive unit cell. (Reproduced with permission from Li et al. [14]. Copyright 2019 by Elsevier)

The periodic conditions necessary in the static deformation (including buckling and post-buckling) analysis and the Bloch conditions required in the wave propagation analysis are all implemented in the CAE environment of ABAQUS. Script files written in Python have been developed to conveniently carry out the related automatic modeling, meshing, and calculations [20].

To compare with the experimental results, we also need to consider the dynamic responses of a finite structure. To this end, the module of steady-state dynamics analysis in Abaqus is utilized to obtain the steady-state response of the structure subject to a harmonic load over a frequency range of interest. With the acceleration amplitudes at the output and input sides of the model, denoted as $A_{output}$ and $A_{input}$ respectively, we can calculate the transmittance $T$ according to the following formula

$$T = 20 \lg(A_{output}/A_{input}). \tag{9.16}$$

### 9.3.3  Numerical Results

In this subsection we present some results obtained via the finite element modeling for the two soft PnCs made of rubber. The material parameters adopted in the numerical modeling are summarized in Table 9.1.

#### 9.3.3.1  The First Soft PnC

For the first soft PnC, we use tension instead of compression to yield the pre-deformation which is in turn utilized to tune the wave propagation. Since tension generally doesn't induce buckling, we focus on the wave propagation behavior only. The in-plane size of the RVE is taken to be $2L_0 = 10$ mm, and the thickness is very large so that a plane-strain state is assumed. The results here are only part of those reported in Ref. [13], wherein in-depth discussions also can be found.

Figure 9.5 shows the influences of the two geometric parameters (i.e. the porosity $\psi$ and the major-to-minor half-axis ratio $\alpha$) on the band structure of the first soft PnC without pre-deformation. It is seen that both the width and number of bandgaps increase with $\alpha$. The porosity $\psi$ also affects the band structure obviously. In particular, there is no complete bandgap when $\psi = 40\%$, while there are two bandgaps for $\psi = 60\%$, with a very wide one appearing in the low-frequency range.

**Table 9.1**  Material properties

| Type of PnC | $\rho_0$ (g·cm$^{-3}$) | $K_0$ (MPa) | $C_0$ (MPa) |
|---|---|---|---|
| The first | 1.05 | 55 | 0.55 |
| The second | 1.30 | 50 | 0.25 |
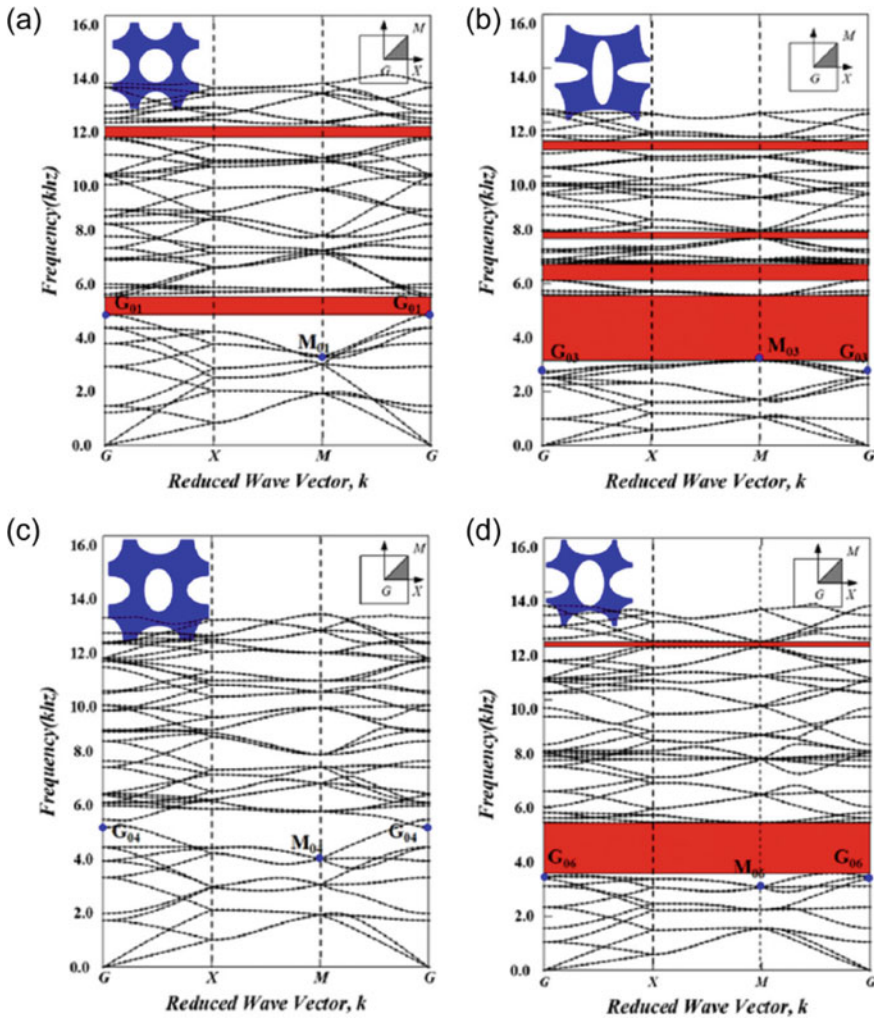
**Fig. 9.5** The band structure of the unloaded first PnC: **a** and **b** The porosity is fixed at $\psi = 50\%$, while the major-to-minor half-axis ratio is taken to be $\alpha = 1.0, 3.0$ respectively; **c** and **d** the major-to-minor half-axis ratio is fixed at $\alpha = 1.5$, while the porosity is taken as $\psi = 40, 60\%$ respectively. (Reproduced with permission from Gao et al. [13]. Copyright 2018 by Springer Nature)

The effects of the tensile load on the band structure of the first PnC are shown in Fig. 9.6. It is seen that increasing the tensile load continuously reduces the frequency range of the main bandgap. The number and frequency range of other bandgaps also vary with the loading magnitude and pattern (i.e. uniaxial or biaxial, depending on the loading path angle in Eq. (9.10)). It is worth pointing out that, the consequence of

tuning elastic waves using tensile load is just opposite to that using compressive load [7, 8], as expected. But there is a major difference, i.e. the tuning effect is very robust since the tension-induced deformation is insensitive to the initial imperfections that may exist in the PnC. This will be confirmed by the experiments to be shown later.
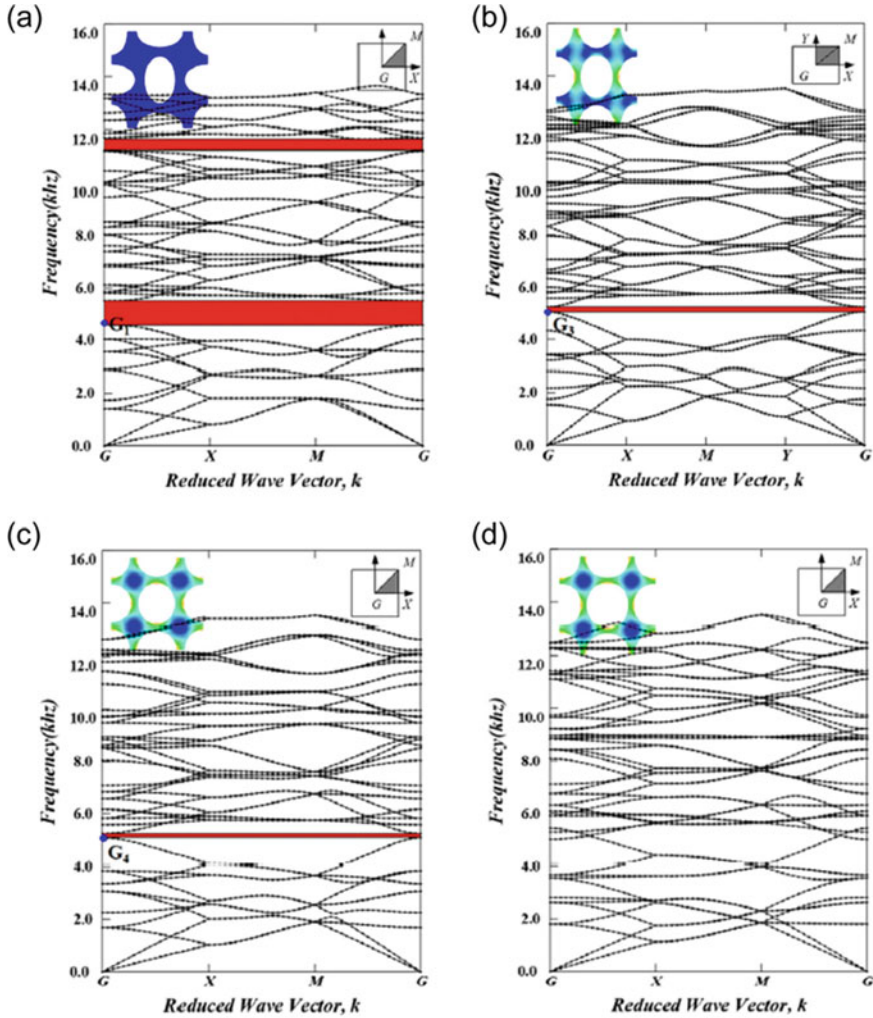


**Fig. 9.6** The band structure in the first PnC for $\psi = 50\%$ and $\alpha = 1.5$ under different tensile loads: **a** Unloading; **b** uniaxial tension $\varepsilon = 20\%$; **c** equi-biaxial tension $\varepsilon = 10\%$; and **d** equi-biaxial tension $\varepsilon = 10\%$. (Reproduced with permission from Gao et al. [13]. Copyright 2018 by Springer Nature)

### 9.3.3.2 The Second Soft PnC

For the second soft PnC, although we still use compression to make the pre-deformation, just like Refs. [7, 8], we insert rigid inclusions (made of steel, with Young's modulus 194.02 GPa, Poisson's ratio 0.3, and density 7930 kg/m$^3$) into some holes so as to enhance the robustness. The width of the RVE is taken to be $w$ =18.212 mm, its height is $h = \sqrt{3}w$, and the diameter of the circular hole is set as $d = 8$ mm. In this case, the porosity of the PnC without inclusions is $\psi = 70$ %. The results here are taken from Ref. [14], wherein in-depth discussions also can be found.

Compression will induce buckling. Figure 9.7 displays the first two buckling modes and the corresponding critical loads in the case of uniaxial compression in the $x$ or $y$ direction. While the first-order critical loads for the two loading cases are almost the same ($-0.056$), the difference between the first two critical loads in each loading case is quite obvious. This feature is very important since, to induce the subsequent post-buckling deformation, we need to introduce the initial geometrical imperfection, which corresponds to the first-order buckling mode, into the structure. If two buckling modes/loads are very close to each other, keeping the robustness of the post-buckling deformation corresponding to any buckling mode will become a big challenge either numerically or experimentally [16].

Figure 9.8 shows the effects on the band structure of inserting rigid inclusions into the holes of the second PnC without loading. It is interesting to observe that, only in the first case (i.e. when there are two rigid inclusions in a column), there are multiple complete bandgaps (gray areas) for frequencies lower than 1200 Hz. In the other three cases, only directional bandgaps (in the direction of G-Y, green areas) could be found. Thus, making a proper arrangement of the inserted rigid inclusions can enable the unidirectional suppression or propagation of elastic waves in the second PnC.
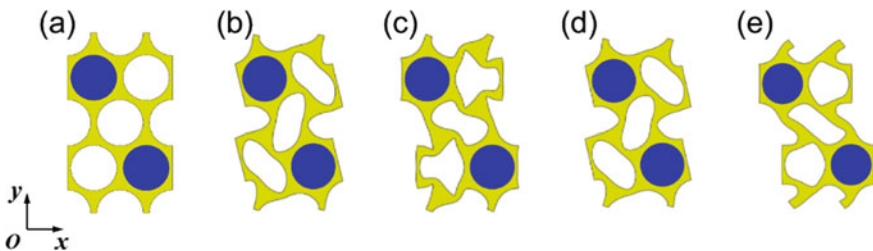


**Fig. 9.7** The first two buckling modes and the corresponding critical loads of the second PnC in the case of uniaxial compression: **a** RVE with two inclusions **b** $\varepsilon_x^{cr,1} = -0.056$; **c** $\varepsilon_x^{cr,2} = -0.165$; **d** $\varepsilon_y^{cr,1} = -0.056$; and **e** $\varepsilon_y^{cr,2} = -0.093$. Here in the superscript, "cr" denotes the critical load, $i = 1,\ 2$ signifies the order of the buckling mode. (Reproduced with permission from Li et al. [14]. Copyright 2019 by Elsevier)
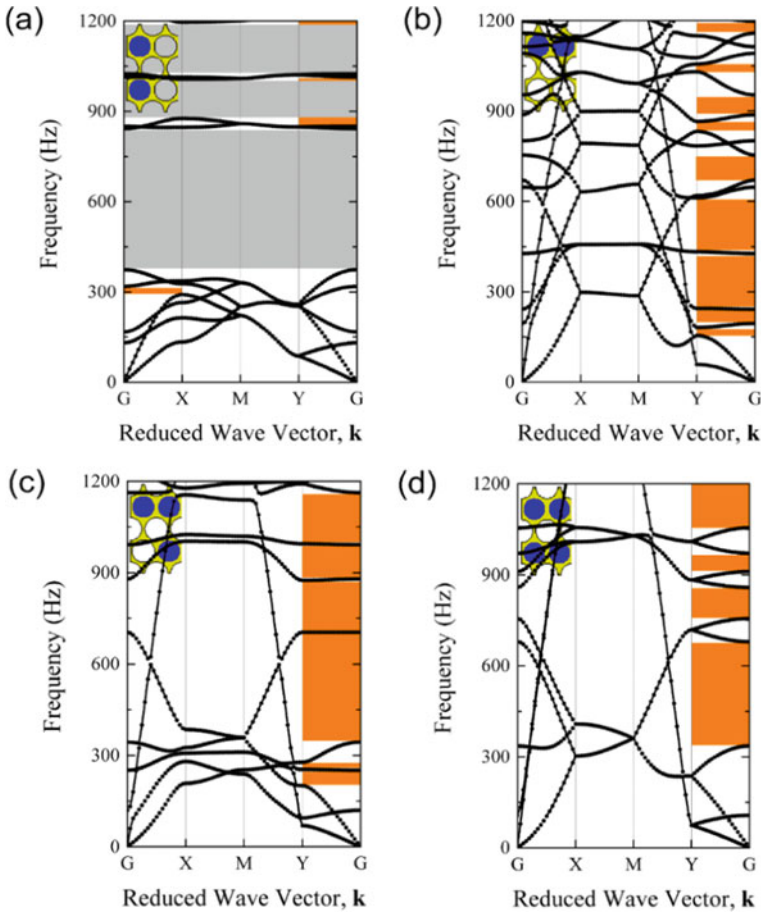
**Fig. 9.8** Effects of inserted rigid inclusions on the band structure of the second PnC without loading: **a** Two inclusions in a column; **b** Two inclusions in a row; **c** three inclusions; and **d** four inclusions. (Reproduced with permission from Li et al. [14]. Copyright 2019 by Elsevier)

We have numerically clarified that inserting two rigid inclusions in diagonal (as shown in Fig. 9.7) will ensure the robustness of the post-buckling deformation corresponding to either the first or second buckling mode. Now in Fig. 9.9, we present the effects of large deformation on the band structure of the second soft PnC with two diagonally inserted inclusions. It is seen that, in the case of no deformation, there will be a very wide complete bandgap with its frequency ranging from 314 to 1143 Hz. When there is an external compressive load, this complete bandgap narrows, but new bandgaps are present either in the lower or higher frequency range.
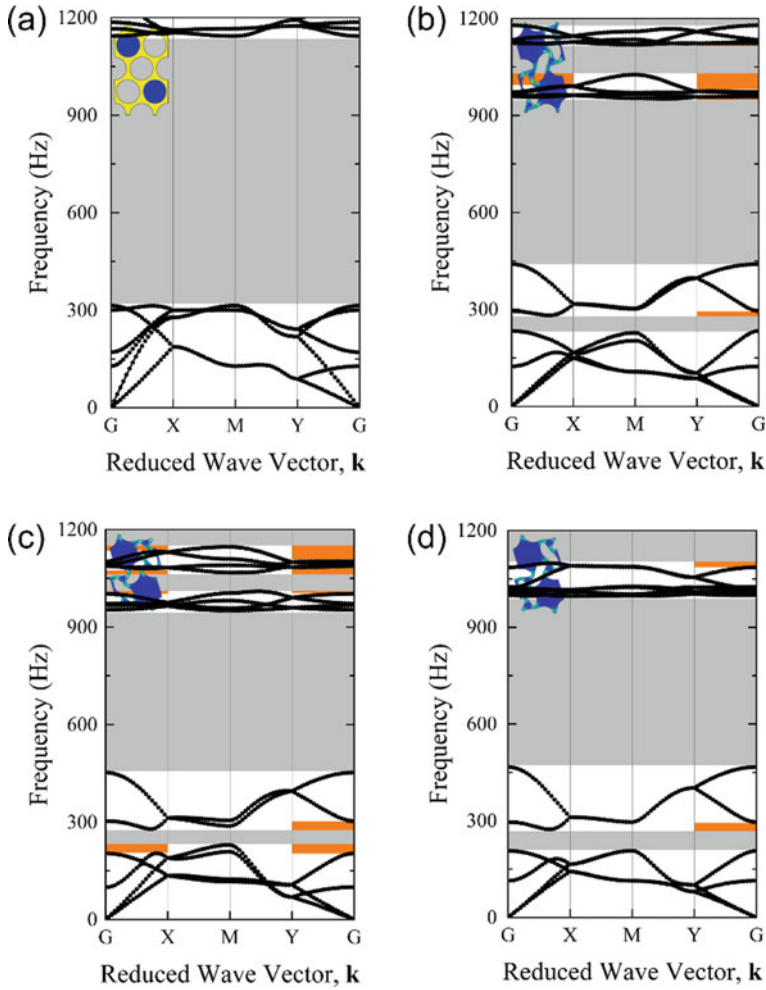
**Fig. 9.9** Effects of post-buckling deformation on the band structure of the second PnC under different compressions: **a** Unloading; **b** uniaxial compression in the $x$ direction with $\varepsilon_x = -0.15$; **c** uniaxial compression in the $y$ direction with $\varepsilon_y = -0.15$; and **d** equi-biaxial compression with $\varepsilon_x = \varepsilon_y = -0.15$. The inset in each panel gives the deformed configuration. (Reproduced with permission from Li et al. [14]. Copyright 2019 by Elsevier)

## 9.4 Experimental Validation

In Sect. 9.3, we have shown numerically that applying a tensile load on the first soft PnC and inserting rigid inclusions into certain holes of the second soft PnC can both robustly tune their deformation and wave propagation characteristics. Here in this section, we will present some typical experimental results and compare them with

the numerical simulations. More details of the experiments as well as the related discussions could be found in Refs. [14, 21].

## 9.4.1 Experiments on the First PnC

The sample of the first soft PnC used in experiments is shown in Fig. 9.10. The sample is made of silicone rubber (Mold Max 30, Smooth-On), and its total size is $240 \times 200 \times 6$ mm (Height×Width×Thickness). The actual material properties are shown in Table 9.2, and the experimental setup is also shown in Fig. 9.10 with the detailed descriptions given in Ref. [21].
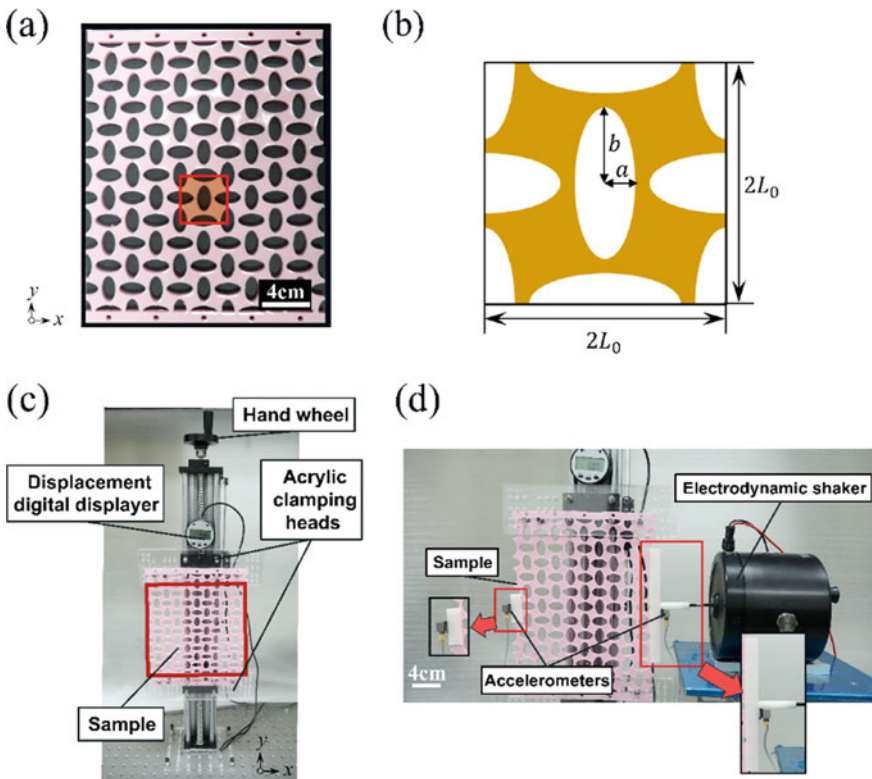


Fig. 9.10 Experiments on the first PnC: **a** The sample with the initial porosity $\psi = 52.84$ %, $\alpha = 2.0$ (the yellow-shaded area is an RVE); **b** the RVE; **c** device for uniaxial tension (in the vertical direction) and the red solid part is the effective part; **d** parts of the dynamic experimental setup with a harmonic excitation. (Reproduced from Ref. [21] with permission from the Royal Society of Chemistry)

**Table 9.2** Actual material properties of the second PnC in experiments

| $\rho_0\,(\mathrm{g\ cm}^{-3})$ | $K_0$ (MPa) | $C_0$ (MPa) |
|---|---|---|
| 1.05 | 63.92 | 0.13 |

Shown in Fig. 9.11 is the comparison of band structure and transmission (in the GX direction, or ΓX as indicated in the figure) of the first soft PnC between different methods (experimental, numerical) and situations (unloaded, uniaxially loaded). The comparison of the directional bandgap between experiment and simulation for the unloaded sample indicates a perfect agreement. Moreover, the numerical variation of the bandgap with the applied tension also agrees with that obtained experimentally. The comparison in Fig. 9.11 not only validates either the numerical method or the experimental approach, but also verifies the robustness of the first soft PnC.

### 9.4.2 Experiments on the Second PnC

The geometry of sample of the second soft PnC used in experiments is the same as that indicated in Fig. 9.3, comprising 5×3 RVEs. It is again made of rubber, with somewhat different material properties from the first PnC, as shown in Table 9.1. The in-plane size of the RVE is the same as that employed in numerical simulation. The thickness is about 50 mm so that the static and dynamic responses of the sample can be well controlled in an approximate plane-strain state. The static and dynamic experimental setups are shown in Figs. 9.12 and 9.13, respectively, while more details have been provided in Ref. [14].

To illustrate the inclusion-enhanced robustness of deformation of the second soft PnC, the intact one without inclusions is first considered. Two samples taken from the same batch are compressed uniaxially when the compressive strain is $\varepsilon = -0.20$. It is seen that the post-buckling deformation of the sample in Fig. 9.14a belongs to mode I as called by Shan et al. [16]. It is the numerically predicted first buckling mode of the intact PnC. But the second sample shown in Fig. 9.14b experiences a different situation. The post-buckling deformation in certain areas of the sample seems to be triggered by another buckling mode (mode II in the figure), deviating obviously from the numerical prediction.

Inserting rigid inclusions into the holes of the samples could enhance the robustness of the deformation of the second PnC, which is confirmed by the experiment as shown in Fig. 9.15 for three different compressive loads. The comparison with the numerical simulation also given in that figure clearly indicates perfect consistency between the two approaches. It is noted that the three deformed configurations shown in Fig. 9.15 are very similar and all induced by the same chiral mode. Thus, the post-buckling deformation of the second soft PnC with certain inserted rigid inclusions seems to be insensitive to the loading type and is much more robust than the intact PnC.
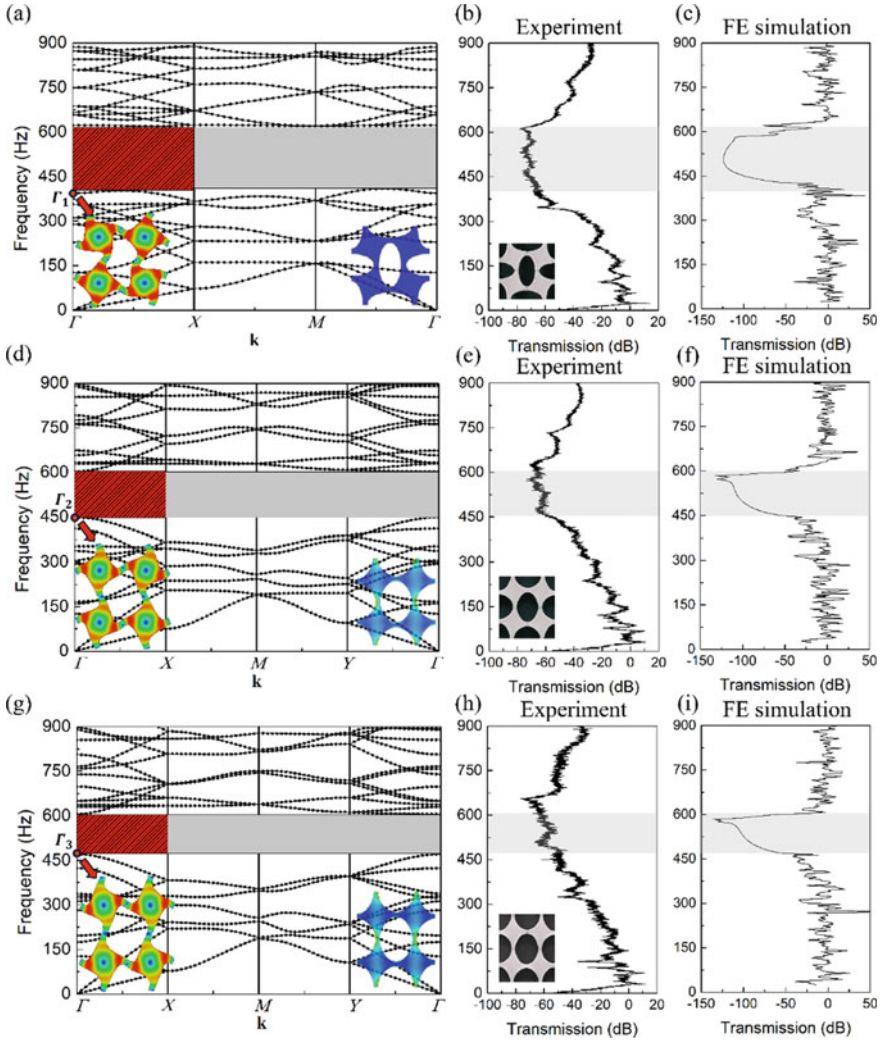
**Fig. 9.11** Effects of uniaxial tension on the low-frequency band structure: **a–c** are the simulated band diagram, experimental transmission spectrum and simulated transmission spectrum when $\varepsilon = 0$, respectively; **d–f** are those when $\varepsilon = 0.15$; **g–i** are those when $\varepsilon = 0.25$. (Reproduced from Ref. [21] with permission from the Royal Society of Chemistry)

The wave propagation characteristics in the second soft PnC could also be tuned by, in addition to the large deformation, inserting rigid inclusions into its holes. The experimental transmittance curves for waves propagating both in the G-X and G-Y directions obtained by the testing devices shown in Fig. 9.13 are displayed in Fig. 9.16, which are compared with the numerical transmittance curves and the band structures (also given in Fig. 9.8a). The comparison indicates a good agreement
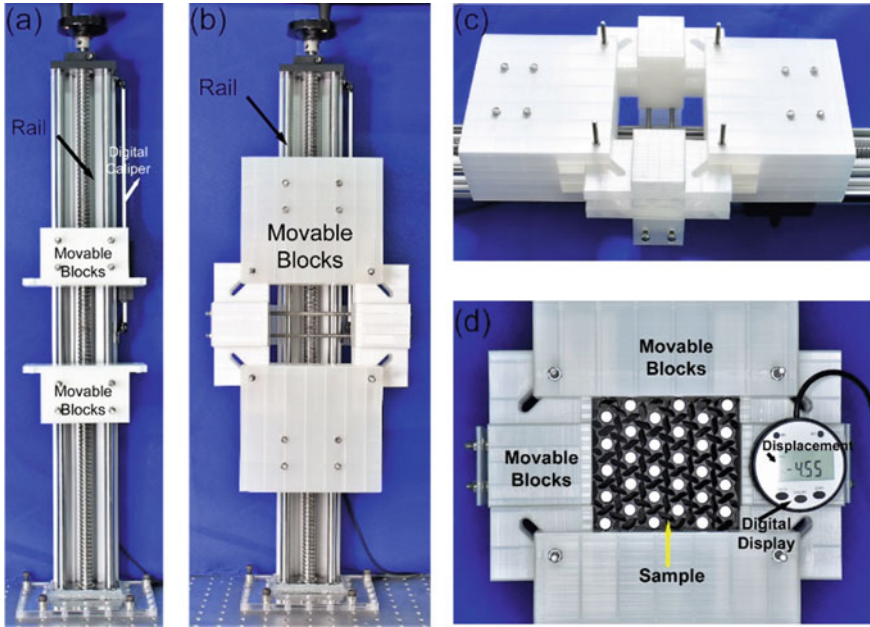
**Fig. 9.12** Devices for uniaxial and equi-biaxial compression tests: **a** Uniaxial compression; **b** equi-biaxial compression; **c** axonometric picture of equi-biaxial compression device; **d** process of equi-biaxial compression. (Reproduced with permission from Li et al. [14]. Copyright 2019 by Elsevier)

between the experimental and numerical results, especially in terms of the bandgaps. Nevertheless, the experiment shows a remarkable attenuation characteristic in the high-frequency range (and also outside the main bandgap). This observation could be attributed to the material damping in rubber that should be taken into consideration for the second soft PnC with a very large thickness. By incorporating the material loss factor $\eta = 0.061$ (which is experimentally evaluated via the DMA test [14]) into the simulation, the same phenomenon can be observed numerically, as shown in Fig. 9.16.

## 9.5 Conclusions

In this chapter, we present two designs of soft PnCs, both can be seen as a high-contrast elastic composite. It is shown that the periodicity of the meso-structure in such composites may realize particular band structures that are needed for novel acoustic devices. The capability of reversible large deformation (including buckling and post-buckling) can be invoked to tune the deformation and wave propagation characteristics in the soft PnCs. However, the existing tunable soft PnCs reported
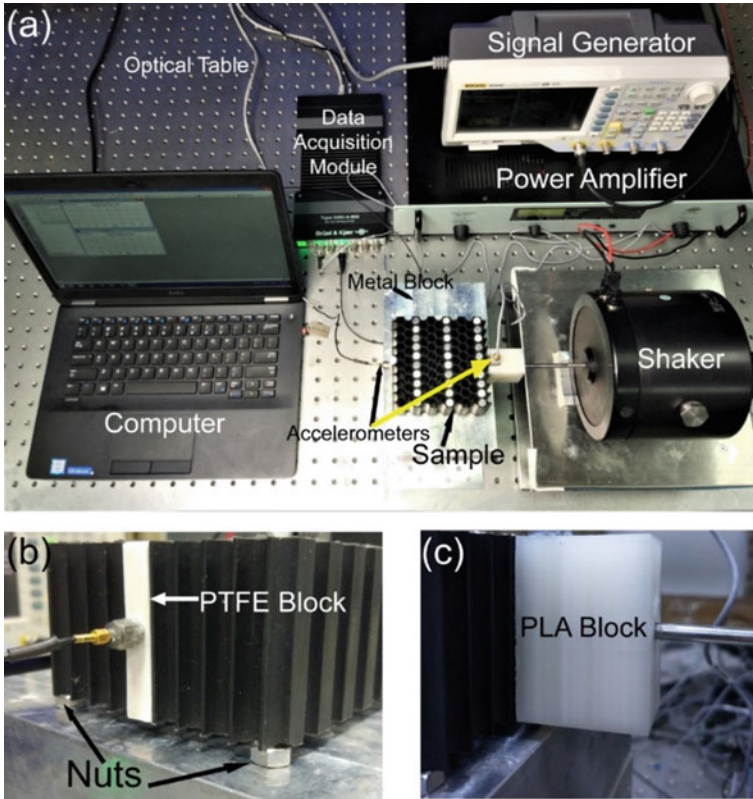
**Fig. 9.13** Devices for wave propagation test. (Reproduced with permission from Li et al. [14]. Copyright 2019 by Elsevier)
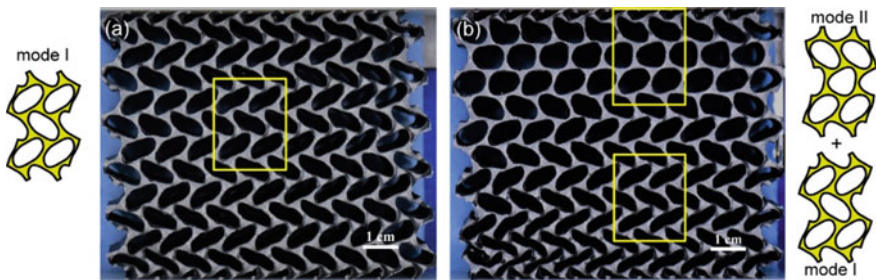


**Fig. 9.14** Comparison between two samples of the second PnC with possibly different geometric imperfections subject to the same compression. (Reproduced with permission from Li et al. [14]. Copyright 2019 by Elsevier)
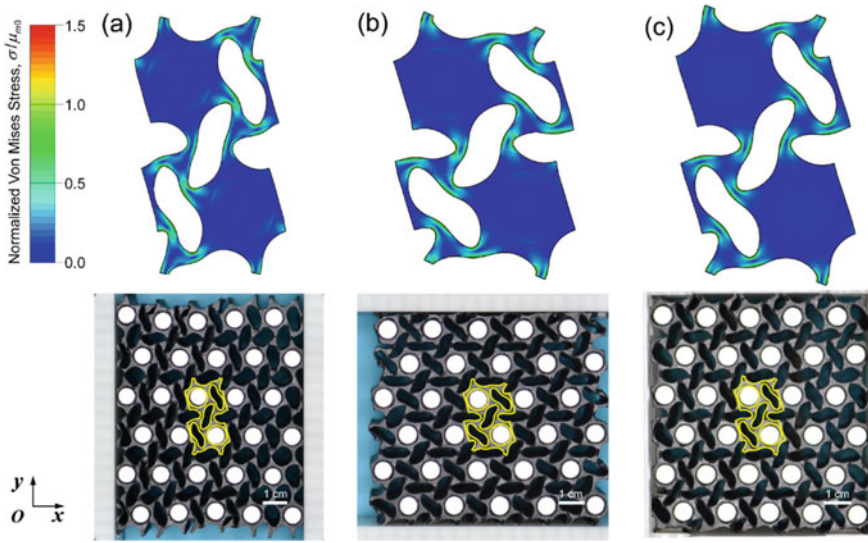
**Fig. 9.15** Experimental and numerical results for the second PnC with diagonally inserted rigid inclusions under compressive loads: **a** Uniaxial compression in the $x$ direction with $\varepsilon_x = -0.15$; **b** uniaxial compression in the $y$ direction with $\varepsilon_y = -0.15$; and **c** equi-biaxial compression with $\varepsilon_x = \varepsilon_y = -0.15$. (Reproduced with permission from Li et al. [14]. Copyright 2019 by Elsevier)
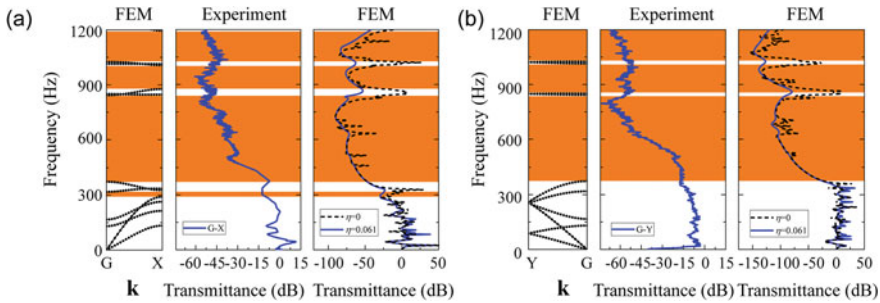


**Fig. 9.16** Experimental transmittance curves for the second soft PnC with inserted rigid inclusions in a column in the RVE without loading and their comparison with the calculated band structures and transmittance spectra: **a** In the direction of G-X; and **b** in the direction of G-Y. $\eta$ is the loss factor, which characterizes the magnitude of material damping and can be readily incorporated into the wave propagation simulation in ABAQUS. (Reproduced with permission from Li et al. [14]. Copyright 2019 by Elsevier)

by other researchers are usually subject to a compressive load to induce large post-buckling deformation, which is susceptible to the initial flaws in the structure. To surmount the difficulty so as to enhance the robustness of deformation and wave propagation, we introduce two approaches to the design of tunable soft PnCs. One is to use tension instead of compression to induce large deformation in a soft porous

PnC with criss-crossed elliptical holes. The other is to insert rigid inclusions into certain holes of a soft porous PnC with circular holes subjected to compression. Both numerical and experimental efforts have been made to illustrate the feasibility of robustly tuning these two soft PnCs.

The results presented in this chapter should be helpful to the reader who is interested in developing practically useful soft PnCs. The results are just a brief summary of our published papers [13, 14, 21], and the reader is referred to these publications for more details concerning numerical simulations, experiments and discussions.

Recently, topological acoustic metamaterials, which can reproduce the classical quantum effects remarkably at macroscale, have become an intensive research focus [22–24]. Soft hyperelastic materials have been shown to be a perfect candidate to realize various tunable acoustic topological states [25, 26]. Combining soft (porous) materials with hard inclusions to make high-contrast elastic composites, we then may be able to create more possibilities to arrive at novel, high-performance, and practically useful tunable topological acoustic devices.

# References

1. Kushwaha MS, Halevi P, Dobrzynski L, Djafari-Rouhani B (1993) Acoustic band structure of periodic elastic composites. Phys Rev Lett 71(13):2022–2025
2. Hussein MI, Leamy MJ, Ruzzene M (2014) Dynamics of phononic materials and structures: historical origins, recent progress, and future outlook. Appl Mech Rev 66(4):040802
3. Zhu XN, Zhang X (2018) Metamaterials: Artificial materials beyond nature. Natl Sci Rev 5(2):131
4. Kadic M, Milton GW, van Hecke M, Wegener M (2019) 3D metamaterials. Nature Reviews Physics 1:198–210
5. Goffaux C, Vigneron JP (2001) Theoretical study of a tunable phononic band gap system. Phys Rev B 64:075118
6. Wang YF, Wang YZ, Wu B, Chen WQ, Wang YS (2020) Tunable and active phononic crystals and metamaterials. Appl Mech Rev 72(4):040801
7. Bertoldi K, Boyce MC (2008) Mechanically-triggered transformations of phononic band gaps in periodic elastomeric structures. Phys Rev B 77:052105
8. Bertoldi K, Boyce MC (2008) Wave propagation and instabilities in monolithic and periodically structured elastomeric materials undergoing large deformations. Phys Rev B 78:184107
9. Wang L, Bertoldi K (2012) Mechanically tunable phononic band gaps in three-dimensional periodic elastomeric structures. Int J Solids Struct 49:2881–2885
10. Wang P, Shim J, Bertoldi K (2013) Effects of geometric and material non-linearities on the tunable response of phononic crystals. Phys Rev B 88:014304
11. Wang P, Casadei F, Shan S, Weaver JC, Bertoldi K (2014) Harnessing buckling to design tunable locally resonant acoustic metamaterials. Phys Rev Lett 113:014301
12. Babaee S, Wang P, Bertoldi K (2015) Three-dimensional adaptive soft phononic crystals. J Appl Phys 117:244903

13. Gao N, Huang YL, Bao RH, Chen WQ (2018) Robustly tuning bandgaps in two-dimensional soft phononic crystals with criss-crossed elliptical holes. Acta Mech Solida Sin 31(5):573–588
14. Li J, Wang YT, Chen WQ, Wang YS, Bao RH (2019) Harnessing inclusions to tune post-buckling deformation and bandgaps of soft porous periodic structures. J Sound Vib 459:11848
15. Ogden RW (1997) Non-linear Elastic Deformations. Dover Publications, New York
16. Shan S, Kang SH, Wang P, Qu C, Shian S, Chen ER, Bertoldi K (2014) Harnessing multiple folding mechanisms in soft periodic structures for tunable control of elastic waves. Adv Func Mater 24:4935–4942
17. Dassault S Simulia Corp (2014) Abaqus analysis user's guide. Providence, Rhode Island
18. Brillouin L (1953) Wave Propagation in Periodic Structures. Dover, New York
19. Åberg M, Gudmundson P (1997) The usage of standard finite element codes for computation of dispersion relations in materials with periodic microstructure. J Acoust Soc Am 102:2007–2013
20. Huang Y, Gao N, Chen WQ, Bao RH (2018) Extension/compression-controlled complete band gaps in 2D chiral square-lattice-like structures. Acta Mech Solida Sin 31(1):51–65
21. Gao N, Li J, Bao RH, Chen WQ (2019) Harnessing uniaxial tension to tune Poisson's ratio and wave propagation in soft porous phononic crystals: An experimental study. Soft Matter 15:2921–2927
22. Ge H, Yang M, Ma C, Lu MH, Chen YF, Fang N, Sheng P (2018) Breaking the barriers: Advances in acoustic functional materials. Natl Sci Rev 5(2):159–182
23. Gao N, Qu SC, Si L, Wang J, Chen WQ (2021) Broadband topological valley transport of elastic wave in reconfigurable phononic crystal plate. Appl Phys Lett 118:063502
24. Chen Y, Zhang Q, Zhang YF, Xia BZ, Liu XN, Zhou XM, Chen CQ, Hu GK (2021) Research progress of elastic topological materials. Advances in Mechanics 51(2):1–69 (in Chinese)
25. Huang YL, Huang Y, Chen WQ, Bao RH (2020) Flexible manipulation of topologically protected waves in one-dimensional soft periodic plates. Int J Mech Sci 170:150348
26. Chen YJ, Wu B, Li J, Rudykh S, Chen WQ (2021) Low-frequency tunable topological interface states in soft phononic crystal cylinders. Int J Mech Sci 191:106098

# Chapter 10
# Blur Effect in a Multiple Particle Inverse Problem for Fiber-Reinforced Composites

**V. Mityushev, Zh. Zhunussova, K. Dosmagulova, and H. Akca**

**Abstract** The Prony method of scattering data analysis is extended to an inverse problem for a fiber-reinforced composite. Unidirectional fibers of shear moduli $\mu_k$ ($k = 1, 2, \ldots, n$) are embedded in the host of shear modulus $\mu$. We consider antiplane strain of the fibrous composite when a section perpendicular to the axis of fibers is the unit disk which contains $n$ non-overlapping inclusions. The contact between the components is supposed to be perfect. The main attention is paid to rigid inclusions when $\mu_k \gg \mu$. Let the longitudinal displacement $u$ be given on the unit circle. Other components of displacement vanish in the unit disk in the antiplane statement. The considered problem is written in terms of complex potentials and solved by a method of functional equations. In particular, the out-of-plane traction proportional to the normal derivative $\frac{\partial u}{\partial \mathbf{n}}$ is found on the unit circle. This yields a constructive method to the symbolic approximation of the Dirichlet-to-Neumann operator for an arbitrary multiply connected circular domain. The method is applied to the inverse problem for non-overlapping equal disks whose centers $a_k$ ($k = 1, 2, \ldots, n$) have to be determined. Let the displacement $u$ and the traction $\mu \frac{\partial u}{\partial \mathbf{n}}$ be given on the outer unit circle. We construct explicitly a polynomial $P_n(z)$ whose complex roots coincide with the centers of inclusions $a_k$. This result can be considered as a solution to the special Prony problem. The considered examples demonstrate the effect of blurring for large $n$ when disks in the near-boundary vicinity are properly determined. The location of the deeper disks is blurry and can be determined by the same equation $P_n(z) = 0$ but solved with higher accuracy.

V. Mityushev
Faculty of Computer Science and Telecommunications, Cracow University of Technology, Kraków, Poland

V. Mityushev (✉) · Zh. Zhunussova · K. Dosmagulova
Institute of Mathematics and Mathematical Modeling, Almaty, Kazakhstan
e-mail: wladimir.mitiuszew@pk.edu.pl

Zh. Zhunussova · K. Dosmagulova
Al-Farabi Kazakh National University, Almaty, Kazakhstan

H. Akca
Abu-Dhabi University, Adu-Dhabi, UAE
e-mail: haydar.akca@adu.ac.ae

## 10.1  Introduction

Reconstruction of inhomogeneities from boundary measurements is a fundamental problem of geophysics and material sciences [1, 2]. Inhomogeneities in dispersed two-phase media can be considered as a set of particles located in the host material. An inverse problem consists in the determination of particle location and their physical properties by boundary data [3]. The developed mathematical methods allow determining the location of a few particles near the boundary and their shapes. Determination of the location of a large number of particles distributed by the depth from the boundary is a challenging problem having various applications in porous media and material science. The present paper is devoted to the statement of a new inverse-type problem for a large number of inclusions. The shape of inclusions is supposed to be given contrary to the traditional statement and their location is the goal of our study. We state such a problem for circular inclusions and develop an algorithm to detect their centers. The numerical examples demonstrate its efficiency near the boundary and the blurring location of particles at the critical depth.

The antiplane strain is governed by the Laplace equation. Analogous problems are studied in the theory of the steady heat conduction and other topics of physics [1, 2, 4–7]. The literature on the uniqueness and stability of the shape inverse problems is very rich and covers a wide range of questions discussed in [8–12].

The standard Dirichlet and Neumann boundary conditions are used on the fixed outer boundary of the multiply connected domain $D$ displayed in Fig. 10.1, when the displacement component $u$ parallel to the axis of fibrous composite and the normal derivative $\frac{\partial u}{\partial \mathbf{n}}$ (traction) are given on the unit circle. The contact between the host $D$ and the inclusions $D_k$ is assumed to be perfect. The shapes of $\partial D_k$ are supposed to be known.

In the present paper, we propose a new statement of the inverse problem when the shape of each inclusion is fixed as a disk of radius $r_k$ ($k = 1, 2, \ldots, n$). Though the method is theoretically developed for different radii, its implementation is performed for equal radii when $r_k = r$. We detect the centers of unidirectional fibers $a_k$ ($k = 1, 2, \ldots, n$) in a section perpendicular to their direction. This problem may yield an approximate solution to the two-dimensional shape problem since any shape can be arbitrarily approximated by packing disks [13]. Though the statement of the previously discussed inverse shape problem formally includes a multiply connected domain with an arbitrary connectivity $n$, the existing publications actually contain numerical results at most for three inclusions. We develop an analytical method for the detection of inclusions with the concentration $\phi = nr^2$ in the unit disk. The case of large $n \sim 150$, small $r$ and the moderate concentration $\phi$ is discussed. In the considered statement, the values $\phi$ and $r$ are assumed to be given.

It is worth noting that the discussed inverse problem with the given external stresses essentially differs from the trivial problem with point sources. Moreover, the problem with active interior points cannot be used as an approximation to the problem with passive inclusions, since the problem with point sources has vanishing

**Fig. 10.1** Circular
inclusions in the unit disk
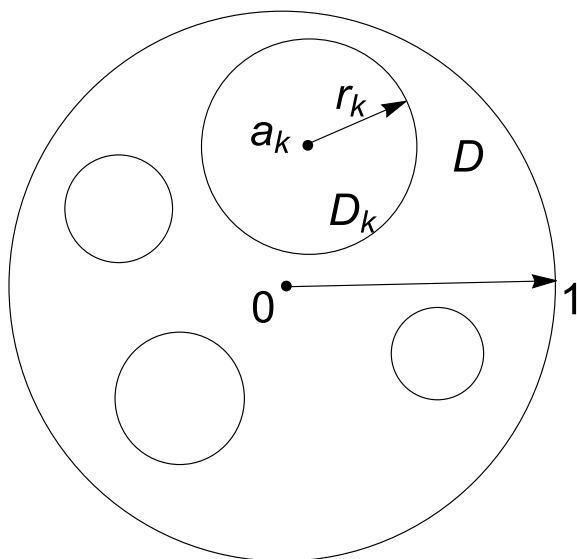


concentration. Such a source problem becomes similar to our problem when a source belongs to an inclusion whose size is not infinitesimally small.

This paper is organized as follows. The direct boundary value problem is discussed in Sect. 10.2. The longitudinal displacement $u$ is given on the unit circle and satisfies the Laplace equation in the components of the unit disk. This problem is solved by a method of functional equations [14, 15]. Using this result, we find the normal derivative $\frac{\partial u}{\partial \mathbf{n}}$ on the outer unit circle. The symbolic approximation of the Dirichlet-to-Neumann operator for an arbitrary multiply connected circular domain is described in Sect. 10.2.1. In Sect. 10.2.1.1, we pass to the inverse problem and equate the calculated function $\frac{\partial u}{\partial \mathbf{n}}$ on the unit circle to a given function. This yields a functional relation which contains a discrete set of unknown parameters.

The further investigation is similar to the Prony model for radar cross-section data [16]. The obtained functional relation is reduced to the following algebraic equations:

$$\sum_{k=0}^{n} X_k a_k^s = b_s, \qquad s = 0, 1, \ldots, N-1, \tag{10.1}$$

where $b_s$ are given complex numbers. The centers of inclusions $a_k$ ($k = 1, 2, \ldots, n$) are considered as unknown complex numbers. The real parameter $X_k$ is related by a simple formula with the shear modulus of inclusion $\mu_k$ ($k = 1, 2, \ldots, n$). The number of equations $N$ has to be preselected. Equation (10.1) were used in [16] for approximation of target, e.g., a simply connected domain, by means of the set of discrete scattering centers. It was proved that there exists a monic polynomial $P_N(z)$ of degree $N \geq n$ whose $n$ roots correspond to the scattering centers and the remaining roots are spurious. The coefficients of $P_N(z)$ satisfy the system of linear

algebraic equations written in [16]. The general solvability conditions for the inverse problems and their relations to a harmonic moments problem are beyond the scope of this paper and can be found in [12, 17]. We concentrate our attention on the exact formulas in the special statement.

In the case of two-phase high-contrast monodispersed composites, all $X_k$ can be normalized to unity. In the present paper, the outlined above Prony method can be simplified for such a composite. Using general relations on symmetric polynomials, we construct the polynomial $P_n(z)$ explicitly, where $n$ is the number of unknown inclusions. This result is new, since the coefficients of $P_n(z)$ were found numerically in the previous works through a system of linear algebraic equations.

In the present paper, we discover the effect of blurring when the roots of equation $P_n(z) = 0$ for $n \approx 150$ near the boundary $|z| = 1$ are accurately detected. The roots located far away from $|z| = 1$ could not be found except by very high-precision computations.

## 10.2  Boundary Value Problem for a Multiply Connected Domain

Consider $n$ unidirectional fibers of shear moduli $\mu_k$ $(k = 1, 2, \ldots, n)$ embedded in the host of shear modulus $\mu$. Let the fibers be directed along the $x_3$ coordinate axis, and a section perpendicular to fibers belong to the plane $(x_1, x_2)$. Introduce a complex variable $z = x_1 + ix_2$. Let the sections of fibers be mutually disjoint disks $|z - a_k| < r_k$ denoted below by $D_k$ $(k = 1, 2, \ldots, n)$. Here, the centers of disks are expressed in terms of complex numbers $a_k$. The complement of all the disks $|z - a_k| \leq r_k$ to the unit disk is denoted by $D$. For definiteness, let the point $z = 0$ belong to $D$, hence, $|a_k| > r_k$ for all $k = 1, 2, \ldots, n$. An example of the unit disk with circular inclusions is displayed in Fig. 10.1.

The antiplane strain problem can be stated as a boundary value problem for complex potentials defined in the domains $D$ and $D_k$ $(k = 1, 2, \ldots, n)$ of the complex plane [18]. Let $u_k(z)$ and $u(z)$ denote the longitudinal component of displacement in $|z - a| < r_k$ and in $D$, respectively. These functions satisfy the Laplace equation in the corresponding domains, for instance,

$$\frac{\partial^2 u}{\partial x_1^2} + \frac{\partial^2 u}{\partial x_2^2} = 0 \quad \text{in } D. \tag{10.2}$$

The stresses are expressed through the derivatives of the displacement

$$\sigma_{13} = \sigma_{31} = \mu \frac{\partial u}{\partial x_1}, \quad \sigma_{23} = \sigma_{32} = \mu \frac{\partial u}{\partial x_2} \quad \text{in } D. \tag{10.3}$$

Analogous formulas take place in $D_k$. Other components of displacement and stress tensor vanish in the antiplane statement.

The perfect contact along the circle $|z - a_k| = r_k$ is expressed by equal displacements and normal stresses from both sides of the circle. It can be written in the form of the following two equations [15, 18]:

$$u(z) = u_k(z), \qquad \mu \frac{\partial u}{\partial \mathbf{n}}(z) = \mu_k \frac{\partial u_k}{\partial \mathbf{n}}(z), \qquad |z - a_k| = r_k, \qquad (10.4)$$

where $\frac{\partial}{\partial \mathbf{n}}$ denote the normal derivative to the circle $|z - a_k| = r_k$. Let the displacement $u(z)$ be given at the outer boundary

$$u(z) = h(z), \qquad |z| = 1, \qquad (10.5)$$

where $h(z) = \mathrm{Re}\ f(z)$ with $f(z)$ analytic in $|z| < 1$. It is assumed that the derivative of $f(z)$ is Hölder-continuous in $|z| \le 1$.

Introduce the complex potentials $\varphi_k(z)$ in $|z - a| < r_k$ and $\varphi(z)$ in $D$ in such a way that

$$u(z) = \mathrm{Re}\ \varphi(z), \quad u_k(z) = \frac{2\mu}{\mu + \mu_k} \mathrm{Re}\ \varphi_k(z) \equiv (1 - \varrho_k)\ \mathrm{Re}\ \varphi_k(z), \qquad (10.6)$$

where $\varrho_k$ denotes the contrast parameter  introduced by Bergman [19]

$$\varrho_k = \frac{\mu_k - \mu}{\mu_k + \mu}. \qquad (10.7)$$

The stresses are expressed through the complex potentials by equations

$$\sigma_{13} - i\sigma_{23} = \mu\varphi'(z),\ z \in D, \quad \sigma_{13} - i\sigma_{23} = \frac{2\mu_k\mu}{\mu + \mu_k}\varphi_k'(z),\ z \in D_k. \qquad (10.8)$$

The functions $\varphi_k(z)$ and $\varphi(z)$ are analytic in $|z - a| < r_k$ and $D$, respectively, continuously differentiable in the closures of the considered domains. Two real conjugation conditions (10.4) can be written as one complex $\mathbb{R}$-linear condition [15]

$$\varphi(t) = \varphi_k(t) - \varrho_k\overline{\varphi_k(t)}, \quad |t - a| = r_k. \qquad (10.9)$$

The conditions (10.5) can be written in the form [15]

$$\varphi(t) = \varphi_0(t) - \overline{\varphi_0(t)} + f(t), \quad |t| = 1, \qquad (10.10)$$

where the functions $\varphi_0(z)$ and $f(z)$ are analytic in $|z| > 1$ and $|z| < 1$, respectively, and continuously differentiable in $|z| \ge 1$ and $|z| \le 1$.

Following [15], on differentiating (10.8) and (10.9), we deduce

$$\varphi'(t) = \varphi_k'(t) + \frac{\varrho_k r_k^2}{(t - a_k)^2} \overline{\varphi_k'(t)}, \quad |t - a| = r_k, \tag{10.11}$$

$$\varphi'(t) = \varphi_0'(t) + \frac{1}{t^2} \overline{\varphi_0'(t)} + f'(t), \quad |t| = 1.$$

Introduce the function analytic in $D$ and continuous in its closure

$$\psi(z) = z\varphi'(z). \tag{10.12}$$

Along similar lines, introduce the functions $\psi_0(z) = z\varphi_0'(z)$ and $\psi_k(z) = z\varphi_k'(z)$ analytic in $|z| > 1$ and $|z - a_k| < r_k$, respectively. Consider the inversion with respect to the circle $|t - a| = r_k$

$$z_{(k)}^* = \frac{r_k^2}{\overline{z - a_k}} + a_k. \tag{10.13}$$

Using the relation $t = t_{(m)}^*$ on $|t - a_k| = r_k$, we rewrite (10.11), in the form

$$\psi(t) = \psi_k(t) + \frac{\varrho_k r_k^2 t}{(t - a_k)(\overline{a_k}t + r_k^2 - |a_k|^2)} \overline{\psi_k(t)}, \quad |t - a_k| = r_k, \tag{10.14}$$

$$\psi(t) = \psi_0(t) + \overline{\psi_0(t)} + tf'(t), \quad |t| = 1.) \tag{10.15}$$

We reduce the boundary value problem (10.14), (10.15) to a system of functional equations. First, introduce the function

$$\Phi(z) = \begin{cases} \psi_k(z) - \sum_{m \neq k} \frac{\varrho_m r_m^2 z}{(z - a_m)(\overline{a_m} z + r_m^2 - |a_m|^2)} \overline{\psi_m\left(z_{(m)}^*\right)} - \overline{\psi_0\left(\frac{1}{z}\right)} \\ -zf'(z), \ |z - a_k| \leq r_k \ (k = 1, 2, \ldots, n), \\ \\ \psi_0(z) - \sum_{m=1}^n \frac{\varrho_m r_m^2 z}{(z - a_m)(\overline{a_m} z + r_m^2 - |a_m|^2)} \overline{\psi_m\left(z_{(m)}^*\right)}, \ |z| \geq 1, \\ \\ \psi(z) - \sum_{m=1}^n \frac{\varrho_m r_m^2 z}{(z - a_m)(\overline{a}z + r_m^2 - |a_m|^2)} \overline{\psi_m\left(z_{(m)}^*\right)} - \overline{\psi_0\left(\frac{1}{z}\right)} \\ -zf'(z), \ z \in D. \end{cases} \tag{10.16}$$

This function is constructed by a selection of combinations of analytic functions in such a way that the limit values of $\Phi(z)$ coincide on all the circles $|t - a_k| = r_k$ ($k = 1, 2, \ldots, n$) and $|t| = 1$. The choice of $\Phi(z)$ can be explained by an equilibrium of all fictitious point forces produced by analytic functions out of their domain of analyticity. Formally, one can check after calculations that $\Phi^+(t) = \Phi^-(t)$ on every circle where $\Phi^\pm(t)$ denotes the limit values of $\Phi(z)$ from the different sides of the considered curve. Using the principal of analytic continuation, Liouville's theorem and decay condition $\psi_0(\infty) = 0$, one can demonstrate that $\Phi(z) \equiv 0$ [14, 15]. Then, the definition of $\Phi(z)$ yields the functional equations

$$\psi_k(z) = \sum_{m \neq k} \frac{\varrho_m r_m^2 z}{(z - a_m)(\overline{a_m}z + r_m^2 - |a_m|^2)} \overline{\psi_m\left(z_{(m)}^*\right)} \qquad (10.17)$$

$$+ \overline{\psi_0\left(\frac{1}{z}\right)} + z f'(z), \ |z - a_k| \leq r_k \ (k = 1, 2, \ldots, n),$$

$$\psi_0(z) = \sum_{m=1}^{n} \frac{\varrho_m r_m^2 z}{(z - a_m)(\overline{a_m}z + r_m^2 - |a_m|^2)} \overline{\psi_m\left(z_{(m)}^*\right)}, \ |z| \geq 1. \qquad (10.18)$$

The functional equations (10.17) and (10.18) express the elastic force equilibrium mentioned above. For instance, Eq. (10.17) means that the force of the disk $D_k$ expressed by the complex potential $\psi_k(z)$ is balanced by the force produced by the potential in the right part of (10.17).

Substituting $\psi_0$ from (10.18) into (10.17), we arrive at the functional equations

$$\psi_k(z) = \sum_{m \neq k} \frac{\varrho_m r_m^2 z}{(z - a_m)(\overline{a_m}z + r_m^2 - |a_m|^2)} \overline{\psi_m\left(z_{(m)}^*\right)} \quad (10.19)$$

$$+ \sum_{m=1}^{n} \frac{\varrho_m r_m^2 z}{(1 - \overline{a_m}z)(a_m + (r_m^2 - |a_m|^2)z)} \overline{\psi_m\left(a_m + \frac{r_m^2 z}{1 - \overline{a_m}z}\right)} + z f'(z),$$

$$|z - a_k| \leq r_k \quad (k = 1, 2, \ldots, n).$$

It is shown in [14] that the system of equations (10.19) has a unique solution. It can be found by the method of successive approximations uniformly convergent in $|z - a_k| \leq r_k \ (k = 1, 2, \ldots, n)$. When $\psi_k$ are constructed, the function $\psi_0(z)$ can be found by (10.18) and $\psi(z)$ by (10.16)

$$\psi(z) = \sum_{m=1}^{n} \frac{\varrho_m r_m^2 z}{(z - a_m)(\overline{a_m}z + r_m^2 - |a_m|^2)} \overline{\psi_m\left(z_{(m)}^*\right)} \quad (10.20)$$

$$+ \sum_{m=1}^{n} \frac{\varrho_m r_m^2 z}{(1 - \overline{a_m}z)(a_m + (r_m^2 - |a_m|^2)z)} \overline{\psi_m\left(a_m + \frac{r_m^2 z}{1 - \overline{a_m}z}\right)} + z f'(z),$$

$$z \in D.$$

### 10.2.1  Constructive form of the Dirichlet-to-Neumann Operator

In the present section, we construct the function $\psi(z)$ up to $O(r^4)$, where $r = \max_j r_j$. The radii are dimensionless, since the external circle is normalized to the unit circle. It follows from (10.19) that

$$\psi_k(z) = \sum_{m \neq k} \frac{\varrho_m r_m^2 z}{(z - a_m)(\overline{a_m} z + r_m^2 - |a_m|^2)} \overline{\psi_m(a_m)} \qquad (10.21)$$

$$+ \sum_{m=1}^{n} \frac{\varrho_m r_m^2 z}{(1 - \overline{a_m} z)(a_m + (r_m^2 - |a_m|^2) z)} \psi_m(a_m) + z f'(z) + O(r^4),$$

$$|z - a_k| \leq r_k \quad (k = 1, 2, \ldots, n).$$

In the zeroth approximation, we have

$$\psi_k(a_k) = a_k f'(a_k) + O(r^2). \qquad (10.22)$$

Then, (10.20) yields

$$\psi(z) = z \sum_{m=1}^{n} \varrho_m r_m^2 \left[ \frac{\overline{f'(a_m)}}{(z - a_m)^2} + \frac{f'(a_m)}{(1 - \overline{a_m} z)^2} \right] + z f'(z) + O(r^4), \ z \in D. \qquad (10.23)$$

The normal derivative $\frac{\partial u}{\partial \mathbf{n}}$ on the unit circle can be calculated by

$$g(z) := \frac{\partial u}{\partial \mathbf{n}}(z) = \text{Re } \psi(z), \qquad |z| = 1. \qquad (10.24)$$

Here, Eq. (10.12) and the following relation are used:

$$\frac{\partial u}{\partial \mathbf{n}}(z) = \text{Re} \left[ (x_1 + i x_2) \left( \frac{\partial u}{\partial x_1} - i \frac{\partial u}{\partial x_2} \right) \right], \qquad |z| = 1. \qquad (10.25)$$

We recall that the unit outward normal vector to the unit circle has the form $\mathbf{n} = (x_1, x_2)$. Then, the normal derivative becomes $\frac{\partial u}{\partial \mathbf{n}}(z) = x_1 \frac{\partial u}{\partial x_1} + x_2 \frac{\partial u}{\partial x_2}$. The corresponding complex derivative can be calculated in terms of the partial derivatives $\varphi'(z) = \frac{\partial u}{\partial x_1} - i \frac{\partial u}{\partial x_2}$. One can see that the relation (10.24) yields an approximation up to $O(r^4)$ of the Dirichlet-to-Neumann operator $DtN : h \mapsto g$. More precisely, consider a given boundary function $h$ from the boundary condition (10.5) on the outer unit circle. First, the function $f(z)$ analytic in $|z| < 1$ satisfying the relation $h(z) = \text{Re } f(z)$ is constructed by the Schwarz operator [14]

$$f(z) = \frac{1}{2\pi i} \int_{|\zeta|=1} h(\zeta) \frac{\zeta + z}{\zeta - z} \frac{d\zeta}{\zeta}, \quad |z| \leq 1. \qquad (10.26)$$

Next, $f'(a_m)$ is calculated and used in (10.23) to construct the function $\psi(z)$. The function $g(z)$ is found from (10.24) up to $O(r^4)$

$$g(z) = \text{Re}[zf'(z)] + 2 \sum_{m=1}^{n} \varrho_m r_m^2 \text{Re} \left[ z \, \frac{\overline{f'(a_m)}}{(z - a_m)^2} \right] + O(r^4), \ |z| = 1. \quad (10.27)$$

**Computational remark** [20]. The method of iterations can be applied to the functional equations (10.19) in symbolic-numerical form practically without restrictions. This will give higher order formulas improving the asymptotic equation (10.27). It requires an advanced computer implementation like the procedure developed in [20, Chap. 2] for the effective properties of composites. An example is given at the end of the present section.

**Theoretical remark** [15]. The relation (10.24) determines the Dirichlet-to-Neumann operator on the unit circle $DtN : h \mapsto g$. This operator acts from the space $C^{(1,\alpha)}$ consisting of functions differentiable on $\partial D$ whose partial derivatives belong to the Hölder space $H^\alpha$. The resulting function $g$ belongs to the space of continuous functions.

Consider the special case $h(z) = \text{Re} \, z = x_1$, hence, $f(z) = z$. It has clear applications to the inverse problem discussed below. Consider the vanishing inclusions when $r_k = 0$. The displacement in the unit disk becomes $u = x$ and the trace $\mathbf{q}_0 = -\mu \nabla u = -\mu(1, 0)$. The same displacement $u = x_1$ is obtained for the external trace $\mathbf{q}_0$, i.e., for the Neumann problem $-\mu \frac{\partial u}{\partial \mathbf{n}}(t) = \mathbf{q}_0 \cdot \mathbf{n}, \ |t| = 1$. It is worth noting that $g(z) = z$ by (10.27). Therefore, the Dirichlet-to-Neumann operator transforms the function $\text{Re} \, z$ into itself in this simple case.

Let now the inclusions not degenerate, i.e., $r_k > 0$. Then, the above-considered fields are perturbed by the impact of inclusions. The trace has a similar behavior but only on a macroscale. In microscale, it oscillates as shown in the papers [21–23]. It can be seen from the function $g(z)$ which now becomes

$$g(z) = \text{Re} \, z + 2 \sum_{m=1}^{n} \varrho_m r_m^2 \text{Re} \frac{z}{(z - a_m)^2} + O(r^4). \quad (10.28)$$

We refer to the papers [21–23] concerning the mechanism of oscillations and further discussion devoted to the resurgence effects.

We now outline how to derive the next approximations. The case $f'(z) = 1$ is considered for simplicity. Substituting (10.22) into (10.21), we obtain the next approximation

$$\psi_k(z) = z \left[ \sum_{m \neq k} \frac{\varrho_m r_m^2}{(z - a_m)^2} + \sum_{m=1}^{n} \frac{\varrho_m r_m^2}{(1 - \overline{a_m} z)^2} + 1 \right] + O(r^4), \quad (10.29)$$

$$k = 1, 2, \ldots, n.$$

Calculate

$$\overline{\psi_k\left(z_{(k)}^*\right)} = \overline{\psi_k\left(a_k\right)} + \frac{r_k^2}{z - a_k}\overline{\psi_k'\left(a_k\right)} + O(r^4) \tag{10.30}$$

and

$$\psi_k\left(a_k + \frac{r_k^2 z}{1 - \overline{a_k}z}\right) = \psi_k\left(a_k\right) + \frac{r_m^2 z}{1 - \overline{a_m}z}\psi_k'\left(a_k\right) + O(r^4). \tag{10.31}$$

In order to get the next approximation, we substitute $\psi_k'\left(a_k\right) = 1 + O(r^2)$ and

$$\psi_k(a_k) = a_k\left[\sum_{m\neq k}\frac{\varrho_m r_m^2}{(a_k - a_m)^2} + \sum_{m=1}^{n}\frac{\varrho_m r_m^2}{(1 - \overline{a_m}a_k)^2} + 1\right] + O(r^4) \tag{10.32}$$

into (10.30)–(10.31). The obtained expressions (10.30)–(10.32) after substitution into (10.20) will determine the function $\psi(z)$ up to $O(r^6)$. The ultimate formula is rather lengthy and is not presented here for the sake of brevity. However, it can be presented as a set of sequence formulas. First, $\psi_k(a_k)$ is calculated by (10.32). Next, $\overline{\psi_k\left(z_{(k)}^*\right)}$ and $\psi_k\left(a_k + \frac{r_k^2 z}{1 - \overline{a_k}z}\right)$ are calculated by (10.30)–(10.31). The obtained expressions are substituted into (10.20).

### 10.2.1.1 Inverse Multiple Particle Problem and Blurring

The new inverse boundary value problem is stated as follows. Consider a composite cylinder with unidirectional fibers. Let a section perpendicular to the axis be the unit disk containing $n$ non-overlapping disks of radii $r_k$; see Fig. 10.1. Let the $k$th fiber have the shear modulus $\mu_k$ determined by the contrast parameter $\varrho_k$ defined by (10.7). The boundary conditions take the same form (10.4), (10.5) as in the direct problem.

Introduce the concentration of inclusions $\phi = \sum_{k=1}^{n} r_k^2$ in the unit disk. Let the displacement $u = \text{Re } z$ and the trace $-\mu g(z)$ be given at the outer boundary $|z| = 1$.

Let the number $n$ and the radii $r_k$ of fibers of, and, hence, the concentration $\phi$ be known. The unknown parameters are the centers of disks $a_k$ $(k = 1, 2, \ldots, n)$ and the contrast parameters $\varrho_k$. Therefore, we do not know the location of fibers and their shear moduli. The inverse problem in this statement contains $n$ complex unknown centers $a_k$ $(k = 1, 2, \ldots, n)$ and the real contrast parameters $\varrho_k$. When $\varrho_k$ will be determined, the shear moduli of fibers will be calculated by the formula

$$\mu_k = \mu\,\frac{1 + \varrho_k}{1 - \varrho_k}, \tag{10.33}$$

where $\mu$ stands for the given shear modulus of the host.

The considered inverse boundary value problem is reduced to the determination of the centers $a_k$ by means of equation (10.28) on the unit circle where the function $g(z)$ is known. It follows from (10.28) that the Fourier series of the normalized external flux $g(e^{i\theta})$ with $g$ satisfy equation

$$g(e^{i\theta}) = \cos\theta + 2\sum_{m=1}^{n} \varrho_m r_m^2 \sum_{s=0}^{\infty} \text{Re}[sa_m^s e^{-(s+1)i\theta}] + O(r^4). \tag{10.34}$$

The Fourier coefficient in $\cos\theta$ has the form

$$g_0 = \frac{1}{\pi}\int_{-\pi}^{\pi} g(e^{i\theta})\cos\theta \, d\theta = 1 + 2\sum_{m=1}^{n} \varrho_m r_m^2. \tag{10.35}$$

Selecting the coefficients in $\cos s\theta$ and $\sin s\theta$, we obtain equations

$$g_s = 2s\sum_{m=1}^{n} \varrho_m r_m^2 a_m^s, \quad s = 1, 2, \ldots, \tag{10.36}$$

where $g_s = g_s' + ig_s''$, $g_s'$ is the coefficient of $g(e^{i\theta})$ on $\cos(s+1)\theta$ and $g_l''$ on $\sin(s+1)\theta$. Introduce the real parameters $X_m = \varrho_m r_m^2$. Then, Eq. (10.36) is reduced to algebraic equations on $X_m$ and $a_m$

$$\sum_{m=1}^{n} X_m a_m^s = h_s, \quad s = 0, 1, 2, \ldots, \tag{10.37}$$

where $h_0 = \frac{1}{2}(g_0 - 1)$ and $h_s = \frac{g_s}{2s}$ ($s = 1, 2, \ldots$).

The same Eq. (10.37) arises in the Prony method [16] devoted to a signal processing technique where the values $X_m$ and $a_m$ express the amplitude and phase of the radar return from the target at each frequency. In the present paper, $X_m$ and $a_m$ express the contrast parameter and location of inclusions in the composite. Hence, Eq. (10.37) is considered in the other context concerning material science.

Consider the case when all inclusions consist in the same material and have the same radius, i.e., $\varrho_m = \varrho$, $\mu_m = \mu_1$ and $r_m = r$, hence $X_m = \varrho r^2$. Equation (10.35) equivalent to the zeroth Eq. (10.37) becomes $g_0 = 1 + 2\varrho\phi$. Therefore,

$$\varrho = \frac{g_0 - 1}{2\phi}, \tag{10.38}$$

and the shear modulus of inclusions $\mu_1$ has the form (10.33). The restriction $|\varrho| \le 1$ must hold for (10.38). If it is not fulfilled for the properly measured $g_0$ and $\phi$, one can assume that we are out of the classical elasticity, for instance, the inclusions are filled by a metamaterial [25–27]. If $\varrho$ is known and (10.38) gives another value, it

may be the case of imperfect contact. One can find a method to estimate a parameter of imperfectness in [20, Chap. 5] and [24].

After determination of $\varrho$, the system (10.37) is reduced to equations

$$\sum_{m=1}^{n} a_m^s = b_s, \qquad s = 1, 2, \ldots, \tag{10.39}$$

where $b_s = n \frac{h_s}{h_0}$. It is worth noting that $b_s$ does not depend on $\varrho r^2$, since $h_s = \frac{g_s}{2s}$ is proportional to $\varrho r^2$ for the same inclusions; see (10.36). It is natural to reduce the number of equations to $n$ and to consider the algebraic system

$$\sum_{m=1}^{n} a_m^s = b_s, \qquad s = 1, 2, \ldots, n. \tag{10.40}$$

Consider the polynomials $p_s(z_1, z_2, \ldots, z_n) = \sum_{m=1}^{n} z_m^s$, where the complex variables $z_1, z_2, \ldots, z_n$ belong to the unit disk. Then, Eq. (10.40) can be written in the form

$$p_s(a_1, a_2, \ldots, a_n) = b_s, \qquad s = 1, 2, \ldots, n. \tag{10.41}$$

Introduce the symmetric polynomials

$$e_1 = \sum_{1 \leq m \leq n} z_m, \ e_2 = \sum_{1 \leq m_1 < m_2 \leq n} z_{m_1} z_{m_2}, \ \ldots, \ e_n = z_1 z_2 \ldots z_n. \tag{10.42}$$

The polynomials can be expressed in terms of the symmetric polynomials by the relation [28]

$$e_j = \frac{1}{j!} \begin{vmatrix} p_1 & 1 & 0 & 0 & \cdots \\ p_2 & p_1 & 2 & 0 & \cdots \\ \vdots & & \ddots & \ddots & \ddots \\ p_{j-1} & p_{j-2} & \cdots & p_1 & j-1 \\ p_j & p_{j-1} & \cdots & p_2 & p_1 \end{vmatrix}. \tag{10.43}$$

By Vieta's theorem, $a_m$ ($m = 1, 2, \ldots, n$) satisfy the polynomial equation

$$z^n + \sum_{s=1}^{n} (-1)^s e_s \, z^{n-s} = 0. \tag{10.44}$$

Here, $e_s = e_s(a_1, a_2, \ldots, a_n)$ are calculated by (10.43) after substitution of the corresponding $b_s$. Therefore, in order to determine $a_m$ ($m = 1, 2, \ldots, n$), it is sufficient to solve equation (10.44). This observation essentially simplifies the numerical solution to the considered inverse problem.

**Fig. 10.2** 67 randomly distributed non-overlapping disks of radius $r = 0.05$ are shown in black. The simulated 67 disks whose centers are the roots of equation (10.44) of degree 67 are shown in gray. The complete coincidence of black and gray disks is observed in this example
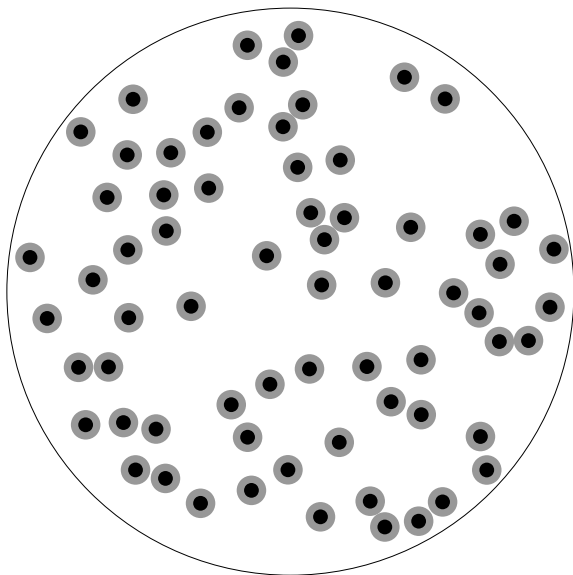
Two numerical examples are presented in Figs. 10.2 and 10.3. In both examples, random non-overlapping disks of the same radius are generated, and the corresponding direct problem is solved up to $O(r^4)$. It is assumed that the inclusions are perfect conductor, hence, $\varrho = 1$ and Eq. (10.38) is skipped. The polynomial equation (10.44) is constructed by the explicit formulas (10.40)–(10.43).

Solution to the inverse problem is based on the determination of $n$ complex roots of equation (10.44). In Figs. 10.2 and 10.3, the given locations of disks are presented by black disks (radius of which is artificially reduced two times for visibility). The roots of equation (10.44), the centers of simulated disks, are shown in gray. Figure 10.2 demonstrates the perfect coincidence of the simulated disks (gray) to the given disks (black).

With the increasing $n$, one can note the blurring effects. Figure 10.3 displays such a case when a part of the simulated disks nearer the boundary fits with the given disks. The deeper disks are not properly determined. The numerical divergence is related to the coefficients of the monic polynomial equation (10.44) of degree 144. Some of them have an order less than $10^{-14}$. The observed effect may be called by blurring in the inverse problem for dispersed composites. The considered example demonstrates this effect when the correct location of disks in a ring adjoining the boundary is determined. The location of deeper disks is blurred.

In the considered examples of perfectly rigid inclusions

$$\frac{\mu_k}{\mu} = +\infty \iff \varrho = 1, \tag{10.45}$$
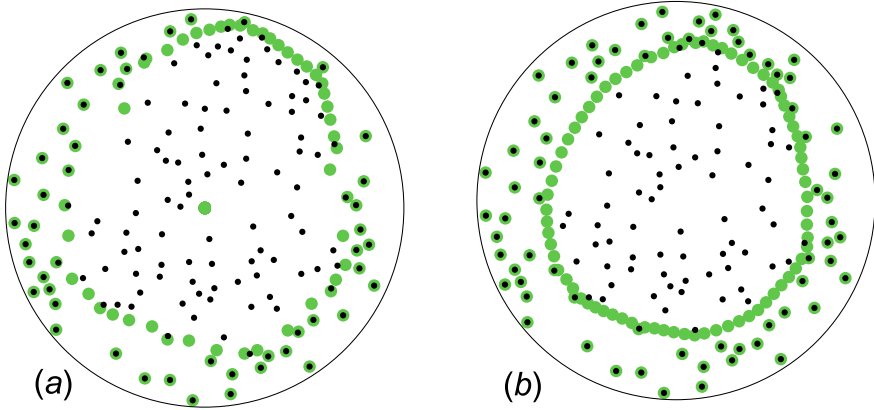
**Fig. 10.3** 144 randomly distributed non-overlapping disks of radius $r = 0.03$ are shown in black. The simulated 144 disks whose centers are the roots of equation (10.44) of degree 144 are shown in green. The coefficients of equation (10.44) are taken with the precision: **a** $10^{-8}$, **b** $10^{-14}$. The roots are computed with the precision $10^{-14}$ in both cases (**a**) and (**b**)

the blurring effect enhances with the increasing $n$. It can be explained by a rough division of the center sets onto exterior $E$ and interior $I$ sets for which $|a_m|$ are closer to 1 and $|a_m|$ closer to 0, respectively, when (10.40) becomes

$$\sum_{a_m \in E} a_m^s + \sum_{a_m \in I} a_m^s = b_s, \qquad s = 1, 2, \ldots, n. \tag{10.46}$$

The second sum in (10.46) can be neglected during the computation of the exterior centers. At the same time, equation for the interior points contains unknowns of small modulus in the left part $\sum_{a_m \in I} a_m^s$ and the right part $b_s - \sum_{a_m \in E} a_m^s$ obtained by subtraction of values of large moduli. For such an equation, the computational error may be too high. For instance, a root $a_m$ lying in the disk of radius 0.7 can be found with the precision $10^{-14}$ from a polynomial equation of degree at most 90, since $(0.7)^s = 10^{-14}$ for $s = 90.34$.

Let the contrast parameter $\varrho$ be determined by (10.38) and $|\varrho|$ be sufficiently small. Equation $b_s = \frac{g_s}{2sr^2\varrho}$ ($s = 1, 2, \ldots, n$) implies that $|b_s|$ becomes large for small $|\varrho|$ for fixed other parameters. Based on (10.46), one may suggest that the blurring effect enhances for small $|\varrho|$.

## 10.3 Discussion and Conclusion

In the present paper, the problem of reconstruction of inhomogeneities from boundary measurements is investigated for 2D fiber-reinforced composites. It is assumed that a section perpendicular to the unidirectional fibers is the unit disk containing non-

overlapping disks. Following [14, 15], we state a boundary value problem for a circular multiply connected domain in terms of complex potentials and solve it by a method of functional equations.

Having at our disposal the approximate analytical formula (10.27) for the normal derivative $g(z) \equiv \frac{\partial u}{\partial \mathbf{n}}(z)$ on the unit circle, we can consider it as a relation to determine the centers $a_k$ $(k = 1, 2, \dots, n)$ of inclusions and its shear modulus. The problem is stated for different moduli of inclusions and discussed in detail for the same modulus in all the inclusions of the same radius. Using the properties of symmetric polynomial, we construct a polynomial equation of degree $n$ whose roots coincide with the centers. The theoretical formulas are illustrated by numerical examples.

It is established that the considered antiplane elastic inverse problem for a composite is formally equivalent to the Prony equations (10.37) arising in scattering data analysis. The physical interpretation of unknowns in Eq. (10.37) from [16] differs from the stationary elasticity phenomena discussed in the present paper.

In the context of material science, the problem for a two-phase composite is reduced to Eq. (10.40) which is reduced to the polynomial equation (10.44). Therefore, the centers $a_k$ $(k = 1, 2, \dots, n)$ of inclusions satisfy the explicitly written monic polynomial equation (10.44). One may stop at this theoretical result and further apply a high precision method to Eq. (10.44) in order to reach the coincidence in simulations as in Fig. 10.2. However, such a precision may not be accessible in practice, especially, for small contrast parameters discussed at the end of Sect. 10.2.1.1.

We propose to consider this computational problem of roots as the blur effect illustrated in Fig. 10.3. It follows from the computational examples that the roots can be accurately found near the boundary without extended precision implementations. Instead of the proper interior points, we observe a shield of spurious roots remote on the distance $r_{error}$ from $z = 0$ decreasing with the increasing computational precision. The origin $z = 0$ may be artificially assigned to roots if the term $e_n$ from (10.43) is rounded to 0.0. Here, we arrive at the classification problem of random dispersed composites when the probabilistic distribution of inclusions is one of the main aims of material science. A part of inclusions may be used in order to describe the macroscopic properties of composite [15, 20] if it is known that this part is representative and the invisible blurry part has the same statistical properties as the whole composite.

The proposed approach might have the potential to be developed in future not only in a static framework but also within the low-frequency dynamics range (when static behavior will be leading order approximation and next order low-frequency correction will be possible), using the asymptotic results for strongly inhomogeneous composite structures when at leading order the hard components perform rigid body motions; see the contributions addressing multi-span rods [29, 30], and 2D elastic bodies within the framework of antiplane elasticity [31].

# References

1. Beck JV, Blackwell B, Charles JR (1985) Inverse heat conduction, 1st edn. Wiley Inc, New York
2. Alifanov OM, Artyukhin EA, Rumyantsev SV (1995) Extreme methods for solving ill-posed problems with applications to inverse heat transfer problems. Begell House Inc., New York
3. Cherkaeva E, Tripp AC (1996) Inverse conductivity problem for inaccurate measurements. Inverse Probl 12:869–883
4. Kuchment P (2013) The radon transform and medical imaging, CBMS-NSF regional conference series in applied mathematics
5. Necat Ozisik M (2000) Inverse heat transfer: fundamentals and applications. CRC Press, Boca Raton
6. Hetmaniok E, Slota D, Witula R, Zielonka A (2015) An analytical method for solving the two-phase inverse Stefan problem. Bull Polish Acad Sci Tech Sci 63:583–590
7. Hetmaniok E, Slota D, Zielonka A (2015) Using the swarm intelligence algorithms in solution of the two-dimensional inverse Stefan problem. Comput Math Appl 69(4):347–361
8. Colton D, Kress R (2013) Inverse acoustic and electromagnetic scattering theory. Springer, Berlin
9. Isakov V (2017) Inverse problems for partial differential equations. Springer, Berlin
10. Kress R (2012) Inverse problems and conformal mapping. Complex Var Elliptic Equ 57:301–316
11. Ammari H, Garnier J, Kang H, Lim M, Yu S (2014) Generalized polarization tensors for shape description. Numer Math 126:199–224
12. Munnier A, Ramdani K (2018) Calderón cavities inverse problem as a shape-from-moments problem. Quart Appl Math 76:407–435
13. Czapla R (2016) Basic sums as parameters characterizing, Silesian. J Pure Appl Math 6:85–96
14. Mityushev VV, Rogosin SV (2000) Constructive methods for linear and nonlinear boundary value problems for analytic functions. Chapman & Hall/CRC, Boca Raton
15. Gluzman S, Mityushev V, Nawalaniec W (2018) Computational analysis of structured media. Elsevier, Amsterdam
16. Carriere R, Moses RL (1992) High resolution radar target modeling using a modified Prony estimator. IEEE Trans Antennas Propag 40:13–18
17. Ebenfelt P, Gustafsson B, Khavinson D, Putinar M (eds) (2005) Quadrature domains and their applications. Advances and applications, operator theory. Birkhäuser Verlag, Basel
18. Muskhelishvili NI (1966) Some basic problems of the mathematical theory of elasticity, 5th edn. (Russian) Nauka, Moscow
19. Bergman DJ (1976) Calculation of bounds for some average bulk properties of composite materials. Phys Rev B 14:4304
20. Drygaś P, Gluzman S, Mityushev V, Nawalaniec W (2020) Applied analysis of composite media. Analytical and computational results for materials scientists and engineers. Elsevier, Amsterdam
21. Rylko N (2015) Edge effects for heat flux in fibrous composites. Comput Math Appl 70:2283–2291
22. Rylko N (2015) Fractal local fields in random composites. Comput Math Appl 69:247–254
23. Rylko N, Wojnar R (2015) Resurgence edge effects in composites: fortuity and geometry. In: Mladenov IM, Hadzhilazova M, Kovalchuk V (eds) Geometry, integrability, mechanics and quantization. Avangard Prima, Sofia, pp 342–349
24. Drygaś P, Mityushev V (2009) Effective conductivity of arrays of unidirectional cylinders with interfacial resistance, Q. J Mech Appl Math 62:235–262
25. McPhedran R, Shadrivov I, Kuhlmey B et al (2011) Metamaterials and metaoptics. NPG Asia Mater 3:100–108
26. Craster RV, Kaplunov J (2013) Dynamic localization phenomena in elasticity. Acoustics and electromagnetism. Springer, Vienna

27. Palmer SJ, Xiao X, Pazos-Perez N et al (2019) Extraordinarily transparent compact metallic metamaterials. Nat Commun 10:2118
28. Cadogan CC (1971) The Möbius function and connected graphs. J Combin Th B 11:193–200
29. Kaplunov J, Prikazchikov DA, Sergushova O (2016) Multi-parametric analysis of the lowest natural frequencies of strongly inhomogeneous elastic rods. J Sound Vib 366:264–276
30. Kaplunov J, Prikazchikov DA, Prikazchikova LA, Sergushova O (2019) The lowest vibration spectra of multi-component structures with contrast material properties. J Sound Vib 445:132–147
31. Kaplunov J, Prikazchikov DA, Sergushova O (2017) Lowest vibration modes of strongly inhomogeneous elastic structures. In: Altenbach H, Goldstein R, Murashkin E (eds) Mechanics for materials and technologies. Advanced structured materials. Springer, Cham, pp 265–277

# Chapter 11
# Asymptotic Theory of Generalised Rayleigh Beams and the Dynamic Coupling

**Michael J. Nieves and Alexander B. Movchan**

**Abstract** We consider the effective dynamic response of an infinite asymmetric structure formed from a beam attached to a periodic array of resonators. The array couples the axial and flexural motions of the beam. We develop a point-wise description of the response of the system and demonstrate that when the separation of the resonators is small, the structure is approximated by the generalised Rayleigh beam: a beam attached to an elastic resonant layer that engages flexural-longitudinal wave coupling. The passage to the effective model utilises a dynamic homogenisation based on the method of meso-scale approximations, whose efficiency is not limited to the typical low-frequency regime of usual homogenisation approaches. The dispersion properties of this effective system are completely characterised and we illustrate the multi-coupling of waves through the analysis of Green's matrix of this flexural system, which is constructed in the explicit form. The analytical results are also accompanied by illustrative numerical computations.

## 11.1 Introduction

Effective models for stratified elastic media are useful in rapidly providing information on how various internal structures at differing scales influence the overall response of the medium in several dynamic regimes [1–7]. They are particularly important in understanding vibration in advanced materials and civil engineering, where periodicity is a prominent feature of elastic meta-materials and societal struc-

M. J. Nieves (✉)
School of Computer Science and Mathematics, Keele University, Keele, ST5 5BG, UK
e-mail: m.nieves@keele.ac.uk

A. B. Movchan
Department of Mathematical Sciences, University of Liverpool, Liverpool, L69 7ZL, UK
e-mail: abm@liv.ac.uk

**Fig. 11.1** The generalised Rayleigh beam, formed from an elastic resonant coupling layer attached to an Euler-Bernoulli beam
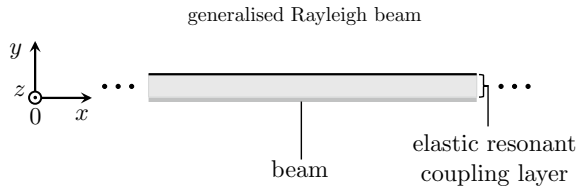
tures. For the latter, simplified models of elastic networks of beams are sufficient for predicting the dynamic response of, for instance, buildings, bridges and railways [8–12] and their failure [13–18]. Despite their lower dimensionality, the models offer ways of accurately incorporating complex responses due to the coupling of different physical effects [19, 20].

In advanced materials, analogous structured systems that utilise passive or active mechanical features enable wave control and special dynamic responses at a range of frequencies. Examples include those which produce negative refraction [21] and localisation [22, 23], dynamic anisotropy [24, 25], uni-directional edge [26] and interfacial [27] waves and highly localised bulk waves [28]. The concept of a microstructured medium can also be employed in designing materials with unusual quasi-static [29–31] and thermal properties [32]. As an alternative to using a discrete system, formed by the interconnection of many internal elastic components, in controlling waves one can also employ the combination of several continuous systems to achieve atypical dynamic responses as in [33, 36].

Here, we investigate vibrations propagating through a continuous system involving an Euler-Bernoulli beam that is attached to a resonant elastic coupling layer that confers negative translational and rotational inertial effects to the beam. The resulting asymmetric system is referred to as the generalised Rayleigh beam (see Fig. 11.1), that engages the multi-coupling of flexural and longitudinal motions of the main beam. Formerly, a Rayleigh beam is a continuous mechanical element that possesses additional rotational inertia [34]. This rotational inertia can be motivated through the consideration of microstructured flexural systems [35]. The effect of this rotational inertia on the vibration of these continuous elements, including Green's functions and their quasi-periodic analogues for Rayleigh beams, has been addressed in [33]. As a collective within a network, Rayleigh beams have been shown to be useful in promoting unusual dynamic effects [23, 25]. Further, the analysis of waves and exotic vibration modes propagating through lattice systems of beams possessing torsional inertia have been studied in [24].

The model for the generalised Rayleigh beam was derived in [37]. This model can involve either a finite or infinite beam attached to an elastic resonant coupling material occupying a finite segment of the beam. Its derivation relies on the application of analytical point-wise descriptions of an analogous microstructured medium. The solutions developed to describe the microstructured medium were based on meso-scale solutions often employed in characterising multiscale composites [38].

Meso-scale approximations were first introduced in [39, 40] to provide highly accurate predictions for the responses of finite or infinite densely perforated media in configurations where techniques such as homogenisation are no longer applicable. These approximations provide point-wise information about the system and work up to the boundaries of small perforations and, where applicable, external boundaries. They are also capable of efficiently predicting the interaction of internal and external boundaries and can treat problems involving dilute perforations. Further, they lead to homogenisation approximations when the number of perforations is large. The corresponding effective models, such as those considered here, become important in quickly providing information on the behaviour of the physical systems when the application of the meso-scale asymptotic model becomes expensive.

Here, we adopt the method of meso-scale approximations to obtain the model for the generalised Rayleigh beam. This is an effective model approximating a beam with a discrete distribution of resonators with flexural and compressional motion. Important to the application of the method is the use of dynamic model fields in describing the motion of the discrete system. Simultaneously, this enables the resulting effective model to be efficient in capturing the high-frequency dynamic behaviour of discrete medium when the resonators are closely situated.

An example demonstrating the efficiency of the dynamic homogenisation procedure adopted here in obtaining the model of the generalised Rayleigh beam is shown in Fig. 11.2. There, it can be seen that the dispersion curves of this beam provide an excellent agreement with the results attributed to a Fourier analysis of the analogous discrete medium. We note different efficient and robust homogenisation procedures can be used to trace the effective dynamic properties of a periodic medium with the typical restriction to low-frequency regimes [1–3] or at high frequencies [4] in the vicinity of standing modes and dispersion degeneracies such as Dirac points. On the other hand, when the microstructure of the discrete medium is sufficiently dense, Fig. 11.2 shows the agreement enabled by the dynamic homogenisation via meso-scale approximations holds for a wide range of frequencies and wavenumbers not necessarily associated with the ranges of applicability of the methods in [1–7].

Meso-scale approximations have been developed for range of quasi-static problems in mathematical physics which includes electrostatics [39, 40], steady heat flow [41], elasticity [42, 43] and low-frequency acoustics [44]. More recently, meso-scale asymptotic models have been introduced to tackle dynamic problems for membranes with dense clusters of small rigid masses [45]. Following this, exact meso-scale descriptions of waves propagating in slender elastic systems with non-uniform inertial properties have appeared in [37]. Here, we use a similar approach as in [37] to describe the response of a continuous system with uniformly distributed perturbations in its inertial features, but unlike [37], our emphasis is on the behaviour obtained from the effective model based on the meso-scale description of this system.

In [37], the model of the generalised Rayleigh beam appears by considering a dense collection of resonators within a finite region. The resonators produce a flexural and compressional response during motion and this subsequently promotes the coupling of axial and flexural waves in the main beam. Analytical, numerical
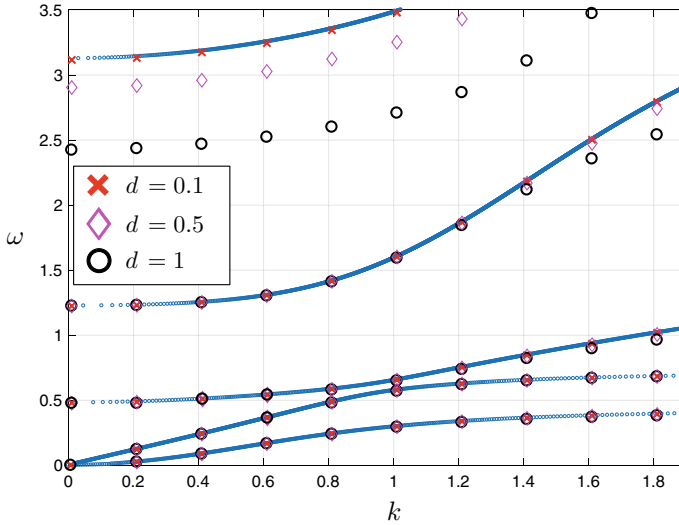
**Fig. 11.2** Dispersion curves for the generalised Rayleigh beam derived via the method of meso-scale approximations represented by blue curves. Results retrieved from the application of Fourier methods in analysing the analogous discrete medium, formed from a beam attached to a periodic array of flexural resonators, are shown as markers for various separations $d$ of the resonators. For further details we refer to Sects. 11.2 and 11.3

and experimental works studying wave attenuation due to this coupling in similar discrete systems have appeared in [46–50].

Previous works dealing with the influence of resonators with compressional behaviour have led to important designs of metasurfaces acting as discrete seismic shields [51, 52]. Resonators with spring-like effects have also been used in elastic media to create counter-intuitive and useful dynamic responses such as localisation [53] and neutrality, negative refraction and blocking in [54]. More recently, wave control in elastic solids with square arrays of flexural and compressional resonators have been studied in [55], which has also included the derivation of effective surface conditions for the medium at low frequencies.

In Sect. 11.2, we introduce an infinite asymmetric flexural medium involving a main beam attached to a periodic resonant microstructure. Using a meso-scale approximation, we also derive the model of a generalised Rayleigh beam, involving a beam attached to an elastic resonant coupling layer. In Sect. 11.3, we investigate the general dispersive properties of the system and the flexural-longitudinal wave coupling in the associated modes influenced by the resonant coupling layer. This section also contains an illustrative examples demonstrating the efficiency of the dynamic homogenisation technique, based on meso-scale approximations, in capturing the high-frequency behaviour of a periodic discrete medium with a small separation between neighbouring resonant elements within its microstructure. Some associated results concerning the structure's response at resonance frequencies are

also discussed in Appendix A. Section 11.4 contains the closed form representation for Green's matrix for the generalised Rayleigh beam, representing the system's response to longitudinal and transverse acting sinusoidal point forces. Finally, in Sect. 11.5 we give some conclusions and discussions based on the work.

## 11.2 A Generalised Rayleigh Beam

### 11.2.1 Model for a Generalised Rayleigh Beam

Here we introduce the equations governing the motion of the generalised Rayleigh beam as shown in Fig. 11.1, which is formed from a regular beam attached to an elastic resonant coupling layer. We assume that at a given point $x$ along this beam, the structure has the axial displacement $U(x)$ and the flexural displacement $V(x)$. These functions satisfy the partial differential equations

$$\rho A \omega^2 U(x) + EAU''(x) = -\omega^2 \left[ \Psi_{\text{eff}}(\omega) U(x) + \Pi_{\text{eff}}(\omega) V'(x) \right] , \qquad (11.1)$$

$$-\rho A \omega^2 V(x) + EJV''''(x) = \omega^2 [\Phi_{\text{eff}}(\omega) V(x) - \Pi_{\text{eff}}(\omega) U'(x) - \Upsilon_{\text{eff}}(\omega) V''(x)] , \qquad (11.2)$$

where $E$ is the beam's Young's modulus, $A$ is the area of the beam's cross section, $\rho$ is the density of the beam and $J$ is the second moment of area of the cross section of the beam. Here $\omega$ is the radian frequency of vibration in the beam and the dynamic contributions in the above right-hand sides are influenced by

$$\Phi_{\text{eff}}(\omega) = \frac{\mu_{\text{eff}} K_{\text{eff}}}{(K_{\text{eff}} - \mu_{\text{eff}} \omega^2)} , \quad \Psi_{\text{eff}}(\omega) = -\frac{12 b K_{\text{eff}} \mu_{\text{eff}} (a \mu_{\text{eff}} \omega^2 - b K_{\text{eff}})}{\mathcal{D}_{\text{eff}}} ,$$

$$\Pi_{\text{eff}}(\omega) = \frac{6 b K_{\text{eff}} \mu_{\text{eff}} L_r (a \mu_{\text{eff}} \omega^2 - 2 b K_{\text{eff}})}{\mathcal{D}_{\text{eff}}} , \qquad (11.3)$$

and

$$\Upsilon_{\text{eff}}(\omega) = -\frac{4 b K_{\text{eff}} \mu_{\text{eff}} L_r^2 (-3[1+a] b K_{\text{eff}} + a \mu_{\text{eff}} \omega^2)}{\mathcal{D}_{\text{eff}}} \qquad (11.4)$$

with

$$\mathcal{D}_{\text{eff}} = a \mu_{\text{eff}}^2 \omega^4 - 4 b K_{\text{eff}} (1 + 3a) \mu_{\text{eff}} \omega^2 + 12 (b K_{\text{eff}})^2 .$$

In the above, $a$ and $b$ are non-negative dimensionless parameters (see (11.17) and (11.18) in Sect. 11.2.4) and $\mu_{\text{eff}}$ and $K_{\text{eff}}$ represent the effective density and stiffness, respectively, of the resonant coupling layer atop the beam. The parameter $L_r$ is the transverse width of the resonant layer. In what follows, we derive the Eqs. (11.1) and (11.2) governing the dynamic motion of the generalised Rayleigh beam by considering a beam attached to a regular uniform array of flexural resonators.
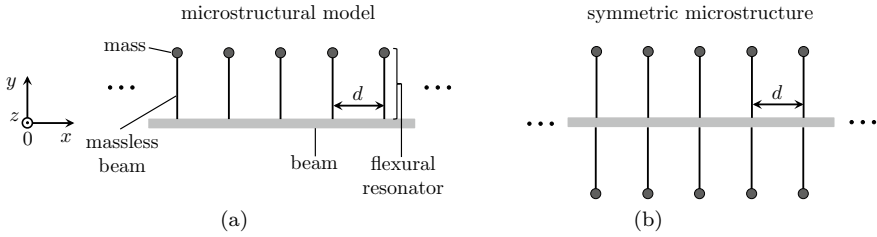
**Fig. 11.3  a** The analogous microstructural model for the generalised Rayleigh beam, formed from a beam attached to a periodic distribution of flexural resonators. **b** A beam with a symmetric microstructure

## 11.2.2  A Beam with a Resonant Microstructure: Derivation of the Generalised Rayleigh Beam

We now consider a beam with a periodic distribution of flexural resonators as shown in Fig. 11.3a. Note this model gives the microstructural description of the generalised Rayleigh beam of Fig. 11.1.

Similar structures to those shown in Fig. 11.3 have been considered in [51, 52, 55], where studies on the influence of the discrete medium on the dynamic response of the continuum is considered. This is not our objective here but instead we focus on the effective continuum and the dynamic input of the coupling provided by the resonators.

Each resonator in Fig. 11.3a is formed from a massless beam of length $L_r$ attached to a node having mass $m$ and moment of inertia $I_z$. The massless beams have Young's modulus $E_r$ and second moment of area $J_r$.

The resonators supply point forces and moments to the lateral beam and the form of these quantities were derived in [37]. Accordingly, vibrations propagating through this comb structure are governed by

$$\rho A \omega^2 U(x) + EAU''(x) = -\sum_{j=-\infty}^{\infty} \omega^2 \left[ \Psi(\omega)U(jd) + \Pi(\omega)V'(jd) \right] \delta(x - jd) ,$$

(11.5)

and

$$-\rho A \omega^2 V(x) + EJV''''(x) = \sum_{j=-\infty}^{\infty} \omega^2 \Phi(\omega)V(jd)\delta(x - jd)$$

$$-\sum_{j=-\infty}^{\infty} \omega^2 \left[ \Pi(\omega)U(jd) + \Upsilon(\omega)V'(jd) \right] \delta'(x - jd) , \quad (11.6)$$

where $U(x)$ and $V(x)$ are the axial and flexural displacements, respectively, of the lateral beam. Additionally, the magnitudes of the point forces and moments supplied by the resonators are

$$\Phi(\omega) = \frac{E_r A_r m}{E_r A_r - m\omega^2 L_r}, \quad \Pi(\omega) = \frac{6 E_r J_r L_r m(L_r I_z \omega^2 - 2 E_r J_r)}{\mathcal{D}},$$

$$\Psi(\omega) = -\frac{12 E_r J_r m(L_r I_z \omega^2 - E_r J_r)}{\mathcal{D}}$$

and

$$\Upsilon(\omega) = -\frac{4 E_r J_r(-3[L_r^2 m + I_z]E_r J_r + I_z L_r^3 m\omega^2)}{\mathcal{D}}, \tag{11.7}$$

with

$$\mathcal{D} = I_z L_r^4 m\omega^4 - 4 L_r E_r J_r(L_r^2 m + 3 I_z)\omega^2 + 12 E_r^2 J_r^2.$$

Before deriving (11.1) and (11.2) we mention that if one considers a symmetric distribution of resonators along the beam (see Fig. 11.3b) then in the associated effective model, the coupling between principal displacements (i.e. the axial and transverse displacement) of the beam is absent. In fact there, the approach adopted in the next section retrieves an equation for the flexural displacement possessing the form of the classical Rayleigh beam, but with terms that demonstrate the effective medium can have negative displacement and/or rotational inertia. We note that similar homogenisation approximations for discrete flexural systems with standard inertial effects have been derived in [35], where the atypical dispersive properties of this microstructured medium are considered in detail.

### 11.2.3  Solution for the Displacements

The axial and flexural displacements for the lateral beam (11.6) and (11.7) can be written in the form

$$U(x) = \sum_{j=-\infty}^{\infty} \omega^2 \left[ \Psi(\omega)U(jd) + \Pi(\omega)V'(jd) \right] g(x - jd),$$

$$V(x) = -\sum_{j=-\infty}^{\infty} \omega^2 \Phi(\omega)V(jd)G(x - jd)$$
$$+ \sum_{j=-\infty}^{\infty} \omega^2 \left[ \Pi(\omega)U(jd) + \Upsilon(\omega)V'(jd) \right] G'(x - jd), \tag{11.8}$$

where $g(x)$ and $G(x)$ are Green's functions dictating the response of lateral beam to axially and vertically applied point forces, respectively. These functions satisfy

$$\rho A \omega^2 g(x) + E A g''(x) + \delta(x) = 0 , \qquad (11.9)$$

and

$$- \rho A \omega^2 G(x) + E J G''''(x) + \delta(x) = 0 . \qquad (11.10)$$

They take the form:

$$g(x) = \frac{\mathrm{i}}{2 E A k_R} \exp\left(\mathrm{i} k_R |x|\right) ,$$

$$G(x) = \frac{1}{4 E J k_B^3} \left[ \exp(-k_B |x|) - \mathrm{i} \exp(\mathrm{i} k_B |x|) \right] , \qquad (11.11)$$

with

$$k_R = \left( \frac{\rho \omega^2}{E} \right)^{1/2} \qquad \text{and} \qquad k_B = \left( \frac{\rho A \omega^2}{E J} \right)^{1/4} .$$

Further, the coefficients $U(jd)$, $V(jd)$, $V'(jd)$, $j \in \mathbb{Z}$, in (11.8) are unknown. They can be determined by taking the projection of the expressions in (11.8) and of $V'(x)$, at the bases of the resonators $x = jd$, $j \in \mathbb{Z}$, to give an infinite algebraic system:

$$U(md) = \sum_{j=-\infty}^{\infty} \omega^2 \left[ \Psi(\omega) U(jd) + \Pi(\omega) V'(jd) \right] g((m-j)d) \qquad (11.12)$$

$$V(md) = - \sum_{j=-\infty}^{\infty} \omega^2 \Phi(\omega) V(jd) G((m-j)d)$$

$$+ \sum_{j=-\infty}^{\infty} \omega^2 \left[ \Pi(\omega) U(jd) + \Upsilon(\omega) V'(jd) \right] G'((m-j)d) \qquad (11.13)$$

and

$$\frac{\mathrm{d}V}{\mathrm{d}x}(md) = - \sum_{j=-\infty}^{\infty} \omega^2 \Phi(\omega) V(jd) G'((m-j)d)$$

$$+ \sum_{j=-\infty}^{\infty} \omega^2 \left[ \Pi(\omega) U(jd) + \Upsilon(\omega) V'(jd) \right] G''((m-j)d) , \qquad (11.14)$$

for $m \in \mathbb{Z}$. These unknown quantities can then be identified by premultiplying (11.12)–(11.14) by $\exp(\mathrm{i}mkd)$ and summing each equation over $m \in \mathbb{Z}$. Following this, employing standard results involving the application of the discrete Fourier transform to convolution-type sums, leads to a homogeneous system in terms of the discrete Fourier Transforms of the unknown coefficients in the form:

$$\mathbf{A}(k)\mathbf{u}(k) = \mathbf{0}$$

where

$$
\mathbf{A}(k) =
\begin{pmatrix}
1 - \omega^2 \Psi(\omega)[g]^{\mathrm{F}}(k) & 0 & -\omega^2 \Pi(\omega)[g]^{\mathrm{F}}(k) \\
-\omega^2 \Pi(\omega)[G']^{\mathrm{F}}(k) & 1 + \omega^2 \Phi(\omega)[G]^{\mathrm{F}}(k) & -\omega^2 \Upsilon(\omega)[G']^{\mathrm{F}}(k) \\
-\omega^2 \Pi(\omega)[G'']^{\mathrm{F}}(k) & \omega^2 \Phi(\omega)[G']^{\mathrm{F}}(k) & 1 - \omega^2 \Upsilon(\omega)[G'']^{\mathrm{F}}(k)
\end{pmatrix},
$$

(11.15)

$$\mathbf{u}(k) = \big([U]^{\mathrm{F}}(k), [V]^{\mathrm{F}}(k), [V']^{\mathrm{F}}(k)\big)^{\mathrm{T}}$$

and the notation

$$[S]^{\mathrm{F}} = \sum_{m=-\infty}^{\infty} S(md)e^{ikmd}, \tag{11.16}$$

with $k$ being the wavenumber. In (11.15), $[g]^F$ is the quasi-periodic Green's function for the axial displacement of the beam with periodically placed axial forces. Based on (11.11) and (11.16) it is given as (see [56, Chapter 2]):

$$[g]^F = \frac{i}{2EAk_R}\left\{\frac{e^{i(k_R+k)d}}{1 - e^{i(k_R+k)d}} + \frac{1}{1 - e^{-i(k-k_R)d}}\right\}.$$

On the other hand, $[G]^F$, $[G']^F$ and $[G'']^F$ denote the quasi-periodic Green's functions associated with the zeroth, first and second derivatives of $G$, respectively, for an Euler-Bernoulli beam with a periodic distribution of point forces. In a similar way to the above, they are computed as

$$
[G]^F = \frac{1}{4EJk_B^3}\left\{\frac{e^{(ik-k_B)d}}{1 - e^{(ik-k_B)d}} + \frac{1}{1 - e^{-(ik+k_B)d}} \right. 
$$
$$
\left. - \frac{ie^{i(k+k_B)d}}{1 - e^{i(k+k_B)d}} - \frac{i}{1 - e^{-i(k-k_B)d}}\right\},
$$

$$
[G']^F = \frac{1}{4EJk_B^2}\left\{-\frac{1}{1 - e^{(ik-k_B)d}} + \frac{1}{1 - e^{-(ik+k_B)d}} \right.
$$
$$
\left. + \frac{1}{1 - e^{i(k+k_B)d}} - \frac{1}{1 - e^{-i(k-k_B)d}}\right\},
$$

and

$$[G'']^F = \frac{1}{4EJk_B}\left\{\frac{e^{(ik-k_B)d}}{1-e^{(ik-k_B)d}} + \frac{1}{1-e^{-(ik+k_B)d}}\right.$$
$$\left. + \frac{ie^{i(k+k_B)d}}{1-e^{i(k+k_B)d}} + \frac{i}{1-e^{-i(k-k_B)d}}\right\}.$$

The determinant of $\mathbf{A}(k)$ provides the dispersion relations for the periodic system, but for the sake of brevity, we do not investigate the pass band structure and its dependency on the material parameters of the periodic system. However, in Sect. 11.3, we compare the associated curves with those of the generalised Rayleigh beam in the limit $d \to +0$.

### 11.2.4  Dynamic Homogenisation versus Meso-scale Approximations: The Generalised Rayleigh Beam

To retrieve the model for the generalised Rayleigh beam, we employ the algebraic equations (11.12) and (11.13) associated with the meso-scale solution (11.8) and analyse these equations as the resonator separation $d \to 0$. Later, in Sect. 11.4, we demonstrate the accuracy of the derived model in recovering the behaviour of the microstructured system having small spacing between the resonators and outside the low-frequency regime. Additionally, to enable this, we make an appropriate choice of the properties of the flexural resonators.

Concerning the masses forming these resonators we choose:

$$m = \mu_{\text{eff}}d, \quad I_z = a\mu_{\text{eff}}L_r^2d, \tag{11.17}$$

whereas the elastic properties of the massless beams are taken as

$$E_r A_r = K_{\text{eff}}L_r d, \quad E_r J_r = bK_{\text{eff}}L_r^3 d. \tag{11.18}$$

Here, $\mu_{\text{eff}}$ is the mass per unit length and $K_{\text{eff}}$ is the elastic stiffness, having the dimension of force per unit area, of the effective resonant coupling material. With these choices, the terms (11.7) take the equivalent representations involving in (11.3) and (11.4):

$$\Psi(\omega) = d\,\Psi_{\text{eff}}(\omega), \quad \Phi(\omega) = d\,\Phi_{\text{eff}}(\omega),$$

$$\Pi(\omega) = d\,\Pi_{\text{eff}}(\omega), \quad \Upsilon(\omega) = d\,\Upsilon_{\text{eff}}(\omega).$$

Returning to (11.12) and (11.13), with this we then obtain

$$U(kd) = \sum_{j=-\infty}^{\infty} \omega^2 \left[ \Psi_{\text{eff}}(\omega)U(jd) + \Pi_{\text{eff}}(\omega)V'(jd) \right] g((k-j)d)d$$

$$V(kd) = -\sum_{j=-\infty}^{\infty} \omega^2 \Phi_{\text{eff}}(\omega)V(jd)G((k-j)d)d$$

$$+ \sum_{j=-\infty}^{\infty} \omega^2 \left[ \Pi_{\text{eff}}(\omega)U(jd) + \Upsilon_{\text{eff}}(\omega)V'(jd) \right] G'((k-j)d)d .$$

In allowing $d \to 0$, one can replace the discrete sums in the above right-hand sides by integrals, allowing these equations to be updated to

$$U(x) = \omega^2 \int_{-\infty}^{\infty} \left[ \Psi_{\text{eff}}(\omega)U(\hat{x}) + \Pi_{\text{eff}}(\omega)V'(\hat{x}) \right] g(x-\hat{x})\mathrm{d}\hat{x} \qquad (11.19)$$

$$V(x) = -\omega^2 \int_{-\infty}^{\infty} \Phi_{\text{eff}}(\omega)V(\hat{x})G(x-\hat{x})\mathrm{d}\hat{x}$$

$$+\omega^2 \int_{-\infty}^{\infty} \left[ \Pi_{\text{eff}}(\omega)U(\hat{x}) + \Upsilon_{\text{eff}}(\omega)V'(\hat{x}) \right] G'(x-\hat{x})\mathrm{d}\hat{x} . \quad (11.20)$$

Next, we apply the differential operator associated with the definition of the Green's functions $g$ and $G$ in (11.9) and (11.10) to both sides of (11.19) and (11.20), respectively. Finally, in evaluating the resulting integrals, which incorporate delta functions, we obtain (11.1) and (11.2).

## 11.3 Dispersive Properties of a Generalised Rayleigh Beam

Information concerning waves supported by the generalised Rayleigh beam is obtained by introducing the displacements as

$$U(x) = Ae^{\mathrm{i}(kx-\omega t)} \quad \text{and} \quad V(x) = Be^{\mathrm{i}(kx-\omega t)}$$

and substituting these into (11.1) and (11.2). Upon doing so, we retrieve the homogeneous system

$$\mathscr{A}(\mathrm{i}k, \omega)\boldsymbol{v} = \boldsymbol{0}$$

where $\boldsymbol{v} = (A, B)^{\mathrm{T}}$ and

$$\mathscr{A}(s, \omega) = \begin{pmatrix} \omega^2(\rho A + \Psi_{\text{eff}}(\omega)) + EAs^2 & \omega^2 s \Pi_{\text{eff}}(\omega) \\ \omega^2 s \Pi_{\text{eff}}(\omega) & -(\rho A + \Phi_{\text{eff}}(\omega))\omega^2 + \omega^2 s^2 \Upsilon_{\text{eff}}(\omega) + EJs^4 \end{pmatrix} . \quad (11.21)$$

The degeneracies of the preceding matrix allow us to determine the waves supported by the generalised Rayleigh beam and are useful in characterising the dynamic

response of the medium to forcing (see Sect. 11.4). In attempting to identify these, we subsequently investigate the roots of a sixth order polynomial with respect to wavenumber:

$$
\begin{aligned}
0 = {} & E^2 A J k^6 - [EA\Upsilon_{\text{eff}}(\omega) + EJ(\rho A + \Psi_{\text{eff}}(\omega))]\omega^2 k^4 \\
& + [\omega^2 \Upsilon_{\text{eff}}(\omega)(\rho A + \Psi_{\text{eff}}(\omega)) - \omega^2 \Pi_{\text{eff}}^2(\omega) - EA(\rho A + \Phi_{\text{eff}}(\omega))]\omega^2 k^2 \\
& + \omega^4 (\rho A + \Psi_{\text{eff}}(\omega))(\rho A + \Phi_{\text{eff}}(\omega)) \ .
\end{aligned}
\tag{11.22}
$$

Thus, for any frequency $\omega > 0$, excluding the degenerate frequencies of (11.7), the generalised Rayleigh beam supports the propagation of at most six waveforms having the complex amplitudes

$$
\boldsymbol{U}(x, k) = \begin{pmatrix} 1 \\ h(\omega, k) \end{pmatrix} e^{\mathrm{i}(kx-\omega t)} \ , \quad h(\omega, k) = \frac{\mathrm{i}\omega^2 k \Pi_{\text{eff}}(\omega)}{(\rho A + \Phi_{\text{eff}}(\omega))\omega^2 + \omega^2 k^2 \Upsilon_{\text{eff}}(\omega) - EJk^4} \ , \tag{11.23}
$$

where $\boldsymbol{U} = (U, V)^{\mathrm{T}}$.

### 11.3.1 Comparison of Dispersive Features of the Effective Continuum and the Periodic Medium

Here we compare the dispersion curves associated with the microstructured medium discussed in Sect. 11.2 and those of the generalised Rayleigh beam based on (11.22).

Figure 11.4a and b shows dispersion curves based on (11.22) in two configurations; the case when the generalised Rayleigh beam possesses a stop band and the situation where there is an infinite pass band for the medium (except at resonance frequencies of the elastic resonant coupling layer). In both cases, computations for the dispersive features of the periodic microstructured medium are supplied based on the determinant of (11.15) for different separations $d$ of the resonators.

A main difference between the dispersion curves for both mechanical systems is the discrete system possesses periodic dispersion curves in $k$, with the period defined via the separation $d$, whereas this feature is not present in the generalised Rayleigh beam model. Even so, the results in Fig. 11.4a and b indicate that when $d$ is small, the dispersion curves of the generalised Rayleigh beam approximate those possessed by the microstructured medium. In particular, the approximation works well for high-frequency curves and for finite wavenumbers especially in the cases when the separation is $d$ is not so small.

Here, the dynamic homogenisation is performed via an exact meso-scale solution constructed via dynamic Green's functions that help in capturing the vibration responses of the medium. As with [1–7], the corresponding effective model provides the envelope bounding the actual response of the microstructure when $d$ is small. At high frequencies, the response of individual elementary cells in the discrete medium becomes important and here, the exact meso-scale solution (11.8) will expedite such information. In particular, in the case when $d \to 0$, the unknown coefficients can be
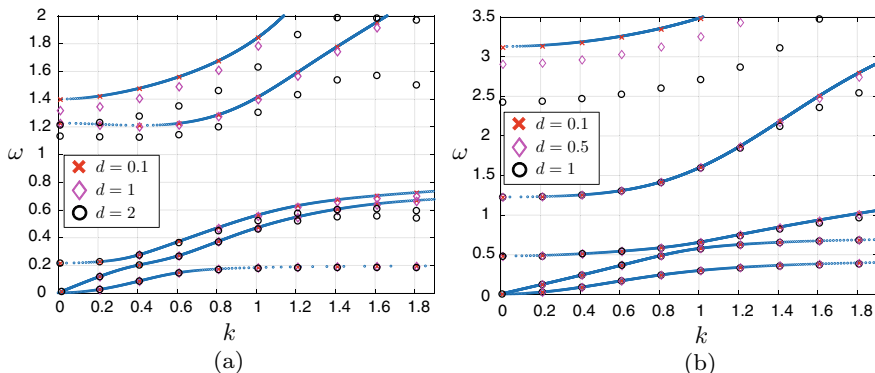
**Fig. 11.4** Comparison of dispersion curves based on (11.22) (blue curves) and those associated with the determinant of (11.15) (for different $d$ indicated by markers specified in the legends. Here, $\mu_{\text{eff}} = 2$ and $b$ is varied, while keeping all other parameters equal to unity. We show the case when the generalised Rayleigh beam possesses **a** a stop band ($b = 0.1$) and **b** an infinite pass band ($b = 0.5$)

easily computed from the solution of (11.1) and (11.2), without the need tackling the infinite algebraic system (11.12)–(11.14) and its discrete Fourier transform (11.15) (see [41])

Further, it is clear that the use of the meso-scale solution has allowed us to recover the effective dispersive behaviour of the system for a substantial range of frequencies and wavenumbers. This is an atypical feature when compared to other homogenisation techniques that provide highly accurate results at either low frequencies [1–3] or high frequencies in the neighbourhood of dispersion degeneracies and standing modes [4–7] when the nominal separation of elements within the microstructure is small.

### 11.3.2 Wave Phenomena and Structure of Solutions to (11.22)

The generalised Rayleigh beam supports the propagation of purely evanescent modes and evanescent waves, in addition to sinusoidal waves. This is evident from Fig. 11.5 that shows the solutions of (11.22).

There, the solutions of (11.22) can be imaginary, complex or real, defining this collection of linear waves. Note that evanescent waves are not a feature of either classical model for a rod or an Euler-Bernoulli beam, without damping, and this effect is attributed to attaching the resonant coupling layer to the ordinary Euler-Bernoulli beam.

Equation (11.22) possesses 6 roots for the wavenumber at frequencies not coinciding with resonances of the layer. If one of these roots, say $k^*$, is complex, then $\pm\overline{k^*}$
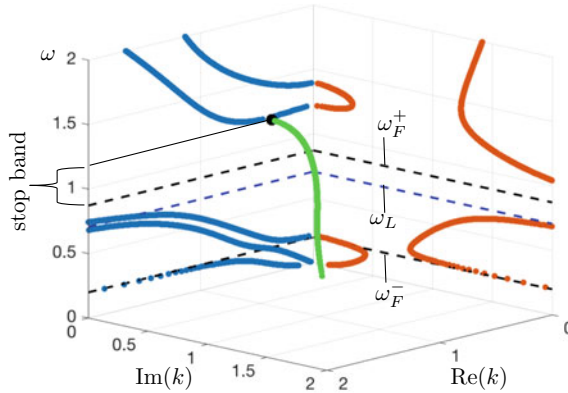
**Fig. 11.5** Dispersion diagram based on (11.22). Real solutions are indicated as blue curves and imaginary solutions are the orange curves. Complex solutions of (11.22) appear as green curves. The resonant axial and flexural frequencies of the elastic coupling layer are denoted as $\omega_L$ and $\omega_F^{\pm}$, respectively. They are indicated by the blue and black dashed lines, respectively (see Sect. 11.3.3). Here $b = 0.1$ and $\mu_{\text{eff}} = 2$, all other parameters are set equal to unity

and $-k^*$ define three other roots of (11.22), where the bar here represents complex conjugate. The remaining pair of roots are then either given by a pair of real distinct roots with opposite sign or they are complex conjugate pair of imaginary roots. An example of such a scenario is demonstrated in Fig. 11.5, where this occurs inside the stop band for the medium. If $k^*$ is not complex, the roots only involved combinations of pairs of real zeros and/or imaginary zeros.

### 11.3.3 Dispersion Curves

Here, we describe some typical features of the dispersion curves linked to wave propagation in the generalised Rayleigh beam.

#### 11.3.3.1 Nature of the Dispersion Curves

The dispersion relation (11.22) yields five dispersion curves for a fixed value of the wavenumber. A further example of the possible dispersion diagram for the medium is shown in Fig. 11.6. Note all curves are monotonically increasing with increasing wavenumber here (compare with Fig. 11.5 where in the vicinity of the black dot, the blue branch passing through this point is non-monotonic).

As shown in Fig. 11.6, two of the dispersion curves are of the acoustic type and pass through the origin of the dispersion diagram at $k = 0$ (see also Fig. 11.8 for a magnification of the dispersion curves in Fig. 11.6 near the origin of the wavenumber-
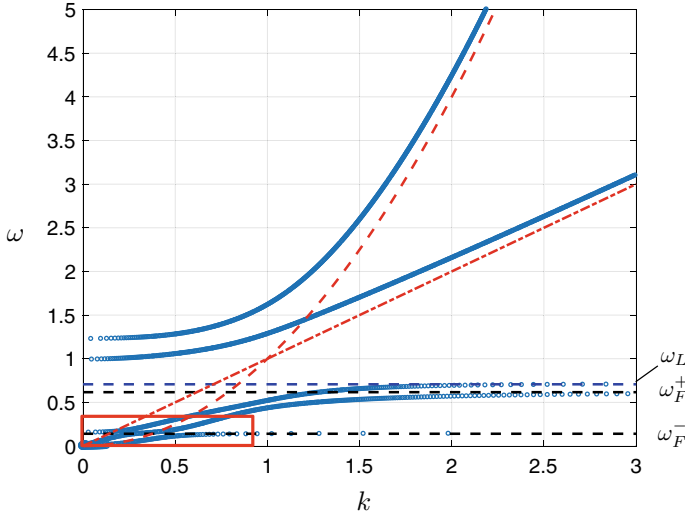
**Fig. 11.6** Dispersion diagram computed using (11.22) for the case when $b = 0.05$ and $\mu_{\text{eff}} = 2$ and all other parameters are set equal to unity. All solutions of (11.22) are represented by blue curves. High-frequency asymptotes for the highest pair of optical curves are presented and based on (11.29)$_1$ (red dash-dot line) and (11.29)$_2$ (red dashed line) below. A magnification of the results based on (11.22) and contained within the red box are found in Fig. 11.8, where low-frequency approximations to the two acoustic curves are considered

frequency space). The three remaining curves are analogous to optical curves and cross the frequency axis at the non-zero values:

$$\sqrt{\frac{K_{\text{eff}}(\rho A + \mu_{\text{eff}})}{\rho A \mu_{\text{eff}}}}$$

and

$$\sqrt{\frac{2bK_{\text{eff}}[3a\mu_{\text{eff}} + (1 + 3a)\rho A \pm \sqrt{(3a\mu_{\text{eff}} + (1 + 3a)\rho A)^2 - 3a\rho A(\rho A + \mu_{\text{eff}})}]}{a\rho A \mu_{\text{eff}}}}.$$

$$(11.24)$$

Further, horizontal asymptotes of the first 3 positive solutions to (11.22) occur resonance frequencies for the layer defined by:

$$\omega_L = \sqrt{\frac{K_{\text{eff}}}{\mu_{\text{eff}}}}, \qquad \omega_F^{\pm} = \sqrt{\frac{2bK_{\text{eff}}[3a + 1 \pm \sqrt{(3a + 1)^2 - 3a}]}{a\mu_{\text{eff}}}}, \qquad (11.25)$$

that are indicated in Figs. 11.5 and 11.6. Here $\omega_L$ and $\omega_F^{\pm}$ correspond to resonant frequencies for the longitudinal and flexural motion, respectively, of the elastic res-

onant coupling layer atop the generalised Rayleigh beam. Note that depending on the value of contrast parameters $a$ and $b$, the position of the horizontal asymptote defined by the longitudinal resonant frequency $\omega_L$ relative to the interval $[\omega_F^-, \omega_F^+]$ can change and this is discussed below.

### 11.3.3.2 Frequency Regimes

Additionally, there exist three frequency regimes characterising the dynamic response of the medium:

- a *low-frequency regime*, bounded above by the lowest resonance frequency of the elastic layer, that takes into account the behaviour of the layer at small frequencies.
- an *intermediate resonance frequency regime*, defined by

$$\omega_r^- < \omega < \omega_r^+ \, , \quad \omega_r^+ = \max\{\omega_L, \omega_F^+\} \, , \quad \omega_r^- = \min\{\omega_L, \omega_F^-\} \, , \qquad (11.26)$$

  where resonant frequencies for the layer (and the equivalent microstructured medium) occur at the boundaries of and/or within this interval.
- and a *super-resonance frequency regime*, bounded below by the highest resonant frequency of the layer and where the dispersive features of the medium begin to neglect the influence of the layer for large frequencies.

These regimes, their corresponding physical interpretations and behaviour are discussed below.

### 11.3.3.3 Dependency of Frequency Regimes on the Contrast Parameters

The size of the frequency intervals for these regimes is shown in Fig. 11.7, as functions of the contrast parameters $a$ and $b$. There, we indicate three regions I (low-frequency regime), II (intermediate frequency regime) and III (super-resonance frequency regime) defined in accordance with (11.26).

Figure 11.7a shows that the regions I and III can shrink and expand, respectively, with increase of $a$ when $b$ is fixed. In fact as $a$ becomes large, the width of region II becomes fixed and converges to the interval $(0, 2\sqrt{3bK_{\text{eff}}/\mu_{\text{eff}}})$.

On the other hand, Fig. 11.7b shows that if $a$ is fixed and $b$ increases, the upper bound for region I becomes the axial resonance frequency $\omega_L$ of the layer, whereas region II expands. There, stop bands for the medium are also visible in regions II and III and this is discussed further below.
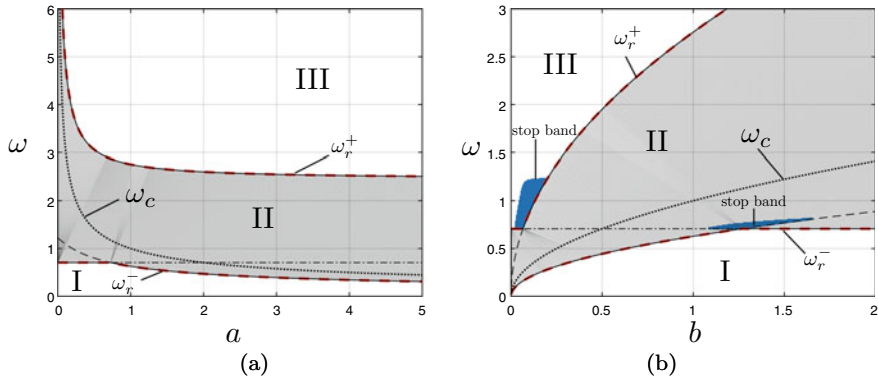
**Fig. 11.7** Behaviour of the regions I (low-frequency regime), II (intermediate resonant regime shown as the grey regions bounded by red dashed lines) and III (super-resonant frequency regime) as functions of **a** $a$ and **b** $b$ based on (11.22). The black dash-dot line corresponds $\omega_L$, whereas black dashed lines are the frequencies $\omega_F^{\pm}$ (see (11.25)). The dotted line corresponds to a frequency $\omega_c$ where the flexural and longitudinal waves in the generalised Rayleigh beam decouple and this is discussed further in Sect. 11.4. In these computations $\mu_{\text{eff}} = 2$ and all other parameters are set equal to unity

#### 11.3.3.4 Low-Frequency Regime

At low frequencies, the coupling between the orthogonal principal motions of the system is small. Indeed, one of the acoustic curves is non-dispersive and is approximated by

$$\omega = \sqrt{\frac{EA}{\rho A + \mu_{\text{eff}}}} k \; , \tag{11.27}$$

and along this $h(\omega, k) = O(k)$ for $k \to 0$ (see (11.23)). Hence the predominant motions of the beam are axial deformations. On the other hand, the remaining acoustic curve behaves as

$$\omega = \sqrt{\frac{EJ}{\rho A + \mu_{\text{eff}}}} k^2 \; , \tag{11.28}$$

near $k = 0$ and for $k$ approaching this value we also have $h(k, \omega) = O(k^{-1})$ (see (11.23)). This implies the generalised Rayleigh beam undergoes mostly flexural deformations.

A comparison of the curves in (11.27) and (11.28) with the dispersion curves obtained from (11.22) is given in Fig. 11.8, where it is evident (11.27) and (11.28) provide a good approximation of the acoustic curves at low frequencies.

The above low-frequency asymptotes (11.27) and (11.28) suggest the behaviour of the beam exhibits longitudinal and flexural motions occurring at frequencies equiva-
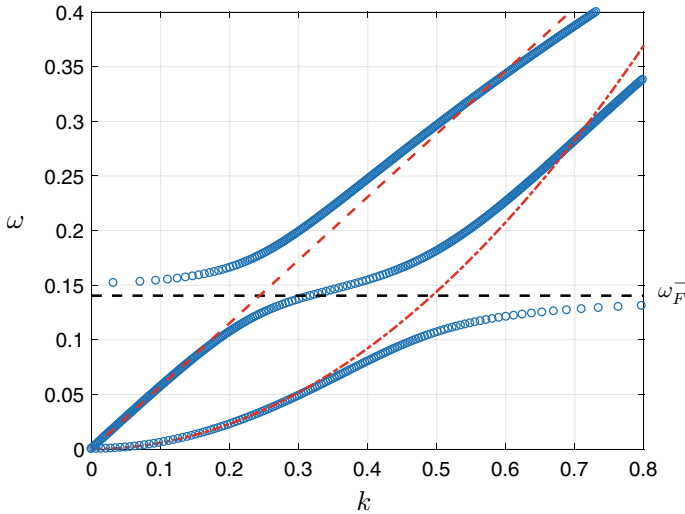
**Fig. 11.8** The plot shows a magnification of the results in the red box of Fig. 11.6 concerning the dispersion curves obtained from (11.22) (represented by blue curves). We refer to there for the description of the computational parameters. Here, the low-frequency asymptotes for the two acoustic curves are presented based on (11.27) (red dashed line) and (11.28) (red dash-dot curve)

lent to those of an ordinary Euler-Bernoulli beam with added mass density, brought by the presence of the elastic resonant coupling medium atop this beam.

#### 11.3.3.5 Intermediate Resonant Frequency Regime

The resonant frequencies defining this interval can also be identified in the model encountered in Sect. 11.2.2, involving a beam attached to a periodic array of resonators. Within the interval defined by (11.26), there exists an additional single resonant frequency that migrates through region II in Fig. 11.7 with the change of the contrast parameters $a$ or $b$. There, this particular resonant frequency is formed from the curve involving the black dashed and dashed dot curves and remains within (11.26) as shown in Fig. 11.7. At the limits of the interval (11.26) the layer resonates leaving the Euler-Bernoulli beam either undisturbed or assuming a non-trivial flexural motion, where the latter is discussed in Appendix A.

We note, $\omega_r^-$ defines the upper limit for the first acoustic curve, which has parabolic behaviour near $k = 0$. The frequency $\omega_r^+$ acts as the upper limit to the first optical curve, whereas the resonant frequency located in the interval (11.26) is the supremum for the second acoustic curve. At the limits of (11.26), the magnitude of the group velocity of the associated dispersion curves becomes smaller and tends to zero when $k \to \pm\infty$. Physically, when the group velocity of the waves is close to zero for a

given frequency, this indicates a regime where waves generated, say, by some locally applied excitation move slowly away from the load's location along the beam.

### 11.3.3.6  Stop Bands

Additionally, depending on the material composition of the generalised Rayleigh beam, the upper bound of the resonant regime can define the lower limit of a finite stop band, where no waves can propagate in main beam. Stop bands for the medium and their dependency on $b$ are shown in Fig. 11.7b. One appears in region III and its width is controlled by $\omega_r^+$ and the behaviour of the lowest optical curve in region III. This optical curve may exhibit additional zero group velocity points for non-zero values of the wavenumber (indicated by the black dot in Fig. 11.5). On the other hand, as demonstrated in Fig. 11.6, such a point on the corresponding second optical curve may not exist, and in this case, the maximum of the stop band is controlled by the minimum of this curve at $k = 0$ (see (11.24)).

The other stop band can exist in region II. Figure 11.7 demonstrates this can exist for a narrow range of parameter values. Its width depends on $\max\{\omega_F^-, \omega_L\}$ and the behaviour of the first optical curve for the generalised Rayleigh beam.

### 11.3.3.7  Super-Resonance Frequency Regime

In this regime, the frequency of waves propagating through the generalised Rayleigh beam can be determined through the usual dispersion curves for axial and flexural motions of an Euler-Bernoulli beam:

$$\omega = \sqrt{\frac{EA}{\rho A}}k \,, \quad \text{and} \quad \omega = \sqrt{\frac{EJ}{\rho A}}k^2 \,. \tag{11.29}$$

In Fig. 11.6, we compare these curves with the dispersion curves obtained from (11.22). There, it is clear that as $k \to \infty$, the resulting solutions of (11.22) tend to the preceding curves.

Note that as indicated by these expressions, effects from the elastic resonant coupling layer attached to the beam are neglected in this frequency regime. This is expected for high frequencies, as continuous models cannot account for dynamic phenomena occurring at smaller internal scales (for instance, see [56]). The above result suggests that in this regime the meso-scale solution (11.8), (11.13), (11.14) should be used with (11.17), (11.18), to recover the microscale influence of the resonator array on the behaviour of the medium.

Next, we use the information discussed here in considering the response of the generalised Rayleigh beam to a point force, where new features are encountered at different frequencies and at particular frequencies the flexural and longitudinal waves can decouple.

## 11.4    Green's Matrix for the Generalised Rayleigh Beam

In this section, we construct Green's matrix for the generalised Rayleigh beam in the closed form. This is a $2 \times 2$ matrix, which we denote by $\boldsymbol{\Gamma}(x)$, whose first and second columns correspond to the response of the system when subjected to a harmonic point force of unit amplitude and frequency $\omega$ at the origin in the horizontal and vertical directions, respectively.

The first and second columns of $\boldsymbol{\Gamma}$ solve equations (11.1) and (11.2) with an appropriate delta function placed in either (11.1) or (11.2), respectively. Using (11.21), we then write the governing equation for $\boldsymbol{\Gamma}$ as follows:

$$\mathscr{A}\left(\frac{\mathrm{d}}{\mathrm{d}x}, \omega\right)\boldsymbol{\Gamma}(x) = -\delta(x)\mathbf{I} , \qquad (11.30)$$

where $\mathscr{A}(\frac{\mathrm{d}}{\mathrm{d}x}, \omega)$ (see (11.21)) is now a matrix differential operator, $\delta(x)$ is the Dirac delta function and $\mathbf{I}$ is the $2 \times 2$ identity matrix.

### 11.4.1    Closed form Representation of $\boldsymbol{\Gamma}$

Here we state the form of the matrix $\boldsymbol{\Gamma}$ assuming the solutions of (11.22) are distinct. The case of repeated roots corresponds to points $(k, \omega)$ in the wavenumber-frequency space where the group velocity along associated dispersion curves is zero, leading to resonance modes for the beam. For these modes, energy is unable to leave the location of the applied force and the energy density on the medium becomes unbounded in time. For the study of such responses we refer to [56].

In order to construct $\boldsymbol{\Gamma}$, we need the following sets. Based on Sect. 11.3 and information concerning (11.22) it is useful to construct the sets:

$$S_+ := \{k : \ k \text{ satisfies (11.22) with Im } (k) > 0 \text{ or Im } (k) = 0 \text{ with } v_g > 0\}$$

and

$$S_- := \{k : \ k \text{ satisfies (11.22) with Im } (k) < 0 \text{ or Im } (k) = 0 \text{ with } v_g < 0\} .$$

We note $|S_\pm| = 3$. Here $S_+$ ($S_-$) defines wave phenomena propagating to the right (left) of the applied point force at $x = 0$, which includes waves, purely evanescent deformations and evanescent waves (associated with real, imaginary and complex roots of (11.22), respectively).

Green's matrix $\boldsymbol{\Gamma}$ then takes the form

$$
\boldsymbol{\Gamma}(x) = \begin{cases} -\mathrm{i} \displaystyle\sum_{k \in S^+} \left[ \frac{\mathrm{d}}{\mathrm{d}k} (\det \mathscr{A}(\mathrm{i}k, \omega)) \right]^{-1} \mathrm{adj}(\mathscr{A}(\mathrm{i}k, \omega)) e^{\mathrm{i}kx} \,, \quad \text{for } x > 0 \,, \\[2em] \mathrm{i} \displaystyle\sum_{k \in S^-} \left[ \frac{\mathrm{d}}{\mathrm{d}k} (\det \mathscr{A}(\mathrm{i}k, \omega)) \right]^{-1} \mathrm{adj}(\mathscr{A}(\mathrm{i}k, \omega)) e^{\mathrm{i}kx} \,, \quad \text{for } x < 0 \,, \end{cases}
$$

$$(11.31)$$

where $\mathrm{adj}(\boldsymbol{B})$ represents the adjoint matrix of $\boldsymbol{B}$.

### 11.4.2 Flexural-Longitudinal Coupling of Waves

Here we provide an illustrative example of the deformations assumed by the generalised Rayleigh beam when loaded by either a horizontal or vertical point force. In particular, we investigate the coupling phenomenon between principal motions of the main beam at different frequencies shown as '1'–'4' in Fig. 11.9.

Figure 11.10 shows the response of the beam to sinusoidal point forces at a selection of frequencies. The deformation produced by the horizontal point force at $x = 0$ is given in (a), (c), (e) and (g). There, the point load is applied at various frequencies indicated on the insets of each figure. The position of frequencies relative to the dispersion curves in the wavenumber-frequency space is shown in Fig. 11.9. The application of the low frequency load in Fig. 11.10a shows the coupling phenomenon initiates a significant flexural deformation, when compared with Fig. 11.10c, e and g. Note the amplitude of the flexural deformation is not monotonic with respect to the load frequency.

Further, Fig. 11.10c shows only an axial deformation of the generalised Rayleigh beam. In fact, the longitudinal and flexural beam motions can be completely decoupled at a selected frequency, which has been chosen in Fig. 11.10c. Indeed, this frequency coincides with the zero of the $\Pi_{\mathrm{eff}}(\omega)$ and is:

$$
\omega = \omega_c := \sqrt{\frac{2K_{\mathrm{eff}} b}{a \mu_{\mathrm{eff}}}} \,. \tag{11.32}
$$

This frequency $\omega_c$ is also presented in Fig. 11.7 which shows this is always located in the intermediate resonant frequency regime. At this frequency the Eqs. (11.1) and (11.2) decouple and reduce to

$$
\rho A \omega_c^2 U(x) + E A U''(x) + \omega_c^2 \Psi_{\mathrm{eff}}(\omega_c) U(x) = 0 \,, \tag{11.33}
$$

$$
-\rho A \omega_c^2 V(x) + E J V''''(x) - \omega_c^2 \Phi_{\mathrm{eff}}(\omega_c) V(x) + \omega_c^2 \Upsilon_{\mathrm{eff}}(\omega_c) V''(x) = 0 \,. \tag{11.34}
$$
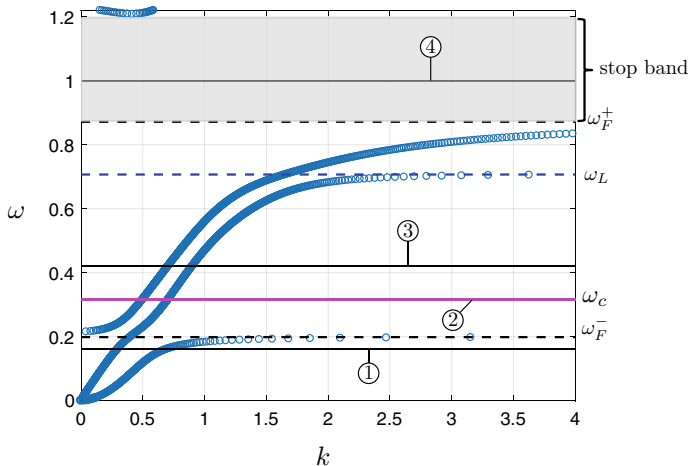
**Fig. 11.9** Dispersion diagram based on (11.22) for $b = 0.1$, $\mu_{\text{eff}} = 2$ and all other material parameters set equal to unity. Loading frequencies are indicated by horizontal solid lines with "1", "2","3" and "4" corresponding to the pairs of computations (**a**) and (**b**), (**c**) and (**d**), (**e**) and (**f**), (**g**) and (**h**), respectively, in Fig. 11.10

Thus, when the generalised Rayleigh beam is subjected to either dynamic longitudinal or flexural loading, the medium supports only the propagation of longitudinal or flexural waves governed by the modified Eq. (11.33) or (11.34), respectively.

Figure 11.10b, d, f and h show the response of the beam to a vertical point load, where the amplitudes of the flexural deformations are monotonically decreasing with respect to the increase in the frequency of the applied load. Here, axial deformations appear to be negligible for frequencies not located near $\omega_c$ and all computations indicate that the effect of the coupling can be small for flexural loads.

Finally, we note Fig. 11.10a–f demonstrates the response of a pass band Green's function. Figure 11.10g and h refer to computations for the stop band Green's function where, in particular, the frequency is selected so that the load generates purely evanescent modes as well as evanescent oscillations. We recall the latter is not a feature of the classical models for axial and flexural motion of an Euler-Bernoulli beam without damping. As expected, the stop band Green's function corresponds to a localised deformation.

## 11.5 Conclusions

Here, we have analysed vibrations propagating through a continuous asymmetric system we define as the generalised Rayleigh beam, formed from attaching a beam to an elastic resonant coupling layer. The layer brings negative translational and rotational inertial effects to the beam. We have demonstrated via the method of
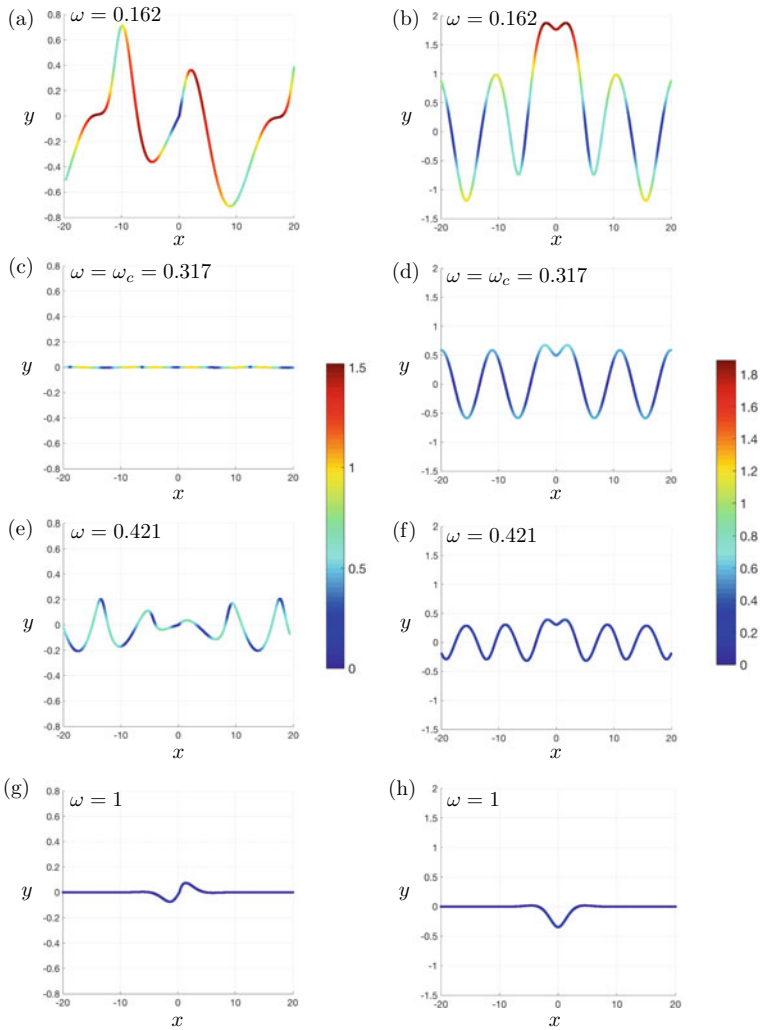
**Fig. 11.10** Deformations of the generalised Rayleigh beam induced by a horizontal point load in **a**, **c**, **e**, **g** and vertical point load **b**, **d**, **f** and **h**. The colour scale for **a**, **c**, **e**, **g** (**b**, **d**, **f** and **h**) is shown to the right of the figures and represents the total displacement in the medium. The computations are based on the real part of (11.31), with frequencies of the loads in each case specified in the figure insets. Here, $\mu_{\text{eff}} = 2$, $b = 0.1$ and the remaining parameters are set equal to unity

meso-scale approximations that this medium approximates the behaviour of discrete system where the layer is replaced by a dense arrangement of flexural resonators.

The dispersive behaviour of the generalised Rayleigh beam has been completely described. This investigation revealed three important dynamic regimes for the medium defined by the resonant frequencies of the elastic layer atop of the beam. At low frequencies, the dispersive properties of the generalised Rayleigh beam resemble those encountered in classical problem of an Euler-Bernoulli beam where flexural and longitudinal motions are decoupled. In contrast, at these frequencies the generalised Rayleigh beam brings a weak coupling between such modes and an effective mass attributed to the elastic layer. On the other hand, at high frequencies similar comparisons can be made but there the dispersive features of the system neglect the influence of the layer. Within an intermediate frequency regime the layer possesses resonant frequencies and they can define stop bands in the medium. Within the stop bands we can encounter evanescent oscillations and purely evanescent modes supported by the medium. The former are not features of the solution to the classical problem involving the decoupled flexural and axial motion of an Euler-Bernoulli beam without damping, whereas the pure evanescent phenomenon is absent in corresponding dynamic problem for longitudinal deformations.

Additionally, the meso-scale solution developed has been shown to be efficient in recovering the low and high frequency behaviour of the periodic discrete system when its microstructure is dense. Further, this solution, used in the dynamic homogenisation procedure, utilises fundamental model solutions in its construction, namely, Green's functions. These enable the solution to be effective in capturing the full dynamic response of the periodic medium. This has consequently led to an effective model in the form of the generalised Rayleigh beam that is efficient in tracing a substantial collection of structural responses of the microstructured medium at high/low frequencies and for a wide range of wavenumbers.

We have also derived the expression for Green's matrix for the generalised Rayleigh beam. This matrix is paramount in constructing solutions representing the vibration response of a generalised Rayleigh beam or its microstructural equivalent when subjected to a range of dynamic loads. There, we identified that axial dynamic phenomena can promote significant flexural motions of the beam and there exists a frequency where the dynamic coupling of the principal beam motions is nullified.

It is envisaged that the model studied here and the associated results will be important in applications such as civil engineering, seismic protection and the design of advanced materials where controlling wave phenomena is of major importance.

## Appendix A: Resonance Modes

Here we discuss the response of the generalised Rayleigh beam at the resonant frequencies (11.25).

**Resonant Response at $\omega_L$**

Here $\omega_L$ corresponds to the longitudinal resonance of the medium atop the lateral beam. When $\omega_L$ is distinct from $\omega_F^\pm$, the system (11.1) and (11.2) implies $V(x) = 0$ and the longitudinal displacement obeys

$$(\rho A + \Psi_{\text{eff}}(\omega_L))\omega_L^2 U(x) + EAU''(x) = 0 ,$$

for $-\infty < x < \infty$. Its solution is standard and given as

$$U(x) = A \sin \left( \sqrt{\frac{\rho A + \Psi_{\text{eff}}(\omega_L)}{EA}} \omega_L x \right) + B \cos \left( \sqrt{\frac{\rho A + \Psi_{\text{eff}}(\omega_L)}{EA}} \omega_L x \right) ,$$

where $A$ and $B$ are arbitrary constants. Hence in this resonance regime, flexural deformations of the system are not supported, whereas longitudinal waves can propagate through the medium.

**Resonant Response at $\omega_F^\pm$**

The frequency $\omega_F^\pm$ represents the flexural resonant response of the layer atop the beam. If this is distinct from $\omega_L$, one has at this frequency that $U(x)$ and $V(x)$ satisfy

$$\Psi_{\text{eff}}^*(\omega^*)U(x) + \Pi_{\text{eff}}^*(\omega^*)V'(x) = 0$$

$$-\Pi_{\text{eff}}^*(\omega^*)U'(x) + \Upsilon_{\text{eff}}^*(\omega^*)V''(x) = 0$$

where $\omega = \omega_F^\pm$ and the notation $Q^*(\omega^*)$ represents

$$Q^*(\omega^*) = \lim_{\omega \to \omega^*} (\omega - \omega^*)Q(\omega) .$$

This previous system admits the solution:

$$U(x) = -\frac{A\Pi_{\text{eff}}^*(\omega^*)}{\Psi_{\text{eff}}^*(\omega^*)} , \qquad V(x) = Ax + B$$

where $A$ and $B$ are arbitrary constants, provided

$$\Psi_{\text{eff}}^*(\omega^*)\Upsilon_{\text{eff}}^*(\omega^*) + (\Pi_{\text{eff}}^*(\omega^*))^2 \neq 0 .$$

The result suggests at this resonance frequency the flexural displacement is linear and this is accompanied by a constant axial deformation.

# References

1. Bakhvalov N, Panasenko G (1989) Homogenisation: averaging processes in periodic media: mathematical problems in the mechanics of composite materials. Mathematics and its applications series. Springer, Dordrecht
2. Sanchez-Palencia E (1980) Non-Homogeneous Media and Vibration Theory. Lecture Notes in Physics, Springer, Berlin, Heidelberg
3. Marchenko VA, Khruslov YE (2006) Homogenization of partial differential equations. Progress in mathematical physics. Birkhäuser, Boston
4. Craster RV, Kaplunov J, Pichugin AV (2010) High-frequency homogenization for periodic media. Proc R Soc A 466:2341–2362
5. Nolde E, Craster RV, Kaplunov J (2011) High frequency homogenization for structural mechanics. J Mech Phys Solids 59(3):651–671
6. Craster RV, Kaplunov J, Nolde E, Guenneau S (2011) High-frequency homogenization for checkerboard structures: defect modes, ultrarefraction, and all-angle negative refraction. JOSA A 28(6):1032–1040
7. Craster RV, Kaplunov J, Nolde E, Guenneau S (2012) Bloch dispersion and high frequency homogenization for separable doubly-periodic structures. Wave Motion 49(2):333–346
8. Brun M, Giaccu GF, Movchan AB, Movchan NV (2012) Asymptotics of eigenfrequencies in the dynamic response of elongated multi-structures. Proc. R. Soc. Lond. A 468:378–394
9. Carta G, Giaccu GF, Brun M (2017) A phononic band gap model for long bridges. The 'Brabau' bridge case. Eng Struct 140:66–76
10. Kurze J (1997) Refined calculations or improved understanding of rail vibrations. Acta Acust 83:506–515
11. Nordborg A (1998) Vertical rail vibrations: point force excitation. Acta Acust 84:280–288
12. Hamat J-F (1999) Railway noise: use of the Timoshenko model in rail vibration studies. Acta Acust 85:54–62
13. Cherkaev A, Ryvkin M (2019) Damage propagation in 2d beam lattices: 1. Uncertainty and assumptions. Arch Appl Mech 89:485–501
14. Cherkaev A, Ryvkin M (2019) Damage propagation in 2d beam lattices: 2. Design of an isotropic fault-tolerant lattice. Arch Appl Mech 89:503–519
15. Brun M, Movchan AB, Slepyan LI (2013) Transition wave in a supported heavy beam. J Mech Phys Solids 61(10):2067–2085
16. Brun M, Giaccu GF, Movchan AB, Slepyan LI (2014) Transition wave in the collapse of the San Saba bridge. Front Mater 1:12
17. Nieves MJ, Mishuris GS, Slepyan LI (2016) Transient wave in a transformable periodic flexural structure. Int J Solids Struct 112:185–208
18. Nieves MJ, Mishuris GS, Slepyan LI (2016) Analysis of dynamic damage propagation in discrete beam structures. Int J Solids Struct 97–98:699–713
19. Heckl M (2002) Coupled waves on a periodically supported beam. J Sound Vib 252(5):849–882
20. Iqbal M, Jaya MM, Bursi OS, Kumar A, Ceravolo R (2020) Flexural band gaps and response attenuation of periodic piping systems enhanced with localized and distributed resonators. Sci Rep 10:85
21. Bordiga G, Cabras L, Piccolroaz A, Bigoni D (2019) Prestress tuning of negative refraction and wave channeling from flexural sources. Appl Phys Lett 114:041901
22. Colquitt DJ, Jones IS, Movchan NV, Movchan AB (2011) Dispersion and localization of elastic waves in materials with microstructure. Proc R Soc A 467:2874–2895
23. Bordiga G, Cabras L, Bigoni D, Piccolroaz A (2019) Free and forced wave propagation in a Rayleigh-beam grid: flat bands, dirac cones, and vibration localization versus isotropization. Int J Solids Struct 161:64–81
24. Madine KH, Colquitt DJ (2021) Dynamic Green's functions in discrete flexural systems. Quart. J Mech Appl Math 74(3):323–350
25. Piccolroaz A, Movchan AB, Cabras L (2017) Rotational inertia interface in a dynamic lattice of flexural beams. Int J Solids Struct 112:43–53

26. Nieves MJ, Carta G, Pagneux V, Brun M (2020) Rayleigh waves in micro-structured elastic systems: non-reciprocity and energy symmetry breaking. Int J Eng Sci 156:103365
27. Garau M, Carta G, Nieves MJ, Jones IS, Movchan NV, Movchan AB (2018) Interfacial wave-forms in chiral lattices with gyroscopic spinners. Proc R Soc Lond A 474:20180132
28. Carta G, Jones IS, Movchan NV, Movchan AB, Nieves MJ (2017) "Deflecting elastic prism" and unidirectional localisation for waves in chiral elastic systems. Sci Rep 7:26
29. Carta G, Cabras L, Brun M (2016) Continuous and discrete microstructured materials with null Poisson's ratio. J Eur Cera Soc 36(9):2183–2192
30. Berinskii IE (2018) In-plane elastic properties of auxetic multilattices. Smart Mater Struct 27(7):075012
31. Morvaridi M, Carta G, Bosia F, Gliozzi AS, Pugno NM, Misseroni D, Brun M (2021) Hierarchical auxetic and isotropic porous medium with extremely negative Poisson's ratio. Extreme Mech Lett 48:101405
32. Cabras L, Brun M, Misseroni D (2019) Micro-structured medium with large isotropic negative thermal expansion. Proc R Soc 475(2232):20190468
33. Piccolroaz A, Movchan AB (2014) Dispersion and localisation in structured Rayleigh beams. Int J Solids Struct 25–26:4452–4461
34. Graff KF (1975) Micromechanics of materials, with applications. Oxford University Press, Oxford
35. Nieves MJ, Brun M (2019) Dynamic characterization of a periodic microstructured flexural system with rotational inertia. Philos T R Soc A 377(2156):20190113
36. Slepyan LI, Ayzenberg-Stenenko M, Mishuris G (2015) Forerunning mode transition in a continuous waveguide. J Mech Phys Solids 78:32–45
37. Nieves M, Movchan A (2022) Meso-scale method of asymptotic analysis of elastic vibrations in periodic and non-periodic multi-structures. Q J Mech Appl Math 75(3):171–214
38. Maz'ya V, Movchan A, Nieves M (2013) Green's kernels and meso-scale approximations in perforated domains. Lecture notes in mathematics. Springer Cham
39. Maz'ya V, Movchan A (2010) Asymptotic treatment of perforated domains without homogenization. Math Nach 283(1):104–125
40. Maz'ya V, Movchan A, Nieves M (2011) Mesoscale asymptotic approximations to solutions of mixed boundary value problems in perforated domains. Multiscale Model Simul 9(1):424–448
41. Nieves MJ (2017) Asymptotic analysis of solutions to transmission problems in solids with many inclusions. SIAM J Appl Math 77(4):1417–1443
42. Maz'ya VG, Movchan AB, Nieves MJ (2014) Mesoscale approximations for solutions of the Dirichlet problem in a perforated elastic body. J Math Sci (NY) 202(2):215–244
43. Maz'ya VG, Movchan AB, Nieves MJ (2016) Mesoscale models and approximate solutions for solids containing clouds of voids. Multiscale Model Simul 14(1):138–172
44. Maz'ya VG, Movchan AB, Nieves MJ (2017) Eigenvalue problem in a solid with many inclusions: asymptotic analysis. Multiscale Model Simul 15(2):1003–1047
45. Maz'ya VG, Movchan AB, Nieves MJ (2020) On meso-scale approximations for vibrations of membranes with lower-dimensional clusters of inertial inclusions. Algebra i Analiz, 3:219–237
46. Mead DJ (1975) Wave propagation and natural modes in periodic systems II: multi-coupled systems with and without damping. J Sound Vib 40(1):19–39
47. Mead DJ, Markuš Š (1983) Coupled flexural-longitudinal wave motion in a periodic beam. J Sound Vib 90(1):1–24
48. Friis L, Ohlrich M (2005) Coupling of flexural and longitudinal wave motion in a periodic structure with asymmetrically arranged transverse beams. J Acoust Soc Am 118:3010
49. Yun Y, Mak CM (2009) A study of coupled flexural-longitudinal wave motion in a periodic dual-beam structure with transverse connection. J Acoust Soc Am 126:114
50. Yun Y, Mak CM (2011) Experimental study of coupled vibration in a finite periodic dual-layered structure with transverse connection. Appl Acoust 72:287–296
51. Colombi A, Colquitt D, Roux P, Guenneau S, Craster RV (2016) A seismic metamaterial: the resonant metawedge. Sci Rep 6:27717

52. Colombi A, Roux P, Guenneau S, Gueguen P, Craster RV (2016) Forests as a natural seismic metamaterial: Rayleigh wave bandgaps induced by local resonances. Sci Rep 6:19238
53. Xiao Y, Wen J, Wen X (2012) Flexural wave band gaps in locally resonant thin plates with periodically attached spring-mass resonators. J Phys D: Appl Phys 45(19):195401
54. Haslinger SG, Movchan NV, Movchan AB, Jones IS, Craster RV (2017) Controlling flexural waves in semi-infinite platonic crystals with resonator-type scatterers. Quart J Mech Appl Math 70(3):216–247
55. Marigo J-J, Pham K, Maurel A, Guenneau S (2020) Effective model for elastic waves propagating in a substrate supporting a dense array of plates/beams with flexural resonances. J Mech Phys Solids 143:104029
56. Slepyan LI (2002) Models and phenomena in fracture mechanics. Springer, Berlin

# Chapter 12
# Higher-Order and Nonlocal One-Dimensional Thermal Lattices with Short- and Long-Range Interactions

**E. Nuñez del Prado, Noel Challamel, and V. Picandet**

**Abstract** The present paper deals with heat conduction in a uni-dimensional two-neighbor interaction lattice. An exact solution based on the method of separation of variables and the use of trigonometric series, for given initial and boundary conditions, is obtained. The solution is then compared to the classical Fourier solution and to a nonlocal solution. The nonlocal solution is based on an Eringen-type differential model of Fourier, and the length scale parameter for this model is calibrated by applying a continualization method to the lattice equation. Finally, an error analysis is performed in order to verify the efficiency of the local and nonlocal approximations.

**Keywords** Heat equation · Fourier's law · Heat transfer · Lattice · Nonlocality

## 12.1 Introduction

The classical heat equation or Fourier's law [1] establishes a linear relationship between the heat flux $q$ and the gradient of temperature $\nabla T$ and has been proved to be sufficiently accurate when representing the behavior of heat propagation at a macroscopic scale. However, when working with small scales [2–4], the so-called local fundamental law of heat transfer is not necessarily valid, due to the material size being of the same order (or smaller) as the mean-free path of energy carriers. In this case, nonlocal effects can be significant and have to be taken into account. Nonlocal laws may be related to the heterogeneous nature or the discrete nature of the material at the considered scale. Such continuum laws that possess internal length scales may be elaborated from lattice models or discrete models with repetitive cells. From a pure mechanical point of view, [5–10] showed that mechanical lattices behaved as nonlocal continuous axial models with additional stress gradient terms (also called Eringen's type nonlocal differential models [8]). The length scale in this model is either calibrated with respect to the long-range limit (as suggested by

E. Nuñez del Prado · N. Challamel (✉) · V. Picandet
Universitè Bretagne Sud - Institut Dupuy de Lôme, Centre de Recherche, Rue de Saint Maudè, BP92116, 56321 Lorient Cedex, France
e-mail: noel.challamel@univubs.fr

[5, 8] or [9]) or with respect to the Brillouin zone of the wave dispersive relation of the lattice model [6–8]. The mechanical lattice can be composed of particles which interact with their direct neighbors, thus leading to a lattice with short-range interactions. This is the case of Lagrange lattice, composed of equal masses connected between each other by linear springs (also mathematically equivalent to a lattice string—see [11]). The generalization of Lagrange lattice with direct and indirect interactions (which accounts for short- and long-range interactions) is not new and has been already considered during the nineteenth century with the development of the so-called molecular elasticity approach. The reader can refer to the works of Piola during the nineteenth century (see historical analysis of [12] or [13]). More recently, [14], in his seminal book, investigated the wave dispersive properties in a generalized lattice with short- and long-range interaction. The wave dispersive properties in a generalized infinite lattice has been also studied by [15, 16], with $p = 2$ interactions or in the general case, with $p$ interactions. Exact eigenfrequencies of finite generalized (mechanical) lattices with short- and long-range interactions have been calculated for various boundary conditions by [17]. Reference [18] also has shown the extreme sensitivity of the frequency response of lattices with direct and indirect interactions, with respect to the higher-order boundary conditions of the generalized lattice. Reference [19] highlighted the possible localization and static oscillatory phenomenon of generalized lattices for specific higher-order boundary conditions. The capability of a nonlocal continuum to capture generalized lattices was shown by [16, 17] for pure mechanical interactions.

The study of deterministic thermal lattices from their mathematical properties of mixed differential-difference equation is much more recent. Reference [20] studied a diffusive lattice with only direct interactions, and proposed a nonlocal diffusion equation which contains scale effects and included mixed spatial and temporal derivatives. References [21, 22] obtained the exact solution of the (discrete) thermal lattice with only direct interactions. References [21, 22] also showed the efficiency of the continuous nonlocal heat equation, to capture the scale effects of the lattice problem. Reference [23] investigated the evolution problem of a finite thermal lattice based on Cattaneo-Vernotte's equation. In this paper, we propose a nonlocal model capable of representing the behavior of heat transfer in a lattice with second neighbor interactions. The results are then extended to a thermal lattice with $p$ general interactions, both from the discrete approach and its nonlocal continuum representation.

We propose then, in this paper, a nonlocal model capable of representing the behavior of heat transfer in a lattice with second neighbor interactions.

The considered lattice is represented in Fig. 12.1.
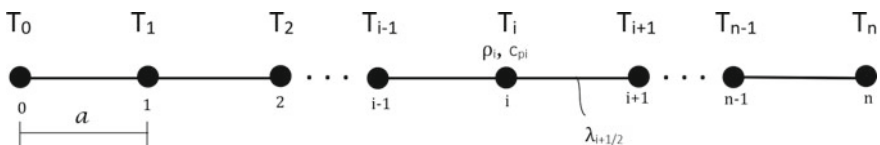


**Fig. 12.1** Discrete scheme for the lattice model

where $T_i$ is the temperature at node $i$, $\rho$ is the material's density, $c_p$ is the specific heat, $\lambda$ is the thermal conductivity and $a$ is the lattice spacing. For the lattice with second neighbor interaction, the heat flux is

$$q_{i+\frac{1}{2}} = -\lambda \left( \beta_1 \frac{T_{i+1} - T_i}{a} + \beta_2 \frac{T_{i+2} - T_i}{4a} + \beta_2 \frac{T_{i+1} - T_{i-1}}{4a} \right) \tag{12.1}$$

where $\beta_1$ and $\beta_2$ are weighting coefficients for the short- and long-range interactions, respectively, such that $\beta_1 > \beta_2 > 0$ and $\beta_1 + \beta_2 = 1$. The heat flux equation is combined with the equation of conservation of energy:

$$\rho c_p \dot{T}_i = -\frac{q_{i+1/2} - q_{i-1/2}}{a} \tag{12.2}$$

and finally, the heat transfer equation in a discrete media with second order neighbor interactions is obtained as

$$\dot{T}_i = \alpha \left( \beta_1 \frac{T_{i+1} - 2T_i + T_{i-1}}{a^2} + \beta_2 \frac{T_{i+2} - 2T_i + T_{i-2}}{4a^2} \right) \tag{12.3}$$

where $\alpha = \frac{\lambda}{\rho c_p}$ is the thermal diffusivity.

In [21], a nonlocal model based on an Eringen-type differential model of Fourier's law with a length scale calibrated with respect to the lattice spacing was developed:

$$q - l_c^2 \frac{\partial^2 q}{\partial x^2} = -\lambda \frac{\partial T}{\partial x} \tag{12.4}$$

where $l_c^2 = \frac{a^2}{12}$ is the length scale parameter, leading to the following nonlocal heat equation:

$$\dot{T} = \alpha \frac{\partial^2 T}{\partial x^2} + l_c^2 \frac{\partial^3 T}{\partial t \partial x^2} \tag{12.5}$$

It was shown that this type of nonlocal law could efficiently approximate the behavior of heat transfer in a direct neighbor interaction lattice. In this paper, we extend this work to the study of second-order neighbor interaction. In Sect. 12.2, an analytical solution to Eq. (12.3) is derived and it is verified by using numerical methods in Sect. 12.3. Then, the analytical solution to the nonlocal equation and the length scale are determined in Sect. 12.4. Finally, the nonlocal solution and the classical analytical solution of Fourier's heat equation are compared to the lattice model in Sect. 12.6.

## 12.2   Analytical Solution to the Discrete Equation

In this section, the discrete equation is solved by using the method of separation of variables. We set $T_i(t) = X_i Z(t)$, obtaining the following equation:

$$\dot{Z}X_i = \alpha \left( \beta_1 \frac{(X_{i+1} - 2X_i + X_{i-1})Z(t)}{a^2} + \beta_2 \frac{(X_{i+2} - 2X_i + X_{i-2})Z(t)}{4a^2} \right)$$
(12.6)

$$\implies \frac{\dot{Z}}{Z} = \frac{\alpha}{4} \frac{\beta_2 X_{i+2} + 4\beta_1 X_{i+1} - 2(4\beta_1 + \beta_2)X_i + 4\beta_1 X_{i-1} + \beta_2 X_{i-2}}{a^2 X_i} = -\gamma\alpha$$
(12.7)

$$\implies \beta_2 X_{i+2} + 4\beta_1 X_{i+1} - 2(4\beta_1 + \beta_2 - 2\gamma a^2)X_i + 4\beta_1 X_{i-1} + \beta_2 X_{i-2} = 0$$
(12.8)

Equation (12.8) is a linear homogeneous fourth-order difference equation with constant coefficients, which admits the following auxiliary equation (see [24, 25]):

$$\beta_2 f^4 + 4\beta_1 f^3 - 2(4\beta_1 + \beta_2 - 2\gamma a^2)f^2 + 4\beta f + \beta_2 = 0$$
(12.9)

which is equivalent to

$$\beta_2 f^2 + 4\beta_1 f - 2(4\beta_1 + \beta_2 - 2\gamma a^2) + 4\beta_1 \frac{1}{f} + \beta_2 \frac{1}{f^2} = 0$$
(12.10)

By setting $\tau = f + \frac{1}{f}$, (12.10) can be rewritten as

$$\beta_2 \tau^2 + 4\beta_1 \tau - 2(4\beta_1 + 2\beta_2 - 2\gamma a^2) = 0$$
(12.11)

The discriminant of equation (12.11) is

$$\Delta = 16\beta_1^2 + 32\beta_1\beta_2 + 16\beta_2^2 - 16\gamma a^2 \beta_2$$
(12.12)

Therefore, the solutions of equation (12.11) are

$$\tau = -2\frac{\beta_1}{\beta_2} \pm \sqrt{4\frac{\beta_1^2}{\beta_2^2} + 8\frac{\beta_1}{\beta_2} + 4 - 4\frac{\gamma a^2}{\beta_2}}$$
(12.13)

$$\implies \frac{\tau}{2} = -\frac{\beta_1}{\beta_2} \pm \sqrt{(\frac{\beta_1}{\beta_2} + 1)^2 - \frac{\gamma a^2}{\beta_2}}$$
(12.14)

We have that

$$f^2 - \tau f + 1 = 0$$
(12.15)

The solutions of $f$ are then

$$f = \frac{\tau \pm \sqrt{\tau^2 - 4}}{2} \tag{12.16}$$

Finally, we find that

$$\begin{cases} f_1 = \frac{\tau_1 + \sqrt{\tau_1^2 - 4}}{2} \\ f_2 = \frac{\tau_1 - \sqrt{\tau_1^2 - 4}}{2} \\ f_3 = \frac{\tau_2 + \sqrt{\tau_2^2 - 4}}{2} \\ f_4 = \frac{\tau_2 - \sqrt{\tau_2^2 - 4}}{2} \end{cases} \tag{12.17}$$

We have that $\beta_1 > \beta_2 > 0$. If we suppose that $\gamma > 0$,

$$\frac{\beta_1}{\beta_2} + 1 > 0 \implies (\frac{\beta_1}{\beta_2} + 1)^2 > (\frac{\beta_1}{\beta_2} + 1)^2 - \frac{\gamma a^2}{\beta_2} \implies \frac{\beta_1}{\beta_2} + 1 > \sqrt{(\frac{\beta_1}{\beta_2} + 1)^2 - \frac{\gamma a^2}{\beta_2}} \tag{12.18}$$

Finally,

$$-\frac{\beta_1}{\beta_2} + \sqrt{(\frac{\beta_1}{\beta_2} + 1)^2 - \frac{\gamma a^2}{\beta_2}} < 1 \tag{12.19}$$

We now suppose that $(\frac{\beta_1}{\beta_2} + 1)^2 \frac{\beta_2}{a^2} \geq \gamma$, then:

$$-\frac{\beta_1}{\beta_2} - \sqrt{(\frac{\beta_1}{\beta_2} + 1)^2 - \frac{\gamma a^2}{\beta_2}} < -1 \tag{12.20}$$

From (12.19) and (12.20), we can set

$$\begin{cases} cos(\phi) = \frac{\tau_1}{2} = -\frac{\beta_1}{\beta_2} + \sqrt{(\frac{\beta_1}{\beta_2} + 1)^2 - \frac{\gamma a^2}{\beta_2}} \\ cosh(\theta) = -\frac{\tau_2}{2} = \frac{\beta_1}{\beta_2} + \sqrt{(\frac{\beta_1}{\beta_2} + 1)^2 - \frac{\gamma a^2}{\beta_2}} \end{cases} \tag{12.21}$$

We find from (12.17) and (12.21) the solutions for the auxiliary equation:

$$\begin{cases} f_1 = cos(\phi) + \sqrt{cos^2(\phi) - 1} = cos(\phi) + \sqrt{-sin^2(\phi)} = cos(\phi) + isin(\phi) \\ f_2 = cos(\phi) - isin(\phi) \\ f_3 = -cosh(\theta) + \sqrt{cosh^2(\theta) - 1} = -cosh(\theta) + \sqrt{sinh^2(\theta)} = -cosh(\theta) + sinh(\theta) \\ f_4 = -cosh(\theta) - sinh(\theta) \end{cases} \tag{12.22}$$

The solution to (12.8) is finally written for non-repeated roots of the auxiliary equation:

$$X_k = \sum_{k \in \{1,2,3,4\}} C_p f_p^k \tag{12.23}$$

By using de Moivre's theorem, we find

$$X_k = A\cos(k\phi) + B\sin(k\phi) + C(-1)^k \cosh(k\theta) + D(-1)^k \sinh(k\theta) \tag{12.24}$$

To find the constants in (12.24), we impose the following boundary conditions:

$$\begin{cases} T_0(t) = T_n(t) = 0 \implies X_0 = X_n = 0 \\ T_{-1}(t) = -T_1(t) \implies X_{-1} = -X_1 \\ T_{n-1}(t) = -T_{n+1}(t) \implies X_{n-1} = -X_{n+1} \end{cases} \tag{12.25}$$

By applying the boundary conditions, we find that

$$\begin{cases} X_0 = A + C = 0 \\ X_{-1} = -X_1 \\ \implies A\cos(-\phi) + B\sin(-\phi) - C\cosh(-\theta) - D\sinh(-\theta) = \\ -A\cos(\phi) - B\sin(\phi) + C\cosh(\theta) + D\sinh(\theta) \\ \implies 2A\cos(\phi) - 2C\cosh(\phi) = 0 \\ \implies A = C = 0 \end{cases} \tag{12.26}$$

and

$$\begin{cases} X_n = 0 \implies B\sin(n\phi) + D(-1)^n \sinh(n\theta) = 0 \\ D(-1)^n \sinh(n\theta) = 0 \implies D = 0 \\ B\sin(n\phi) \implies \phi = \frac{m\pi}{n} \text{ (non trivial solution)} \end{cases} \tag{12.27}$$

The solution in space is therefore

$$X_k = B\sin(\frac{m\pi k}{n}) \tag{12.28}$$

From (12.21), it is possible to find the value of $\gamma$:

$$\begin{cases} \cos(\frac{m\pi}{n}) = -\frac{\beta_1}{\beta_2} + \sqrt{(\frac{\beta_1}{\beta_2} + 1)^2 - \frac{\gamma a^2}{\beta_2}} \\ \implies \gamma = (-(\cos(\frac{m\pi}{n}) + \frac{\beta_1}{\beta_2})^2 + (\frac{\beta_1}{\beta_2} + 1)^2)\frac{\beta_2}{a^2} \end{cases} \tag{12.29}$$

It is clear from (12.29) that the conditions $(\frac{\beta_1}{\beta_2} + 1)^2 \frac{\beta_2}{a^2} \geq \gamma$ and $\gamma \geq 0$ are fulfilled, so the initial supposition is true. Knowing the value of $\gamma$, we now solve the temporal equation. We have that

$$\dot{Z} = -\gamma \alpha Z \tag{12.30}$$

By injecting (12.28) into (12.7), we can find another way to write $\gamma$:

$$-\gamma a^2 sin\left(\frac{m\pi i}{n}\right) = \beta_1 \left[ sin\left(\frac{m\pi(i+1)}{n}\right) - 2sin\left(\frac{m\pi i}{n}\right) + sin\left(\frac{m\pi(i-1)}{n}\right) \right]$$

$$+ \frac{\beta_2}{4} \left[ sin\left(\frac{m\pi(i+2)}{n}\right) - 2sin\left(\frac{m\pi i}{n}\right) + sin\left(\frac{m\pi(i-2)}{n}\right) \right] \tag{12.31}$$

$$\implies \gamma = 4\frac{\beta_1}{a^2} sin^2\left(\frac{m\pi}{2n}\right) + \frac{\beta_2}{a^2} sin^2\left(\frac{m\pi}{n}\right) \tag{12.32}$$

The solution to the temporal equation is then

$$Z(t) = e^{-\alpha\gamma t} \tag{12.33}$$

Finally, the complete solution to the problem may be written as

$$T_k(t) = \sum_{m=1}^{\infty} B_m sin\left(\frac{m\pi k}{n}\right) e^{-\alpha\gamma t} \tag{12.34}$$

To find the remaining constant in Eq. (12.34), we propose the following initial condition:

$$T_k(0) = f(x) = \begin{cases} 2T_0 \frac{x}{L} & \text{for } 0 \le x \le L/2 \\ 2T_0(1 - \frac{x}{L}) & \text{for } L/2 \le x \le L \end{cases} \tag{12.35}$$

We then have

$$B_m = \frac{2}{L} \int_0^L f(x) sin\left(\frac{m\pi k}{n}\right) dx = \frac{8T_0}{(m\pi)^2} sin\left(\frac{m\pi}{2}\right) \tag{12.36}$$

By setting $T^* = \frac{T}{T_0}$, $\tau = \frac{\alpha t}{L^2}$ and $\eta = (4\beta_1 sin^2(\frac{m\pi}{2n}) + \beta_2 sin^2(\frac{m\pi}{n}))n^2$, Eq. (12.34) may be written in a dimensionless form:

$$T_k^*(\tau) = \sum_{m=1}^{\infty} \frac{8}{m\pi^2} sin(\frac{m\pi}{2}) sin(\frac{m\pi k}{n}) e^{-\eta\tau} \tag{12.37}$$

## 12.3 Numerical Solution to the Discrete Equation

To verify the analytical solution, the analytical solution is compared to a numerical solution. The numerical solution is obtained by using the Crank-Nicolson method of resolution for the dimensionless equation, which combines the stability of the implicit method and the accuracy of a second-order method [26, 27]:

$$\frac{\partial T_0 T_i^*}{\partial (\frac{a^2 n^2 \tau}{\alpha})} = \frac{\alpha}{a^2} \left[ \beta_1 T_0 (T_{i+1}^* - 2T_i^* + T_{i-1}^*) + \frac{1}{4} \beta_2 T_0 (T_{i+2}^* - 2T_i^* + T_{i-2}^*) \right]$$
(12.38)

$$\implies \frac{\partial T_i^*}{\partial \tau} = n^2 \left[ \beta_1 (T_{i+1}^* - 2T_i^* + T_{i-1}^*) + \frac{1}{4} \beta_2 (T_{i+2}^* - 2T_i^* + T_{i-2}^*) \right] \quad (12.39)$$

By applying the implicit method,

$$\frac{T_i^{*N+1} - T_i^{*N}}{\Delta \tau} = n^2 \bigg( \beta_1 \frac{(T_{i+1}^{*N+1} - 2T_i^{*N+1} + T_{i-1}^{*N+1}) + (T_{i+1}^{*N} - 2T_i^{*N} + T_{i-1}^{*N})}{2}$$

$$+ \beta_2 \frac{(T_{i+2}^{*N+1} - 2T_i^{*N+1} + T_{i-2}^{*N+1}) + (T_{i+2}^{*N} - 2T_i^{*N} + T_{i-2}^{*N})}{8} \bigg)$$
(12.40)

From (12.40), we obtain

$$- b_2 T_{i+2}^{*N+1} - b_1 T_{i+1}^{*N+1} + (2b_1 + 2b_2 + 1) T_i^{*N+1} - b_1 T_{i-1}^{*N+1} - b_2 T_{i-2}^{*N+1} =$$
$$b_2 T_{i+2}^{*N} + b_1 T_{i+1}^{*N} - (2b_1 + 2b_2 - 1) T_i^{*N} + b_1 T_{i-1}^{*N} + b_2 T_{i-2}^{*N}$$
(12.41)

where $b_1 = \beta_1 \frac{n^2 \Delta \tau}{2}$ and $b_2 = \beta_2 \frac{n^2 \Delta \tau}{8}$. By applying the initial (12.35) and the boundary conditions (12.25) into (12.64), it is then possible to find, by performing iterations, the value of the temperature in the next time step.

## 12.4  Analytical Solution to the Nonlocal Equation

The nonlocal model is based on an Eringen-type differential model of Fourier's model (Eq. (12.4)), which leads to the nonlocal heat equation (12.5). By applying the method of separation of variables and the initial (12.35) and boundary (12.25) conditions, we obtain the solution presented in [21] for Eq. (12.5):

$$T(x, t) = \sum_{m=1}^{\infty} \frac{8T_0}{(m\pi)^2} sin \left( \frac{m\pi}{2} \right) sin \left( \frac{m\pi x}{L} \right) e^{\frac{-\alpha m^2 \pi^2 t}{\tilde{l}_c^2 m^2 \pi^2 + L^2}}$$
(12.42)

which can be expressed in a dimensionless form by setting $T^* = \frac{T}{T_0}, \tau = \frac{\alpha t}{L^2}, \tilde{x} = \frac{x}{L}$ and $\tilde{l}_c = \frac{l_c}{L}$:

$$T^*(\tilde{x}, \tau) = \sum_{m=1}^{\infty} \frac{8}{(m\pi)^2} sin \left( \frac{m\pi}{2} \right) sin(m\pi \tilde{x}) e^{\frac{-m^2 \pi^2}{1 + \tilde{l}_c^2 m^2 \pi^2} \tau}$$
(12.43)

The characteristic length $l_c$ accounts for the specific lattice effect of the equivalent quasi-continuum and can be calculated by applying a continualization method to the discrete equation (12.3) and by using Taylor's approximation.

By setting $T_i = T(x = ia)$ and by applying a Taylor's development on $T_{i+1} = T(x + a)$ and $T_{i-1} = T(x - a)$, it is found that

$$
\begin{cases}
T(x + a) = T(x) + a\frac{\partial T}{\partial x} + \frac{a^2}{2}\frac{\partial^2 T}{\partial x^2} + \frac{a^3}{3!}\frac{\partial^3 T}{\partial x^3} + \frac{a^4}{4!}\frac{\partial^4 T}{\partial x^4} + \cdots \\
T(x - a) = T(x) - a\frac{\partial T}{\partial x} + \frac{a^2}{2}\frac{\partial^2 T}{\partial x^2} - \frac{a^3}{3!}\frac{\partial^3 T}{\partial x^3} + \frac{a^4}{4!}\frac{\partial^4 T}{\partial x^4} + \cdots
\end{cases}
\tag{12.44}
$$

And from (12.44):

$$
T_{i+1} - 2T_i + T_{i-1} = \left( a^2\frac{\partial^2}{\partial x^2} + a^4\frac{2}{4!}\frac{\partial^4}{\partial x^4} + a^6\frac{2}{6!}\frac{\partial^6}{\partial x^6} + \cdots \right) T(x)
\tag{12.45}
$$

Taylor's development of a hyperbolic cosine can be recognized in (12.45):

$$
\left( a^2\frac{\partial^2}{\partial x^2} + a^4\frac{2}{4!}\frac{\partial^4}{\partial x^4} + a^6\frac{2}{6!}\frac{\partial^6}{\partial x^6} + \cdots \right) = 2\left( cosh\left( a\frac{\partial}{\partial x} \right) - 1 \right) = e^{a\partial_x} + e^{-a\partial_x} - 2
\tag{12.46}
$$

Equation (12.45) can therefore be rewritten by using (12.46) as

$$
T_{i+1} - 2T_i + T_{i-1} = 2\left( cosh\left( a\frac{\partial}{\partial x} \right) - 1 \right) T(x) = 4sinh^2\left( \frac{a}{2}\frac{\partial}{\partial x} \right) T(x)
\tag{12.47}
$$

Finally, by replacing into Eq. (12.3), the following equation is obtained:

$$
\dot{T} = \frac{4\alpha}{a^2}\left( \beta_1 sinh^2\left( \frac{a}{2}\frac{\partial}{\partial x} \right) + \frac{\beta_2}{4}sinh^2\left( a\frac{\partial}{\partial x} \right) \right) T
\tag{12.48}
$$

The pseudo differential operator from (12.48) can be approximated by using a Padè approximant of order [2, 2]:

$$
\frac{4}{a^2}\left( \beta_1 sinh^2\left( \frac{a}{2}\frac{\partial}{\partial x} \right) + \frac{\beta_2}{4}sinh^2\left( a\frac{\partial}{\partial x} \right) \right) = \frac{\partial_x^2}{1 - \frac{a^2}{12}(\beta_1 + 4\beta_2)\partial_x^2} + \cdots
\tag{12.49}
$$

where $\partial_x = \frac{\partial}{\partial x}$. We set $l_c^2 = \frac{a^2}{12}(\beta_1 + 4\beta_2)$.

By inserting (12.49) into (12.48) and by multiplying by $1 - l_c^2\partial_x^2$, the following equation is determined:

$$
(1 - l_c^2\partial_x^2)\dot{T} = \alpha\partial_x^2 T
\tag{12.50}
$$

which is equivalent to the nonlocal heat equation (12.5). In the following calculations, we will therefore use a value of $l_c^2 = \frac{a^2}{12}(\beta_1 + 4\beta_2)$.

## 12.5 Extension to p-Order Neighbor Equation

### 12.5.1 Analytical Solution

In this section, the procedure of Sects. 12.2–12.4 is followed for a p-order neighbor interaction. The heat equation corresponding to this problem is written as

$$\dot{T}_k = \alpha \sum_{j=1}^{p} \beta_j \frac{T_{k+j} - 2T_k + T_{k-j}}{(ja)^2} \tag{12.51}$$

As for the 2-neighbor interaction problem, $\beta_j$ are weighting coefficients for the interactions with the $j$th neighbor. We take in this case $\sum_{j=1}^{p} \beta_j = 1$ and $\beta_1 > \beta_2 > ... > \beta_p > 0$. Also, the following boundary conditions are taken:

$$\begin{cases} T_{-(k-1)} = -T_{(k-1)} \\ T_{-(n-k)} = -T_{(n+k)} \end{cases} \quad \text{for } k \in \{1; 2; ...; p\} \tag{12.52}$$

By applying the method of separation of variables, the following equation can be obtained:

$$\frac{\dot{Z}}{Z} = \alpha \sum_{j=1}^{p} \beta_j \frac{X_{k+j} - 2X_k + X_{k-j}}{(ja)^2 X_k} = -\gamma_2 \alpha \tag{12.53}$$

It is assumed that the spatial solution is

$$X_k = B_2 sin \left( \frac{m\pi}{n} k \right) \tag{12.54}$$

Therefore,

$$\sum_{j=1}^{p} \frac{\beta_j}{j^2} B_2 \left[ sin \left( \frac{m\pi}{n} (k+j) \right) - 2sin \left( \frac{m\pi}{n} k \right) + sin \left( \frac{m\pi}{n} (k-j) \right) \right] = -\gamma_2 a^2 X_k \tag{12.55}$$

By using some trigonometric identities, the coefficient $\gamma_2$ is found from (12.55):

$$\gamma_2 a^2 = \sum_{j=1}^{p} \frac{\beta_j}{j^2} 4sin^2 \left( \frac{m\pi j}{2n} \right) \tag{12.56}$$

The temporal solution is then

$$Z(t) = e^{-\alpha \sum_{j=1}^{p} \frac{\beta_j}{j^2} \frac{4}{a^2} sin^2(\frac{m\pi j}{2n})t} \tag{12.57}$$

Finally, the complete solution is written as

$$T_k(t) = \sum_{m=1}^{\infty} B_m e^{-\alpha \sum_{j=1}^{p} \frac{\beta_j}{j^2} \frac{4}{a^2} sin^2\left(\frac{m\pi j}{2n}\right)t} sin\left(\frac{m\pi}{n}k\right) \qquad (12.58)$$

From the initial conditions (Eq. (12.35)), we can find the constant $B_m$, which is the same as found in Eq. (12.36). Then, the equation can be written in its dimensionless form, with the same parameters as used in Sect. 12.2 ($T_k^* = \frac{T}{T_0}$, $\tau = \frac{\alpha t}{L^2}$) and $\eta_p = 4n^2 \sum_{j=1}^{p} \frac{\beta_j}{j^2} sin^2(\frac{m\pi j}{2n})$:

$$T_k^*(\tau) = \sum_{m=1}^{\infty} \frac{8}{(m\pi)^2} sin\left(\frac{m\pi}{2}\right) e^{-\eta_p \tau} sin\left(\frac{m\pi}{n}k\right) \qquad (12.59)$$

We note that for $p = 2$, we have that

$$\eta_{p=2} = n^2\left(4\beta_1 sin\left(\frac{m\pi}{2n}\right) + \beta_2 sin^2\left(\frac{m\pi}{n}\right)\right) \qquad (12.60)$$

which is the same value as found in Sect. 12.2 in the solution of the second-order neighbor interaction equation, validating the solution for a $p$-order neighbor interaction.

### 12.5.2 Numerical Solution

To verify the analytical solution, it is compared to a numerical solution by using an implicit method of resolution for the dimensionless equation:

$$\frac{\partial T_0 T_i^*}{\partial\left(\frac{a^2 n^2 \tau}{\alpha}\right)} = \frac{\alpha}{a^2} \sum_{j=1}^{p} \frac{\beta_j}{j^2} T_0(T_{i+j}^* - 2T_i^* + T_{i-j}^*) \qquad (12.61)$$

$$\implies \frac{\partial T_i^*}{\partial\tau} = n^2 \sum_{j=1}^{p} \frac{\beta_j}{j^2}(T_{i+j}^* - 2T_i^* + T_{i-j}^*) \qquad (12.62)$$

By applying the implicit method,

$$\frac{T_i^{*N+1} - T_i^{*N}}{\Delta\tau} = n^2 \sum_{j=1}^{p} \frac{\beta_j}{j^2} \frac{(T_{i+j}^{*N+1} - 2T_i^{*N+1} + T_{i-j}^{*N+1}) + (T_{i+j}^{*N} - 2T_i^{*N} + T_{i-j}^{*N})}{2}$$

$$(12.63)$$

From (12.63), we obtain

$$T_i^{*^{N+1}} + \sum_{j=1}^{p}(-b_j T_{i+j}^{*^{N+1}} + 2b_j T_i^{*^{N+1}} - b_j T_{i-j}^{*^{N+1}}) = T_i^{*^N} \sum_{j=1}^{p} b_j(T_{i+j}^{*^N} - 2b_j T_i^{*^N} + b_j T_{i-j}^{*^N})$$

$$(12.64)$$

where $b_j = \frac{n^2 \beta_j \Delta \tau}{2 j^2}$.

### 12.5.3 Nonlocal Length Scale Calibration

To calibrate the nonlocal length scale parameter in this problem, Eq. (12.47) is inserted into Eq. (12.51):

$$\dot{T} = \frac{4\alpha}{a^2} \sum_{j=1}^{p} \frac{\beta_j}{j^2} sinh^2 \left( \frac{ja}{2} \frac{\partial}{\partial x} \right) T \qquad (12.65)$$

As suggested in [16, 17], for a similar mechanical problem, the pseudo differential operator from Eq. (12.65) can be approximated with a Padè approximant of order [2, 2]:

$$\frac{4}{a^2} \sum_{j=1}^{p} \frac{\beta_j}{j^2} sinh^2 \left( \frac{ja}{2} \frac{\partial}{\partial x} \right) = \frac{\partial_x^2}{1 - \frac{a^2}{12} \sum_{j=1}^{p} j^2 \beta_j \partial_x^2} + \cdots \qquad (12.66)$$

leading to the following nonlocal length scale parameter:

$$l_c^2 = \frac{a^2}{12} \sum_{j=1}^{p} j^2 \beta_j \qquad (12.67)$$

## 12.6 Results

In Fig. 12.2, we represent the evolution of the dimensionless temperature for $n = 4$ elements and $\beta_1 = 0.6$ and $\beta_1 = 0.4$ obtained with Eq. (12.37). The evolution of the classical solution to Fourier's equation and the evolution of the nonlocal solution are also represented for comparison. The classical heat equation is found when the nonlocal parameter is equal to zero. The solution to this equation can therefore be found from the nonlocal solution (12.68) by setting $l_c = 0$:

$$T_{Fourier}^*(\tilde{x}, \tau) = \sum_{m=1}^{\infty} \frac{8}{(m\pi)^2} sin \left( \frac{m\pi}{2} \right) sin(m\pi\tilde{x}) e^{-m^2\pi^2\tau} \qquad (12.68)$$
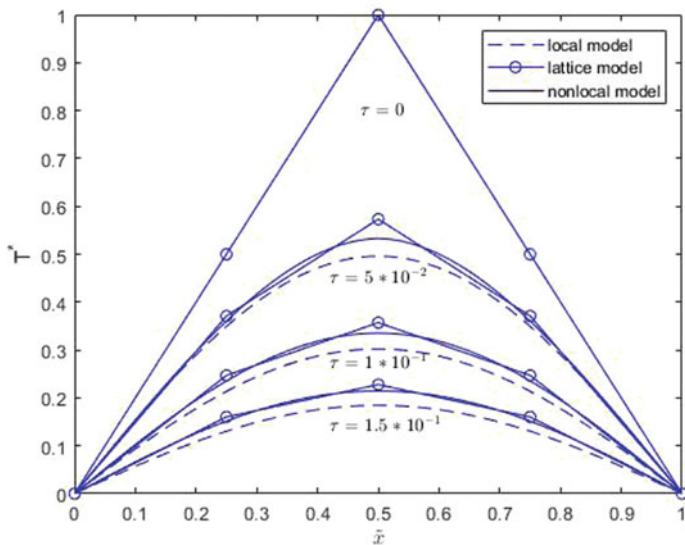
**Fig. 12.2** Temperature evolution of the thermal lattice and the continuous heat models for $n = 4$, $\beta_1 = 0.6$ and $\beta_2 = 0.4$

It is observed in Fig. 12.2 that the continuous solutions, but especially the nonlocal model, are a good approximation of the discrete analytical solution.

Figure 12.3 shows the comparison of the analytical discrete curve shown in Fig. 12.2 with the numerical curve obtained from Eq. (12.64). For all the values of $\tau$ plotted in this figure, the two curves show the same behavior, and the values obtained with the numerical solution are very close to the analytical values, validating the analytical solution presented in Sect. 12.2.

As previously mentioned, Fig. 12.2 shows that the nonlocal and the local approximations are good. Nevertheless, it is clear that in the middle of the bar, the error is important for both the local and the nonlocal approximations. Therefore, computations of the error in the nodes are performed to study its evolution in time. For this, the relative error for both approximations is calculated as follows:

$$Err(k, \tau) = \frac{T_k^*(\tau) - T^*(\tau, \tilde{x} = k/n)}{T_k^*(\tau)} \tag{12.69}$$

In Fig. 12.4, the relative errors for $\tilde{x} = 1/4$ and $\tilde{x} = 1/2$ are presented. It can be noted that for $\tilde{x} = 1/4$, for very short times the local error is smaller than the nonlocal one. To better observe the curve in the short times, we plot in Fig. 12.5 the same curves as in Fig. 12.4 for $\tau \in [0; 0.1]$ and with a logarithmic abscissa.

It is clear from Fig. 12.5 that for $\tilde{x} = 1/2$, the nonlocal model represents better the discrete model in the middle of the bar. Nevertheless, the relative errors in the time interval $[0; 0.1]$ are greater for the nonlocal model than for the local model for
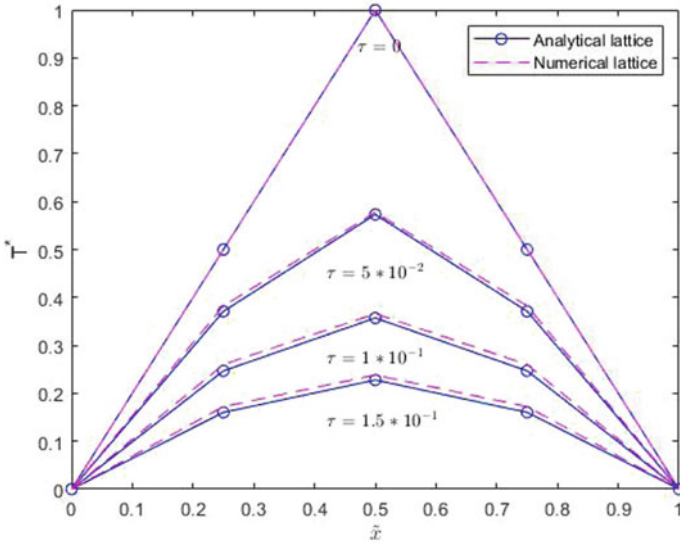
**Fig. 12.3** Temperature evolution of the thermal lattice for $n = 4$, $\beta_1 = 0.6$ and $\beta_2 = 0.4$—Comparison of the numerical and the analytical solution
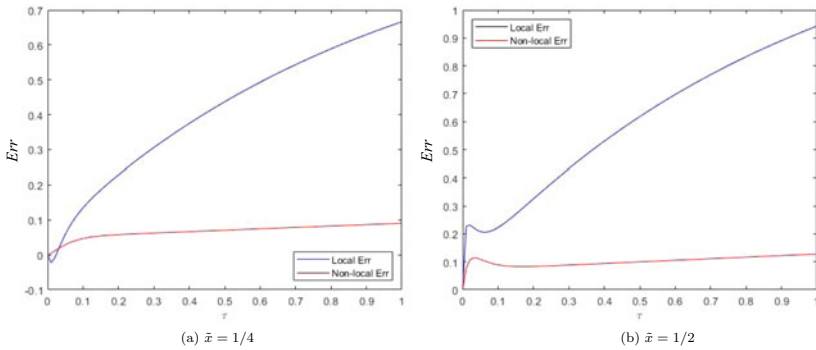


**Fig. 12.4** Relative error of the nonlocal model and the local model with respect to the lattice model for $n = 4$, $\beta_1 = 0.6$ and $\beta_2 = 0.4$

$\tilde{x} = 1/4$. However, it can be considered that the difference between these two errors in this time interval is sufficiently small to be neglected, unlike the difference for higher times, where the local error seems to infinitely increase whereas the nonlocal error quickly stabilizes with a small value. From this figure, we can therefore conclude that the nonlocal approximation is globally better than the local approximation.

The same work is now performed for $n = 8$ elements.

In Figs. 12.6, 12.7 and 12.8, we observe the same behavior as for $n = 4$ but with smaller errors for both the local and nonlocal models. Figures 12.7 and 12.8 show
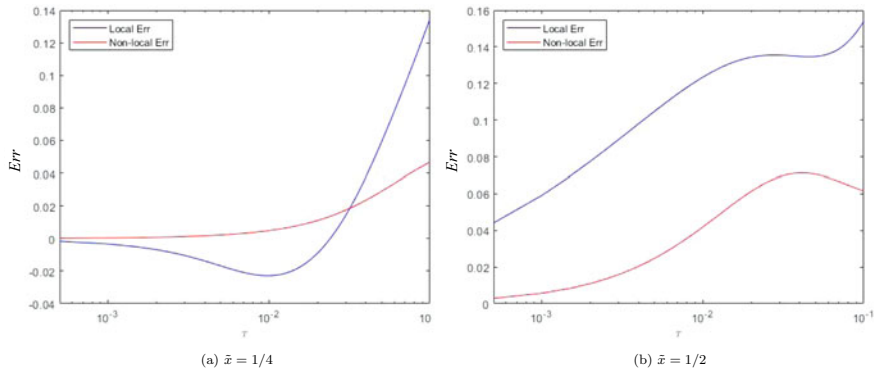
Fig. 12.5  Relative error of the nonlocal model and the local model for $\tau \in [0; 1]$ with respect to the lattice model for $n = 4$, $\beta_1 = 0.6$ and $\beta_2 = 0.4$
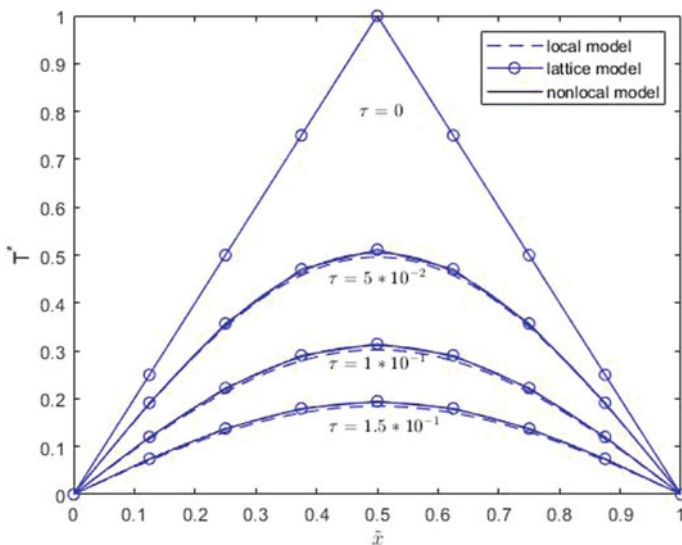


Fig. 12.6  Temperature evolution for $n = 8$, $\beta_1 = 0.6$ and $\beta_2 = 0.4$

that, even though the local Fourier model approximates better the lattice model than in the previous figure, the nonlocal model is still globally superior.

The behavior of the solutions for different values of $\beta_1$ is now studied. In Fig. 12.9, the evolution of the temperature for the lattice, nonlocal and local models is represented for various values of $\beta_1$. It is shown in this figure that the temperatures of the lattice and the nonlocal models decrease when $\beta_1$ increases. Note that the local model is independent of $\beta_1$ and $\beta_2$ and therefore this curve only varies with time. Furthermore, when $\beta_1$ decreases, the nonlocal and lattice models get closer to the local model. This means that, when the second-order neighbor interaction is

(a) $\tilde{x} = 1/4$

(b) $\tilde{x} = 1/2$
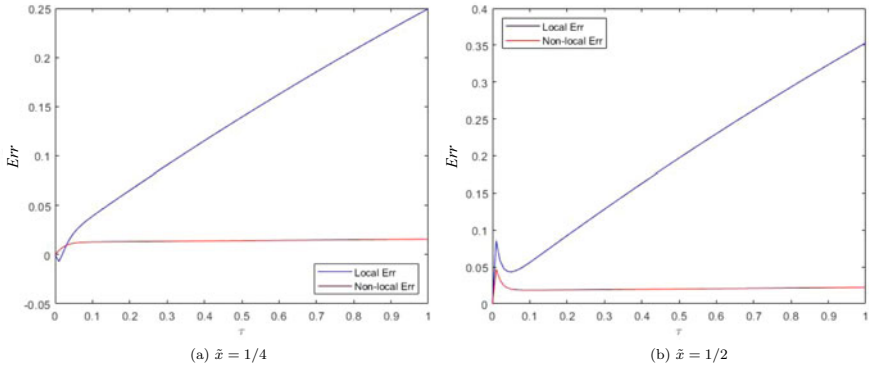
**Fig. 12.7** Relative error of the nonlocal model and the local model with respect to the lattice model for $n = 8$, $\beta_1 = 0.6$ and $\beta_2 = 0.4$



(a) $\tilde{x} = 1/4$

(b) $\tilde{x} = 1/2$
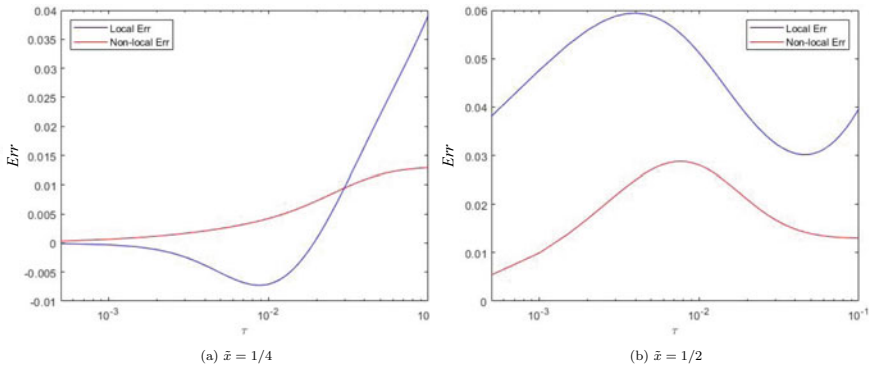
**Fig. 12.8** Relative error of the nonlocal model and the local model for $\tau \in [0; 1]$ with respect to the lattice model for $n = 8$, $\beta_1 = 0.6$ and $\beta_2 = 0.4$

important, the local model fails to represent the heat transfer in the lattice. Finally, it can be observed in this figure that when $\beta_1$ increases, the nonlocal error increases. Nevertheless, the nonlocal model is, for all cases, a better approximation of the lattice model.

In Fig. 12.10, the evolution of the temperature for $n = 8$ and for a third- and fourth-order neighbor interactions is presented. It can be observed that for both values of $p$, the curves present the same behavior and that the values obtained are very close for both figures. Figure 12.10 can also be compared to Fig. 12.6. Even though the coefficients $\beta_j$ are not calculated in the same manner, the same observations can be made. The temperatures for the discrete models obtained in Fig. 12.10 are compared to the Crank-Nicolson numerical solution.

As for p = 2, Fig. 12.11 shows that the numerical curves present the same behavior as the analytical curves and that the values are very close. The analytical solution for the generalization of p-neighbor interactions is therefore valid.
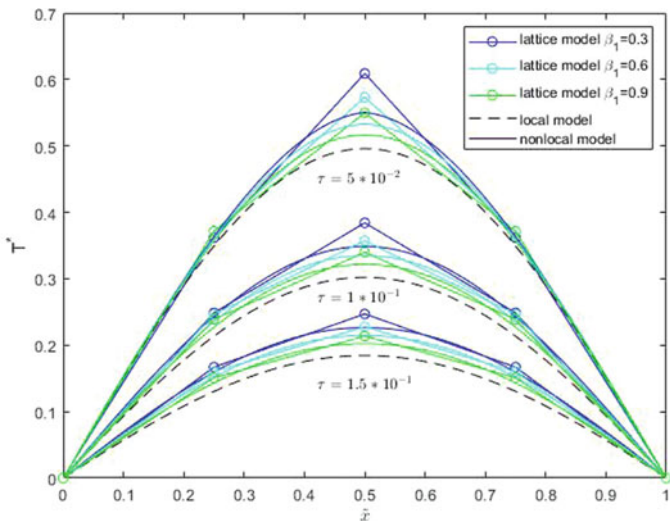
**Fig. 12.9** Temperature evolution for $n = 4$ and various values of $\beta_1$ and $\beta_2$



(a) $p = 3$, $\beta_0 = 0.546$

(b) $p = 4$, $\beta_0 = 0.480$
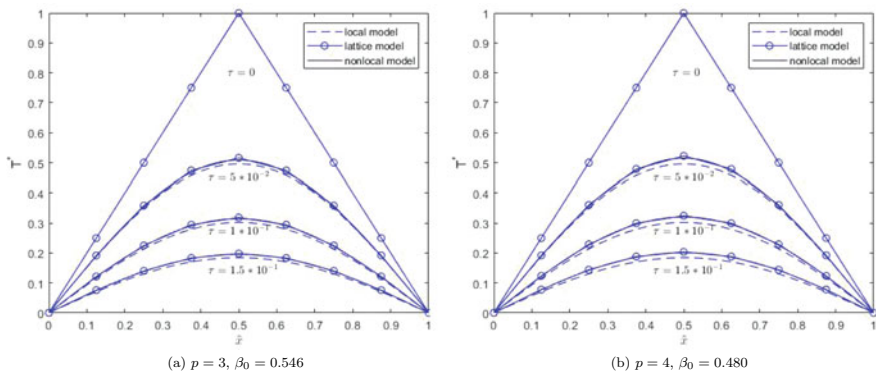
**Fig. 12.10** Temperature evolution for $n = 8$, $\beta_j = \frac{\beta_0}{j}$ and $\beta_0 = \frac{1}{\sum_{j=1}^{p} 1/j}$

The relative errors are also calculated in the same way as that for $p = 2$.

From Figs. 12.12 and 12.13, as for Fig. 12.10, the figures for different values of $p$ show the same behavior of the curves for all cases. The comparison also shows that when the value of $p$ increases, the relative error for the local model also increases, whereas the nonlocal error decreases. This observation can be more clearly made in Figs. 12.14 and 12.15.

In Figs. 12.10, 12.11, 12.12, 12.13, 12.14 and 12.15, an inverse kernel was used. It is also possible to calculate a temperature evolution using other types of kernels, such as exponentially based kernel, as is done in [17] for the vibration of axial lattices. In Fig. 12.16, we consider the following weighting used in [17]:
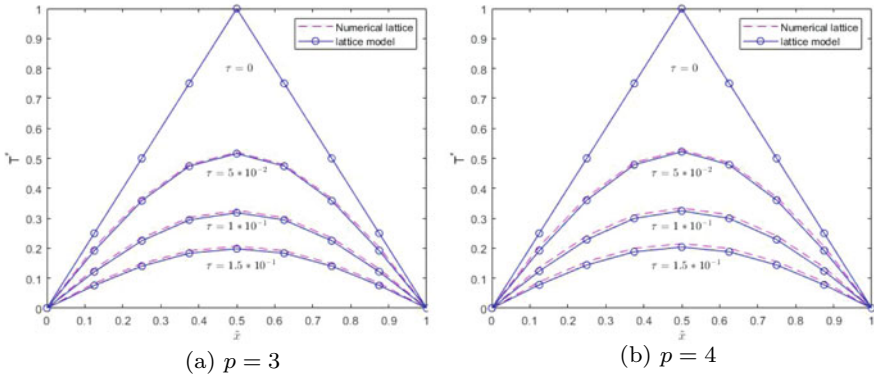
**Fig. 12.11** Discrete solution versus numerical solution $n = 8$, $\beta_j = \frac{\beta_0}{j}$ and $\beta_0 = \frac{1}{\sum_{j=1}^{p} 1/j}$
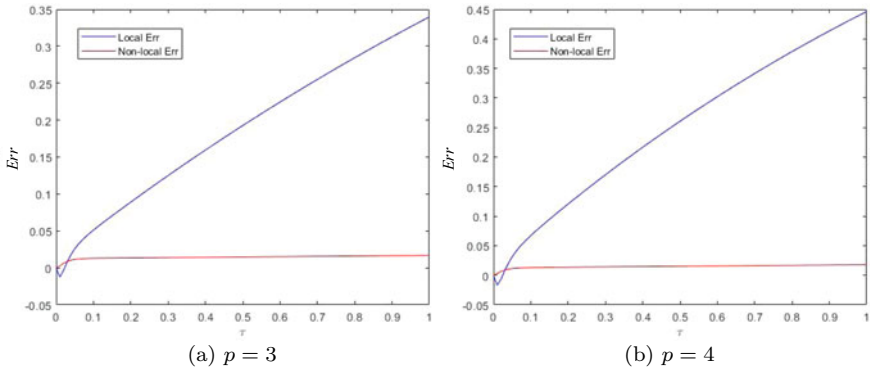


**Fig. 12.12** Relative error of the nonlocal model and the local model with respect to the lattice model for $n = 8$ and $x = 1/4$; $\beta_j = \frac{\beta_0}{j}$ and $\beta_0 = \frac{1}{\sum_{j=1}^{p} 1/j}$

$$\tilde{\beta}_j = \tilde{\beta}_0 e^{-\tilde{\alpha} j} \tag{12.70}$$

with $\tilde{\beta}_0 = \frac{1}{\sum_{j=1}^{p} e^{-\tilde{\alpha} j}}$ and $\tilde{\alpha} = 0.52$.

Figure 12.16 shows the same behavior for the temperature evolution as in Fig. 12.10. The values and the difference between the different models are also very similar, showing that this type of kernel can also be used in the nonlocal and the discrete models with good results.
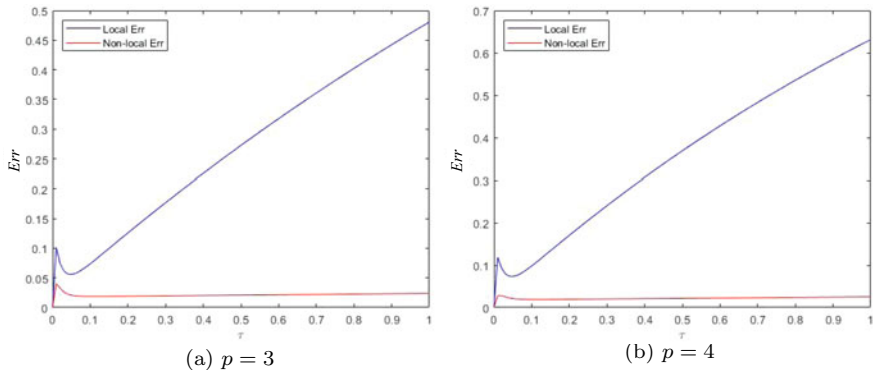
**Fig. 12.13** Relative error of the nonlocal model and the local model with respect to the lattice model for $n = 8$ and $x = 1/2$; $\beta_j = \frac{\beta_0}{j}$ and $\beta_0 = \frac{1}{\sum_{j=1}^{P} 1/j}$
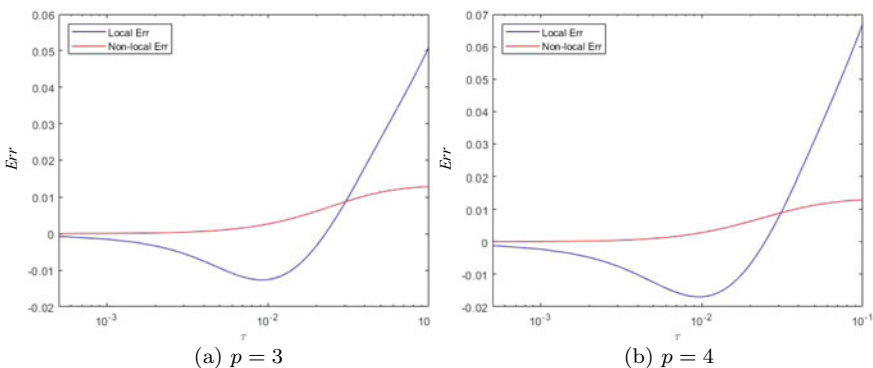


**Fig. 12.14** Relative error of the nonlocal model and the local model for $\tau \in [0; 1]$ with respect to the lattice model for $n = 8$ and $x = 1/4$; $\beta_j = \frac{\beta_0}{j}$ and $\beta_0 = \frac{1}{\sum_{j=1}^{P} 1/j}$

## 12.7 Conclusion

In this paper, we investigated the transitory behavior of a thermal lattice, which accounts for short- and long-range interactions. The discrete system is ruled by a mixed differential-difference equation, whose difference order in space is controlled by the number of neighboring interactions. Thanks to the method of separation of variables, it is possible to get an exact solution to the thermal evolution problem, from the resolution of some higher-order difference equations. The solution is presented for various discrete kernels associated with the long-range dependence of the discrete interactions. This thermal discrete solution is then compared to an approximate continuous solution, which contains length scale effects. The length scale of the continuous nonlocal heat equation is calibrated for any number of interactions. For

(a) $p = 3$        (b) $p = 4$
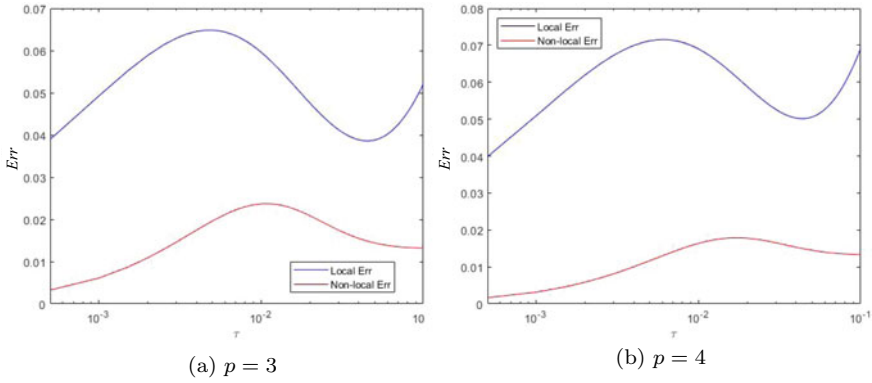
**Fig. 12.15** Relative error of the nonlocal model and the local model for $\tau \in [0; 1]$ with respect to the lattice model for $n = 8$ and $x = 1/2$; $\beta_j = \frac{\beta_0}{j}$ and $\beta_0 = \frac{1}{\sum_{j=1}^{p} 1/j}$



(a) $p = 3$, $\tilde{\beta}_0 = 0.513$        (b) $p = 4$, $\tilde{\beta}_0 = 0.463$
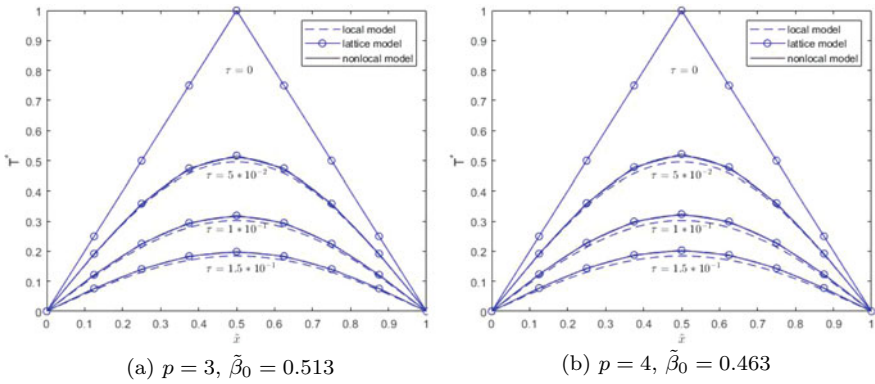
**Fig. 12.16** Temperature evolution for $n = 8$, $\tilde{\alpha} = 0.52$, $\tilde{\beta}_j = \tilde{\beta}_0 e^{-\tilde{\alpha} j}$ and $\tilde{\beta}_0 = \frac{1}{\sum_{j=1}^{p} e^{-\tilde{\alpha} j}}$

a similar diffusive lattice with only direct interactions, [20] also derived a nonlocal diffusion equation with mixed spatial and temporal derivatives. References [21, 22] obtained an exact solution of the (discrete) thermal lattice with only direct interactions. The efficiency of the continuous nonlocal heat equation was shown to capture the scale effects of the lattice problem. In this paper, these results have been extended for a general lattice whatever the number of interactions. The present results, valid for one-dimensional lattices, could be extended to multi-dimensional systems.

# References

1. Fourier J (1822) Théorie analytique de la chaleur, Chez Firmin Didot, Père et fils, Libraires pour les mathèmatiques, l'architecture hydraulique et la marine. Rue Jacob, Paris
2. Majumdar A (1993) Microscale Heat Conduction in dielectric Thin Films. J Heat Transfer 115:7
3. Sobolev S, Kudinov I (2021) Heat conduction across 1D nano film: Local thermal conductivity and extrapolation length. Int J Therm Sci 159:106632
4. Xu M (2018) A non-local constitutive model for nano-scale heat conduction. Int J Therm Sci 134:594–600
5. Jaberolanssar H, Peddieson J Jr (1981) On continuum representation of mechanical behavior of discrete lattices. Mech Res Commun 8(4):251–257
6. Kunin IA (1983) Elastic media with microstructure I: one-dimensional models. Springer, Berlin
7. Kunin IA, Elastic media with microstructure II: three-dimensional models
8. Eringen AC (1983) On differential equations of nonlocal elasticity and solutions of screw dislocation and surface waves. J Appl Phys 54(9):4703–4710
9. Rosenau P (1986) Dynamics of nonlinear mass-spring chains near the continuum limit. Phys Lett A 118(5):222–227
10. Challamel N, Wang CM, Zhang H, Elishakoff I (2021) Lattice-based nonlocal elastic structural models. Theory and applications, size-dependent continuum mechanics approaches, pp 1–50
11. Lagrange JL (1759) Recherches sur la nature et la propagation du son, Miscellanea Philosophico-Mathematica Societatis Privatae Taurinensis I, 2rd Pagination, i-112 (see also OEuvres de Lagrange, Tome 1:39–148, Gauthier-Villars, Paris, 1867)
12. Dell'Isola F, Maier G, Perego U, Andreaus U, Esposito R, Forest S (2014) The complete works of Gabrio Piola. Adv Struct Mater 38:1–813
13. Dell' Isola F, Andreaus U, Placidi L (2015) At the origins and in the vanguard of peridynamics, non-local and higher-gradient continuum mechanics: an underestimated and still topical contribution of Gabrio Piola. Math Mech Solids 20(8):887–928
14. Brillouin L (1946) Periodic structure: electronic filters and crystal lattices
15. Eaton H, Peddieson J Jr (1973) On continuum description of one-dimensional lattice mechanics. J Tennessee Acad Sci 48:96–100
16. Rosenau P (1987) Dynamics of dense lattices. Phys Rev B 36(11):5868
17. Challamel N, Wang CM, Zhang H, Kitipornchai S (2018) Exact and nonlocal solutions for vibration of axial lattice with direct and indirect neighboring interactions. J Eng Mech 144(5):04018025
18. Challamel N, Zhang H, Wang C, Kaplunov J (2019) Scale effect and higher-order boundary conditions for generalized lattices, with direct and indirect interactions. Mech Res Commun 97:1–7
19. Challamel N, Picandet V (2021) Localization in the static response of higher-order lattices with long-range interactions. Modern trends in structural and solid mechanics 1: statics and stability, pp 67–89
20. Rosenau P (1993) Random walker and the telegrapher's equation: a paradigm of a generalized hydrodynamics. Phys Rev E 48(2):R655–R667
21. Challamel N, Grazide C, Picandet V, Perrot A, Zhang Y (2015) A nonlocal Fourier's law and its application to the heat conduction of one-dimensional and two-dimensional thermal lattices. Comptes Rendus Mècanique 344(6):388–401. ISSN 16310721
22. Picandet V, Challamel N (2021) Nonlocal thermal diffusion in one-dimensional periodic lattice. Int J Heat Mass Transf 180:121753
23. Nuñez del Prado E, Challamel N, Picandet V (2022) Discrete and nonlocal solutions for the lattice Cattaneo-Vernotte heat diffusion equation. Math Mech Complex Syst 9(4):367–396
24. Goldberg S (1958) Introduction to difference equations: with illustrative examples from economics, psychology and sociology. Wiley, New York. ISBN 978-0-471-31051-8, oCLC: 833783962

25. Elaydi S (2005) An introduction to difference equations. Springer, New York. ISBN 978-0-471-31051-8
26. Crank J, Nicolson P (1947) A practical method for numerical evaluation of solutions of partial differential equations of the heat-conduction type. In: Proceedings of the Cambridge philosophical society. Mathematical Physical science, vol 43. Cambridge University Press, pp 50–67
27. Crank J (1975) The mathematics of diffusion. Oxford University Press, Oxford

# Chapter 13
# Large Deformations and Stability of the Two-Bar Truss Under Vertical Loads

**Matteo Pelliciari, Federico Oyedeji Falope, Luca Lanzoni, and Angelo Marcello Tarantino**

**Abstract** Analytical formulations for the static equilibrium of truss structures are often based on concepts of linear elasticity. Geometric nonlinearities are taken into account, but the nonlinear constitutive behavior of the material is not considered. However, the assumption of linear elastic material is not consistent with the response of solids subjected to large deformations. In light of this, accurate models must take into account both geometric and constitutive nonlinearities. In the present work, we investigate the problem of the von Mises (or two-bar) truss subjected to a vertical load. The bars of the truss are composed of rubber so as to observe large displacements and deformations. We propose a theoretical model that is entirely developed in three-dimensional nonlinear elasticity. A compressible Mooney-Rivlin law is employed for the constitutive behavior of the rubber. Experimental tests on the von Mises truss subjected to a vertical load are carried out. Snap-through is observed and good agreement is found with the analytical predictions. Finally, a simple formulation to predict the critical Euler buckling load is presented and validated through experimental observation.

## 13.1 Introduction

The static equilibrium of the planar von Mises (or two-bar) truss subjected to a vertical load is a benchmark problem in the analysis of the stability of truss structures [1, 9, 12, 16]. Applications of this structure can be found in different fields of engineering, such

M. Pelliciari (✉) · F. O. Falope · L. Lanzoni · A. M. Tarantino
DIEF, Department of Engineering "Enzo Ferrari", via Pietro Vivarelli 10, 41125 Modena, Italy
e-mail: matteo.pelliciari@unimore.it

F. O. Falope
e-mail: federicooyedeji.falope@unimore.it

L. Lanzoni
e-mail: luca.lanzoni@unimore.it

A. M. Tarantino
e-mail: angelomarcello.tarantino@unimore.it

as lattice truss structures [8, 15], metamaterials [11, 19] and multi-stable mechanical systems [10, 17].

Analytical solutions for the equilibrium of the two-bar truss are important for the validation of numerical and finite element (FE) models. A solution with the assumption of linear elastic (LE) material was proposed in [6]. This assumption was then abandoned in the works [5, 13], proposing a formulation entirely developed in finite elasticity.

In this contribution, the two-bar truss subjected to a vertical load is analyzed from analytical, numerical and experimental points of view. The bars of the truss are composed of rubber so that large deformations are observed. The experimental tests are carried out through a device specifically designed to avoid Euler buckling. This condition reproduces a behavior as close as possible to that of truss structures. Finally, an analytical approach to account for Euler buckling of the bars in nonlinear elasticity is presented. Additional experimental tests are carried out and Euler buckling is experimentally observed, providing a validation of the analytical method proposed.

The analytical solution is based on the formulation proposed in [5] and it is presented in Sect. 13.2, assuming a compressible Mooney-Rivlin (MR) constitutive law. The case of LE constitutive law is also outlined and corresponds to the theory proposed in [6]. The uniaxial tests for rubber characterization and the experiments on the von Mises truss are described in Sect. 13.3. Section 13.4 contains a description of the FE models, and Sect. 13.5 presents the calibration of the constitutive model based on the experimental data. Analytical, numerical and experimental results are presented and discussed in Sect. 13.6. The effect of Euler buckling on the behavior of the truss is investigated with additional experiments. Conclusions are given in Sect. 13.7.

## 13.2 Analytical Formulation

The two-bar truss of Fig. 13.1 consists of two equal straight bars connected through a hinge at node $C$. The bars are composed of an inner deformable material, while the terminal parts are rigid elements. The length of the terminal parts is $L_r$, and it represents the space occupied by the hinge in the experimental device. The length of the inner deformable part is $L_m$.

The apex node $C$ is loaded by the external dead force $F$, acting in the $Z$ direction of the global reference system $C_1 XYZ$. Under the effect of the external load, node $C$ undergoes vertical displacement $\hat{w}$. The horizontal degree of freedom of point $C$ is not considered because in [13], it is demonstrated that stable solutions can be found only along the vertical degree of freedom.
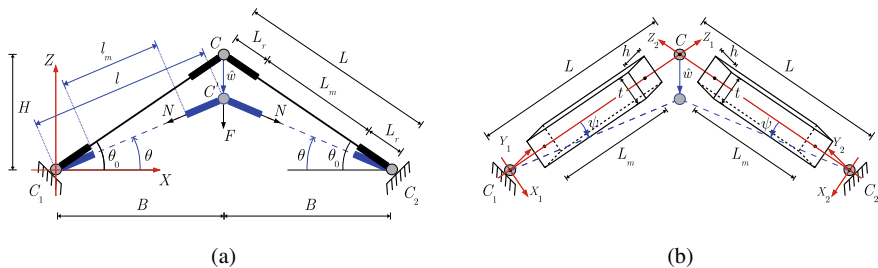
**Fig. 13.1** The von Mises (or two-bar) truss: **a** Deformed configuration under vertical load; **b** Bars of the truss seen as three-dimensional bodies

The entire length of both bars in the reference configuration is $L = \sqrt{B^2 + H^2}$, while in deformed configuration $l = \sqrt{B^2 + (H - \hat{w})^2}$. The length of the deformable part of the bars in the reference configuration is

$$L_m = \sqrt{(B - 2L_r\cos\theta_0)^2 + (H - 2L_r\sin\theta_0)^2}, \tag{13.1}$$

whereas in the deformed configuration

$$l_m = \sqrt{(B - 2L_r\cos\theta)^2 + \left(H - \hat{w} - 2L_r\sin\theta\right)^2}, \tag{13.2}$$

where

$$\cos\theta_0 = \frac{B}{L}, \quad \cos\theta = \frac{B}{l}, \quad \sin\theta_0 = \frac{H}{L}, \quad \sin\theta = \frac{H - \hat{w}}{l}, \tag{13.3}$$

with $\theta_0$ and $\theta$ being the inclination angle of the truss in reference and deformed configurations, respectively.

The bars are three-dimensional bodies with a rectangular cross section of width $t$ and height $h$, as shown in Fig. 13.1b. It is assumed that the material is homogeneous, isotropic and hyperelastic. The deformation of the bodies is assumed to be homogeneous throughout, even close to the rigid links.

The material coordinate systems $C_iX_iY_iZ_i$ ($i = 1, 2$) are defined, as depicted in Fig. 13.1b. These reference systems are principal. We indicate the principal stretches of the bars with $\lambda_j$ ($j = X, Y, Z$). We introduce the stored energy function $W(\iota_1, \iota_2, \iota_3)$, which depends only on the principal invariants of the Cauchy-Green deformation tensor

$$\iota_1 = \lambda_X^2 + \lambda_Y^2 + \lambda_Z^2, \quad \iota_2 = \lambda_X^2\lambda_Y^2 + \lambda_X^2\lambda_Z^2 + \lambda_Y^2\lambda_Z^2, \quad \iota_3 = \lambda_X^2\lambda_Y^2\lambda_Z^2.$$

Due to symmetry, the two bars undergo the same deformation field. The expression of the longitudinal stretch of the bars is
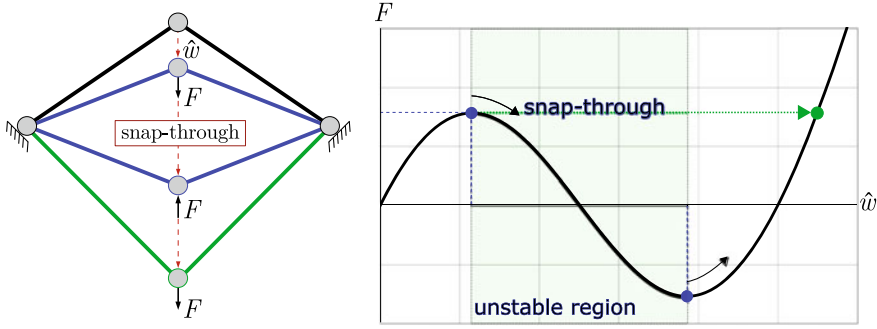
**Fig. 13.2** Equilibrium path and snap-through instability

$$\lambda_Z = \frac{l_m}{L_m} = \frac{\sqrt{(B - 2L_r\cos\theta)^2 + (H - \hat{w} - 2L_r\sin\theta)^2}}{\sqrt{(B - 2L_r\cos\theta_0)^2 + (H - 2L_r\sin\theta_0)^2}}. \tag{13.4}$$

The equilibrium in the deformed configuration is expressed by

$$F + 2N\sin\theta = 0, \tag{13.5}$$

where $N$ is the axial stress resultant of the bars (Fig. 13.2).

The body forces are disregarded, and the surface tractions generated by the concentrated load $F$ are uniformly and orthogonally distributed on the basis of the bodies. Under the aforementioned assumptions, the solution to the boundary value problem leads to the following relations [13]:

$$\lambda_X = \lambda_Y = \lambda = \sqrt{-\frac{W_{,1} + \lambda_Z^2 W_{,2}}{W_{,2} + \lambda_Z^2 W_{,3}}}, \tag{13.6}$$

$$N = -2th\lambda_Z \left(W_{,2}^2 - W_{,1}W_{,3}\right) \frac{W_{,1} + 2\lambda_Z^2 W_{,2} + \lambda_Z^4 W_{,3}}{\left(W_{,2} + \lambda_Z^2 W_{,3}\right)^2}, \tag{13.7}$$

where $W_{,j} = \partial W / \partial \iota_j$ ($j = 1, 2, 3$). By introducing Eqs. (13.3), (13.6) and (13.7) into Eq. (13.5), the global equilibrium equation of the von Mises truss becomes

$$F - 4th\lambda_Z \frac{H - \hat{w}}{\sqrt{B^2 + \left(H - \hat{w}\right)^2}} \left(W_{,2}^2 - W_{,1}W_{,3}\right) \frac{W_{,1} + 2\lambda_Z^2 W_{,2} + \lambda_Z^4 W_{,3}}{\left(W_{,2} + \lambda_Z^2 W_{,3}\right)^2} = 0. \tag{13.8}$$

Equation (13.8) provides a relation between external load $F$ and vertical displacement $\hat{w}$, namely the equilibrium path.

### 13.2.1    Material Models

#### 13.2.1.1    Mooney-Rivlin (MR) Material

We assume that the constitutive behavior of the rubber is described by the compressible MR law, which is defined by the stored energy function [2]

$$W(\iota_1,\ \iota_2,\ \iota_3) = a\,(\iota_1 - 3) + b\,(\iota_2 - 3) + c\,(\iota_3 - 1) - (a + 2b + c)\log(\iota_3),$$
(13.9)

where $a$, $b$ and $c$ are positive constants. The derivatives of the stored energy function (13.9) with respect to the invariants are computed and, by substitution into Eq. (13.8), the equilibrium equation in case of compressible MR material becomes

$$\bar{F} - 4\lambda_Z \frac{H - \hat{w}}{\sqrt{B^2 + \left(H - \hat{w}\right)^2}} Q = 0,$$
(13.10)

where

$$Q = \left(\bar{b}^2 - \bar{c} + P\right) \frac{1 + 2\bar{b}\lambda_Z^2 + \lambda_Z^4\,(\bar{c} - P)}{\left[\bar{b} + \lambda_Z^2\,(\bar{c} - P)\right]^2},$$

$$P = \frac{4(1 + 2\bar{b} + \bar{c})\left(\bar{b} + \bar{c}\lambda_Z^2\right)^2}{\lambda_Z^2\left[1 + \bar{b}\lambda_Z^2 - \sqrt{4(1 + 2\bar{b} + \bar{c})\left(\bar{b} + \bar{c}\lambda_Z^2\right) + \left(1 + \bar{b}\lambda_Z^2\right)^2}\right]^2},$$

and $\bar{F} = F/(tha)$, $\bar{b} = b/a$, $\bar{c} = c/a$.

#### 13.2.1.2    Linear Elastic (LE) Material

The equilibrium problem of truss structures is often analyzed by considering only geometric nonlinearities [6, 7]. This approach is outlined in the present section with the purpose of providing a comparison with the fully nonlinear formulation described previously, where a MR material is adopted.

In the model proposed in [6, 7], the material is assumed to behave according to a linearly elastic constitutive law characterized by the following stored energy function:

$$W\,(\epsilon_Z) = \frac{1}{2}E\epsilon_Z^2,$$

where $E$ denotes Young's modulus and $\epsilon_Z = \left(l_m^2 - L_m^2\right)/\left(2L_m^2\right)$ is the axial component of strain given by the Green-Lagrange strain measure. The axial stress resultant acting on the rod is computed as

$$N_{LE} = th \frac{\partial W}{\partial \epsilon_Z} = th E \frac{l_m^2 - L_m^2}{2L_m^2}. \tag{13.11}$$

The equilibrium equation of the von Mises truss in the case of linear elastic material is derived by substituting Eq. (13.11) into Eq. (13.5), obtaining

$$F + 2th E \frac{l_m^2 - L_m^2}{2L_m^2} \sin \theta = 0.$$

Recalling Eqs. (13.1) and (13.2), the kinematic relations (13.3) and the definition of the longitudinal stretch (13.4), the equilibrium takes the form

$$F - th E \left( \lambda_Z^2 - 1 \right) \frac{H - \hat{w}}{\sqrt{B^2 + \left( H - \hat{w} \right)^2}} = 0. \tag{13.12}$$

## 13.3 Experimental Investigation

### 13.3.1 Uniaxial Tests for Rubber Characterization

The material used is synthetic neoprene rubber. The rubber characterization is performed by carrying out separately uniaxial compression and tension tests. The testing machine is the Instron 5567, equipped with a 30 kN load cell for the compression test and a 1 kN load cell for the tension test.

Three squat cylindrical specimens of 28.85 mm diameter and 10.56 mm thickness are tested under compression. Three dog-bone specimens of 83.43 mm² cross-section area and 65.25 mm effective length are tested under tension. The displacement rate is 0.5 and 50 mm/min for compression and tensile tests, respectively.

Nominal stress and stretch are computed for each test. The nominal stress versus stretch curves in compression and tension are merged and the three resulting experimental curves are named $S_1$, $S_2$ and $S_3$.

### 13.3.2 Experimental Test on the von Mises Truss

The experimental device of Fig. 13.3 is designed specifically to simulate the von Mises truss subjected to a vertical load.

The device is composed of three steel guides fixed on a supporting table. Control point $C$ is forced to slide along the vertical guide, allowing only the vertical degree of freedom $\hat{w}$. Nodes $C_1$ and $C_2$ are placed on the horizontal guides, and their distance can be adjusted according to the geometry of the problem (Fig. 13.3).

**Fig. 13.3** Experimental device for the von Mises truss under vertical load
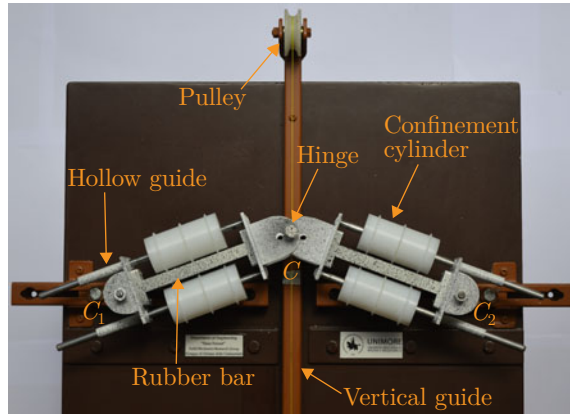
The hinges of the truss are realized with steel blocks that rotate around the corresponding nodes. The hinge in node $C$ is connected to the hinges in $C_1$ and $C_2$ using two steel rods that avoid relative rotations. The steel rods slide through hollow cylindrical guides. This allows the axial deformation of the rubber specimen, which is glued to the hinge blocks with an adhesion primer for steel-rubber connection.

Two hollow cylinders made of nylon are inserted into the steel rods. The function of the cylinders is to confine the rubber specimen so as to limit its bending deformation and prevent Euler buckling. The first tests are carried out with this set. Afterwards, additional experiments are carried out without confinement cylinders. This allows observing Euler buckling and investigate its effect on the equilibrium path.

The concentrated load $F$ is applied through two synthetic fishing lines. One end of both the lines is tied to the central hinge $C$, while the other ends are connected to containers where the load is manually placed. Two pulleys are placed on the two opposite sides of the vertical guide, between hinge $C$ and the load containers. Each line slides through the corresponding pulley. In this way, the vertical load can be applied in both upward and downward directions.

Three pairs of specimens are tested with the following geometry: $\theta_0 = 20°$, $L = 146.5$ mm, $L_m = 90$ mm, $L_r = 28.25$ mm, $t = 10$ mm and $h = 20.5$ mm. The test consists in the application of a load that is gradually increased by adding weight to the container. For each load increment, the vertical displacement of node $C$ is monitored by means of digital image correlation (DIC).

The instrumentation used to acquire the displacement field is Dantec Dynamics Q400. The monitoring is performed in stereo mode by placing two cameras above the truss (Fig. 13.4). The DIC cameras acquire a single frame for each load increment.

**Fig. 13.4** Setup of DIC instrumentation during the experimental test



## 13.4 Finite Element Simulation

The FE models are realized by using the FE code COMSOL Multiphysics® v.5.5 [3]. Two different FE models are created, which differ only in an internal solid constraint. A detailed description of each model is given in the following.

The first model, named model 1, does not include the Euler buckling of the rubber specimen. This model simulates the condition of the experimental test performed in this work, where the confinement cylinders prevent buckling phenomena. The second model, named model 2, simulates the response of the system without confinement cylinders. In this circumstance, Euler buckling takes place. Model 1 differs from model 2 only for an added constraint in order to avoid Euler buckling.

In both FE models, the MR material is defined by setting the MR stored energy function (13.9) in the user defined material. Hexagonal elements with quadratic serendipity shape functions are used for the mesh. Due to symmetry, only half of the truss is modeled (Fig. 13.5).

The hinge blocks are accounted for by using the feature rigid connector of the FE code. A lower rigid connector is applied to the lower final cross section of the rubber specimen and associated with the fixed center of rotation $C_1$. Likewise, an upper rigid connector is attributed to the final cross section of the rubber specimen and associated with the moving center of rotation $C$.

A nonlinear incremental analysis is performed by applying a vertical displacement $\hat{w}$ at the upper center of rotation $C$. The incremental displacement step is $-0.1$ mm, ranging in the interval $\hat{w} \in [0, -3H]$. In addition, both rigid connectors are constrained to rotate the rigid rotation $\psi(\hat{w})$ around the corresponding center of
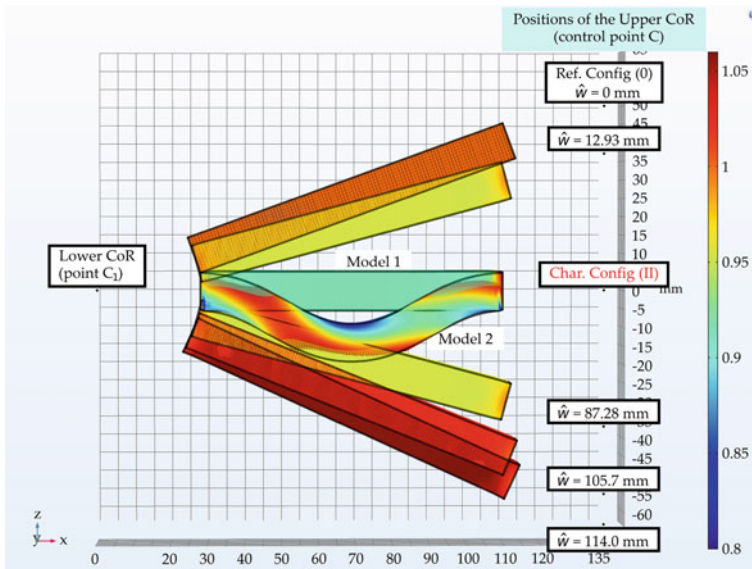
**Fig. 13.5** FE model 1, where Euler buckling is avoided, and FE model 2, where Euler buckling takes place

rotation. This constraint ensures that the final cross sections of the specimen remain coaxial during the deformation.

As previously pointed out, model 1 contains an additional constraint to the ones described above. Specifically, also the middle cross section of the specimen is constrained to rotate by $\psi(\hat{w})$ around the lower center of rotation $C_1$. This kinematic constraint of model 1 ensures the absence of Euler buckling in the solution. In fact, the deformed configurations of Fig. 13.5 show that only model 2 is affected by buckling.

## 13.5  Calibration of the Rubber Constitutive Model

Stress and stretch data obtained from the uniaxial tests are used to perform a nonlinear fitting of the MR constitutive parameters $a$, $b$ and $c$.

The parameters are collected into the parameter vector $\mathbf{p} = [a, \ b, \ c]^\mathrm{T}$. The fitting function $s(\lambda_Z, \mathbf{p})$ is the nominal stress versus stretch relation for a compressible MR material, which is obtained by writing Eq. (13.7) in case of MR material ($s = N/th$). The objective function obj($\mathbf{p}$) is defined as the averaged sum of normalized square error between simulated and experimental data, namely

$$\text{obj}(\mathbf{p}) = \sqrt{\frac{\sum_i^n \left[ s(\lambda_{Zi}, \, \mathbf{p}) - s_i \right]^2}{\sum_i^n s(\lambda_{zi}, \, \mathbf{p})^2}}, \tag{13.13}$$

where $n$ is the number of data points, $s_i$ and $\lambda_{Zi}$ are experimental nominal stress and stretch respectively, while $s(\lambda_{Zi}, \, \text{p})$ is the fitting function sampled at the data points.

The minimization of the objective function (13.13) is performed via a genetic algorithm [18]. Specifically, the fitting procedure is implemented in a MATLAB® code by using the *ga* function of the *global optimization toolbox*, which is based on fitness function *fmincon* [14]. A constrained optimization was later carried out. The following lower and upper bounds of parameters were set: $a \in [10^2, 10^4]$, $b \in [10^2, 10^4]$ and $c \in [10^3, 2 \times 10^5]$. The values are expressed in kPa.

It is worth mentioning that, concerning the nonlinear fitting of the MR model, multiple minimization candidates are possible. Such solutions may give entirely different extrapolation results. It is thus recommended to analyze carefully the result of the optimization and check its physical plausibility.

## 13.6 Results and Discussion

The stress versus stretch curves $S_1$, $S_2$ and $S_3$ resulting from the experimental uniaxial tests are shown in Fig. 13.6.

The constrained optimization is carried out for each of these three sets of data. The mean best fitting parameters obtained are $a = 457$ kPa, $b = 381$ kPa and $c = 31758$ kPa. As shown in Fig. 13.6, good agreement is found between experimental data and analytical fitting constitutive law with MR material.

The parameters given above are used to compute the analytical equilibrium path of the von Mises truss by using Eqs. (13.10) and (13.12), for the cases of MR and

**Fig. 13.6** Uniaxial nominal stress versus stretch curves from experimental tests on rubber specimens $S_1$, $S_2$ and $S_3$ and analytical law (MR and LE materials)
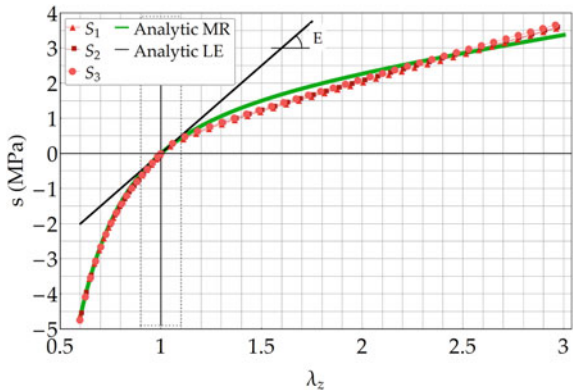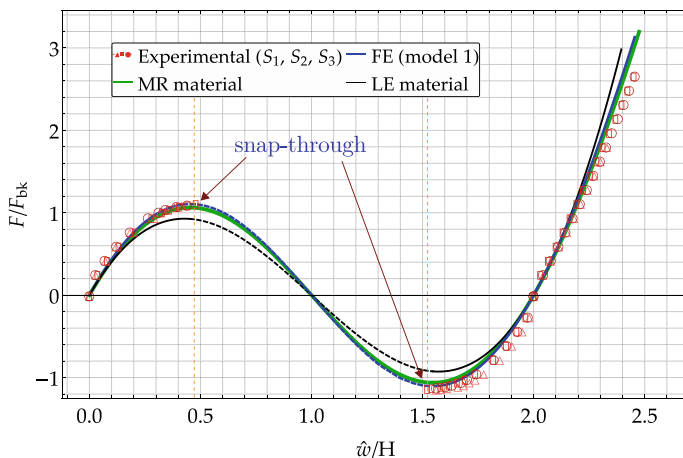
**Fig. 13.7** Experimental, analytical (MR and LE materials) and FE equilibrium paths of the von Mises truss

LE materials, respectively. The equilibrium paths derived from experimental tests, analytical model and FE simulation are shown in Fig. 13.7.

Displacement $\hat{w}$ is normalized with respect to the height $H$ of the truss, and load $F$ is normalized with respect to the Euler buckling load of the system in undeformed configuration, expressed as

$$F_{bk} = \frac{8\pi^2 E I_x}{L_m^2} \sin(\theta_0), \tag{13.14}$$

where $I_x$ is the cross section's moment of inertia with respect to axis $x$ and $E$ is Young's modulus of the rubber, which is computed from the MR constitutive parameters as [4]

$$E = \frac{4(a + b)(a + 4b + 3c)}{a + 3b + 2c}.$$

Note that the rubber specimens are considered clamped to the hinge blocks. Accordingly, Eq. (13.14) is derived introducing the buckling load of a double-clamped beam $N_{bk} = 4\pi^2 E I_x / L_m^2$ into Eq. (13.5).

Overall, there is a good agreement between experimental results, analytical path with MR material and FE path. The three main reasons for the discrepancy between these results are discussed in the following. Considerations on the equilibrium path with the assumption of LE material will be given at the end of this section.

Firstly, the equilibrium equation (13.10) is based on the hypothesis of homogeneous deformation. However, in both FE model and experimental test this is not true. In both cases, the final cross sections of the specimen are clamped to the rigid hinge blocks. This influences the deformation of the areas near the hinges. Secondly, as

shown in Fig. 13.6, the experimental constitutive behavior is accurate but of course, it does not depict perfectly the experimental behavior. This especially for large extensions of the bars, for which the discrepancy among experimental, analytical and FE results increases. Lastly, geometric imperfections and friction in the guides of the experimental device play a role in the accuracy of the data. Although friction is reduced by using lubricant, its contribution is not negligible, especially for low values of load.

The solution derived with the assumption of LE material, expressed by Eq. (13.12), is also represented in Fig. 13.7. As expected, for low values of $\hat{w}$ this solution provides a good approximation of the behavior of the truss. However, as the magnitude of displacement increases, the discrepancy rises. The sensible difference between experimental results and the equilibrium path with LE material shows that, in general, this assumption is not appropriate. An accurate analysis of the equilibrium and stability of truss structures requires a fully nonlinear model. In a general case, it is not true that the deformations are small enough to adopt a linear constitutive law.

### 13.6.1  Effect of Euler Buckling

Additional experiments are carried out after removing the confinement cylinders. In this way, Euler buckling of the bars is observed. The outcome in terms of equilibrium path is shown in Fig. 13.8. Before reaching the snap-through load, buckling takes place and the equilibrium becomes unstable.
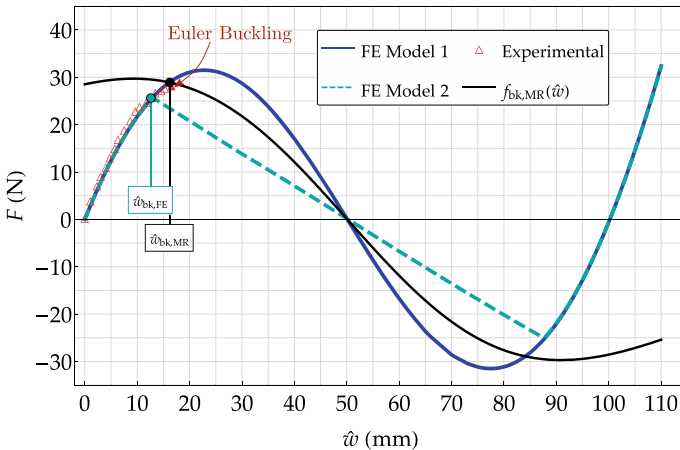


**Fig. 13.8**  Effect of Euler instability: experimental test without confinement cylinders in comparison with analytical and FE predictions

The simulation provided by FE model 2 is shown in Fig. 13.8. The load paths of model 1 and model 2 perfectly agree until the critical buckling load is reached at $\hat{w}_{bk,FE}$. At this point, model 2 experiences buckling and deviates from model 1.

From an analytical point of view, buckling occurs at the intersection between the equilibrium path and Euler buckling load. To derive the expression of the Euler buckling load in deformed configuration, we firstly introduce the tangent elastic modulus, defined as a derivative of the nominal axial stress $s = N/th$ (Eq. (13.7)) with respect to stretch $\lambda_Z$

$$
\begin{aligned}
E(\lambda_Z) = \frac{\partial s}{\partial \lambda_Z} = 2\big[4\lambda_Z\lambda\lambda'\left(\lambda^2 W_{,3} + \lambda W_{,2}\right) + \\
\lambda^4\left(\lambda_Z W'_{,3} + W_{,3}\right) + 2\lambda^2\left(\lambda_Z W'_{,2} + W_{,2}\right) + \lambda_Z W'_{,1} + W_{,1}\big],
\end{aligned}
\tag{13.15}
$$

where $\lambda$ is the transversal stretch given by Eq. (13.6) and symbol $'$ indicates the derivative with respect to stretch $\lambda_Z$. The expression of $E(\lambda_Z)$ for a MR material is obtained by specializing Eq. (13.15) to the stored energy function of Eq. (13.9). Moment of inertia $I_x$ in deformed configuration is

$$
I_x(\lambda_Z) = \frac{1}{12}\left(\lambda h\right)\left(\lambda t\right)^3,
\tag{13.16}
$$

where again $\lambda$ is the transversal stretch given as a function of $\lambda_Z$ by Eq. (13.6). Finally, the Euler buckling load for a MR material computed in deformed configuration is expressed as

$$
f_{bk,MR}(\hat{w}) = \frac{8\pi^2 E(\lambda_Z)I_x(\lambda_Z)}{l_m^2}\sin\theta,
\tag{13.17}
$$

in which $E(\lambda_Z)$ and $I_x(\lambda_Z)$ are given by Eqs. (13.15) and (13.16), respectively. The critical load curve of Eq. (13.17) is depicted in Fig. 13.8 with black color.

From Fig. 13.8, it is clearly visible that the prediction of Euler instability given by the formulation proposed in the present work (Eq. (13.17)) is very accurate. The result provided by FE model 2 also deserves some consideration. The reason why FE model 2 is not very accurate is that the best fitting parameters of the MR constitutive law are obtained by fitting the model to uniaxial compressive and tensile tests only. Hence, it is not guaranteed that such parameters provide accurate solutions also in case of bending of the specimens. In light of this, it is obvious that the simulation of FE model 2, which involves bending of the bars, cannot be considered reliable. However, it still gives an idea of the Euler buckling load and adds confidence in both experimental and analytical predictions.

## 13.7  Conclusions

The von Mises truss subjected to a vertical load was analyzed from theoretical, numerical and experimental points of view. The equilibrium was written in the deformed configuration and specialized to the case of compressible MR constitutive law. A LE constitutive behavior was also considered with the purpose of providing a comparison between the results. An experimental device that reproduces the von Mises truss subjected to a vertical load was presented, and the tests were monitored with DIC technology. Two FE models were developed in order to give comparisons and discuss the effect of Euler buckling on the equilibrium paths.

The theoretical formulation was validated by comparing the results with the FE simulations and the experiments. Hence, the analytical model presented in this work gives an accurate description of the equilibrium and post-critical behavior of truss structures. Furthermore, the comparison with the results obtained under the assumption of LE constitutive law showed that the material nonlinearity cannot be neglected. This approximation is, in general, not accurate for the analysis of truss structures with large displacements.

The kinematics of the analytical model for the von Mises truss does not consider bending deformation due to Euler buckling. However, a simple formulation to predict Euler instability was derived by using the kinematic and constitutive relations furnished by the analytical model, which allowed considering both geometrical and material nonlinearities. Additional experiments were carried out removing the confinement cylinders, and Euler buckling was experimentally observed. The comparison of the results showed that the analytical approach presented in this work gives an accurate prediction of this phenomenon.

## References

1. Bellini PX (1972) The concept of snap-buckling illustrated by a simple model. Int J Non-Linear Mech 7(6):643–650
2. Ciarlet PG, Geymonat G (1982) Sur les lois de comportement en élasticité non linéaire compressible. C R Acad Sci Ser II(295):423–426
3. Comsol A (2005) COMSOL multiphysics user's guide. Version: September 10, 333
4. Falope F, Lanzoni L, Tarantino AM (2019) The bending of fully nonlinear beams. Theoretical, numerical and experimental analyses. Int J Eng Sci 145:103167
5. Falope FO, Pelliciari M, Lanzoni L, Tarantino AM (2021) Snap-through and Eulerian buckling of the bi-stable von Mises truss in nonlinear elasticity: a theoretical, numerical and experimental investigation. Int J Non-Linear Mech 134:103739
6. Kwasniewski L (2009) Complete equilibrium paths for Mises trusses. Int J Non-Linear Mech 44(1):19–26
7. Ligaro SS, Valvo PS (2006) Large displacement analysis of elastic pyramidal trusses. Int J Solids Struct 43(16):4867–4887
8. López A, Puente I, Serna MA (2007) Numerical model and experimental tests on single-layer latticed domes with semi-rigid joints. Comput Struct 85(7–8):360–374
9. Mises R (1923) Über die stabilitätsprobleme der elastizitätstheorie. ZAMM-J Appl Math Mech/Zeitschrift für Angewandte Mathematik und Mechanik 3(6):406–422

10. Moser P, Barbarino S, Gandhi F (2014) Helicopter rotor-blade chord extension morphing using a centrifugally actuated von Mises truss. J Aircr 51(5):1422–1431
11. Paulose J, Meeussen AS, Vitelli V (2015) Selective buckling via states of self-stress in topological metamaterials. Proc Natl Acad Sci 112(25):7639–7644
12. Pecknold DA, Ghaboussi J, Healey TJ (1985) Snap-through and bifurcation in a simple structure. J Eng Mech 111(7):909–922
13. Pelliciari M, Tarantino AM (2020) Equilibrium paths for von Mises trusses in finite elasticity. J Elast 138(2):145–168
14. Pelliciari M, Tarantino AM (2021) Equilibrium and stability of anisotropic hyperelastic graphene membranes. J Elast 144:169–195
15. Pelliciari M, Tarantino AM (2021) A nonlinear molecular mechanics model for graphene subjected to large in-plane deformations. Int J Eng Sci 167:103527
16. Savi MA, Pacheco PMCL, Braga AMB (2002) Chaos in a shape memory two-bar truss. Int J Non-Linear Mech 37(8):1387–1395
17. Silva WTM, Ribeiro KQ (2021) Spatial asymmetric/symmetric buckling of Mises truss with out-of-plane lateral linear spring. Int J Non-Linear Mech 137:103810
18. Whitley D (1994) A genetic algorithm tutorial. Stat Comput 4(2):65–85
19. Zhang Y, Tichem M, van Keulen F (2021) Rotational snap-through behavior of multi-stable beam-type metastructures. Int J Mech Sci 193:106172

# Chapter 14
# Coupling Finite Element Method with Incremental Harmonic Balance Method for Analysis of Nonlinear Vibrations of Stepped Beams and Frames

**Rudolf R. Pušenjak and Anatolij Nikonov**

**Abstract** The developed numerical methodology allows analysis of nonlinear vibrations of stepped beams and frames with contrast elastic properties. The principle of virtual work is applied to derive nonlinear ordinary matrix differential equations of longitudinal and transverse vibrations in terms of nodal displacement vectors. The steady-state periodic solution is computed by using the IHB method with time scale in the form of truncated Fourier series. The IHB method consists of the Newton-Raphson iterative procedure in which the linearized matrix partial differential equations are derived and the Galerkin procedure, where the corresponding variational equations are integrated and resulting linear algebraic equations are solved for unknown vectors of increments of Fourier coefficients. By exchanging the Newton-Raphson iterative procedure with the augmentation process in which some system parameter is changed, the various branches of solutions can be traced for fundamental, superharmonic and subharmonic resonances of beams.

## 14.1 Introduction

The analysis of nonlinear vibrations of beams has been the subject of extensive research by many authors in last decades. Nayfeh [13] classified the developed methods for solving vibration problems of various structures, such as beams, strings, plates, membranes, etc., into three groups, e.g. using analytical, numerical and numerical-analitic methods. Analytical methods are limited to simple structures with simple boundaries, and numerical methods are intended to investigate dynamic phenomena, but present a difficulty for computing complicated beam and plate vibrations and are also time consuming. Numerical-analitic methods are computationally powerful and efficient, however they distinguish through three types of approaches. The

R. R. Pušenjak
Faculty of Industrial Engineering Novo Mesto, Novo Mesto, Slovenia
e-mail: rudolf.pusenjak@fini-unm.si

A. Nikonov (✉)
University of Ljubljana, Faculty of Mechanical Engineering, Ljubljana, Slovenia
e-mail: anatolij.nikonov@fs.uni-lj.si

first approach uses the finite element model consisting of nonlinear matrix differential equation including global mass, damping and a nonlinear stiffness matrices, respectively, which is solved for the global displacement vector using the method of equivalent linearization. Characteristic for other two approaches is separation of the spatial and temporal variation of the structural response, where in the first approach the temporal functional form is assumed or must be known a priori. In the second of these approaches, the displacement is expressed by the sum of vibration modes, where each mode is represented in the form of the product of the temporal variation by the linear undamped natural modes of the system. The finite element method is used to determine the spatial variation of these natural modes. In this monographic article we propose the coupling of finite element method (FEM) with the incremental harmonic balance (IHB) method [15] for computing nonlinear steady-state periodic vibration of beams that belongs to the numerical-analytic methods.

For beams with weak nonlinearities, the perturbation methods such as Lindstedt-Poincare method, averaging method and the method of multiple scales are widely applied. By introducing multiple time scales, the Extended L-P method is presented by Pušenjak [16] for computation of nonstationary resonances of clamped-hinged beam. Chen and Cheung [3] modified the Lindstedt- Poincare method (ML-P) by transforming the originally large expansion parameter into a small positive parameter to compute the fundamental, superharmonic and subharmonic resonances of highly nonlinear clamped-clamped and clamped-hinged beam. Pušenjak et al. [17] introduced multiple time scales in ML-P method to enable computation of almost periodic vibrations and applied the presented method in the case of combination resonance of clamped-hinged beam. All these works treat transverse vibration of the beam.

Recently, numerous advanced applications of composite materials with high-contrast properties in engineering require vibration analysis of multi-component structures. Also in this area, we can find that generalized perturbation procedures represent a very powerful tool in the search for asymptotic solutions. The perturbation schemes are applied in the analysis of lowest vibration modes of multi-component rods and cylinders, composed of alternating stiff and soft parts, see Kaplunov et al. in [7, 9]. As the result, polynomial frequency equations along with algebraic equations for the associated eigenforms are derived. A similar asymptotic approach arising from the concept of almost rigid body motion is developed by Şahin et al. in [18] for evaluating lowest vibration modes of strongly inhomogeneous elastic beam, consisting of alternating stiff and soft components. Kaplunov et al. [8] extended the perturbation procedure to derive two-mode asymptotic polynomial expansions of the Rayleigh-Lamb dispersion relation of elastic waves in a strongly inhomogeneous three-layered plate, evaluating cut-off frequency and approximating the fundamental bending wave and the first harmonic at the shear thickness resonance. An alternative study of dispersion of Lamb waves in a thin three-layered composite plate with contrast properties by using FEM modal analysis is presented by Zupančič et al. [20]. Asymptotic analysis of anti-plane shear problem for three-layered laminate and an asymmetric sandwich plate, leading to shortened dispersion relations are presented in [10, 14]. Prikazchikova et al. [14] developed an asymptotic analysis of anti-plane shear problem for a three-layered laminate with two different geometric

contrast setups of outer stiff layers to the soft interlayer, whereas Kaplunov et al. [10] treat the long-wave low-frequency anti-plane shear of an asymmetric sandwich plate and present the derivation of the shortened polynomial approximations of the original dispersion relation. The asymptotic analysis reveals a low-frequency harmonic supporting a slow quasi-static decay along with the fundamental mode, where asymptotically justified boundary conditions are prescribed using the Saint-Venant's principle.

Asymptotic analysis, based on the perturbation procedure, is also a starting point in modeling media with a periodic structure at microscopic level. The macroscopic solution of the pertinent problem is sought by means of the homogenization process, whose convergence is subject of many researches, e.g. of $\Gamma$-convergence. Cherdantsev and Cherednichenko [4] developed two-scale $\Gamma$-convergence for homogenization of inherently nonlinear high-contrast periodic composites, where the limiting macroscopic solution in general depends on the both slow (associated to the period of the structure) and fast (associated to the contrast of the media) variables.

Free and forced vibrations of multi-component beams are studied by Elishakoff et al. using the alternative normal mode method [5], where comparisons of results are provided by the Galerkin's method. In addition, random vibrations for beams with proportional damping are analyzed first time in the literature. The original and modified version of the Galerkin method are applied by Amato et al. [1] to investigation of flutter of beams with highly contrasting materials. They are shown that the modified Galerkin method in contrast with the original Galerkin method tends to the exact solution in the case of the inhomogeneous setup of beam components.

Leung and Fung [11] developed a finite element method for computing nonlinear steady-state vibrations of frames, where they treated the axial and flexural deformations of the beam induced by axial force along the beam element. Time-dependent nodal displacements in the system of nonlinear ordinary differential equations, which are derived by using the principle of virtual work from the governing partial differential equations of the beam, were expressed by unknown Fourier coefficients. For determination of Fourier coefficients the harmonic balance method was used, resulting in the system of nonlinear algebraic equations.

In this research, we propose an alternative approach to investigate the nonlinear periodic longitudinal and transversal vibrations of beams by considering the induced axial force as the cause of coupling the axial and flexural deformations. Since the spatial variation of longitudinal and transversal displacement vibrations is determined by means of finite element discretization and temporal variation of nodal values of displacements of discretized beam structure is computed by applying the incremental harmonic balance method, we have termed the new approach as "coupling finite element method with incremental harmonic balance method". The whole beam structure (including stepped beams and frames) is first discretized by beam finite elements, where the spatial variation of displacements in the longitudinal and transversal direction is described by shape (interpolation) functions in the form of Hermite polinomials [2, 6, 19]. The principle of the virtual work [2] is used over the length of each individual beam finite element to derive the governing nonlinear partial differential equations of vibration in the longitudinal and transversal direc-

tion, respectively. By substituting beam shape functions and their spatial derivatives and integrating over the beam length, we obtain the nonlinear ordinary matrix differential equations of the beam element, which after assembling the equations of beam elements result in the global nonlinear ordinary matrix differential equation in terms of the global displacement vector and corresponding time derivatives. The obtained nonlinear ordinary matrix differential equations of each individual beam element are further manipulated by applying the IHB method for temporal variations of nodal displacement vectors, where the method, developed in Pušenjak and Oblak [15] is applied. By introducing the single time scale, the nonlinear ordinary matrix differential equations of the beam element are converted into nonlinear matrix partial differential equations, where the selected subharmonic factor enables the treatment of fundamental, superharmonic or subharmonic resonances. Since the steady-state periodic vibrations of the beam are sought in this research, the truncated Fourier series in the compact matrix form are used to describe the periodic temporal variation of nodal vectors. The first step for implementation of the IHB method is the Newton-Raphson iterative procedure in which the linearized matrix partial differential equations in terms of increments of nodal displacement vectors, load force vectors and system parameters, respectively, are obtained in the longitudinal and transversal direction. The second step for implementation of the IHB method is the Galerkin procedure in which the variational equations of corresponding linearized matrix partial differential equations are formed and integrated over one period of the beam vibration. By performing the integration, the system of linear algebraic equations in terms of vectors of Fourier coefficients and corresponding increment vectors of Fourier coefficients is derived. Since the obtained system of algebraic equations is linear, this property proves to be the most obvious advantage of the presented method. The system of obtained linear algebraic equations is solved for unknown vectors of Fourier increments, which are added to the current values of Fourier vectors in the Newton-Raphson iterative procedure. In each step of the iterative procedure, the residual vectors, which occur on the account of the unbalanced harmonic components of the beam vibration, are computed. The Newton-Raphson iterative procedure is stopped, when the chosen norms of appropriate vector sums, containing residual vectors meet the prescribed tolerance criterion. The IHB method can be easily applied to trace various branches of solutions of nonlinear beam vibrations. The developed numerical methodology, based on coupling FEM with IHB method allows analysis of nonlinear vibrations of stepped beams and frames with contrast elastic properties.

## 14.2   Equations of Motion of Beams

The governing partial differential equations describing the nonlinear longitudinal and transversal vibrations of beams based on the Euler-Bernoulli theory of beams are

$$\rho A \frac{\partial^2 u}{\partial t^2} + c_u \frac{\partial u}{\partial t} - EA \frac{\partial}{\partial x} \left[ \frac{\partial u}{\partial x} + \frac{1}{2} \left( \frac{\partial v}{\partial x} \right)^2 \right] = P(x, t), \qquad (14.1)$$

$$\rho A \frac{\partial^2 v}{\partial t^2} + c_v \frac{\partial v}{\partial t} - EA \frac{\partial}{\partial x} \left\{ \left[ \frac{\partial u}{\partial x} + \frac{1}{2} \left( \frac{\partial v}{\partial x} \right)^2 \right] \frac{\partial v}{\partial x} \right\} + EI \frac{\partial^4 v}{\partial x^4} = Q(x, t).$$
$$(14.2)$$

where $u = u(x, t)$ is the displacement of the beam in the longitudinal direction, $v = v(x, t)$ is displacement of the beam in the transversal direction, $x$ is the axial coordinate of the beam, and $t$ denotes the time. Parameters $\rho$, $A$, $E$ and $I$ are the mass density, cross sectional area, Young modulus and the moment of inertia of beam, respectively and $P(x, t)$, $Q(x, t)$ denote external loading in longitudinal or transversal direction, respectively. To incorporate viscous damping, the Euler-Bernoulli equations of beam vibrations are supplemented with appropriate damping terms $c_u \frac{\partial u}{\partial t}$ and $c_v \frac{\partial v}{\partial t}$, where parameters $c_u$ and $c_v$ correspond to the coefficients of modal viscous damping in the longitudinal or transversal direction. The expression

$$S = S(x, t) = EA \left[ \frac{\partial u}{\partial x} + \frac{1}{2} \left( \frac{\partial v}{\partial x} \right)^2 \right] \qquad (14.3)$$

defines the induced axial force. The principle of virtual work [2, 12] gives the following equation

$$\int_0^{l_e} \left[ \delta u \left( \rho A \frac{\partial^2 u}{\partial t^2} + c_u \frac{\partial u}{\partial t} - \frac{\partial S}{\partial x} - P \right) + \delta v \left( \rho A \frac{\partial^2 v}{\partial t^2} + c_v \frac{\partial v}{\partial t} - \frac{\partial}{\partial x} \left( S \frac{\partial v}{\partial x} \right) \right. \right.$$
$$\left. \left. + EI \frac{\partial^4 v}{\partial x^4} - Q \right) \right] dx = 0,$$
$$(14.4)$$

where $l_e$ denotes the length of the beam element. By integrating the Eq. (14.4) by parts twice and using $\frac{\partial(\delta u)}{\partial x} = \delta u'$, $\frac{\partial(\delta v)}{\partial x} = \delta v'$, $\frac{\partial^2(\delta v)}{\partial x^2} = \delta v''$ for partial derivatives of variations according to the axial coordinate $x$, gives

$$\int_0^{l_e} \left( \delta u \rho A \frac{\partial^2 u}{\partial t^2} + \delta u c_u \frac{\partial u}{\partial t} + \delta u' S - \delta u P + \delta v \rho A \frac{\partial^2 v}{\partial t^2} + \delta v c_v \frac{\partial v}{\partial t} + \delta v' S \frac{\partial v}{\partial x} \right.$$
$$\left. + EI \delta v'' \frac{\partial^2 v}{\partial x^2} - \delta v Q \right) dx - \delta u S \Big|_0^{l_e} - \delta v S \frac{\partial v}{\partial x} \Big|_0^{l_e}$$
$$+ EI \left( \delta v \frac{\partial^3 v}{\partial x^3} - \delta v' \frac{\partial^2 v}{\partial x^2} \right) \Big|_0^{l_e} = 0.$$
$$(14.5)$$

## 14.3 Spatial Discretization of the Beam Using Finite Elements

Following the standard procedure of Finite Element Method [2, 19] the beam is discretized with $N_e$ finite elements of the length $l_e$. The longitudinal displacement field $u(x, t)$ and the transversal displacement field $v(x, t)$ over the mesh of finite elements are expressed by means of scalar products of interpolation functions $\mathbf{n}(x)$ and $\mathbf{N}(x)$ by vectors of nodal values of displacements $\mathbf{u}(t)$ and $\mathbf{v}(t)$, respectively:

$$u(x, t) = \mathbf{n}(x)\mathbf{u}(t), \quad \delta u(x, t) = \mathbf{n}(x)\delta\mathbf{u}(t), \tag{14.6}$$

$$v(x, t) = \mathbf{N}(x)\mathbf{v}(t), \quad \delta v(x, t) = \mathbf{N}(x)\delta\mathbf{v}(t). \tag{14.7}$$

By applying the substitutions $\frac{\partial u}{\partial t} = \mathbf{n}(x)\dot{\mathbf{u}}(t), \frac{\partial^2 u}{\partial t^2} = \mathbf{n}(x)\ddot{\mathbf{u}}(t), \frac{\partial u}{\partial x} = \frac{\partial}{\partial x}$ $[\mathbf{n}(x)\mathbf{u}(t)] = \mathbf{n}'(x)\mathbf{u}(t), \delta u' = \frac{\partial(\delta u)}{\partial x} = \frac{\partial}{\partial x}[\mathbf{n}(x)\delta\mathbf{u}(t)] = \mathbf{n}'(x)\delta\mathbf{u}(t)$ and analog substitutions in respect of displacement $v(x, t)$, the principle of virtual work on the length of one finite element of the beam can be formulated as

$$
\begin{aligned}
\int_0^{l_e} &\left( \delta\mathbf{u}^\mathrm{T}\rho A\mathbf{n}^\mathrm{T}\mathbf{n}\ddot{\mathbf{u}} + \delta\mathbf{u}^\mathrm{T}c_u\mathbf{n}^\mathrm{T}\mathbf{n}(x)\dot{\mathbf{u}}(t) + \delta\mathbf{u}^\mathrm{T}\left(\mathbf{n}'\right)^\mathrm{T} S - \delta\mathbf{u}^\mathrm{T}\mathbf{n}^\mathrm{T}P \right. \\
&+ \delta\mathbf{v}^\mathrm{T}\rho A\mathbf{N}^\mathrm{T}\mathbf{N}\ddot{\mathbf{v}} + \delta\mathbf{v}^\mathrm{T}c_v\mathbf{N}^\mathrm{T}\mathbf{N}\dot{\mathbf{v}} + \delta\mathbf{v}^\mathrm{T}\left(\mathbf{N}'\right)^\mathrm{T} S\mathbf{N}'\mathbf{v} + EI\delta\mathbf{v}^\mathrm{T}\left(\mathbf{N}''\right)^\mathrm{T}\mathbf{N}''\mathbf{v} \\
&\left. - \delta\mathbf{v}^\mathrm{T}\mathbf{N}^\mathrm{T}Q \right)\mathrm{d}x - \delta\mathbf{u}^\mathrm{T}\mathbf{n}^\mathrm{T}S\Big|_0^{l_e} - \delta\mathbf{v}^\mathrm{T}\mathbf{N}^\mathrm{T}S\mathbf{N}'\mathbf{v}\Big|_0^{l_e} \\
&+ EI\left(\delta\mathbf{v}^\mathrm{T}\mathbf{N}^\mathrm{T}\mathbf{N}'''\mathbf{v} - \delta\mathbf{v}^\mathrm{T}\left(\mathbf{N}'\right)^\mathrm{T}\mathbf{N}''\mathbf{v}\right)\Big|_0^{l_e} = 0.
\end{aligned}
\tag{14.8}
$$

Since the variations $\delta\mathbf{u}^\mathrm{T}$ and $\delta\mathbf{v}^\mathrm{T}$ are arbitrary and independent on the axial coordinate $x$, and nodal vectors $\mathbf{u}$ and $\mathbf{v}$ are also independent on the coordinate $x$, the above equation can be rewritten into the form

$$
\begin{aligned}
\delta\mathbf{u}^\mathrm{T} &\left[ \mathbf{M_u}\ddot{\mathbf{u}} + \mathbf{C_u}\dot{\mathbf{u}} + \int_0^{l_e}\left(\mathbf{n}'\right)^\mathrm{T} S\mathrm{d}x - \mathbf{P} \right] - \delta\mathbf{u}^\mathrm{T}\mathbf{n}^\mathrm{T}S\Big|_0^{l_e} + \\
\delta\mathbf{v}^\mathrm{T} &\left[ \mathbf{M_v}\ddot{\mathbf{v}} + \mathbf{C_v}\dot{\mathbf{v}} + \left(\int_0^{l_e}\left(\mathbf{N}'\right)^\mathrm{T} S\mathbf{N}'\mathrm{d}x\right)\mathbf{v} + \mathbf{K_v}\mathbf{v} - \mathbf{Q} \right] \\
&- \delta\mathbf{v}^\mathrm{T}\left(\mathbf{N}^\mathrm{T}S\mathbf{N}'\mathbf{v} - EI\mathbf{N}^\mathrm{T}\mathbf{N}'''\mathbf{v} + EI\left(\mathbf{N}'\right)^\mathrm{T}\mathbf{N}''\mathbf{v}\right)\Big|_0^{l_e} = 0,
\end{aligned}
\tag{14.9}
$$

where

$$\mathbf{M_u} = \int_0^{l_e} \rho A \mathbf{n}^T \mathbf{n} dx, \, \mathbf{M_v} = \int_0^{l_e} \rho A \mathbf{N}^T \mathbf{N} dx, \tag{14.10a}$$

$$\mathbf{C_u} = \int_0^{l_e} c_u \mathbf{n}^T \mathbf{n} dx, \, \mathbf{C_v} = \int_0^{l_e} c_v \mathbf{N}^T \mathbf{N} dx, \tag{14.10b}$$

$$\mathbf{K_v} = \int_0^{l_e} EI \left( \mathbf{N}'' \right)^T \mathbf{N}'' dx, \, \mathbf{K}_g = \int_0^{l_e} \left( \mathbf{N}' \right)^T \mathbf{N}' dx, \tag{14.10c}$$

$$\mathbf{P} = \int_0^{l_e} \mathbf{n}^T P d\, x, \, \mathbf{Q} = \int_0^{l_e} \mathbf{N}^T Q dx. \tag{14.10d}$$

By introducing the dimensionless coordinate $\xi = \frac{x}{l_e}$, where $l_e$ denotes the length of an individual beam finite element, it is convenient to express both interpolation functions in dependence on the coordinate $\xi$ [6]

$$\mathbf{n}\,(\xi) = [1 - \xi, \xi] \,,$$
$$\mathbf{N}\,(\xi) = \left[ 1 - 3\xi^2 + 2\xi^3, \xi \left( \xi^2 - 2\xi + 1 \right) l_e, 3\xi^2 - 2\xi^3, \left( \xi^3 - \xi^2 \right) l_e \right]. \tag{14.11}$$

Taking into account the matrices of shape functions (14.11), we derive the equations for computing matrices and vectors (14.10a–d) in the following form:

$$\mathbf{M_u} = \frac{\rho A l_e}{6} \begin{bmatrix} 2 & 1 \\ 1 & 2 \end{bmatrix}, \, \mathbf{M_v} = \frac{\rho A l_e}{420} \begin{bmatrix} 156 & 22l_e & 54 & -13l_e \\ 22l_e & 4l_e^2 & 13l_e & -3l_e^2 \\ 54 & 13l_e & 156 & -22l_e \\ -13l_e & -3l_e^2 & -22l_e & 4l_e^2 \end{bmatrix},$$

$$\mathbf{C_u} = \frac{c_u l_e}{6} \begin{bmatrix} 2 & 1 \\ 1 & 2 \end{bmatrix}, \mathbf{C_v} = \frac{c_v l_e}{420} \begin{bmatrix} 156 & 22l_e & 54 & -13l_e \\ 22l_e & 4l_e^2 & 13l_e & -3l_e^2 \\ 54 & 13l_e & 156 & -22l_e \\ -13l_e & -3l_e^2 & -22l_e & 4l_e^2 \end{bmatrix},$$

$$\mathbf{K_v} = \frac{EI}{l_e^3} \begin{bmatrix} 12 & 6l_e & -12 & 6l_e \\ 6l_e & 4l_e^2 & -6l_e & 2l_e^2 \\ -12 & -6l_e & 12 & -6l_e \\ 6l_e & 2l_e^2 & -6l_e & 4l_e^2 \end{bmatrix},$$

$$\mathbf{K}_g = \frac{1}{60l_e} \begin{bmatrix} 36 & 3l_e & -36 & 3l_e \\ 3l_e & 4l_e^2 & -3l_e & -l_e^2 \\ -36 & -3l_e & 36 & -3l_e \\ 3l_e & -l_e^2 & -3l_e & 4l_e^2 \end{bmatrix}. \tag{14.12}$$

Applying FEM we assume that the axial force is approximated by their average value on the entire length of the finite element. Approximating the axial force in this manner, we suppress the dependency on the axial coordinate $x$ and therefore $S(x, t) \doteq S(t)$. This simplification is justified, if the beam is homogeneous so that both, Young modulus and the cross sectional area of the beam are constants. The fulfillment of both requirements is then reflected by the equation $EA = const$. The validity of the mentioned simplification under the fulfilled conditions can be confirmed by the following derivation

$$
S(x, t) \doteq \frac{1}{l_e} \int_0^{le} EA \left[ \frac{\partial u}{\partial x} + \frac{1}{2} \left( \frac{\partial v}{\partial x} \right)^2 \right] dx = \left( \frac{EA}{l_e} \int_0^{le} \frac{\partial}{\partial x} [\mathbf{n}(x)] \, dx \right) \mathbf{u}(t)
$$
$$
+ [\mathbf{v}(t)]^T \left[ \frac{EA}{2l_e} \int_0^{le} \left( \frac{\partial}{\partial x} [\mathbf{N}(x)] \right)^T \left( \frac{\partial}{\partial x} [\mathbf{N}(x)] \right) dx \right] \mathbf{v}(t).
$$

$$(14.13)$$

In this derivation we write shape functions in the form

$$
\mathbf{n}(x) = \frac{1}{l_e} [l_e - x, x],
$$
$$
\mathbf{N}(x) = \left[ \frac{1}{l_e^3} \left( l_e^3 - 3l_e x^2 + 2x^3 \right), \frac{x}{l_e^2} \left( x^2 - 2l_e x + l_e^2 \right), \frac{1}{l_e^3} \left( 3l_e x^2 - 2x^3 \right), \frac{1}{l_e^2} \left( x^3 - l_e x^2 \right) \right].
$$

Then

$$
S(x, t) \doteq \frac{1}{l_e} \int_0^{l_e} EA \left[ \frac{\partial u}{\partial x} + \frac{1}{2} \left( \frac{\partial v}{\partial x} \right)^2 \right] dx
$$
$$
= \frac{EA}{l_e} \left[ [-1, 1] \mathbf{u}(t) + \frac{1}{2} [\mathbf{v}(t)]^T \mathbf{K}_g \mathbf{v}(t) \right] = S(t).
$$

$$(14.14)$$

Needless to say, this derivation does not apply to inhomogeneous beams and variable cross-sections, i.e. in cases where the Young modulus and/or beam cross-section are functions of axial coordinate $x$, $E = E(x)$, $A = A(x)$. Irrespective of the constraint $EA = const$, the simplification $S(x, t) = S(t)$ can be applied to homogeneous stepped beams with constant cross-sections, if the sum of lengths of individual finite elements corresponds to the length of the beam section on which a certain constant cross-section applies. In Eq. (14.9) appears the integral $\int_0^{l_e} (\mathbf{n}')^T S \, dx$, which according to the approximation $S(x, t) = S(t)$ gives the result

$$
\int_0^{l_e} (\mathbf{n}')^T S(t) \, dx = S(t) \int_0^{l_e} \frac{\partial}{\partial x} (\mathbf{n})^T \, dx = S(t) (\mathbf{n})^T \Big|_0^{l_e}
$$
$$
= S(t) \left\{ \begin{bmatrix} \frac{1}{l_e} (l_e - l_e) \\ \frac{l_e}{l_e} \end{bmatrix} - \begin{bmatrix} \frac{1}{l_e} (l_e - 0) \\ 0 \end{bmatrix} \right\} = \begin{bmatrix} -1 \\ 1 \end{bmatrix} S(t) = (\mathbf{n}')^T S(t) l_e.
$$

$$(14.15)$$

By introducing matrices (14.12) and vectors (14.10d) and by considering the obtained result (14.15) in Eq. (14.9), we finally get

$$
\begin{aligned}
&\delta \mathbf{u}^{\mathrm{T}} \left[ \mathbf{M_u}\ddot{\mathbf{u}} + \mathbf{C_u}\dot{\mathbf{u}} + \left( \mathbf{n}' \right)^{\mathrm{T}} S\left(t\right) l_e - \mathbf{P} \right] \\
&+ \delta \mathbf{v}^{\mathrm{T}} \left[ \mathbf{M_v}\ddot{\mathbf{v}} + \mathbf{C_v}\dot{\mathbf{v}} + S\left(t\right) \mathbf{K}_g \mathbf{v} + \mathbf{K}_v \mathbf{v} - \mathbf{Q} \right] \\
&- \delta \mathbf{u}^{\mathrm{T}} \mathbf{n}^{\mathrm{T}} S\left(t\right) \Big|_0^{l_e} - \delta \mathbf{v}^{\mathrm{T}} S\left(t\right) \mathbf{N}^{\mathrm{T}} \mathbf{N}'\mathbf{v} \Big|_o^{l_e} + \delta \mathbf{v}^{\mathrm{T}} EI \mathbf{N}^{\mathrm{T}} \mathbf{N}'''\mathbf{v} \Big|_0^{l_e} \\
&\qquad\qquad - \delta \mathbf{v}^{\mathrm{T}} EI \left( \mathbf{N}' \right)^{T} \mathbf{N}''\mathbf{v} \Big|_0^{l_e} = 0.
\end{aligned}
$$

$$(14.16)$$

In so far as the vectors of variations $\delta \mathbf{u}^{\mathrm{T}}$ and $\delta \mathbf{v}^{\mathrm{T}}$ are arbitrary, the following equations apply simultaneously

$$
\mathbf{M_u}\ddot{\mathbf{u}} + \mathbf{C_u}\dot{\mathbf{u}} + \left( \mathbf{n}' \right)^{\mathrm{T}} S\left(t\right) l_e - \mathbf{P} = \mathbf{n}^{\mathrm{T}} S\left(t\right) \Big|_0^{l_e} = \overline{\mathbf{P}}, \qquad (14.17)
$$

$$
\begin{aligned}
&\mathbf{M_v}\ddot{\mathbf{v}} + \mathbf{C_v}\dot{\mathbf{v}} + S\left(t\right) \mathbf{K}_g \mathbf{v} + \mathbf{K}_v \mathbf{v} - \mathbf{Q} \\
&= S\left(t\right) \mathbf{N}^{\mathrm{T}}\mathbf{N}'\mathbf{v} \Big|_o^{l_e} - EI\mathbf{N}^{\mathrm{T}}\mathbf{N}'''\mathbf{v} \Big|_0^{l_e} + EI \left( \mathbf{N}' \right)^{T} \mathbf{N}''\mathbf{v} \Big|_0^{l_e} = \overline{\mathbf{Q}}. \qquad (14.18)
\end{aligned}
$$

Coupled Eqs. (14.17) and (14.18) can be conveniently combined to the nonlinear matrix differential equation of the beam element

$$
\mathbf{M}_e \ddot{\mathbf{q}}_e + \mathbf{C}_e \dot{\mathbf{q}}_e + \mathbf{K}\left(\mathbf{q}_e\right) \mathbf{q}_e = \mathbf{F}_e, \qquad (14.19)
$$

where the longitudinal and transversal displacement vectors $\mathbf{u}$ and $\mathbf{v}$ are united into displacement vector $\mathbf{q}_e = \begin{Bmatrix} \mathbf{u} \\ \mathbf{v} \end{Bmatrix}$ of the beam element and matrices $\mathbf{M}_e, \mathbf{C}_e, \mathbf{K}\left(\mathbf{q}_e\right)$ and vector $\mathbf{F}_e$ take the form

$$
\mathbf{M}_e = \begin{bmatrix} \mathbf{M_u} & \mathbf{0} \\ \mathbf{0} & \mathbf{M_v} \end{bmatrix}, \ \mathbf{C}_e = \begin{bmatrix} \mathbf{C_u} & \mathbf{0} \\ \mathbf{0} & \mathbf{C_v} \end{bmatrix}, \ \mathbf{K}\left(\mathbf{q}_e\right) = \begin{bmatrix} \mathbf{0} & \mathbf{0} \\ \mathbf{0} & S\left(t\right) \mathbf{K}_g + \mathbf{K}_v \end{bmatrix},
$$

$$
\mathbf{F}_e = \begin{Bmatrix} \mathbf{P} + \overline{\mathbf{P}} - \left( \mathbf{n}' \right)^{\mathrm{T}} S\left(t\right) l_e \\ \mathbf{Q} + \overline{\mathbf{Q}} \end{Bmatrix}. \qquad (14.20)
$$

After discretization, the structure with finite beam elements (which can include stepped beams), the standard FEM methodology [2, 19] is followed by the assembling process in which global displacement vector $\mathbf{q}$ is formed by assembling local displacement vectors $\mathbf{q}_e$ and global matrices $\mathbf{M}, \mathbf{C}, \mathbf{K}\left(\mathbf{q}\right)$ are constructed by assembling matrices $\mathbf{M}_e, \mathbf{C}_e, \mathbf{K}\left(\mathbf{q}_e\right)$ of beam elements as well as the global vector $\mathbf{F}$ is formed by assembling vectors $\mathbf{F}_e$. Thus, the global nonlinear matrix differential equation of the whole beam structure can be written in the form

$$\mathbf{M}\ddot{\mathbf{q}} + \mathbf{C}\dot{\mathbf{q}} + \mathbf{K}\left(\mathbf{q}\right)\mathbf{q} = \mathbf{F}. \tag{14.21}$$

Since the aim of the developed method is computation of nonlinear steady-state peri-
odic vibration of the beam, only boundary conditions of the beam must be satisfied.
Following Haug et al. [3], this can be achieved by systematic reduction of global
mass, damping and nonlinear stiffness matrices, respectively.

## 14.4  Incremental Harmonic Balance (IHB) Analysis of Periodic Vibrations of Beams

The incremental harmonic balance (IHB) method is one of the most powerful and
efficient tools for analyzing periodic and almost periodic vibrations of dynamical sys-
tems with high nonlinearities [15]. In general, dynamical systems can be autonomous
or are subjected to the external and/or parametric excitation. The almost periodic
response of the nonlinear dynamical system arises, if the external or parametric exci-
tation itself is almost periodic, however it can also occur due to the internal resonance
of the system. If natural angular frequencies of the system are incommensurate, the
almost periodic vibrations as consequence of internal resonance can be excited in
autonomous dynamical systems, too. For performing analysis of various types of
problems, which arise studying the steady-state response of nonlinear dynamical
systems, the introduction of multiple time scales is needed, which in general are
defined as products of several incommensurate angular frequencies by the time $t$ and
by chosen subharmonic factor $\eta$. In this paper, we will do not present the IHB method
in all its generality, but we will limit ourselves on analyzing periodic response of
beams that is excited by external harmonic loading. To achieve this goal, we will
allow that the excitation frequency $\omega$ is parametrically varied so that we will focus
on the study of the periodic response of the beam in the modes of fundamental,
superharmonic and subharmonic resonance. Due to these limitations, it is sufficient
to introduce a single time scale in the analysis of the periodic response of the beam

$$\tau = \eta\omega t, \tag{14.22}$$

where $\omega$ is excitation frequency, $t$ is time and $\eta$ is a subharmonic factor, which has
the value 1 for fundamental and superharmonic resonance, however at subharmonic
resonance it takes a fractional value. By introducing the time scale $\tau$, the ordinary
time derivatives $(\cdot)$ and $(\cdot\cdot)$ must be replaced by differential operators

$$(\cdot) = \frac{\mathrm{d}}{\mathrm{d}t} = \eta\omega\frac{\partial}{\partial\tau}, \quad (\cdot\cdot) = \frac{\mathrm{d}^2}{\mathrm{d}t^2} = \eta^2\omega^2\frac{\partial^2}{\partial\tau^2}, \tag{14.23}$$

what consequently causes the conversion of the ordinary matrix differential equations
(14.17), (14.18) into matrix partial differential equations

$$\eta^2\omega^2\mathbf{M_u}\frac{\partial^2\mathbf{u}}{\partial\tau^2} + \eta\omega\mathbf{C_u}\frac{\partial\mathbf{u}}{\partial\tau} + \left(\mathbf{n}'\right)^T S\left(\tau\right)l_e - \mathbf{P}\left(\tau\right) = \mathbf{n}^T S\left(\tau\right)\Big|_0^{l_e} = \overline{\mathbf{P}}\left(\tau\right),$$

(14.24)

$$\eta^2\omega^2\mathbf{M_v}\frac{\partial^2\mathbf{v}}{\partial\tau^2} + \eta\omega\mathbf{C_v}\frac{\partial\mathbf{v}}{\partial\tau} + S\left(\tau\right)\mathbf{K}_g\mathbf{v} + \mathbf{K}_v\mathbf{v} - \mathbf{Q}\left(\tau\right)$$

$$= S\left(\tau\right)\mathbf{N}^T\mathbf{N}'\mathbf{v}\Big|_o^{l_e} - EI\mathbf{N}^T\mathbf{N}'''\mathbf{v}\Big|_0^{l_e} + EI\left(\mathbf{N}'\right)^T\mathbf{N}''\mathbf{v}\Big|_0^{l_e} = \overline{\mathbf{Q}}\left(\tau\right).$$

(14.25)

### 14.4.1 Fourier Series Describing the Periodic Response of the Beam

In solving governing PDE's (14.24), (14.25) we are interested in the steady-state periodic solutions of the displacement vectors $\mathbf{u}$ and $\mathbf{v}$, which describe the beam vibrations in the longitudinal and transversal direction, respectively. We are looking for a solution with an ansatz in the form of truncated Fourier series

$$\mathbf{u}\left(\tau\right) = \mathbf{u}_0^c + \sum_{i=1}^n \left[\mathbf{u}_i^c \cos\left(i\tau\right) + \mathbf{u}_i^s \sin\left(i\tau\right)\right] = \mathbf{Y_u}\cdot\mathbf{b} = \left(\mathbf{I}_2 \otimes \mathbf{T}\right)\cdot\mathbf{b}, \quad (14.26a)$$

$$\mathbf{v}\left(\tau\right) = \mathbf{v}_0^c + \sum_{i=1}^n \left[\mathbf{v}_i^c \cos\left(i\tau\right) + \mathbf{v}_i^s \sin\left(i\tau\right)\right] = \mathbf{Y_v}\cdot\mathbf{c} = \left(\mathbf{I}_4 \otimes \mathbf{T}\right)\cdot\mathbf{c}, \quad (14.26b)$$

where $\tau = \eta\omega t$ and $\omega$ denotes the fundamental angular frequency of the beam. The cosine and sine terms are summed by the index $i$, which runs from $i = 1$ to $i = n$, where $n$ denotes the number of harmonics of the truncated Fourier series. In addition to harmonics, the series also contain terms $\mathbf{u}_0^c$ and $\mathbf{v}_0^c$, respectively, which can be joined to cosine terms with a frequency equal to zero. The truncated Fourier series (14.26a, 14.26b) can be conveniently expressed in the compact form of a matrix products $\mathbf{Y_u}\cdot\mathbf{b}$ and $\mathbf{Y_v}\cdot\mathbf{c}$, respectively, where matrices

$$\mathbf{Y_u} = \mathbf{I}_2 \otimes \mathbf{T} \in \mathbb{R}^{2\times(4n+2)}, \quad \mathbf{Y_v} = \mathbf{I}_4 \otimes \mathbf{T} \in \mathbb{R}^{4\times(8n+4)}, \quad (14.27)$$

are Kronecker products of identity matrices $\mathbf{I}_2$ and $\mathbf{I}_4$ respectively by matrix $\mathbf{T} \in \mathbb{R}^{1\times(2n+1)}$ of harmonic functions that make up truncated Fourier series

$$\mathbf{T} = \left[\mathbf{T}^c, \mathbf{T}^s\right],$$
$$\mathbf{T}^c = [1, \cos\left(\tau\right), \ldots, \cos\left(n\tau\right)], \quad \mathbf{T}^s = [\sin\left(\tau\right), \ldots, \sin\left(n\tau\right)], \quad (14.28)$$

and $\mathbf{b}$ and $\mathbf{c}$ denote vectors of Fourier coefficients of periodic vibrations of beam in the longitudinal or transversal direction, respectively. The vector $\mathbf{b}$ consists of $4n + 2$ components and vector $\mathbf{c}$ is of order $(8n + 4) \times 1$:

$$\mathbf{b} = \{\mathbf{b}_1^{\mathrm{T}}, \mathbf{b}_2^{\mathrm{T}}\}^{\mathrm{T}} = \left\{ (\mathbf{b}_1^c)^{\mathrm{T}}, (\mathbf{b}_1^s)^{\mathrm{T}}, (\mathbf{b}_2^c)^{\mathrm{T}}, (\mathbf{b}_2^s)^{\mathrm{T}} \right\}^{\mathrm{T}} \in \mathbb{R}^{2(2n+1)\times 1},$$

$$\mathbf{c} = \{\mathbf{c}_1^{\mathrm{T}}, \mathbf{c}_2^{\mathrm{T}}, \mathbf{c}_3^{\mathrm{T}}, \mathbf{c}_4^{\mathrm{T}}\}^{\mathrm{T}}$$

$$= \left\{ (\mathbf{c}_1^c)^{\mathrm{T}}, (\mathbf{c}_1^s)^{\mathrm{T}}, (\mathbf{c}_2^c)^{\mathrm{T}}, (\mathbf{c}_2^s)^{\mathrm{T}}, (\mathbf{c}_3^c)^{\mathrm{T}}, (\mathbf{c}_3^s)^{\mathrm{T}}, (\mathbf{c}_4^c)^{\mathrm{T}}, (\mathbf{c}_4^s)^{\mathrm{T}} \right\}^{\mathrm{T}} \in \mathbb{R}^{4(2n+1)\times 1}.$$

$$(14.29)$$

In equation of motion (14.24), the term $(\mathbf{n}')^{\mathrm{T}} S(\tau) l_e$ appears, in which the average value of the axial force $S(\tau)$ depends on the displacement vectors $\mathbf{u}$ and $\mathbf{v}$ and is thus periodic. It can be expressed in the form of a truncated Fourier series

$$S(\tau) = S_0^c + \sum_{i=1}^{n} \left[ S_i^c \cos(i\tau) + S_i^s \sin(i\tau) \right]. \qquad (14.30)$$

By inserting the Fourier series for the vectors of longitudinal and transversal displacements $\mathbf{u}(\tau)$ and $\mathbf{v}(\tau)$ into Eq. (14.14) for the average value of the axial force $S(\tau)$ we obtain

$$S(\tau) = \frac{EA}{l_e} \left[ [-1, 1] \mathbf{u}(\tau) + \frac{1}{2} [\mathbf{v}(\tau)]^{\mathrm{T}} \mathbf{K}_g \mathbf{v}(\tau) \right]$$

$$= \frac{EA}{l_e} \left[ [-1, 1] \mathbf{u}_0^c + \sum_{i=1}^{n} [-1, 1] \mathbf{u}_i^c \cos(i\tau) + \sum_{i=1}^{n} [-1, 1] \mathbf{u}_i^s \sin(i\tau) \right.$$

$$+ \frac{1}{2} (\mathbf{v}_0^c)^{\mathrm{T}} \mathbf{K}_g \mathbf{v}_0^c + \frac{1}{2} \left( \sum_{i=1}^{n} \left[ \mathbf{v}_i^c \cos(i\tau) + \mathbf{v}_i^s \sin(i\tau) \right] \right)^{\mathrm{T}} \mathbf{K}_g \mathbf{v}_0^c$$

$$+ \frac{1}{2} (\mathbf{v}_0^c)^{\mathrm{T}} \mathbf{K}_g \left( \sum_{k=1}^{n} \left[ \mathbf{v}_k^c \cos(k\tau) + \mathbf{v}_k^s \sin(k\tau) \right] \right)$$

$$+ \frac{1}{2} \left( \sum_{i=1}^{n} \left[ \mathbf{v}_i^c \cos(i\tau) + \mathbf{v}_i^s \sin(i\tau) \right] \right)^{\mathrm{T}}$$

$$\left. \mathbf{K}_g \left( \sum_{k=1}^{n} \left[ \mathbf{v}_k^c \cos(k\tau) + \mathbf{v}_k^s \sin(k\tau) \right] \right) \right]. \qquad (14.31)$$

By using the addition theorems of trigonometric functions, Eq. (14.31) can be transformed into the form

$$S(\tau) = \frac{EA}{l_e} \left[ [-1, 1] \mathbf{u}_0^c + \frac{1}{2} (\mathbf{v}_0^c)^{\mathrm{T}} \mathbf{K}_g \mathbf{v}_0^c \right.$$

$$+ \sum_{i=1}^{n} \left\{ [-1, 1] \mathbf{u}_i^c + (\mathbf{v}_0^c)^{\mathrm{T}} \mathbf{K}_g \mathbf{v}_i^c \right\} \cos(i\tau)$$

$$+\sum_{i=1}^{n}\left\{[-1,1]\,\mathbf{u}_i^s+\left(\mathbf{v}_0^c\right)^{\mathrm{T}}\mathbf{K}_g\mathbf{v}_i^s\right\}\sin{(i\tau)}$$

$$+\frac{1}{4}\sum_{i=1}^{n}\sum_{k=1}^{n}\left\{\left[\left(\mathbf{v}_i^c\right)^{\mathrm{T}}\mathbf{K}_g\mathbf{v}_k^c+\left(\mathbf{v}_i^s\right)^{\mathrm{T}}\mathbf{K}_g\mathbf{v}_k^s\right]\cos{[(i-k)\,\tau]}\right.$$

$$+\left.\left[\left(\mathbf{v}_i^s\right)^{\mathrm{T}}\mathbf{K}_g\mathbf{v}_k^c-\left(\mathbf{v}_i^c\right)^{\mathrm{T}}\mathbf{K}_g\mathbf{v}_k^s\right]\sin{[(i-k)\,\tau]}\right\}$$

$$+\frac{1}{4}\sum_{i=1}^{n}\sum_{k=1}^{n}\left\{\left[\left(\mathbf{v}_i^c\right)^{\mathrm{T}}\mathbf{K}_g\mathbf{v}_k^c-\left(\mathbf{v}_i^s\right)^{\mathrm{T}}\mathbf{K}_g\mathbf{v}_k^s\right]\cos{[(i+k)\,\tau]}\right.$$

$$+\left.\left.\left[\left(\mathbf{v}_i^s\right)^{\mathrm{T}}\mathbf{K}_g\mathbf{v}_k^c+\left(\mathbf{v}_i^c\right)^{\mathrm{T}}\mathbf{K}_g\mathbf{v}_k^s\right]\sin{[(i+k)\,\tau]}\right\}\right]. \tag{14.32}$$

We observe that the double sum

$$\frac{1}{4}\sum_{i=1}^{n}\sum_{k=1}^{n}\left[\left(\mathbf{v}_i^c\right)^{\mathrm{T}}\mathbf{K}_g\mathbf{v}_k^c+\left(\mathbf{v}_i^s\right)^{\mathrm{T}}\mathbf{K}_g\mathbf{v}_k^s\right]\cos{[(i-k)\,\tau]}$$

in Eq. (14.32) forms constant terms when the condition $i=k$ is satisfied. The double sum

$$\frac{1}{4}\sum_{i=1}^{n}\sum_{k=1}^{n}\left[\left(\mathbf{v}_i^s\right)^{\mathrm{T}}\mathbf{K}_g\mathbf{v}_k^c-\left(\mathbf{v}_i^c\right)^{\mathrm{T}}\mathbf{K}_g\mathbf{v}_k^s\right]\sin{[(i-k)\,\tau]}$$

does not form constant terms, because $\sin{[(i-k)\,\tau]}=\sin{(0)}=0$ when this condition is fulfilled. After exposing the constant terms for the indices $i=k$, it is advantageous to rename the index $i$ into the index $i'$ in double sums of Eq. (14.32), since the sum does not depend on the notation of the index by which the terms are summed. By considering this agreement and by carefully extracting terms associated with functions $\cos(i\tau)$ or $\sin(i\tau)$, Eq. (14.32) can be written in the following form

$$S(\tau)=S_0^c+\sum_{i=1}^{n}\left[S_i^c\cos{(i\tau)}+S_i^s\sin{(i\tau)}\right]$$

$$=\frac{EA}{l_e}\left[[-1,1]\,\mathbf{u}_0^c+\frac{1}{2}\left(\mathbf{v}_0^c\right)^{\mathrm{T}}\mathbf{K}_g\mathbf{v}_0^c\right.$$

$$+\frac{1}{4}\sum_{i=1}^{n}\left[\left(\mathbf{v}_i^c\right)^{\mathrm{T}}\mathbf{K}_g\mathbf{v}_i^c+\left(\mathbf{v}_i^s\right)^{\mathrm{T}}\mathbf{K}_g\mathbf{v}_i^s\right]+\sum_{i=1}^{n}\left\{[-1,1]\,\mathbf{u}_i^c+\left(\mathbf{v}_0^c\right)^{\mathrm{T}}\mathbf{K}_g\mathbf{v}_i^c\right.$$

$$+\frac{1}{4}\sum_{k=1}^{n-i}\left[\left(\mathbf{v}_{i+k}^c\right)^{\mathrm{T}}\mathbf{K}_g\mathbf{v}_k^c+\left(\mathbf{v}_{i+k}^s\right)^{\mathrm{T}}\mathbf{K}_g\mathbf{v}_k^s\right]$$

$$+\frac{1}{4}\sum_{k=i+1}^{n}\left[\left(\mathbf{v}_{k-i}^c\right)^{\mathrm{T}}\mathbf{K}_g\mathbf{v}_k^c+\left(\mathbf{v}_{k-i}^s\right)^{\mathrm{T}}\mathbf{K}_g\mathbf{v}_k^s\right]$$

$$+\frac{1}{4}\sum_{i'=1}^{i-1}\left.\left[\left(\mathbf{v}_{i'}^c\right)^{\mathrm{T}}\mathbf{K}_g\mathbf{v}_{i-i'}^c-\left(\mathbf{v}_{i'}^s\right)^{\mathrm{T}}\mathbf{K}_g\mathbf{v}_{i-i'}^s\right]\right\}\cos{(i\tau)}$$

$$+\sum_{i=1}^{n}\left\{[-1,1]\,\mathbf{u}_i^s+\left(\mathbf{v}_0^c\right)^{\mathrm{T}}\mathbf{K}_g\mathbf{v}_i^s+\frac{1}{4}\sum_{k=1}^{n-i}\left[\left(\mathbf{v}_{i+k}^s\right)^{\mathrm{T}}\mathbf{K}_g\mathbf{v}_k^c-\left(\mathbf{v}_{i+k}^c\right)^{\mathrm{T}}\mathbf{K}_g\mathbf{v}_k^s\right]\right.$$

$$-\frac{1}{4}\sum_{k=i+1}^{n}\left[\left(\mathbf{v}_{k-i}^s\right)^{\mathrm{T}}\mathbf{K}_g\mathbf{v}_k^c-\left(\mathbf{v}_{k-i}^c\right)^{\mathrm{T}}\mathbf{K}_g\mathbf{v}_k^s\right]$$

$$+\frac{1}{4}\sum_{i'=1}^{i-1}\left.\left.\left[\left(\mathbf{v}_{i'}^s\right)^{\mathrm{T}}\mathbf{K}_g\mathbf{v}_{i-i'}^c+\left(\mathbf{v}_{i'}^c\right)^{\mathrm{T}}\mathbf{K}_g\mathbf{v}_{i-i'}^s\right]\right\}\sin{(i\tau)}\right].$$

$$\tag{14.33}$$

Finally, we can read the following Fourier coefficients in Eq. (14.33):

$$S_0^c = \frac{EA}{l_e}\left[[-1, 1]\,\mathbf{u}_0^c + \frac{1}{2}\left(\mathbf{v}_0^c\right)^{\mathrm{T}}\mathbf{K}_g\mathbf{v}_0^c + \frac{1}{4}\sum_{i=1}^{n}\left[\left(\mathbf{v}_i^c\right)^{\mathrm{T}}\mathbf{K}_g\mathbf{v}_i^c + \left(\mathbf{v}_i^s\right)^{\mathrm{T}}\mathbf{K}_g\mathbf{v}_i^s\right]\right],$$

(14.34)

$$\begin{aligned}
S_i^c = \frac{EA}{l_e}\Bigg[&[-1, 1]\,\mathbf{u}_i^c + \left(\mathbf{v}_0^c\right)^{\mathrm{T}}\mathbf{K}_g\mathbf{v}_i^c + \frac{1}{4}\sum_{k=1}^{n-i}\left[\left(\mathbf{v}_{i+k}^c\right)^{\mathrm{T}}\mathbf{K}_g\mathbf{v}_k^c + \left(\mathbf{v}_{i+k}^s\right)^{\mathrm{T}}\mathbf{K}_g\mathbf{v}_k^s\right]\\
&+\frac{1}{4}\sum_{k=i+1}^{n}\left[\left(\mathbf{v}_{k-i}^c\right)^{\mathrm{T}}\mathbf{K}_g\mathbf{v}_k^c + \left(\mathbf{v}_{k-i}^s\right)^{\mathrm{T}}\mathbf{K}_g\mathbf{v}_k^s\right]\\
&+\frac{1}{4}\sum_{i'=1}^{i-1}\left[\left(\mathbf{v}_{i'}^c\right)^{\mathrm{T}}\mathbf{K}_g\mathbf{v}_{i-i'}^c - \left(\mathbf{v}_{i'}^s\right)^{\mathrm{T}}\mathbf{K}_g\mathbf{v}_{i-i'}^s\right]\Bigg],
\end{aligned}$$

(14.35)

$$\begin{aligned}
S_i^s = \frac{EA}{l_e}\Bigg[&[-1, 1]\,\mathbf{u}_i^s + \left(\mathbf{v}_0^c\right)^{\mathrm{T}}\mathbf{K}_g\mathbf{v}_i^s + \frac{1}{4}\sum_{k=1}^{n-i}\left[\left(\mathbf{v}_{i+k}^s\right)^{\mathrm{T}}\mathbf{K}_g\mathbf{v}_k^c - \left(\mathbf{v}_{i+k}^c\right)^{\mathrm{T}}\mathbf{K}_g\mathbf{v}_k^s\right]\\
&-\frac{1}{4}\sum_{k=i+1}^{n}\left[\left(\mathbf{v}_{k-i}^s\right)^{\mathrm{T}}\mathbf{K}_g\mathbf{v}_k^c - \left(\mathbf{v}_{k-i}^c\right)^{\mathrm{T}}\mathbf{K}_g\mathbf{v}_k^s\right]\\
&+\frac{1}{4}\sum_{i'=1}^{i-1}\left[\left(\mathbf{v}_{i'}^s\right)^{\mathrm{T}}\mathbf{K}_g\mathbf{v}_{i-i'}^c + \left(\mathbf{v}_{i'}^c\right)^{\mathrm{T}}\mathbf{K}_g\mathbf{v}_{i-i'}^s\right]\Bigg].
\end{aligned}$$

(14.36)

Equation of vibration of the beam in the axial direction

$$\eta^2\omega^2\mathbf{M}_{\mathbf{u}}\frac{\partial^2\mathbf{u}}{\partial\tau^2} + \eta\omega\mathbf{C}_{\mathbf{u}}\frac{\partial\mathbf{u}}{\partial\tau} + \left(\mathbf{n}'\right)^{\mathrm{T}}S(\tau)\,l_e - \mathbf{P}(\tau) = \overline{\mathbf{P}}(\tau),$$

(14.37)

can be developed on the basis of Eq. (14.14)

$$S(\tau) \doteq \frac{EA}{l_e}\left[[-1, 1]\,\mathbf{u}(\tau) + \frac{1}{2}\,[\mathbf{v}(\tau)]^{\mathrm{T}}\mathbf{K}_g\mathbf{v}(\tau)\right],$$

(14.38)

and using Eq. (14.15)

$$\left(\mathbf{n}'\right)^{\mathrm{T}}S(\tau)\,l_e \doteq \begin{bmatrix}-1\\1\end{bmatrix}\frac{EA}{l_e}\left[[-1, 1]\,\mathbf{u}(\tau) + \frac{1}{2}\,[\mathbf{v}(\tau)]^{\mathrm{T}}\mathbf{K}_g\mathbf{v}(\tau)\right]$$

(14.39)

to the form

$$\eta^2\omega^2\mathbf{M_u}\frac{\partial^2\mathbf{u}}{\partial\tau^2} + \eta\omega\mathbf{C_u}\frac{\partial\mathbf{u}}{\partial\tau}$$
$$+ \frac{EA}{l_e}\left[\begin{bmatrix} 1 & -1 \\ -1 & 1 \end{bmatrix}\mathbf{u}(\tau) + \frac{1}{2}\begin{bmatrix} -1 \\ 1 \end{bmatrix}[\mathbf{v}(\tau)]^{\mathrm{T}}\mathbf{K}_g\mathbf{v}(\tau)\right] - \mathbf{P}(\tau) = \overline{\mathbf{P}}(\tau),$$

(14.40)

where

$$\mathbf{K_u} = \frac{EA}{l_e}\begin{bmatrix} 1 & -1 \\ -1 & 1 \end{bmatrix}$$

(14.41)

and

$$\mathbf{K_{uv}} = \frac{EA}{2l_e}\begin{bmatrix} -1 \\ 1 \end{bmatrix}[\mathbf{v}(\tau)]^{\mathrm{T}}\mathbf{K}_g$$
$$= \frac{EA}{2l_e}\begin{bmatrix} -1 \\ 1 \end{bmatrix}.$$
$$\left\{(\mathbf{v}_0^c)^{\mathrm{T}}\mathbf{K}_g + \sum_{i=1}^{n}\left[(\mathbf{v}_i^c)^{\mathrm{T}}\mathbf{K}_g\cos(i\tau) + (\mathbf{v}_i^s)^{\mathrm{T}}\mathbf{K}_g\sin(i\tau)\right]\right\}.$$

(14.42)

Thus, equation of vibration of the beam in the longitudinal direction can be written in compact form as

$$\eta^2\omega^2\mathbf{M_u}\frac{\partial^2\mathbf{u}}{\partial\tau^2} + \eta\omega\mathbf{C_u}\frac{\partial\mathbf{u}}{\partial\tau} + \mathbf{K_u}\mathbf{u}(\tau) + \mathbf{K_{uv}}\mathbf{v}(\tau) - \mathbf{P}(\tau) = \overline{\mathbf{P}}(\tau).$$

(14.43)

In a similar way, we can also develop the equation of vibration of the beam in the transversal direction

$$\eta^2\omega^2\mathbf{M_v}\frac{\partial^2\mathbf{v}}{\partial\tau^2} + \eta\omega\mathbf{C_v}\frac{\partial\mathbf{v}}{\partial\tau} + S(\tau)\mathbf{K}_g\mathbf{v} + \mathbf{K_v}\mathbf{v} - \mathbf{Q}$$
$$= \eta^2\omega^2\mathbf{M_v}\frac{\partial^2\mathbf{v}}{\partial\tau^2} + \eta\omega\mathbf{C_v}\frac{\partial\mathbf{v}}{\partial\tau}$$
$$+ \left(\frac{EA}{l_e}\left[[-1, 1]\mathbf{u}(\tau) + \frac{1}{2}[\mathbf{v}(\tau)]^{\mathrm{T}}\mathbf{K}_g\mathbf{v}(\tau)\right]\right)\mathbf{K}_g\mathbf{v} + \mathbf{K_v}\mathbf{v} - \mathbf{Q} = \overline{\mathbf{Q}}.$$

(14.44)

In the expression inside the parentheses, we note that the terms $[-1, 1]\mathbf{u}(\tau)$ and $[\mathbf{v}(\tau)]^{\mathrm{T}}\mathbf{K}_g\mathbf{v}(\tau)$ are scalars. Due to this, they can be shifted after the matrix product $\mathbf{K}_g\mathbf{v}$

$$\eta^2\omega^2\mathbf{M_v}\frac{\partial^2\mathbf{v}}{\partial\tau^2} + \eta\omega\mathbf{C_v}\frac{\partial\mathbf{v}}{\partial\tau} + \frac{EA}{l_e}\mathbf{K}_g\mathbf{v}[-1, 1]\mathbf{u}$$
$$+ \frac{EA}{2l_e}\mathbf{K}_g\mathbf{v}\mathbf{v}^{\mathrm{T}}\mathbf{K}_g\mathbf{v} + \mathbf{K_v}\mathbf{v} - \mathbf{Q} = \overline{\mathbf{Q}}.$$

(14.45)

In the obtained Eq. (14.45), the matrix product $\frac{EA}{l_e}\mathbf{K}_g\mathbf{v}[-1, 1]$ can be expressed using the transposed matrix $\mathbf{K}_{\mathbf{uv}}^{\mathbf{T}}$

$$2\mathbf{K}_{\mathbf{uv}}^{\mathbf{T}} = \frac{EA}{l_e}\left(\begin{bmatrix} -1 \\ 1 \end{bmatrix}[\mathbf{v}(\tau)]^{\mathrm{T}}\mathbf{K}_g\right)^{\mathrm{T}} = \frac{EA}{l_e}\left(\mathbf{K}_g^{\mathrm{T}}\mathbf{v}(\tau)[-1, 1]\right), \qquad (14.46)$$

where the matrix $\mathbf{K}_g$ is symmetric, $\mathbf{K}_g = \mathbf{K}_g^{\mathrm{T}}$. The matrix $\mathbf{K}_{\mathbf{v}}$ was defined earlier in Eqs. (14.12)

$$\mathbf{K}_{\mathbf{v}} = \int_0^{l_e} EI\left[\mathbf{N}''(x)\right]^{\mathrm{T}}\mathbf{N}''(x)\,\mathrm{d}x = \frac{EI}{l_e^3}\begin{bmatrix} 12 & 6l_e & -12 & 6l_e \\ 6l_e & 4l_e^2 & -6l_e & 2l_e^2 \\ -12 & -6l_e & 12 & -6l_e \\ 6l_e & 2l_e^2 & -6l_e & 4l_e^2 \end{bmatrix}, \qquad (14.47)$$

and the matrix $\mathbf{K}_{\mathbf{vv}}$ is determined by equation:

$$\mathbf{K}_{\mathbf{vv}} = \frac{EA}{2l_e}\mathbf{K}_g\mathbf{v}\mathbf{v}^{\mathrm{T}}\mathbf{K}_g. \qquad (14.48)$$

By inserting the matrix $\mathbf{K}_g$, defined in Eqs. (14.12) and by substituting Eq. (14.26b) for the vector $\mathbf{v}$, the matrix $\mathbf{K}_{\mathbf{vv}}$ can be written in the following explicit form

$$\begin{aligned}
\mathbf{K}_{\mathbf{vv}} &= \frac{EA}{2l_e}\mathbf{K}_g\mathbf{v}\mathbf{v}^{\mathrm{T}}\mathbf{K}_g \\
&= \frac{EA}{2l_e}\mathbf{K}_g\left[\mathbf{v}_0^c\left(\mathbf{v}_0^c\right)^{\mathrm{T}}\right]\mathbf{K}_g \\
&+ \frac{EA}{2l_e}\mathbf{K}_g\mathbf{v}_0^c\sum_{i=1}^{n}\left[\left(\mathbf{v}_i^c\right)^{\mathrm{T}}\cos(i\tau) + \left(\mathbf{v}_i^s\right)^{\mathrm{T}}\sin(i\tau)\right]\mathbf{K}_g \\
&+ \frac{EA}{2l_e}\mathbf{K}_g\sum_{i=1}^{n}\left[\mathbf{v}_i^c\cos(i\tau) + \mathbf{v}_i^s\sin(i\tau)\right]\left(\mathbf{v}_0^c\right)^{\mathrm{T}}\mathbf{K}_g \\
&+ \frac{EA}{4l_e}\mathbf{K}_g\sum_{i=1}^{n}\sum_{j=1}^{n}\left[\mathbf{v}_i^c\left(\mathbf{v}_j^c\right)^{\mathrm{T}}(\cos[(i-j)\tau] + \cos[(i+j)\tau])\right. \\
&\quad + \mathbf{v}_i^c\left(\mathbf{v}_j^s\right)^{\mathrm{T}}(-\sin[(i-j)\tau] + \sin[(i+j)\tau]) \\
&\quad + \mathbf{v}_i^s\left(\mathbf{v}_j^c\right)^{\mathrm{T}}(\sin[(i-j)\tau] + \sin[(i+j)\tau]) \\
&\quad \left. + \mathbf{v}_i^s\left(\mathbf{v}_j^s\right)^{\mathrm{T}}(\cos[(i-j)\tau] - \cos[(i+j)\tau])\right]\mathbf{K}_g.
\end{aligned}$$
$$(14.49)$$

Finally, the equation of beam vibration in the transverse direction using the matrices, defined in Eqs. (14.46), (14.47) and (14.49) reads

$$\eta^2\omega^2\mathbf{M}_{\mathbf{v}}\frac{\partial^2\mathbf{v}}{\partial\tau^2} + \eta\omega\mathbf{C}_{\mathbf{v}}\frac{\partial\mathbf{v}}{\partial\tau} + 2\mathbf{K}_{\mathbf{uv}}^{\mathrm{T}}\mathbf{u} + \mathbf{K}_{\mathbf{vv}}\mathbf{v} + \mathbf{K}_{\mathbf{v}}\mathbf{v} - \mathbf{Q}(\tau) = \overline{\mathbf{Q}}(\tau). \qquad (14.50)$$

### 14.4.2 Application of the Newton-Raphson Iterative Procedure

Matrix partial differential equations (14.43) and (14.50) of longitudinal and transversal beam vibrations, which are discretized using beam finite element matrices, are nonlinear differential equations due to the nonlinear matrix products $\mathbf{K_{uv}v}$, $2\mathbf{K_{uv}^T u}$ and $\mathbf{K_{vv}v}$, induced by action of the periodic axial force. The complexity of nonlinear beam vibration equations is high and their direct solving almost impossible, so we can expect that the solutions of beam vibration equations can be obtained in the form of analytical approximations. Instead of trying to get an exact analytical solution, we prefer to use the Newton-Raphson iterative procedure in which we look for an approximate solution. In this procedure, we assume an initial or guessed solution, which defines an initial state $\mathbf{u}, \mathbf{v}, \omega, \mathbf{P}(\tau), \overline{\mathbf{P}}(\tau), \mathbf{Q}(\tau), \overline{\mathbf{Q}}(\tau)$. By adding small increments $\varDelta\mathbf{u}, \varDelta\mathbf{v}, \varDelta\omega, \varDelta\mathbf{P}(\tau), \varDelta\overline{\mathbf{P}}(\tau), \varDelta\mathbf{Q}(\tau), \varDelta\overline{\mathbf{Q}}(\tau)$ to the actual solution, we compute a new state

$$
\begin{aligned}
\mathbf{u}^{\text{new}} &= \mathbf{u} + \varDelta\mathbf{u}, \; \mathbf{v}^{\text{new}} = \mathbf{v} + \varDelta\mathbf{v}, \; \omega^{\text{new}} = \omega + \varDelta\omega, \\
\mathbf{P}^{\text{new}} &= \mathbf{P} + \varDelta\mathbf{P}, \; \overline{\mathbf{P}}^{\text{new}} = \overline{\mathbf{P}} + \varDelta\overline{\mathbf{P}}, \\
\mathbf{Q}^{\text{new}} &= \mathbf{Q} + \varDelta\mathbf{Q}, \; \overline{\mathbf{Q}}^{\text{new}} = \overline{\mathbf{Q}} + \varDelta\overline{\mathbf{Q}}.
\end{aligned}
\tag{14.51}
$$

By applying Newton-Raphson iterative procedure we first perform the linearization of the beam vibration equation in the longitudinal direction

$$
\eta^2\omega^2\mathbf{M_u}\frac{\partial^2\mathbf{u}}{\partial\tau^2} + \eta\omega\mathbf{C_u}\frac{\partial\mathbf{u}}{\partial\tau} + \mathbf{K_u}\mathbf{u}(\tau) + \mathbf{K_{uv}}\mathbf{v}(\tau) - \mathbf{P}(\tau) = \overline{\mathbf{P}}(\tau).
\tag{14.52}
$$

The beam vibration equation corresponding to the new state is as follows

$$
\begin{aligned}
&\eta^2(\omega + \varDelta\omega)^2\,\mathbf{M_u}\left(\tfrac{\partial^2\mathbf{u}}{\partial\tau^2} + \tfrac{\partial^2\varDelta\mathbf{u}}{\partial\tau^2}\right) + \eta(\omega + \varDelta\omega)\,\mathbf{C_u}\left(\tfrac{\partial\mathbf{u}}{\partial\tau} + \tfrac{\partial\varDelta\mathbf{u}}{\partial\tau}\right) \\
&+ \mathbf{K_u}(\mathbf{u} + \varDelta\mathbf{u}) + \mathbf{K_{uv}}(\mathbf{v} + \varDelta\mathbf{v})\cdot(\mathbf{v} + \varDelta\mathbf{v}) - P - \varDelta P = \overline{\mathbf{P}} + \varDelta\overline{\mathbf{P}}.
\end{aligned}
\tag{14.53}
$$

The nonlinear matrix partial differential equation (14.53) is linearized in the vicinity of the actual (initial) state by developing all terms into Taylor series and retaining only terms of these series that are linear in increments. The term $\mathbf{K_{uv}}(\mathbf{v} + \varDelta\mathbf{v})\cdot(\mathbf{v} + \varDelta\mathbf{v})$ is nonlinear, so we develop it into a Taylor series and keep only the term that is linear in increments

$$
\begin{aligned}
&\mathbf{K_{uv}}(\mathbf{v} + \varDelta\mathbf{v})\cdot(\mathbf{v} + \varDelta\mathbf{v}) \\
&= \mathbf{K_{uv}}(\mathbf{v})\cdot\mathbf{v} + \left[\mathbf{K_{uv}}(\mathbf{v}) + \tfrac{\partial\mathbf{K_{uv}}(\mathbf{v})}{\partial\mathbf{v}}\cdot(\mathbf{I}_4\otimes\mathbf{v})\right]\cdot\varDelta\mathbf{v}.
\end{aligned}
\tag{14.54}
$$

Consistency with respect to the dimensions of matrix products is important in this development. The matrix product $\mathbf{M_u}\left(\frac{\partial^2 \mathbf{u}}{\partial \tau^2} + \frac{\partial^2 \Delta\mathbf{u}}{\partial \tau^2}\right)$ for example is of dimension $2 \times 1$ and such dimension must be all other terms, including the product $\mathbf{K_{uv}}(\mathbf{v}+\Delta\mathbf{v}) \cdot (\mathbf{v}+\Delta\mathbf{v})$. The matrix $\mathbf{K_{uv}}$ has dimension $2 \times 4$, vectors $\mathbf{v}$ and $\Delta\mathbf{v}$ are of order $4 \times 1$ so the products $\mathbf{K_{uv}}(\mathbf{v}) \cdot \mathbf{v}$ and $\mathbf{K_{uv}}(\mathbf{v}) \cdot \Delta\mathbf{v}$, respectively are of order $2 \times 1$ as desired. The derivative $\frac{\partial \mathbf{K_{uv}}(\mathbf{v})}{\partial \mathbf{v}}$ defines a matrix of dimension $2 \times 16$, while the Kronecker product $\mathbf{I}_4 \otimes \mathbf{v}$ is a $16 \times 4$ matrix. Thus the product $\frac{\partial \mathbf{K_{uv}}(\mathbf{v})}{\partial \mathbf{v}} \cdot (\mathbf{I}_4 \otimes \mathbf{v})$ is a $2 \times 4$ matrix and the product $\left[\frac{\partial \mathbf{K_{uv}}(\mathbf{v})}{\partial \mathbf{v}} \cdot (\mathbf{I}_4 \otimes \mathbf{v})\right] \cdot \Delta\mathbf{v}$ is a vector of order $2 \times 1$ as is required. If we naively chose the product $\frac{\partial \mathbf{K_{uv}}(\mathbf{v})}{\partial \mathbf{v}} \Delta\mathbf{v}$ instead of product $\left[\frac{\partial \mathbf{K_{uv}}(\mathbf{v})}{\partial \mathbf{v}} \cdot (\mathbf{I}_4 \otimes \mathbf{v})\right] \cdot \Delta\mathbf{v}$, we would find in the described way that it cannot be multiplied scalarly and that it does not exist at all. Therefore, the linearized equation is as follows

$$
\begin{aligned}
&\eta^2\omega^2\mathbf{M_u}\left(\frac{\partial^2 \mathbf{u}}{\partial \tau^2} + \frac{\partial^2 \Delta\mathbf{u}}{\partial \tau^2}\right) + 2\eta^2\omega\mathbf{M_u}\frac{\partial^2 \mathbf{u}}{\partial \tau^2}\Delta\omega + \eta\omega\mathbf{C_u}\left(\frac{\partial \mathbf{u}}{\partial \tau} + \frac{\partial \Delta\mathbf{u}}{\partial \tau}\right) \\
&+\eta\mathbf{C_u}\frac{\partial \mathbf{u}}{\partial \tau}\Delta\omega + \mathbf{K_u}(\mathbf{u}+\Delta\mathbf{u}) + \mathbf{K_{uv}}(\mathbf{v}) \cdot \mathbf{v} \\
&+\left[\mathbf{K_{uv}}(\mathbf{v}) + \frac{\partial \mathbf{K_{uv}}(\mathbf{v})}{\partial \mathbf{v}} \cdot (\mathbf{I}_4 \otimes \mathbf{v})\right] \cdot \Delta\mathbf{v} - \mathbf{P}-\Delta\mathbf{P} = \overline{\mathbf{P}}+\Delta\overline{\mathbf{P}},
\end{aligned}
$$

$$(14.55)$$

which is rewritten into the form

$$
\begin{aligned}
&\eta^2\omega^2\mathbf{M_u}\frac{\partial^2 \Delta\mathbf{u}}{\partial \tau^2} + \eta\omega\mathbf{C_u}\frac{\partial \Delta\mathbf{u}}{\partial \tau} + \mathbf{K_u}\Delta\mathbf{u} \\
&+\left[\mathbf{K_{uv}}(\mathbf{v}) + \frac{\partial \mathbf{K_{uv}}(\mathbf{v})}{\partial \mathbf{v}}(\mathbf{I}_4 \otimes \mathbf{v})\right]\Delta\mathbf{v} \\
&= -\eta^2\omega^2\mathbf{M_u}\frac{\partial^2 \mathbf{u}}{\partial \tau^2} - \eta\omega\mathbf{C_u}\frac{\partial \mathbf{u}}{\partial \tau} - \mathbf{K_u}\mathbf{u} - \mathbf{K_{uv}}(\mathbf{v})\mathbf{v} \\
&+\mathbf{P}+\overline{\mathbf{P}} + \Delta\mathbf{P}+\Delta\overline{\mathbf{P}} - \left(2\eta^2\omega\mathbf{M_u}\frac{\partial^2 \mathbf{u}}{\partial \tau^2} + \eta\mathbf{C_u}\frac{\partial \mathbf{u}}{\partial \tau}\right)\Delta\omega
\end{aligned}
$$

$$(14.56)$$

to compute unknown increments $\Delta\mathbf{u}$ and $\Delta\mathbf{v}$ on each step of the iterative procedure. By considering equation

$$
\mathbf{K_{uv}} = \frac{EA}{2l_e}\begin{bmatrix} -1 \\ 1 \end{bmatrix}[\mathbf{v}(\tau)]^{\mathrm{T}}\mathbf{K}_g,
$$

$$(14.57)$$

the matrix product $\frac{\partial \mathbf{K_{uv}}(\mathbf{v})}{\partial \mathbf{v}}(\mathbf{I}_4 \otimes \mathbf{v}) = \mathbf{G_{uv}} \in \mathbb{R}^{2\times 4}$ can be determined in the form

$$
\begin{aligned}
\mathbf{G_{uv}} &= \frac{\partial \mathbf{K_{uv}}(\mathbf{v})}{\partial \mathbf{v}}(\mathbf{I}_4 \otimes \mathbf{v}) = \frac{EA}{2l_e}\frac{\partial}{\partial \mathbf{v}}\left(\begin{bmatrix} -1 \\ 1 \end{bmatrix}\mathbf{v}^{\mathrm{T}}\mathbf{K}_g\right)(\mathbf{I}_4 \otimes \mathbf{v}) \\
&= \frac{EA}{120l_e^2}\begin{bmatrix} -\mathbf{e}_1^{\mathrm{T}}, -\mathbf{e}_2^{\mathrm{T}}, -\mathbf{e}_3^{\mathrm{T}}, -\mathbf{e}_4^{\mathrm{T}} \\ \mathbf{e}_1^{\mathrm{T}}, \mathbf{e}_2^{\mathrm{T}}, \mathbf{e}_3^{\mathrm{T}}, \mathbf{e}_4^{\mathrm{T}} \end{bmatrix}\begin{bmatrix} 36\mathbf{v} & 3l_e\mathbf{v} & -36\mathbf{v} & 3l_e\mathbf{v} \\ 3l_e\mathbf{v} & 4l_e^2\mathbf{v} & -3l_e\mathbf{v} & -l_e^2\mathbf{v} \\ -36\mathbf{v} & -3l_e\mathbf{v} & 36\mathbf{v} & -3l_e\mathbf{v} \\ 3l_e\mathbf{v} & -l_e^2\mathbf{v} & -3l_e\mathbf{v} & 4l_e^2\mathbf{v} \end{bmatrix}.
\end{aligned}
$$

$$(14.58)$$

By using matrix $\mathbf{G_{uv}}$ in Eq. (14.58) we can write the equation of increments of beam vibration in the longitudinal direction as follows

$$
\eta^2\omega^2\mathbf{M_u}\frac{\partial^2\Delta\mathbf{u}}{\partial\tau^2} + \eta\omega\mathbf{C_u}\frac{\partial\Delta\mathbf{u}}{\partial\tau} + \mathbf{K_u}\Delta\mathbf{u} + \mathbf{G_{uv}}\Delta\mathbf{v}
$$

$$
= -\left[\eta^2\omega^2\mathbf{M_u}\frac{\partial^2\mathbf{u}}{\partial\tau^2} + \eta\omega\mathbf{C_u}\frac{\partial\mathbf{u}}{\partial\tau} + \mathbf{K_u}\mathbf{u} + \mathbf{K_{uv}}\left(\mathbf{v}\right)\mathbf{v}\right]
$$

$$
+\mathbf{P}+\overline{\mathbf{P}} + \Delta\mathbf{P}+\Delta\overline{\mathbf{P}} - \left(2\eta^2\omega\mathbf{M_u}\frac{\partial^2\mathbf{u}}{\partial\tau^2} + \eta\mathbf{C_u}\frac{\partial\mathbf{u}}{\partial\tau}\right)\Delta\omega. \tag{14.59}
$$

Now we derive the equation of increments of beam vibration in the transverse direction. By introducing small perturbations (14.51) into Eq. (14.50) we get vibration equation

$$
\eta^2\left(\omega + \Delta\omega\right)^2\mathbf{M_v}\left(\frac{\partial^2\mathbf{v}}{\partial\tau^2} + \frac{\partial^2\Delta\mathbf{v}}{\partial\tau^2}\right) + \eta\left(\omega + \Delta\omega\right)\mathbf{C_v}\left(\frac{\partial\mathbf{v}}{\partial\tau} + \frac{\partial\Delta\mathbf{v}}{\partial\tau}\right)
$$
$$
+2\mathbf{K_{uv}^T}\left(\mathbf{u}+\Delta\mathbf{u}\right) + \mathbf{K_{vv}}\left(\mathbf{v}+\Delta\mathbf{v}\right)\cdot\left(\mathbf{v}+\Delta\mathbf{v}\right)
$$
$$
+\mathbf{K_v}\left(\mathbf{v}+\Delta\mathbf{v}\right) -\mathbf{Q}\left(\tau\right) - \Delta\mathbf{Q}\left(\tau\right) = \overline{\mathbf{Q}}\left(\tau\right) + \Delta\overline{\mathbf{Q}}\left(\tau\right),
$$

$$\tag{14.60}$$

which describes the new state due to the addition of small increments. The matrix product $\mathbf{K_{vv}}\left(\mathbf{v}+\Delta\mathbf{v}\right)\cdot\left(\mathbf{v}+\Delta\mathbf{v}\right)$ in Eq. (14.60) is nonlinear, so we develop it into a Taylor series and keep only the term that is linear in increments

$$
\mathbf{K_{vv}}\left(\mathbf{v}+\Delta\mathbf{v}\right)\cdot\left(\mathbf{v}+\Delta\mathbf{v}\right)
$$
$$
= \mathbf{K_{vv}}\left(\mathbf{v}\right)\cdot\mathbf{v}+ \left[\mathbf{K_{vv}}\left(\mathbf{v}\right) + \frac{\partial\mathbf{K_{vv}}(\mathbf{v})}{\partial\mathbf{v}}\cdot\left(\mathbf{I}_4\otimes\mathbf{v}\right)\right]\cdot\Delta\mathbf{v}.
$$

$$\tag{14.61}$$

Linearized equation of beam vibration in the transverse direction thus can be developed into the form

$$
\eta^2\omega^2\mathbf{M_v}\left(\frac{\partial^2\mathbf{v}}{\partial\tau^2} + \frac{\partial^2\Delta\mathbf{v}}{\partial\tau^2}\right) + 2\eta^2\omega\mathbf{M_v}\frac{\partial^2\mathbf{v}}{\partial\tau^2}\Delta\omega + \eta\omega\mathbf{C_v}\left(\frac{\partial\mathbf{v}}{\partial\tau} + \frac{\partial\Delta\mathbf{v}}{\partial\tau}\right)
$$
$$
+\eta\mathbf{C_v}\frac{\partial\mathbf{v}}{\partial\tau}\Delta\omega + 2\mathbf{K_{uv}^T}\left(\mathbf{u}+\Delta\mathbf{u}\right) + \mathbf{K_{vv}}\left(\mathbf{v}\right)\cdot\mathbf{v}
$$
$$
+ \left[\mathbf{K_{vv}}\left(\mathbf{v}\right) + \frac{\partial\mathbf{K_{vv}}(\mathbf{v})}{\partial\mathbf{v}}\cdot\left(\mathbf{I}_4\otimes\mathbf{v}\right)\right]\cdot\Delta\mathbf{v} + \mathbf{K_v}\left(\mathbf{v}+\Delta\mathbf{v}\right) -\mathbf{Q}\left(\tau\right) - \Delta\mathbf{Q}\left(\tau\right)
$$
$$
= \overline{\mathbf{Q}}\left(\tau\right) + \Delta\overline{\mathbf{Q}}\left(\tau\right).
$$

$$\tag{14.62}$$

In the resulting equation it is convenient to introduce the matrix

$$\mathbf{G}_{\mathbf{vv}} = \frac{\partial \mathbf{K}_{\mathbf{vv}}(\mathbf{v})}{\partial \mathbf{v}} = \frac{EA}{2l_e} \frac{\partial}{\partial \mathbf{v}} \left( \mathbf{K}_g \mathbf{v} \mathbf{v}^T \mathbf{K}_g \right) = \frac{EA}{2l_e} \mathbf{K}_g \left[ \frac{\partial \left( \mathbf{v} \mathbf{v}^T \right)}{\partial \mathbf{v}} \cdot \left( \mathbf{K}_g \otimes \mathbf{I}_4 \right) \right]$$

$$= \frac{EA}{2l_e} \mathbf{K}_g \left[ \left( \mathbf{v}^T \otimes \mathbf{I}_4 \right) + \mathbf{v} \cdot \left[ \mathbf{e}_1^T, \mathbf{e}_2^T, \mathbf{e}_3^T, \mathbf{e}_4^T \right] \right] \cdot \left( \mathbf{K}_g \otimes \mathbf{I}_4 \right). \tag{14.63}$$

By using the matrix $\mathbf{G}_{\mathbf{vv}}$ in explicit form (14.63), we finally get the equation of increments of beam vibration in the transverse direction in the following form

$$\eta^2 \omega^2 \mathbf{M}_{\mathbf{v}} \frac{\partial^2 \Delta \mathbf{v}}{\partial \tau^2} + \eta \omega \mathbf{C}_{\mathbf{v}} \frac{\partial \Delta \mathbf{v}}{\partial \tau} + 2 \mathbf{K}_{\mathbf{uv}}^{\mathrm{T}} \Delta \mathbf{u} + \mathbf{G}_{\mathbf{vv}} \cdot (\mathbf{I}_4 \otimes \mathbf{v}) \Delta \mathbf{v} + \mathbf{K}_{\mathbf{v}} \Delta \mathbf{v}$$
$$= -\eta^2 \omega^2 \mathbf{M}_{\mathbf{v}} \frac{\partial^2 \mathbf{v}}{\partial \tau^2} - \eta \omega \mathbf{C}_{\mathbf{v}} \frac{\partial \mathbf{v}}{\partial \tau} - 2 \mathbf{K}_{\mathbf{uv}}^{\mathrm{T}} \mathbf{u} - \mathbf{K}_{\mathbf{vv}}(\mathbf{v}) \mathbf{v} - \mathbf{K}_{\mathbf{v}} \mathbf{v}$$
$$+ \mathbf{Q}(\tau) + \overline{\mathbf{Q}}(\tau) + \Delta \mathbf{Q}(\tau) + \Delta \overline{\mathbf{Q}}(\tau) - \left( 2 \eta^2 \omega \mathbf{M}_{\mathbf{v}} \frac{\partial^2 \mathbf{v}}{\partial \tau^2} + \eta \mathbf{C}_{\mathbf{v}} \frac{\partial \mathbf{v}}{\partial \tau} \right) \Delta \omega. \tag{14.64}$$

### 14.4.3  Application of the Galerkin Procedure

Galerkin procedure represents the second step that together with Newton-Raphson iterative process constitutes the IHB method. In this procedure, linearized equations of increments of beam vibration in the longitudinal and transversal direction, respectively are premultiplied by vectors of arbitrary variations of displacements and integrated over one period of the vibration. The equation of increments of beam vibration in the longitudinal direction passes in the Galerkin procedure into variational equation

$$\left[ \frac{1}{\pi} \int_0^{2\pi} \delta \mathbf{b}^{\mathrm{T}} \mathbf{Y}_{\mathbf{u}}^{\mathrm{T}} \left( \eta^2 \omega^2 \mathbf{M}_{\mathbf{u}} \frac{\partial^2 \mathbf{Y}_{\mathbf{u}}}{\partial \tau^2} + \eta \omega \mathbf{C}_{\mathbf{u}} \frac{\partial \mathbf{Y}_{\mathbf{u}}}{\partial \tau} + \mathbf{K}_{\mathbf{u}} \mathbf{Y}_{\mathbf{u}} \right) d\tau \right] \Delta \mathbf{b}$$

$$+ \left( \frac{1}{\pi} \int_0^{2\pi} \delta \mathbf{b}^{\mathrm{T}} \mathbf{Y}_{\mathbf{u}}^{\mathrm{T}} \mathbf{G}_{\mathbf{uv}} \mathbf{Y}_{\mathbf{v}} d\tau \right) \Delta \mathbf{c}$$

$$= -\frac{1}{\pi} \int_0^{2\pi} \delta \mathbf{b}^{\mathrm{T}} \mathbf{Y}_{\mathbf{u}}^{\mathrm{T}} \left( \eta^2 \omega^2 \mathbf{M}_{\mathbf{u}} \frac{\partial^2 \mathbf{Y}_{\mathbf{u}}}{\partial \tau^2} + \eta \omega \mathbf{C}_{\mathbf{u}} \frac{\partial \mathbf{Y}_{\mathbf{u}}}{\partial \tau} + \mathbf{K}_{\mathbf{u}} \mathbf{Y}_{\mathbf{u}} \right) d\tau \cdot \mathbf{b}$$

$$- \frac{1}{\pi} \int_0^{2\pi} \delta \mathbf{b}^{\mathrm{T}} \mathbf{Y}_{\mathbf{u}}^{\mathrm{T}} \mathbf{K}_{\mathbf{uv}}(\mathbf{v}) \mathbf{Y}_{\mathbf{v}} d\tau \cdot \mathbf{c} + \frac{1}{\pi} \int_0^{2\pi} \delta \mathbf{b}^{\mathrm{T}} \mathbf{Y}_{\mathbf{u}}^{\mathrm{T}} \left( \mathbf{P} + \overline{\mathbf{P}} + \Delta \mathbf{P} + \Delta \overline{\mathbf{P}} \right) d\tau$$

$$- \left[ \frac{1}{\pi} \int_0^{2\pi} \delta \mathbf{b}^{\mathrm{T}} \mathbf{Y}_{\mathbf{u}}^{\mathrm{T}} \left( 2 \eta^2 \omega \mathbf{M}_{\mathbf{u}} \frac{\partial^2 \mathbf{Y}_{\mathbf{u}}}{\partial \tau^2} + \eta \mathbf{C}_{\mathbf{u}} \frac{\partial \mathbf{Y}_{\mathbf{u}}}{\partial \tau} \right) \mathbf{b} d\tau \right] \Delta \omega. \tag{14.65}$$

The variation of the vector of Fourier coefficients of vibration in the longitudinal direction $\delta\mathbf{b}^T$ is arbitrary, so the variational equation can be shortened to produce the linear matrix algebraic equation of incremental vectors of Fourier coefficients of beam vibration in the longitudinal direction

$$\mathbf{H_u}\,\Delta\mathbf{b} + \mathbf{H_{uv}}\,\Delta\mathbf{c} = \mathbf{R_u} + \mathbf{R_{uv}} + \mathbf{F_u} + \Delta\mathbf{F_u} + \mathbf{S_u}\,\Delta\omega, \tag{14.66}$$

where $\mathbf{H_u}$ and $\mathbf{H_{uv}}$ are two tangential matrices of equation of increments in the longitudinal direction

$$\mathbf{H_u} = \frac{1}{\pi}\int\limits_0^{2\pi} \left( \eta^2\omega^2\mathbf{Y_u^T}\mathbf{M_u}\frac{\partial^2\mathbf{Y_u}}{\partial\tau^2} + \eta\omega\mathbf{Y_u^T}\mathbf{C_u}\frac{\partial\mathbf{Y_u}}{\partial\tau} + \mathbf{Y_u^T}\mathbf{K_u}\mathbf{Y_u} \right) d\tau, \tag{14.67a}$$

$$\mathbf{H_{uv}} = \frac{1}{\pi}\int\limits_0^{2\pi}\mathbf{Y_u^T}\mathbf{G_{uv}}\mathbf{Y_v}d\tau \tag{14.67b}$$

and $\Delta\mathbf{b}$ and $\Delta\mathbf{c}$ are vectors of Fourier increments, respectively. The right hand side of equation of increments in the longitudinal direction consists of residual vectors $\mathbf{R_u}$ and $\mathbf{R_{uv}}$,

$$\mathbf{R_u} = -\frac{1}{\pi}\int\limits_0^{2\pi} \left( \eta^2\omega^2\mathbf{Y_u^T}\mathbf{M_u}\frac{\partial^2\mathbf{Y_u}}{\partial\tau^2} + \eta\omega\mathbf{Y_u^T}\mathbf{C_u}\frac{\partial\mathbf{Y_u}}{\partial\tau} + \mathbf{Y_u^T}\mathbf{K_u}\mathbf{Y_u} \right) d\tau \cdot \mathbf{b}, \tag{14.67c}$$

$$\mathbf{R_{uv}} = -\frac{1}{\pi}\int\limits_0^{2\pi}\mathbf{Y_u^T}\mathbf{K_{uv}}\left(\mathbf{v}\right)\mathbf{Y_v}d\tau \cdot \mathbf{c}, \tag{14.67d}$$

the vectors of external forces and the corresponding vectors of increments in the longitudinal direction,

$$\mathbf{F_u} = \frac{1}{\pi}\int\limits_0^{2\pi}\mathbf{Y_u^T}\left(\mathbf{P}+\overline{\mathbf{P}}\right)d\tau, \quad \Delta\mathbf{F_u} = \frac{1}{\pi}\int\limits_0^{2\pi}\mathbf{Y_u^T}\left(\Delta\mathbf{P}+\Delta\overline{\mathbf{P}}\right)d\tau, \tag{14.67e}$$

and the gradient vector in the longitudinal direction

$$\mathbf{S_u} = -\frac{1}{\pi}\int\limits_0^{2\pi} \left( 2\eta^2\omega\mathbf{Y_u^T}\mathbf{M_u}\frac{\partial^2\mathbf{Y_u}}{\partial\tau^2} + \eta\mathbf{Y_u^T}\mathbf{C_u}\frac{\partial\mathbf{Y_u}}{\partial\tau} \right)\mathbf{b}d\tau. \tag{14.67f}$$

The definite integrals in Eq. (14.67a–f) are the integrals of matrices with elements containing trigonometric functions. All these integrals can be calculated in advance. This gives a linear matrix algebraic equation for unknown increments $\Delta \mathbf{b}$, $\Delta \mathbf{c}$, $\Delta \omega$ and $\Delta \mathbf{F}_u$. If we do not change the excitation frequency $\omega$ in the Newton-Raphson iterative procedure, then the increment $\Delta \omega$ is equal zero. If we additionally maintain constant values of the vectors $\mathbf{P}$ and $\overline{\mathbf{P}}$, the increments $\Delta \mathbf{P}$ and $\Delta \overline{\mathbf{P}}$ and hence the increment $\Delta \mathbf{F}_u$ are also equal to the zero vectors. The vectors $\mathbf{R}_u$ and $\mathbf{R}_{uv}$ represent residual vectors in the algebraic equation of unknown increments at each iteration step of the Newton-Raphson procedure in solving the equation of beam vibration in the longitudinal direction. In other words, the vector sum $\mathbf{R}_u + \mathbf{R}_{uv} + \mathbf{F}_u$ expresses the magnitudes of the unbalanced harmonic components of the beam vibration in the longitudinal direction. The purpose of the Newton-Raphson iterative procedure is to reduce some chosen norm of this sum to such a small value that it satisfies the prescribed tolerance criterion or that the vector sum $\mathbf{R}_u + \mathbf{R}_{uv} + \mathbf{F}_u$ eventually becomes equal to the zero vector. It is understandable that Eq. (14.66) is not yet sufficient to determine the increments of the Fourier coefficients $\Delta \mathbf{b}$ and $\Delta \mathbf{c}$, but we also need the variational equation of beam vibration in the transversal direction

$$
\begin{aligned}
&\left( \tfrac{1}{\pi} \int_0^{2\pi} \delta \mathbf{c}^{\mathrm{T}} \mathbf{Y}_{\mathbf{v}}^{\mathrm{T}} 2 \mathbf{K}_{\mathbf{uv}}^{\mathrm{T}} \mathbf{Y}_{\mathbf{u}} \mathrm{d}\tau \right) \Delta \mathbf{b} + \left[ \tfrac{1}{\pi} \int_0^{2\pi} \delta \mathbf{c}^{\mathrm{T}} \mathbf{Y}_{\mathbf{v}}^{\mathrm{T}} \left( \eta^2 \omega^2 \mathbf{M}_{\mathbf{v}} \tfrac{\partial^2 \mathbf{Y}_{\mathbf{v}}}{\partial \tau^2} \right. \right. \\
&\left. \left. + \eta \omega \mathbf{C}_{\mathbf{v}} \tfrac{\partial \mathbf{Y}_{\mathbf{v}}}{\partial \tau} + \mathbf{G}_{\mathbf{vv}} \cdot (\mathbf{I_4} \otimes \mathbf{Y}_{\mathbf{v}} \mathbf{c}) \, \mathbf{Y}_{\mathbf{v}} + \mathbf{K}_{\mathbf{v}} \mathbf{Y}_{\mathbf{v}} \right) \mathrm{d}\tau \right] \Delta \mathbf{c} \\
&= -\left( \tfrac{1}{\pi} \int_0^{2\pi} \delta \mathbf{c}^{\mathrm{T}} \mathbf{Y}_{\mathbf{v}}^{\mathrm{T}} 2 \mathbf{K}_{\mathbf{uv}}^{\mathrm{T}} \mathbf{Y}_{\mathbf{u}} \mathrm{d}\tau \right) \mathbf{b} \\
&- \left[ \tfrac{1}{\pi} \int_0^{2\pi} \delta \mathbf{c}^{\mathrm{T}} \mathbf{Y}_{\mathbf{v}}^{\mathrm{T}} \left( \eta^2 \omega^2 \mathbf{M}_{\mathbf{v}} \tfrac{\partial^2 \mathbf{Y}_{\mathbf{v}}}{\partial \tau^2} + \eta \omega \mathbf{C}_{\mathbf{v}} \tfrac{\partial \mathbf{Y}_{\mathbf{v}}}{\partial \tau} + \mathbf{K}_{\mathbf{vv}} \left( \mathbf{v} \right) \mathbf{Y}_{\mathbf{v}} \right. \right. \\
&\left. + \mathbf{K}_{\mathbf{v}} \mathbf{Y}_{\mathbf{v}} \right) \mathrm{d}\tau \right] \mathbf{c} + \tfrac{1}{\pi} \int_0^{2\pi} \delta \mathbf{c}^{\mathrm{T}} \mathbf{Y}_{\mathbf{v}}^{\mathrm{T}} \left[ \mathbf{Q} \left( \tau \right) + \overline{\mathbf{Q}} \left( \tau \right) + \Delta \mathbf{Q} \left( \tau \right) + \Delta \overline{\mathbf{Q}} \left( \tau \right) \right] \mathrm{d}\tau \\
&- \left[ \tfrac{1}{\pi} \int_0^{2\pi} \delta \mathbf{c}^{\mathrm{T}} \mathbf{Y}_{\mathbf{v}}^{\mathrm{T}} \left( 2 \eta^2 \omega \mathbf{M}_{\mathbf{v}} \tfrac{\partial^2 \mathbf{Y}_{\mathbf{v}}}{\partial \tau^2} + \eta \mathbf{C}_{\mathbf{v}} \tfrac{\partial \mathbf{Y}_{\mathbf{v}}}{\partial \tau} \right) \mathbf{c} \mathrm{d}\tau \right] \Delta \omega.
\end{aligned}
$$

$$(14.68)$$

The variation of the vector of Fourier coefficients of vibration in the transversal direction $\delta \mathbf{c}^{\mathrm{T}}$ is arbitrary, so the variational equation (14.68) can be shortened, resulting in the linear matrix equation of the increments of the vectors of Fourier coefficients of the beam vibration in the transversal direction $\Delta \mathbf{b}$, $\Delta \mathbf{c}$ and increments $\Delta \omega$ and $\Delta \mathbf{F}_{\mathbf{v}}$

$$\mathbf{H}_{\mathbf{vu}} \Delta \mathbf{b} + \mathbf{H}_{\mathbf{v}} \Delta \mathbf{c} = \mathbf{R}_{\mathbf{vu}} + \mathbf{R}_{\mathbf{v}} + \mathbf{F}_{\mathbf{v}} + \Delta \mathbf{F}_{\mathbf{v}} + \mathbf{S}_{\mathbf{v}} \Delta \omega, \qquad (14.69)$$

where $\mathbf{H}_{\mathbf{vu}}$ and $\mathbf{H}_{\mathbf{v}}$ denote the tangential matrices in the transversal direction

$$\mathbf{H_{vu}} = \frac{1}{\pi} \int_0^{2\pi} 2\mathbf{Y_v^T K_{uv}^T Y_u} d\tau, \tag{14.70a}$$

$$\mathbf{H_v} = \frac{1}{\pi} \int_0^{2\pi} \left( \eta^2 \omega^2 \mathbf{Y_v^T M_v} \frac{\partial^2 \mathbf{Y_v}}{\partial \tau^2} + \eta \omega \mathbf{Y_v^T C_v} \frac{\partial \mathbf{Y_v}}{\partial \tau} \right.$$
$$\left. + \mathbf{Y_v^T G_{vv}} \cdot (\mathbf{I_4} \otimes \mathbf{Y_v c}) \, \mathbf{Y_v} + \mathbf{Y_v^T K_v Y} \right) d\tau, \tag{14.70b}$$

$\mathbf{R_{vu}}$ and $\mathbf{R_v}$ denote the residual vectors in the transversal direction

$$\mathbf{R_{vu}} = - \left( \frac{1}{\pi} \int_0^{2\pi} 2\mathbf{Y_v^T K_{uv}^T Y_u} d\tau \right) \mathbf{b}, \tag{14.70c}$$

$$\mathbf{R_v} = - \left[ \frac{1}{\pi} \int_0^{2\pi} \left( \eta^2 \omega^2 \mathbf{Y_v^T M_v} \frac{\partial^2 \mathbf{Y_v}}{\partial \tau^2} + \eta \omega \mathbf{Y_v^T C_v} \frac{\partial \mathbf{Y_v}}{\partial \tau} \right. \right.$$
$$\left. \left. + \mathbf{Y_v^T K_{vv}} \, (\mathbf{v}) \, \mathbf{Y_v} + \mathbf{Y_v^T K_v Y_v} \right) d\tau \right] \mathbf{c}, \tag{14.70d}$$

vector of external transverse forces and the corresponding vector of increments of transverse forces are denoted by

$$\mathbf{F_v} = \frac{1}{\pi} \int_0^{2\pi} \mathbf{Y_v^T} \left[ \mathbf{Q}(\tau) + \overline{\mathbf{Q}}(\tau) \right] d\tau, \, \Delta\mathbf{F_v} = \frac{1}{\pi} \int_0^{2\pi} \mathbf{Y_v^T} \left[ \Delta\mathbf{Q}(\tau) + \Delta\overline{\mathbf{Q}}(\tau) \right] d\tau,$$
$$\tag{14.70e}$$

and the gradient vector in the transversal direction is denoted by

$$\mathbf{S_v} = -\frac{1}{\pi} \int_0^{2\pi} \left( 2\eta^2 \omega \mathbf{Y_v^T M_v} \frac{\partial^2 \mathbf{Y_v}}{\partial \tau^2} + \eta \mathbf{Y_v^T C_v} \frac{\partial \mathbf{Y_v}}{\partial \tau} \right) \mathbf{c} d\tau. \tag{14.70f}$$

The vectors $\mathbf{R_{vu}}$ and $\mathbf{R_v}$ represent residual vectors in the algebraic equation of unknown increments at each iteration step of the Newton-Raphson procedure in solving the equation of beam vibration in the transversal direction. In other words, the vector sum $\mathbf{R_{vu}} + \mathbf{R_v} + \mathbf{F_v}$ represents the unbalanced harmonic components of the beam vibration in the transversal direction. Again, the purpose of the Newton-Raphson iterative procedure is to reduce the chosen norm of this sum to a small value that satisfies the prescribed tolerance criterion or that the vector sum $\mathbf{R_{vu}} + \mathbf{R_v} + \mathbf{F_v}$ eventually becomes equal to the zero vector. In the case that both vector sums $\mathbf{R_u} + \mathbf{R_{uv}} + \mathbf{F_u}$

and $\mathbf{R_{vu}} + \mathbf{R_v} + \mathbf{F_v}$ are zero vectors, then vectors $\mathbf{b}$ and $\mathbf{c}$ are exact solution of the linear matrix algebraic equations (14.66) and (14.69). Such a case is a rare exception, in practice we have to settle for an approximate solution. An approximate solution in the Newton-Raphson iterative procedure is obtained if we achieve the fulfillment of the tolerance criterion, that is $\|\mathbf{R_u} + \mathbf{R_{uv}} + \mathbf{F_u}\| \le tol$ , $\|\mathbf{R_{vu}} + \mathbf{R_v} + \mathbf{F_v}\| \le tol$. When the tolerance criterion is met, the iterative procedure is stopped and computed vectors $\mathbf{b}^{new} = \mathbf{b} + \Delta\mathbf{b}$, $\mathbf{c}^{new} = \mathbf{c} + \Delta\mathbf{c}$ in the last iteration represent the approximate solution. During the Newton-Raphson iterative procedure it is usually assumed, that parameters $\omega$, $\mathbf{P}$, $\overline{\mathbf{P}}$, $\mathbf{Q}$ and $\overline{\mathbf{Q}}$ are kept constant so that the corresponding increments are zero, $\Delta\omega = 0$, $\mathbf{\Delta P = 0}$, $\mathbf{\Delta\overline{P} = 0}$, $\mathbf{\Delta Q = 0}$ and $\mathbf{\Delta\overline{Q} = 0}$. In this way we ensure that the system of algebraic equations (14.66), (14.69) has as many equations as there are unknowns.

The iterative Newton-Raphson procedure is usually followed by the augmentation, in which the value of one of the parameters $\mathbf{P}$, $\overline{\mathbf{P}}$, $\mathbf{Q}, \overline{\mathbf{Q}}$ or $\omega$ is changed by adding increments $\mathbf{\Delta P}, \Delta\overline{\mathbf{P}}$, $\mathbf{\Delta Q}, \Delta\overline{\mathbf{Q}}$ or $\Delta\omega$. After augmentation, we again use the Newton-Raphson iterative procedure, in which we compute the approximate solution of the new state. By exchanging the Newton-Rapson iterative procedure and the augmentation, we can construct the course of various branches of solutions. The exchange of the Newton-Raphson iterative procedure and the augmentation process in principle ensures the tracing of individual branches of the beam vibration solutions until the turning and bifurcation points are encountered. The branch cannot be parameterized in the neighbourhood of folds because the tangential matrices become singular at turning points. To overcome this shortcoming and to reduce the number of iterations an arc length method can be applied [15].

## 14.5  Conclusion

The coupling of the FEM with IHB method is presented in this chapter to enable the computation of nonlinear longitudinal and transversal periodic vibrations of beams, respectively, where the axial and flexural deformations are coupled due the axial force acting along the axis of the beam element. The finite element discretization of the beam is performed using the isoparametric shape functions in the form of Hermite polynomials that leads to the formulation of the nonlinear temporal vibration problem in terms of beam element nodal displacement vectors. The IHB method with single time scale is used for solving the aforementioned problem assuming the periodic solutions in the form of truncated Fourier series, where the introduced subharmonic factor allows the treatment of fundamental, superharmonic and subharmonic resonances. The possibility of introducing the multiple time scales indicates that the presented coupling of the FEM with the IHB method has a substantial potential for further development. The application of the IHB method is done in two steps, where the first step consists of the Newton-Raphson iterative procedure and the second step performs the Galerkin procedure. The Newton-Raphson iterative procedure is formulated for treatment of the linearized temporal vibration problem in terms of

the vectors of increments of Fourier coefficients, whereas the Galerkin procedure transforms the corresponding variational equations into system of linear algebraic equations for unknown vectors of increments. The solving of the temporal vibration problem is done by updating the vector of Fourier coefficients in each iteration until the norms of the residual vectors meet the tolerance criterion. The power of the IHB method is most strongly demonstrated in the construction of various branches of the beam vibration solutions by means of the exchanging of the Newton-Raphson iterative procedure with the augmentation of the selected system parameters and the use of the arc length parametrization.

# References

1. Amato M, Elishakoff I, Reddy JN (2021) Flutter of a multicomponent beam in a supersonic flow. AIAA J 59(11):4342–4353
2. Bathe KJ (2014) Finite element procedures, 2nd edn., Wattertown, MA
3. Chen SH, Cheung YK (1996) A modified Lindstedt-Poincare method for strongly non-linear two degree-of-freedom system. J Sound Vib 193(4):751–762
4. Cherdantsev M, Cherednichenko KD (2012) Two-scale $\Gamma$-convergence of integral functionals and its application to homogenisation of nonlinear high-contrast periodic composites. Archive Ration Mech Anal 204(2):445–478
5. Elishakoff I, Fang T, Jiang C (2021) Free, forced and random vibrations of a beam composed of highly contrasting materials. Appl Math Model 89:1696–1720
6. Haug EJ, Choi KK, Komkov V (1986) Design sensitivity analysis of structural systems. Academic Inc, Orlando
7. Kaplunov J, Prikazchikov D, Sergushova O (2016) Multi-parametric analysis of the lowest natural frequencies of strongly inhomogeneous elastic rods. J Sound Vib 366:264–276
8. Kaplunov J, Prikazchikov DA, Prikazchikova LA (2017) Dispersion of elastic waves in a strongly inhomogeneous three-layered plate. Int J Solids Struct 113:169–179
9. Kaplunov J, Prikazchikov DA, Prikazchikova LA, Sergushova O (2019) The lowest vibration spectra of multi-component structures with contrast material properties. J Sound Vib 445:132–147
10. Kaplunov J, Prikazchikova L, Alkinidri M (2021) Antiplane shear of an asymmetric sandwich plate. Continuum Mech Thermodyn 33(4):1247–1262
11. Leung AYT, Fung TC (1989) Non-linear steady state vibration of frames by finite element method. Int J Numer Meth Eng 28:1599–1618
12. Meirowitch L (1986) Elements of vibration analysis. McGraw Hill, Boston
13. Nayfeh AH, Mook DT (1979) Nonlinear oscillations. Wiley, New York
14. Prikazchikova L, Ece Aydin Y, Erbaş B, Kaplunov J (2020) Asymptotic analysis of an anti-plane dynamic problem for a three-layered strongly inhomogeneous laminate. Math Mech Solids 25(1):3–16
15. Pušenjak RR, Oblak MM (2004) Incremental harmonic balance method with multiple time variables for dynamical systems with cubic non-linearities. Int J Numer Meth Eng 59:255–292
16. Pušenjak RR (2008) Extended Lindstedt-Poincare method for non-stationary resonances of dynamical systems with cubic nonlinearities. J Sound Vib 314:194–216
17. Pušenjak RR, Oblak MM, Tičar I (2010) Modified Lindstedt-Poincare method with multiple time scales for combination resonance of damped dynamical systems with strong non-linearities. Int J Nonlinear Sci Numer Simul 11(3):173–201
18. Şahin O, Erbaş B, Kaplunov J, Savšek T (2020) The lowest vibration modes of an elastic beam composed of alternating stiff and soft components. Arch Appl Mech 90(2):339–352

19. Zienkiewicz OC (1977) The finite element method. McGraw Hill, New York
20. Zupančič B, Prokop Y, Nikonov A (2021) FEM analysis of dispersive elastic waves in three-layered composite plates with contrast properties. Finite Elem Anal Des 193:103553